Universität Passau
Department of Informatics and Mathematics
Institute for Computer Science
Embedded Interactive Systems Laboratory

Cooperative Relative Positioning for Vehicular Environments

Fabian de Ponte Müller

Vollständiger Abdruck der von der Fakultät für Informatik und Mathematik der Universität Passau zur Erlangung des akademischen Grades eines

Doktor rerum naturalium (Dr. rer. nat.)

genehmigten Dissertation.

Vorsitzender	Prof. Dr. Brigitte Forster-Heinlein
Prüfer der Disseration:	1. Prof. Dr. Matthias Kranz
	2. Prof. Dr. Frank Kargl

Die Disseration wurde am 08.09.2016 bei der Universität Passau eingereicht und durch die Fakultät für Informatik und Mathematik am 20.12.2017 angenommen.

Kurzfassung

Fahrerassistenzsysteme sind ein wesentlicher Baustein zur Steigerung der Sicherheit im Straßenverkehr. Vor allem sicherheitsrelevante Applikationen benötigen eine genaue Information über den Ort und der Geschwindigkeit der Fahrzeuge in der unmittelbaren Umgebung, um mögliche Gefahrensituationen vorherzusehen, den Fahrer zu warnen oder eigenständig einzugreifen. Repräsentative Beispiele für Assistenzsysteme, die auf eine genaue, kontinuierliche und zuverlässige Relativpositionierung anderer Verkehrsteilnehmer angewiesen sind, sind Notbremsassitenten, Spurwechselassitenten und Abstandsregeltempomate.

Moderne Lösungsansätze benutzen Umfeldsensorik wie zum Beispiel Radar, Laser Scanner oder Kameras, um die Position benachbarter Fahrzeuge zu schätzen. Dieser Sensorsysteme gemeinsame Nachteile sind deren limitierte Erfassungsreichweite und die Notwendigkeit einer direkten und nicht blockierten Sichtlinie zum Nachbarfahrzeug. Kooperative Lösungen basierend auf einer Fahrzeug-zu-Fahrzeug Kommunikation können die eigene Wahrnehmungsreichweite erhöhen, in dem Positionsinformationen zwischen den Verkehrsteilnehmern ausgetauscht werden.

In dieser Dissertation soll die Möglichkeit der kooperativen Relativpositionierung von Straßenfahrzeugen mittels Fahrzeug-zu-Fahrzeug Kommunikation auf ihre Genauigkeit, Kontinuität und Robustheit untersucht werden. Anstatt die in jedem Fahrzeug unabhängig ermittelte Position zu übertragen, werden in einem neuartigem Ansatz GNSS-Rohdaten, wie Pseudoranges und Doppler-Messungen, ausgetauscht. Dies hat den Vorteil, dass sich korrelierte Fehler in beiden Fahrzeugen potentiell herauskürzen. Dies wird in dieser Dissertation mathematisch untersucht, simulativ modelliert und experimentell verifiziert. Um die Zuverlässigkeit und Kontinuität auch in "gestörten" Umgebungen zu erhöhen, werden in einem Bayesischen Filter die GNSS-Rohdaten mit Inertialsensormessungen aus zwei Fahrzeugen fusioniert. Die Validierung des Sensorfusionsansatzes wurde im Rahmen dieser Dissertation in einem Verkehrs- sowie in einem GNSS-Simulator durchgeführt. Zur experimentellen Untersuchung wurden zwei Testfahrzeuge mit den verschiedenen Sensoren ausgestattet und Messungen in diversen Umgebungen gefahren.

In dieser Arbeit wird gezeigt, dass auf Autobahnen, die Relativposition eines anderen Fahrzeugs mit einer Genauigkeit von unter einem Meter kontinuierlich geschätzt werden kann. Eine hohe Zuverlässigkeit in der longitudinalen und lateralen Richtung können erzielt werden und das System erweist 90 % der Zeit eine Unsicherheit unter 2.5 m. In ländlichen Umgebungen wächst die Unsicherheit in der relativen Position. Mit Hilfe der on-board Sensoren können Fehler bei der Fahrt durch Wälder und Dörfer korrekt gestützt werden. In städtischen Umgebungen werden die Limitierungen des Systems deutlich. Durch die erschwerte Schätzung der Fahrtrichtung des Ego-Fahrzeugs ist vor Allem die longitudinale Komponente der Relativen Position in städtischen Umgebungen stark verfälscht.

Abstract

Advanced driver assistance systems play an important role in increasing the safety on today's roads. The knowledge about the other vehicles' positions is a fundamental prerequisite for numerous safety critical applications, making it possible to foresee critical situations, warn the driver or autonomously intervene. Forward collision avoidance systems, lane change assistants or adaptive cruise control are examples of safety relevant applications that require an accurate, continuous and reliable relative position of surrounding vehicles.

Currently, the positions of surrounding vehicles is estimated by measuring the distance with e.g. radar, laser scanners or camera systems. However, all these techniques have limitations in their perception range, as all of them can only detect objects in their line-of-sight. The limited perception range of today's vehicles can be extended in future by using cooperative approaches based on Vehicle-to-Vehicle (V2V) communication.

In this thesis, the capabilities of cooperative relative positioning for vehicles will be assessed in terms of its accuracy, continuity and reliability. A novel approach where Global Navigation Satellite System (GNSS) raw data is exchanged between the vehicles is presented. Vehicles use GNSS pseudorange and Doppler measurements from surrounding vehicles to estimate the relative positioning vector in a cooperative way. In this thesis, this approach is shown to outperform the absolute position subtraction as it is able to effectively cancel out common errors to both GNSS receivers. This is modeled theoretically and demonstrated empirically using simulated signals from a GNSS constellation simulator.

In order to cope with GNSS outages and to have a sufficiently good relative position estimate even in strong multipath environments, a sensor fusion approach is proposed. In addition to the GNSS raw data, inertial measurements from speedometers, accelerometers and turn rate sensors from each vehicle are exchanged over V2V communication links. A Bayesian approach is applied to consider the uncertainties inherently to each of the information sources. In a dynamic Bayesian network, the temporal relationship of the relative position estimate is predicted by using relative vehicle movement models.

Also real world measurements in highway, rural and urban scenarios are performed in the scope of this work to demonstrate the performance of the cooperative relative positioning approach based on sensor fusion. The results show that the relative position of another vehicle towards the ego vehicle can be estimated with sub-meter accuracy in highway scenarios. Here, good reliability and 90 % availability with an uncertainty of less than 2.5 m is achieved. In rural environments, drives through forests and towns are correctly bridged with the support of on-board sensors. In an urban environment, the difficult estimation of the ego vehicle heading has a mayor impact in the relative position estimate, yielding large errors in its longitudinal component.

Contents

Chapter 1.

Introduction

1.1. Intelligent Transportation Systems

Society faces the strong need for personal mobility. Every European citizen traveled 12.869 km inside Europe in the year 2010. Road transport represents the largest share with 73,7% of all displacements. Passengers that traveled by plane account for a share of only 8.2% [1]. Almost half of the transport of goods inside the European Union occurs over roads. Both, passenger and freight transport are growing from year to year. This increasing trend over the last decades has also strong economical and environmental implications. Further increase in the traffic density leads to more congestion and environmental pollution. The CO_2 emissions from road transport have increased by almost 23 % in the period from 1990 to 2010 [1].

In the context of increasing road traffic, safety is an important issue to account for. In 2011, 30.268 casualties were counted in road accidents in Europe [2]. Although this figure steadily decreases from year to year [3], huge efforts are made in further minimizing the number of accidents and their consequences. Over 100 Million road accidents involving personal injury and incurring in high material costs occur every year in Europe. Thus, along with the high human and societal costs, road accidents produce an important economic cost. In 2011, a white paper from the European Commission proposed an ambitious target: achieving zero casualties on the road by 2050 [4]. This goal is known now as *Zero Vision*.

Many safety systems have been progressively introduced since the three-point seat belt was first fitted into commercial vehicles in the 1960's and was made mandatory in the 1970's. Seat belts belong to the category of so-called passive safety systems, which aim at reducing the consequences of an accident. Airbags, deformation zones, and enforced body structures are further examples of passive safety systems. Active safety systems, on the other hand, aim at avoiding dangerous situations. Active safety systems that can be encountered in today's vehicles are, for example, Anti-lock Braking Systems (ABSs), that prevent the wheels from blocking and loose steering control of the vehicle, or Electronic Stability Programs (ESPs), that aim at avoiding vehicle's skidding and mitigating the effects of driver's over- and under-steering.

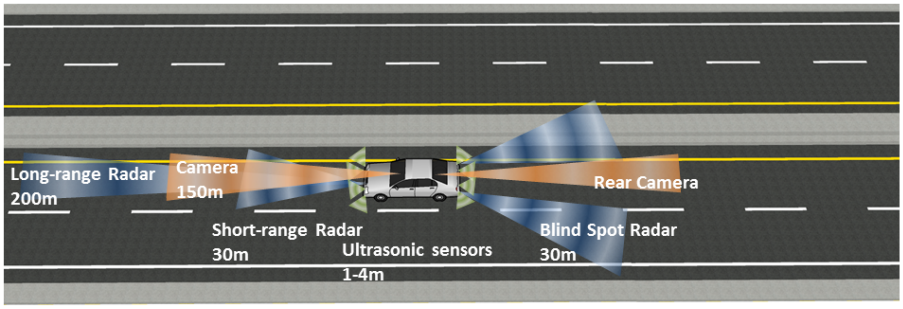

Figure 1.1.: To perceive the immediate environment of the vehicle, radar, camera and ultrasonic sensors are installed in modern vehicles. Automatic parking assistants, automatic cruise control or forward collision applications use this information to make driving safer and more comfortable.

Information and Communication Technologies (ICT) are expected to boost the development of the second generation of active safety systems [5]. The term Intelligent Transportation Systems (ITS) embraces all strategies where new technologies are brought into the transportation domain in order to increase safety, efficiency, mobility and comfort. In the special case of road transport, these include technological advances for users, vehicles, infrastructure and transportation authorities. Especially in road vehicles, great advances in sensor and actuator technologies and the rapid development of processing capabilities in the last years, have promoted the introduction of so-called Advanced Driver Assistance Systems (ADASs). These systems are developed to support, complement and even substitute the driver in the complex task of controlling a vehicle. ADASs warn the driver about potential risks, maintain safety distances to the vehicle driving in front, keep the vehicle on its lane, monitor the blind spot of the driver, and avoid collisions with other vehicles or pedestrians by e.g. automatically braking down the vehicle. These automated systems are paving the way towards fully autonomous vehicles.

Analogous to the term "fly-by-wire" used in the aeronautic industry, "drive-by-wire" refers to the use of electrical systems to replace traditionally mechanical actuators and linkages [6]. These technologies have fostered the development of semi-autonomous or fully-autonomous driver assistance systems, such as collision avoidance systems, Automatic Cruise Control (ACC) or parking assistants. Sensors, on the other end, provide the required perception of the environment that the driver assistance system needs (see Figure 1.1). While ultrasonic sensors cover the short-range distance up to several meters, cameras, radar sensors and laser scanners cover the medium-range distance up to 100 meters. Dedicated ACC long-range radars have even an extended range of up to 200 meters[1].

However, all of these sensors have some common limitations. The distance of up to 200 meters is of special relevance because of the risk of collision [7]. This corresponds to a 5-second-reaction-

[1]Bosch LRR3

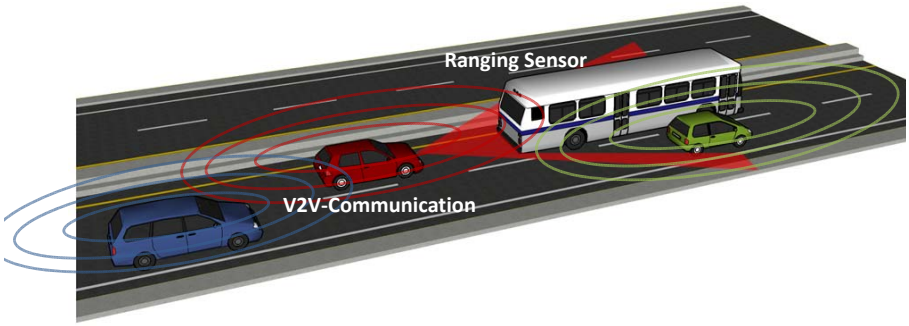

Figure 1.2.: Cooperative approaches based on direct communication between vehicles are able to extend the perception range of the ego vehicle beyond the LoS of current ranging sensors.

time when driving at 150 km/h, which can be regarded as safe enough to warn the driver, start breaking smoothly or hand over the control of the vehicle. Although most of the ranging sensors are able to cover this area, their main drawback is the Line-of-Sight (LoS) requirement. Radar, laser scanners and vision based systems are not able to detect obstacles or track vehicles that are hidden by other vehicles or drive behind curves or crests. Some applications, as for instance cooperative ACC or intersection assistants could highly profit from an extended perception range beyond the LoS.

The advent of inter-vehicle communication, also known as Vehicle-to-Vehicle (V2V) communication offers the potential of an increased perception range to driver assistance systems. In the last decade, standardization organizations in the United States, Europe and Japan have worked towards the adoption of a common standard for V2V communication. Already in 1998, the US Federal Communications Commission allocated 75 MHz of spectrum in the 5.9 GHz band to be used for ITS [8]. In 2008, the European Commission allocated 30 MHz in this same band for this purpose[9]. IEEE 802.11p, an amendment to the IEEE 802.11 communications standard for wireless local area networks, was adopted for the lower layer communication, namely physical and medium access layers [10]. The European counterpart to IEEE 802.11p is ITS-G5 which is standardized by the European Telecommunications Standards Institute (ETSI) [11].

This communication technology enables vehicles to exchange information directly between each other or with road side infrastructure over a distance up to 1000 m. Hence, V2V communication is able to potentially provide an extension of the perception range of the vehicle beyond what is possible with the aforementioned ranging sensors (see Figure 1.2). V2V communication has the possibility to enhance and complement modern driver assistance systems with external sources of information. For instance, ACC can be adapted to incorporate dynamic information of several vehicles ahead of the in front driving vehicle and, in this way, better predict sudden changes in the traffic situation. Also, fully new assistance systems that make use of Vehicle-to-Vehicle or Vehicle-to-Infrastructure communication can be designed. Green Light Optimal Speed Advisory (GLOSA)

is an application, by which traffic lights broadcast the light phases so that vehicles can adapt their speed in order to optimize the traffic flow.

ETSI is currently working on the definition of a set of messages for the European V2V technology [12]. For instance, each vehicle will transmit periodically Cooperative Awareness Messages (CAMs) containing basic information such as position, speed and heading [13]. Since these parameters are not precisely measured, the uncertainty related to each of them is also included in the payload. CAM messages are intended to inform surrounding vehicles about the presence of other road participants. These beacon messages are sent with an update rate of 1 Hz to 10 Hz, depending on the current change in position, speed and heading [13].

1.2. Positioning in Vehicular Environments

Self-positioning plays an important role in vehicular environments. The vision is that every vehicle is able to position itself on the road with lane level accuracy. Especially the deployment of Global Navigation Satellite Systems (GNSS), as the American Global Positioning System (GPS) or the European satellite navigation system Galileo, are foreseen to strongly contribute to this aim. In recent years, GNSS positioning devices are entering the mass market. GNSS receivers can be found in any smartphone and are integrated into middle and premium class vehicles. The primary applications of GNSS in road transport are navigation, route guidance and fleet management [14]. Drivers get their location on a digital map and are guided to their destination. Fleet management systems provide an overview of the position and status of large fleets of vehicles for companies, such as car rental services, car pool companies, or freight companies. Car insurance companies use GNSS to monitor the driving behavior in exchange of a fee reduction. New uses of GNSS in road transportation include automatic tolling and emergency call [14].

Many of these applications require to know where the vehicle is located. Electronic street maps are used in the navigation devices and in fleet management software. For displaying purposes, maps are very convenient, as they allow to interpret a position in relation to the environment. The process by which a two- or three-dimensional position estimate is mapped onto a street is called map-matching [15].

However, the accuracy, availability and robustness of GNSS are still far from meeting the stringent requirements of safety-critical systems in the road environment. Great efforts are performed to introduce GNSS for civil safety-critical systems in aviation. Ground-Based Augmentation System (GBAS) is a strong competitor to the currently used Instrumental Landing System (ILS), that provides guidance to aircraft while approaching and landing on equipped airports [16]. By using a set of ground base stations GBAS can improve the performance of GNSS in terms of integrity, continuity, accuracy and availability.

Also in the vehicular environment, efforts have been made towards augmenting GNSS, mainly with the use of further information sources [17]. A common approach is the fusion of GNSS with inertial, odometer or steering wheel sensors inside the vehicle [18–20]. The fusion of image [21], video [22] or laser scanner [23] with inertial sensors and GNSS are current research topics. Further approaches to enhance the absolute positioning of a vehicle are using so-called "signals of opportunity" such as LTE or WiFi [24].

1.3. Relative Positioning for Safety-Critical Applications

One example of a safety-critical driver assistance system requiring a precise *absolute position* is a lane departure warning system. This system monitors the position of the vehicle with regard to the occupied lane and warns the driver when the vehicle is drifting out of the lane. However, the vast majority of safety applications require precise knowledge about the *relative position* of other vehicles, pedestrians or obstacles. In the following, three different hazardous situations, which can be overcome by reliable and accurate relative positioning technologies, are described:

Forward Collision Avoidance Systems

John is driving with his car on a rural road. He is driving at an adequate speed, given the good weather and pavement conditions. The road is curvy and trees or slope changes often obstruct John's view. Every now and then, a side road merges at the right side. Johns is driving towards a bend. Suddenly, his car stops accelerating and starts softly braking, while at the same time a light flashes in John's car's dashboard. A slowly driving tractor suddenly appears in front of him, but his car is now slow enough for John to take safe control over the situation.

Forward collision avoidance systems are systems that either warn the driver or autonomously intervene in the control of the car in the case of imminent collisions [25]. By means of a relative positioning technology these systems are able to scan the environment in front of the car, detect other vehicles, bicycles or pedestrians, evaluate critical situations and perform required countermeasures to avoid a collision or, at least, reduce its damage.

Lane Change Assistant

John decides to take the highway which brings him faster to his destination. A short turn, a roundabout, and he is on the access lane of the highway. A few vehicles drive on the lane to his left. John checks the side-view and rear-view mirrors, looking for the cars on the overtaking lane. Feeling sure that he is able to merge onto the highway, John slowly turns the steering wheel to the left. He feels heavy haptic feedback from the steering wheel to the right. At the same time, a quiet 'Beep' sounds. John has no time to realize this, but the next thing he sees is a car appear just on the next lane to his left. John is surprised. His Lane Change Assistant *just saved him and the driver in the other car of entering into an unsafe situation.*

Lane change or merging assistants provide warnings to the drivers if it is unsafe to change the lane or merge into a line of traffic. These assistant systems monitor the relative position of the surrounding vehicle within the road environment and the intention of the driver. Especially vehicles driving in the blind spot of the driver have to be detected on time.

Platooning

John has managed to merge safely the highway. He feels a bit fuddled about the risky experiences he has encountered. John has still more than one hour to drive and he is feeling a bit tired. He decides to use the ACC functionality of his car, which is capable of following automatically a foregoing vehicle. He can lift his right foot from the throttle pedal. The car is smoothly following the front car at a distance that makes him feel comfortable and, at the same time, adheres to the given traffic rules. Suddenly, the braking lights of the in front driving car start flashing and immediately John's car performs a strong brake, even before John can realize it. His car comes to a standstill at a safe distance to the car in front.

ACC is capable of adjusting the speed of the ego vehicle to the flow of traffic, while maintaining the safety distance to the preceding vehicle. It is envisioned that these systems eventually take over the task of steering and are able to safely follow a preceding car autonomously. A train of vehicles following each other is called a *platoon*. Platooning systems will not only rely on on-board ranging sensors, but will be supported by V2V communications. Intra-platoon communication is not only necessary for platoon coordination, e.g. entering and leaving the platoon, but especially to maintain its stability, by correctly adapting to changing dynamics of the vehicles [26].

Although the knowledge about the absolute position is a prerequisite for many ITS applications, certain safety-critical applications require precise knowledge about the relative position of surrounding vehicles in order to avoid collisions. While relative position accuracy is one of the most important requirements, relative speed is as important, since it enables to have a precise prediction of the future relative position. Further important requirements are the system's reliability and availability, the robustness to changing environmental conditions, the perception range and field of view, and the capability to resolve different targets.

The above mentioned three scenarios are examples of situations where common ranging sensor reveal their limitations and could be intelligently supported by cooperative solutions relying on V2V communication.

1.4. Objective, Research Questions and Methodology

This thesis aims at demonstrating the suitability of using a cooperative approach based on V2V communication for relative positioning between vehicles. To this end, a probabilistic method based on a Bayesian approach is proposed, in which the two dimensional relative position and relative

velocity towards another vehicle is tracked over time in the ego vehicle reference frame along with a measure of its uncertainty. A cooperative approach is based on the exchange of GNSS information between neighboring vehicles. In this thesis, the exchange of absolute positions and the exchange of GNSS raw measurements are considered and their performance is compared to each other. Both GNSS information and on-board sensor output are fused in order to give a continuous, stable and robust estimate of the relative position. The cooperative approach will be evaluated according to its accuracy, reliability and availability by computer simulations and in real-world scenarios.

The research questions this thesis addresses are the following:

1. Which are the advantages in exchanging GNSS raw measurements between vehicles and which is its gain over exchanging absolute positions for vehicle relative positioning?
2. Which increase in robustness is achieved by fusing GNSS raw measurements with sensors available in today's vehicles?
3. Which performance in the estimation of the relative position can be expected in typical environments regarding accuracy, reliability and availability?
4. Is it possible to achieve with a cooperative approach a better performance than on-board ranging sensors?

The methodology followed to answer these research questions starts by defining the problem of relative position between vehicles. The problem is contained by setting up assumptions, which help to efficiently approach the research questions. The driver assistance system making use of the relative position estimate sets the requirements. Since these requirements are not known, in the scope of this thesis, the requirements on the system are defined through the performance of modern ranging sensors. Along with the system requirements, performance metrics are defined. A novel relative positioning system is proposed based on theory regarding GNSS and inertial navigation, Bayesian estimation and sensor fusion. In the evaluation phase, the subsystems are validated in controlled environments, such as simulators and hardware-in-the-loop emulators. In a second step, the system is tested in real-world environments. A test setup is described and a suited reference system is chosen. After applying the defined performance metrics, the results are presented and the conclusions are drawn.

1.5. Outline of the Thesis

A schematic representation of the structure of this thesis is presented in Figure 1.3. The thesis is divided into eight chapters as follows: After this introduction, in Chapter 2, a review of the requirements posed on relative positioning systems and current solutions for relative positioning in vehicular environments are presented. In Chapter 3, the fundamentals of satellite navigation,

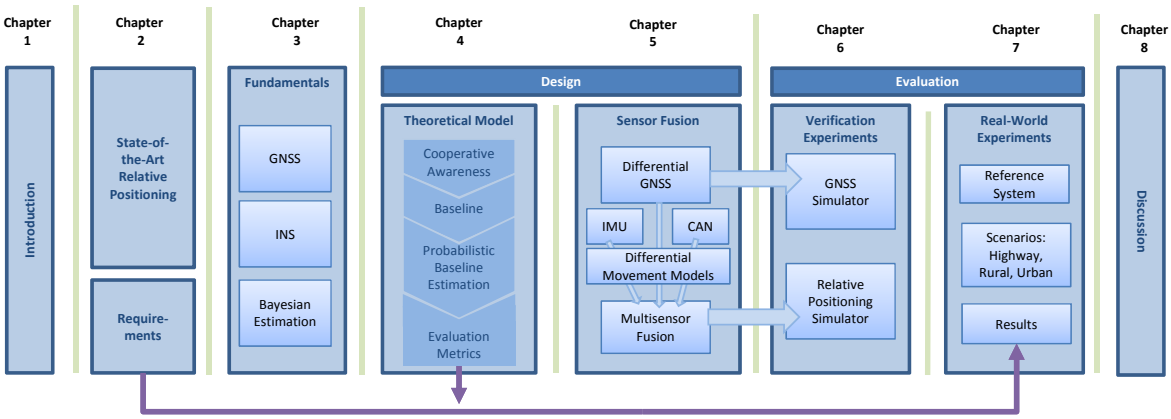

Figure 1.3.: The picture shows a schematic representation of the outline of this thesis.

inertial navigation and Bayesian estimation theory are reviewed as far as they are relevant for the scope of this thesis. The theoretical model for the cooperative relative position estimation given by a dynamic Bayesian network will be presented in Chapter 4. The concept of baseline and other relevant definitions are also presented in this chapter. In Chapter 5, the models for GNSS, inertial sensors and vehicle movement are explained. The multisensor fusion of the three information sources is explained here. The proposed approaches for cooperative relative positioning are evaluated, once, in a vehicle simulator and, second, under controlled conditions using a GNSS simulator. These results will be presented in Chapter 6, whereas the real-world experiments with two vehicles driving in different environments are presented in Chapter 7. Chapter 8 concludes the thesis by summarizing the main contributions of the presented work, answering the research questions and giving an outlook to possible future lines of investigation.

Chapter 2.

State-of-the-Art Relative Vehicle Positioning Solutions

Automotive applications, such as Forward Collision Warning (FCW) or Automatic Cruise Control (ACC), need continuous information about the relative position and relative velocity of other vehicles in the vicinity of the ego vehicle. The exact requirements on the relative positioning system are determined by the individual safety-critical application. As a first step, these requirements will be named and quantified, by considering modern safety applications, such as FCW and ACC, and by looking at modern on-board ranging sensors. Later in this chapter, a review on commercially available and state-of-the-art relative positioning solutions is given. Here, a distinction is made between *non-cooperative* solutions, where the ego vehicle perceives passive target vehicles by means of a ranging sensor, and *cooperative* systems, where the target vehicle actively supports the ego vehicle to find its relative position.

2.1. Requirements on Relative Positioning

To define the requirements on relative positioning, on the one hand, driver assistance applications, as for instance FCW and ACC, are considered. However, homogeneous specifications and standards on the performance and the figures of merit of driver assistance systems are not available and every developer applies its own design [27]. Therefore, also the performance of today's on-board ranging sensors is taken into account. FCW and ACC are already today offered in high-end and middle-class vehicles[1,2,3] and they are based on the availability of radar sensors, laser scanners or camera systems. Hence, the stated performance of these sensors can shed light on the requirements of relative positioning systems.

[1] Distronic Plus in Mercedes S-Class and E-Class
[2] Volvo City Safety in Volvo S60
[3] Front Assist in Volkswagen Golf and Jetta

Accuracy The most considered aspect of positioning systems is theis accuracy. In general, the accuracy of a measurement system could be defined as "how close" a measurement is to its true value. This closeness is quantified by the distance between measured and true value. Often, in spoken language, the word precision is used interchangeably when speaking about accuracy. In science, precision is the degree of repeatability or how alike consecutive measurements under the same conditions are. A measurement system with a systematic error or bias might be precise, but not accurate, since the mean of its measurements differs from the true value.

In positioning systems, the accuracy is the length of the three-dimensional vector between the measured position and the true position in a Cartesian coordinate frame. In applications that do not require vertical position, as it could be the case of vehicular applications where cars drive on roads, the accuracy is measured in a two-dimensional plane. Position accuracy is usually quantified by the Root Mean Square (RMS) error [28]. Other conventions are the 95^{th} percentile, which is the confidence interval containing 95 % of the measurements [28]. A measure of this uncertainty in the estimate is important for the application making use of the relative position information.

The relative position of a target vehicle is given, as it will be explained in Chapter 5, in the local coordinate frame attached to the ego vehicle. When evaluating the accuracy of an on-board ranging sensor mount on the front of the vehicle, it is common to differentiate between along-track and across-track accuracy [29]. In polar coordinates, this translates to a distinction between range accuracy and angular accuracy. As will be presented in the subsequent sections, some systems have excellent along-track resolutions, while their across-track accuracy is poor.

Certain systems have an accuracy that degrades the higher the distance between ego and target vehicle, while other systems have a range-invariant accuracy. The requirement from the driver assistance system on the relative position accuracy is distance dependent. An ACC system aims at maintaining a constant time headway to a preceding vehicle, i.e. maintaining a speed-dependent distance, by adapting the velocity of the ego vehicle [30]. A time headway of 1.8 s is experienced by the occupants as safe and comfortable [31]. To maintain this value with 0.1 s accuracy, a relative position accuracy of 5.5 % on the distance is required. This translates to a position accuracy of 1.65 m while driving at 60 $\frac{\text{km}}{\text{h}}$. According to [32], a 10 % position accuracy at a distance of 90 m is sufficient for an ACC application. In order to give precise warnings in FCW systems, a position accuracy of at least 6.6 % is required according to the definitions stated in [27]. In comparison to these values, commercially available radar sensors state ranging accuracies of 10 cm to 25 cm or 1 % to 3 % in distances up to 200 m to 250 m[4,5].

Many applications require to distinguish between different vehicles in the environment. ACC needs to follow the vehicle driving on the same lane ahead of the ego vehicle, while a Lane Change Assistant (LCA) needs to resolve the lane in which a vehicle behind is approaching. The width of

[4] Bosch LRR3
[5] Continental ARS 30x

a highway lane in Germany is 3.75 m [33], while the width of a rural road lane is 3.00 m [34]. This requirement translates to a relative positioning accuracy requirement of 1.875 m on highways and 1.5 m on rural roads.

For some applications, knowing accurately the range rate or relative velocity is of higher importance than knowing its precise range [32]. ACC systems, for example, rely on adapting the speed of the own vehicle to that of the in-front driving car [35]. Radar sensors provide good speed accuracy in the order of 0.1 $\frac{m}{s}$ to 0.3 $\frac{m}{s}$[4]. In safety applications, as for instance, FCW or LCA, the relative speed is used to better predict the future relative position and the Time to Collision (TTC) [27].

It is required that a relative positioning system has a high accuracy, meaning that its relative position measurements are bias-free and precise in both along- and across-track direction, and will additionally output a measure of the current uncertainty of its measurement.

Availability It is of highest importance that a relative positioning system for safety-critical applications is always available. Multiple causes can be the reason for a diminished availability. A Global Navigation Satellite Systems (GNSS)-based positioning system might not be available in situations with complete obstruction in the line of sight to the satellites as, for instance, in tunnels. Not only GNSS, but any type of radio based positioning system, can be made unavailable by jamming the signal. Vision-based ranging systems might not be available in adverse whether conditions, as, for instance, fog or heavy rain or at night. In order to provide a continuous operation of a safety system, the requirement on availability should address a value of 100 $\%$.

Reliability The system's reliability is a highly critical factor in safety-of-life applications. The accuracy of a system might be very high, but if it is not reliable it cannot be accounted on. When looking at integrity, accuracy is a secondary matter. The current accuracy of the system might be poor, but it might be quantified with a great confidence. The 95^{th} percentile is sufficient to characterize the system's performance from an accuracy point of view, whereas probabilities of the system being outside the stated confidence interval are in the order of one in one million to one in one billion in a given time frame [36]. In system engineering, reliability is also called integrity. Integrity gives "a measure of the trust which can be placed in the correctness of the information supplied by the total system" [37]. Integrity also includes the ability to provide alarms when the error tolerance of a certain parameter is exceeded. Integrity analysis yields a *protection level* and an *integrity risk*. The protection level is the confidence interval for a certain parameter, while the integrity risk is the probability that the parameter is not contained within the protection level [36].

While in civil aviation stringent integrity requirements are imposed on all involved operational components, in the field of road transport integrity is starting to be specifically considered. With the introduction of satellite-based augmentation systems, such as the European system EGNOS, GPS has been extended to incorporate integrity services [38]. So-called Ranging and Integrity

Monitoring Stations are responsible for monitoring the space signals and to flag corrupted satellites that should not be used [28]. At the user side, Receiver Autonomous Integrity Monitoring (RAIM) techniques can be applied [28]. By taking advantage of the redundancy in the navigation signals towards several satellites, faulty satellites can be detected.

The Functional Safety for Road Vehicles standard (ISO 26262) defines so-called Automotive Safety Integrity Levels to quantify the risk associated to each software and hardware component inside a vehicle related to safety-critical applications [39]. Consequently, also Advanced Driver Assistance System (ADAS) fall under the ISO26262 requirements. For an Intelligent Transportation Systems (ITS) application to operate safely and manage correctly hardware failures, operating errors and changing environments, the relative positioning system is required to detect other participants with high certainty and deliver a measure of the current confidence [40].

Detecting Range and Field of View When looking at relative positioning systems, a figure of merit is the detecting range and the Field of View (FoV) of the system. Some ranging systems, as for instance laser scanners or visual systems, have Line-of-Sight (LoS) characteristics, meaning that they can only measure the position of neighbors to whom they have direct visibility. They can be obstructed by other vehicles, buildings or the surrounding topography. These systems also have a technical range limitation related to the limited transmit power or sensor sensitivity. Additionally, they also have a limited FoV, defined by the opening angles in azimuth and elevation in which they can scan the environment.

To overcome these limitations for rear-looking driver assistance systems, as for instance, lane-change assistants, multiple instances of a sensor need to be placed around the vehicle to get a 360 degree FoV of the environment. With Vehicle-to-Vehicle (V2V) communication and omnidirectional antennas an all-around perception of the environment is automatically achieved. In this case, a detecting range of several hundreds of meters and up to two kilometers in ideal conditions is achievable [41].

Dimension A position in space is given by a its three Cartesian coordinates. The relative position of a target vehicle in the ego vehicle reference frame is, in general, a three dimensional coordinate. However, many relative positioning systems are only able to measure the relative position in one or two dimensions. A laser scanner uses a rotating mirror around one axis to scan the environment in azimuth angle. Consequently, it can output a two-dimensional relative position while disregarding the vertical component. An Ultra-Wideband (UWB) system, on the other hand, is able to measure the Round-Trip Delay (RTD) of a signal sent by the ego vehicle and returned by a target vehicle. This system is only able to estimate the range between the vehicles, but not the exact two- or three-dimensional position. In vehicular environments where, usually, vehicles drive on the same plane, a two-dimensional relative position estimate is sufficient for many driver

assistance systems. Situations where vehicles drive at different heights, as for instance, at over- and underpasses, require a resolution of the third dimension.

Target Resolution The resolution, i.e. the ability to resolve different targets and objects, is important for driver assistance systems, such as LCA and FCW [27]. This makes it possible to quantify the number of targets and correctly distinguish them. On-board ranging sensors will likely merge vehicles that drive closely together at similar speed into the same target and will give a new identification to every detected vehicle disregarding if it was detected before. A cooperative approach relying on the exchange of information over V2V communication will have the possibility of identifying targets unambiguously, since an identification of each vehicle is provided in the exchanged messages [13].

System Delay For safety relevant driver assistance applications, a fast response is required. It is important for a warning system to give timely alarms, and for a controlling system in ACC to be able to respond smoothly to changes in the speed of the foregoing vehicle. For this, the information from the relative position device has to be outputted at a high rate. In platooning, a fast and reliable control of the speed and steering of the vehicle is pursued. For instance, ACC-graded long range radars have output rates between 10 Hz and 20 Hz. Laser scanners have output rates above 10 Hz. For collision detection and pre-crash sensors higher update rates are needed, with measurement cycles up to 50 Hz [29].

The output rate of measurements is one important factor. However, the delay in the measurement, i.e. the time elapsed since a physical event occurs until the system offers it at its output, is as significant, since it causes a delayed detection for FCW assistants or an unstable controlling in platooning applications. One example is the detection of changes of speed. As radar sensors and laser scanners are not sensible to changes in velocity, they can only estimate acceleration by looking at consecutive measurements and, thus, suffer form an increased delay. A cooperative solution that directly transmits sensor information from the vehicles will overcome this limitation. However, a propagation and communication system delay will be introduced by the V2V communication [42].

Cost The price of the relative positioning system has to be taken into account in commercial passenger and freight vehicles. The cost of a certain relative positioning solution is not only the direct price of the device that needs to be equipped in the car, but also secondary costs need to be considered. Secondary costs can include installation and maintenance costs, power consumption, noise and heat creation and processing power.

Laser scanners, but specially vision-based solutions, are in general computational intensive as large amounts of data need to be processed. Solutions based on radar sensors, on the other hand,

include radio frequency (RF) pre-processing, signal processing and object detection and tracking all on the same device, usually a lightweight and power efficient component.

Specifically with regard to electric vehicles, the power consumption of a system is of increasing relevance. All externally mounted devices can potentially decrease the aerodynamic properties of vehicles in general, which is especially relevant for electric vehicles, have to be taken into account. In this way, rooftop antennas for GNSS, UWB and V2V will cause certain air drag when compared to a radar sensor or a laser scanner that can be effectively hidden inside the vehicle's upper grille or behind the front bumper . The increasing number of sensors, actuators and the related cabling inside the vehicle accounts for more weight, which has a direct impact on the motor's power and fuel consumption or does need to be compensated by a weight loss in other components.

In cooperative solutions based on V2V communication, the necessary communication bandwidth has to be taken into account as one further cost aspect. Although the spectrum for ITS-related communication is reserved in Europe, America and Japan, the communication spectrum is per se a valuable resource [43] that could be used for alternative communication purposes, as for example mobile communications, including 4G-LTE and future mobile communication generations. Automotive radar sensors usually work above common communication frequencies in the 24 GHz and 77 GHz band [44]. However, mutual interference of radar sensors is also becoming a growing issue in radar technology [45, 46].

2.2. Non-Cooperative Approaches for Relative Positioning

In this and the following section current commercially available and state-of-the-art solutions for relative positioning are reviewed. This section focuses on egocentric or non-cooperative approaches, while the following section analyzes cooperative solutions. Egocentric techniques are passive or non-cooperative in a way that a target vehicle is not actively contributing to the estimation of its relative position. It could be argued that having a surface that reflects radio signals from a radar sensor could make a target vehicle being "cooperative". For this reason, in the context of this thesis, cooperative will be considered a vehicle that has installed a device that is for the sole purpose of making other vehicles aware of himself. According to this definition, the chassis of the vehicle that reflects radar signals makes radar be a non-cooperative technique.

2.2.1. Radio Ranging

One simple technique to estimate the range towards another vehicle consists in using electromagnetic waves and measuring the Received Signal Strength (RSS) of a signal transmitted by another vehicle. The signal level is, under ideal conditions such as free-space propagation, proportional to the distance between transmitter and receiver antenna. By assuming a certain model for the power

decay over distance, given by the path loss exponent [47], a rough estimate of the range between two cars can be performed. Since V2V communication technology is foreseen to be integrated in future vehicles, several research groups have analyzed the possibility of performing RSS ranging with this technology. Alam et al. use Doppler measurements in [48] to estimate the path loss exponent. Parker et al. [49] propose a cooperative technique that uses RSS in combination with speed measurements from the vehicles in the cluster. Although they demonstrate theoretically that their approach is accurate, reliable and allows real-time operation, they do not reveal the measurement uncertainty used for the RSS measurements. This is the key issue in RSS-based approaches, since real-world experiments show that only a rough estimate of the transmitter position can be acquired in this way, since shadowing and multipath cause large variations in the received signal strength [50]. In [51], errors above 20 m are reported for short distances between vehicles between 20 m to 45 m.

Radar is a technology that uses high-frequency electromagnetic waves to measure the distance and relative speed of target objects. Radar sensors can already be found today in middle class vehicles for forward collision warning applications, lane change assistants or automatic cruise control. Two main radar technologies exist in the ITS domain. Impulse radar sensors measure the time needed for a short pulse to travel from the radar sensor to the object, reflect and travel back to the sensor. Frequency Modulated Continuous Wave (FMCW) radars transmit a frequency modulated signal with constant power envelope [29]. The frequency difference between the outgoing and incoming wave is directly proportional to the relative distance to the target object. Both radar types are capable of additionally measuring the relative speed by exploiting the Doppler effect and looking at the frequency difference between the outgoing and incoming wave.

Radar sensors work typically in two frequencies. The 77 GHz band is used for, so-called long-range radars[6,7,8]. The 24 GHz UWB band is temporarily allowed in Europe for automotive short-range radar sensors[9]. Also in this band, narrow-band radars can be operated using the 100 MHz Industrial-Scientific-Medical (ISM) band[10]. In this band, radars coexist with radio communication devices and radio astronomy stations that might be impaired if too many automotive radars are operated. Therefore, the European Commission made available the 79 GHz band for long-term operation of radar sensors, seeking worldwide harmonization. This band has the advantage that a common technology for short-range and long-range radars can be developed, along with decreased dimension and weight, and increased Doppler sensitivity [52]. The usage of the 24 GHz UWB band has been prolonged until January 2018 [53].

Typically, a distinction is made between short-range radar up to 20 or 30 m, medium range radar

[6] Bosch LRR3
[7] Delphi ESR
[8] Continental ARS 30x
[9] SMS UMRR
[10] TRW AC100

up to 100 m[10] and long-range sensors that measure beyond this distance up to 250 m[6 7] [54]. Short-range radars are used for collision avoidance and object detection and need higher range resolution and, consequently, more bandwidth (4 GHz at 77 GHz to 81 GHz) [55]. They usually have also wider field of view up to ±30°. Long-range radars, on the other hand, are mainly used for ACC and can work with a lower range resolution and are designed with smaller bandwidths (500 MHz between 76 GHz and 77 GHz). Their field of view is smaller (±8°[10] or ±15°[6]).

In general, the range and speed resolution of a radar is determined by its bandwidth. Products available on the market state range accuracies of 10 cm[6] to 30 cm[9] or 1 % to 2.5 % of the measured distance. The speed accuracies range from 0.12 $\frac{m}{s}$[6] to 0.3 $\frac{m}{s}$[9].

Generally, the across-track accuracy of radars is low. The approach used to estimate the Angle of Arrival (AoA) of the reflected signal is to implement an array of patch antennas and compare the amplitude and phase of signals in partially overlapping beams [29]. Some radar sensors provide moderate angular resolution by using mechanical sweeping radar scanners [44]. Angular accuracies of between 0.5°[10] and 5° are typical, yielding lateral uncertainties from 87 cm to 400 cm at 50 m distance, respectively.

Targets can be easily resolved when they are located in different range and velocity cells [56]. For instance, commercial radar sensors claim to have a correct resolution of objects when their distance is above 2.5 m[10] or their speed difference above 1.4 $\frac{km}{h}$[10]. Target resolution for objects at a similar distance and with similar speed, relies on lateral resolution of objects. The lateral accuracy is dependent on the antenna beam width, which, at the same time, depends on the wavelength. Larger wavelengths yield broader beams for the same antenna dimension and, consequently, a coarser lateral resolution [57]. Therefore, moving from 24 GHz to 79 GHz yields a better lateral resolution and the availability of 4 GHz of bandwidth enhances the overall longitudinal resolution in range and velocity.

Other characteristics of radar sensors are their potential for invisible integration behind electromagnetically transparent materials, as for instance, behind the front bumper. Besides few exceptions, radars usually have no moving parts and are, therefore, more robust and less prone to mechanical failures than laser scanners. In contrast to vision- and laser based systems, radars are robust against environmental conditions such as changes in light, fog or rain. In recent years, the price of radar sensors has dropped considerably and are available in middle and high class vehicles.

2.2.2. Laser Scanners

Light Detection and Ranging (LIDAR) is a laser-based ranging system similar to radar, that, based on the Time of flight (ToF) of reflected light pulses, is able to measure the distance towards an object. These systems usually work in near infra-red region of the electromagnetic spectrum at 905 nm. Their transmit power is limited to comply with eye-safety regulations, which imposes

a practical limit on the measuring range of the sensor [58]. Usually, a rotating device makes it possible to use one to four laser light sources to scan points in space. A device operating in the described manner is called a laser scanner. 2D laser scanners measure points in one plane, while 3D laser scanners are able to also vary the elevation angle. Available products use different scanning planes in order to achieve a small range of elevation angles to account for the inclination of the vehicle.

The use of laser scanners is mainly in the field of obstacle detection, collision mitigation and stop-and-go assistants. Nevertheless, the use of laser scanners for ACC is already finding its place in ITS. Future autonomous cars will likely rely on laser scanner information to get information from surrounding obstacles [59]. Although, laser scanners are not able to measure the relative speed between ego and target vehicle directly, they provide a relative speed measurement by differentiating the range of successive scans [59].

As the output power of automotive laser scanners is limited, their maximum perception range lies between 80 m[11] and 200 m[12] and strongly depends on the light reflectivity index of the object [60]. There are short-range laser scanners for object detection with ranges of around 10 m[13]. With 110°[12] or 120°[11], the FoV of laser scanners is generally broader than that of radar sensors. Even 360° laser scanners that scan the whole surrounding at high revolutions with several laser beams exist[14]. These have been used in autonomous vehicles as "Junior" from Stanford University [61] or the Google self-driving car [62].

Laser scanners have range accuracies between 0.02 m[14] and 0.1 m[12 13] or 0.5 m[11]. The lateral accuracy is given by their angular resolution of around 0.125°[12] and 0.09°[14]. The speed accuracy of 0.5 $\frac{m}{s}$[13] is slightly worse, but comparable, to that of radar sensors.

The operational availability of laser scanners is limited by environmental conditions [60]. Fog, rain, dust, dirt and water heavily detriment the performance of the sensor. Also, incident sunlight in the morning and afternoon hours can cause disturbances on the laser detecting device and thereby affecting the accuracy of the measurements.

The price is still too high for laser scanners being incorporated into commercial vehicles. Nevertheless, they are extensively used by many research groups to test novel advanced driver assistant systems or self-driving vehicles [63, 64].

2.2.3. Time-of-flight Cameras

ToF or 3D cameras are used in many different fields including human-machine interaction, industrial

[11] Hella Alaska Automotive laser scanner
[12] Ibeo LUX
[13] Continental SRL1
[14] Velodyne HDL-64E S2

automation and robotics [65]. In the automotive domain, they can be used in driver assistance and safety applications, such as pedestrian recognition or pre-crash detection [66]. Unlike laser scanners, the ToF camera captures the entire scene with one single light pulse. Each camera pixel measures the time delay of modulated infrared light by comparing the phase of the outgoing and the incoming signal [67, 68]. The distance information is captured simultaneously for the entire scene [69].

When compared to video cameras, ToF camera's Complementary metal–oxide–semiconductor (CMOS) sensors have currently much lower resolution (64x8 pixel [69], 200x200 pixel[15,16] or 176x144 pixel[17]). Typical ranges where ToF cameras operate are between 7 m[15] and 10 m[17]. They are therefore suited for pedestrian recognition and object tracking in automotive environments [70]. A CMOS sensor for a ToF camera that targets a distance of about 20 m is presented in [69]. The field of view is around 40°[15 17].

A typical value for the ranging accuracy is around 1 cm[17] at a distance up to 10 m. The advantage of ToF cameras is that they do not use mechanical components as laser scanners. Compared to video-based techniques, ToF cameras use a single lens and reach more accurate depth information [66]. When compared to laser scanners, ToF cameras have high frame update rates, ranging from 20 fps [71], 50 fps[17], 60 fps[15] and 200 fps [69].

ToF camera's sensors, like laser scanner sensors, have problems with incident sunlight, which is a great drawback for situation awareness in automotive applications. Additionally, the price of ToF cameras, although decreasing in recent years, is still too high for market introduction.

2.2.4. Vision-based Solutions

Machine vision techniques are able to detect and localize objects by processing the images from an imaging device like a camera. Although vision can provide highly valuable information about the environment, image processing techniques are often computationally expensive and, in the ITS domain, still under development. For automotive vision sensors, vision processing of road scenes can provide accurate information that other sensors fail to obtain. Already today, cameras are being introduced in high-class vehicles for detecting lane markings and offer lane keeping assistants or lane departure warning systems[18]. Also, automatic traffic sign recognition systems are already able to inform the driver about the current speed limit and other type of hazards along the road[19]. Further on, cameras are recently incorporated for object detection[20]. Especially

[15] PMD Cam Board
[16] PMD CamCube
[17] SwissRanger SR4000
[18] Lane Departure Warning and Lane Keeping Aid in Ford Focus
[19] Traffic Sign Assist by Continental
[20] Volvo City Safety in Volvo S60

pedestrians detection, that would otherwise fail with radar sensors or laser scanners, can be accomplished with vision-based solutions [72].

Generally, for a camera system it is relatively easy to measure distances in the lateral, cross-track, direction. Depending on the resolution of the camera, a certain lateral accuracy depending on the distance can be obtained. Vision processing is less effective for calculating the longitudinal, along-track, distance of an object. Monocular systems, which use one sole camera, estimate the longitudinal distance by exploiting the geometry of the problem and incorporating knowledge about the size of the objects [32]. On the contrary, stereovision systems use two laterally-displaced cameras that capture the scene in front of the vehicle. By comparing the images from each camera a so-called disparity map, that represents the depth of the scene, can be created [73].

Camera systems typically have a range from 4 m up to 80 m and a field of view of $\pm 20°$ in azimuth [74]. Some commercially available systems state detection ranges and FoV of 100 m and 38° respectively[21]. However, stereovision and depth capability rapidly drops with distance and is limited to a range of up to 40 m [75].

While radar sensors and laser scanners have rather constant ranging errors over distance, the range accuracy of camera systems typically decreases quadratically with distance [76]. At 3 m, a range error of 5 cm is stated in [77], while the error at 40 m is around 3 m. An accuracy of around 1 % at ranges from 10 m to 95 m with a stereovision camera system was obtained in [78].

In [32] it was concluded that a monocular vision sensor offers sufficient accuracy in range and range rate to be used in an ACC application. By using laws of perspective, they have range errors of 5 % at 44 m and 10 % at 90 m. This has been used, e.g., in a monocular vision system for a robotic follower vehicle in [79].

Cameras work usually at frame rates between 15 and 25 fps and have, thus, measuring rates comparable to that of radar sensors and laser scanners. However, relative velocity cannot be directly measured, but has to be differenced from successive images. Camera sensors are, like human visual perception, sensitive to adverse lightning conditions as for instance, fog, rain, low sun, and other vehicle's lights at night.

A common approach to overcome the limitations of certain type of sensor is to fuse its information with other complementary sensors. The limited measuring rate of camera systems and the absence of range rate measurements can be enhanced with the use of a radar sensor, which, on the other hand, will profit from the good lateral resolution of camera systems [80, 81]. The combination of camera and laser scanner is also found in the literature [82]. Non-cooperative approaches involving radar, laser scanner and camera have been explored as well in [83].

[21] Mobileye EyeQ2

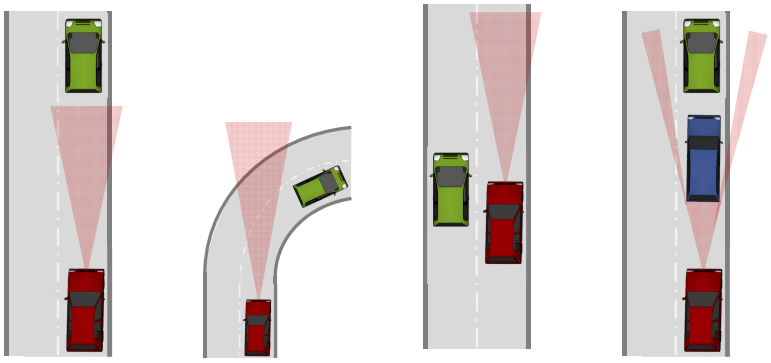

(a) (b) (c) (d)

Figure 2.1.: The figure reveals critical situations where ranging sensors have a poor performance.

2.2.5. Ultrasonic Ranging

Although this technique is often found in today's vehicles, its purpose is to offer short range obstacle detection, mainly for the use in parking assistants[22]. Since the scope of this work lies in safety-critical applications, which additionally are relevant at higher speeds and, consequently, larger distances, this technology will not be further regarded.

2.3. Cooperative Approaches for Relative Positioning

A series of non-cooperative approaches have been presented in the previous section, with radar sensors, laser scanners and vision-based systems being the most representative technologies. A common problem of these three systems is their LoS characteristic. As shown in Figure 2.1, there are many situations in which these sensors are not able to offer a relative position and velocity estimate. The limited range (Figure 2.1a), the limited field of view (Figure 2.1b and 2.1c) and sight blockage by other vehicles (Figure 2.1d) or bends are common situations. The underlying problem is the high frequencies in the radio spectrum where these three technologies work and their inherent propagation characteristics. Millimeter waves, used in radar frequency bands, behave nearly similar to optical frequencies of laser scanners and vision-based solutions. They are mainly line-of-sight and are blocked by cars or buildings. For this reason, all the approaches regarded in this section are able to extend the awareness range of the ego vehicle by using lower frequencies. This section presents cooperative techniques for relative positioning, where target vehicles are no longer passive, but perform a specific action to enable the ego vehicle to estimate their relative position.

[22] Parking Assitant from Bosch

2.3.1. Transponder-based Ranging

One possibility is reusing the idea of radar sensors at lower frequencies. However, due to the larger wavelength, vehicles in relation are rather small and do not offer a sufficiently big surface to reflect radio waves. Therefore, an antenna is installed on a target vehicle and the signals are amplified and "reflected" back to the sender in the ego vehicle. The relative distance of the target vehicle can be estimated by measuring the Round-trip Time (RTT) and multiplying by the speed of light. This technique is typically known as Round-Trip Delay (RTD).

Radio ranging based on Ultra-Wideband (UWB) technology has been investigated in [84]. An UWB signal at 6.35 GHz is used for estimating the range towards other vehicles with decimeter-level precision up to 300 m. This two-way ranging technique is assessed in [85]. In [86], it is concluded that UWB offers 70 cm accurate relative position estimation in kinematic situations.

In [87], 2.4 GHz and 5.9 GHz radios are used to estimate the range towards a set of Road Side Units (RSUs) in order to perform Time Difference of Arrival (TDOA) and absolute position. It has been concluded that ranging performance using V2V technology is highly dependent on relative velocity and distance. In his test setup, the measured ranging errors are up to 0.7 m at distances of up to 90 m in LoS situations. Simulations for absolute positioning fusing GNSS and RTD measurements from several vehicles have been presented in [88].

One problem with RTD is that the delay caused by the target vehicle to reflect the signal back has to be estimated. In [88], the solution was to use physical level timestamping at reception and retransmission. Other limitations to the accuracy are imposed through multipath propagation and, specially, Non-line-of-Sight (NLOS) propagation [89].

Radio ranging systems based on RTD will output an estimate of the range between the antennas, corresponding to the distance between ego and target vehicle. Consequently, it is not possible to obtain a full two- or three-dimensional relative position towards other vehicles.

Other transponder-based solutions rely on Time of Arrival (ToA), in which the absolute time between transmission and reception is measured to estimate the distance. This, however, requires precisely synchronized clocks at every vehicle, in order to compare the transmission and reception timestamps [90].

2.3.2. GNSS-based Cooperative Positioning

In cooperative positioning two or more mobile stations working together to improve their position solutions by communicating directly with each other. Different to the previous techniques, cooperative positioning relies on information sent over a communication link. With the introduction of a comprehensive and standardized communication technology for ITS, the idea of performing

cooperative positioning in vehicular ad-hoc networks becomes possible. So-called Cooperative Awareness Message (CAM) are beaconing messages that include the information about the absolute position, the speed and the heading of each ITS station. Along with this information, the estimation error shall also be included in the CAM.

ETSI's standard for CAM messages [13] does not specify the technique used for computing the position, speed and heading estimate in each vehicle. GNSS will be used as the primary source for absolute position information. The use of several GNSS constellations in parallel, as for instance the American GPS [91], the Russian GLONASS [92] or the European Galileo system [24], can be exploited. By using multiple constellations, more satellites can be tracked and used for position, velocity and time estimation and, thus, an increased availability and improved accuracy can be achieved.

Further on, the usage of multi-frequency GNSS receivers can help to estimate the delay of the dispersive parts of the atmosphere [93]. Besides the L1 and L2 frequency bands in early GPS, the new L5/E5 band will enhance this capability [24]. However, dual- or multi-frequency receivers are usually more expensive and are usually not used in mass-market applications.

Differential GNSS Differential GNSS is a technique, which is able to reduce atmospheric and other common errors. Differential GPS (DGPS) [28] was targeted to overcome the random satellite clock error and ephemeris data truncation to artificially decrease the system's accuracy for civil users, also known as Selective Availability (S/A). In DGPS, a receiver located at a known position (a so-called base station) can determine the offset on the range towards each satellite and send this information to other receivers (so-called rovers). Since S/A is an error common to all receivers, the broadcasted offset can be directly used to correct each pseudorange prior calculating the absolute position.

In general, ground-based augmentation systems (GBAS), as for instance DGPS, use base stations at known locations to transmit real-time correction data for GNSS positioning. The transmission is accomplished using some communication technology, as for instance a dedicated radio communication link or a cellular communication system. When GNSS correction data is transmitted from geostationary satellites, it is referred as satellite-based augmentation systems (SBAS). For instance, the American system WAAS [94] or the European system EGNOS [95] provide wide area coverage of differential corrections.

The general rule applies that the nearer the base station, the more correlated the errors between base station and rover are, and the larger improvement of the position solution can be expected. This way, atmospheric errors can be corrected, in general, for rovers at a maximum distance of 20 km to a base station [38].

The usage of GBAS or SBAS requires the deployment and maintenance of a network of base

stations and the availability of a communication technology to provide the correction information to each vehicle. GBAS is mainly deployed at airports for automatic landing systems of aircraft [96]. Due to the low elevation of SBAS satellites at our latitudes, the reception of differential corrections is difficult in certain scenarios, such as urban canyons.

GNSS and On-Board sensors Further on, vehicles also apply sensor fusion techniques with on-board sensors to support the GNSS position solution in GNSS impaired environments, such as under dense tree canopy, in urban canyons or while driving in tunnels. Commonly used on-board sensors for absolute positioning in vehicular environments are wheel speed sensors, odometers, steering wheel angle, accelerometers, barometers and magnetic compasses [97].

The fusion of GNSS with inertial sensors, composed of two triads of accelerometers and gyroscopes, is a well-known technique for supporting GNSS in aircraft, missiles and ships [98]. In the last decade, these techniques have been extended to vehicle positioning, by moving from high-graded and expensive ring laser and fiber optic gyroscopes to low-cost inertial Microelectromechanical Systems (MEMS) sensors [99].

Absolute Positioning Absolute positioning has received a lot of attention. Enhancing GNSS to mitigate the influence of multipath has been explored in [100–104]. Fusion of GNSS with on-board sensors has been addressed, e.g. by [105, 106]. Augmenting GNSS with opportunistic signals, such as cellular networks or WiFi access points, has been analyzed [107–109]. The fusion of GNSS with either laser scanners or vision-based systems is addressed in [63, 110, 111]. An enhancement of GNSS positioning with maps has been developed by [112]. Last but not least, cooperative approaches for deriving absolute positions have been proposed in [113–117]. In all this work, absolute positioning is the major point of research.

Relative Positioning Approaching the problem of relative positioning, in which the position towards other vehicles is the mayor aim, from a cooperative perspective has experienced less attention. Probably due to the ever-growing availability of precise and cheaper ranging sensors, the usage of GNSS for relative positioning has been relegated to a second place. The aim in GNSS-based relative positioning is to offer equal capabilities to the on-board ranging sensors and, in addition, extend their limited perception range. This includes to provide accurate relative position and velocity in an ego vehicle frame meeting the stringent requirements of safety-critical driver assistance applications.

The use of GNSS absolute positions and speed contained in CAMs to estimate the relative position to other vehicles using a particle filter has been analyzed in [57, 118]. In [119], the effectiveness of sharing absolute positions using low-end, mid-range and high-end GNSS receivers has been identified by comparing its output to a radar sensor has been identified. It has been concluded

that low-cost GPS receivers are not capable to meet the requirements of safety-critical applications as they showed longitudinal errors of around 2 m and lateral errors above 3 m while driving in a highway environment.

Relative positioning with Raw GNSS Measurements The concepts of differential GNSS can be extended by moving from the classic base-station/rover setup for absolute positioning towards a two-rover setup for relative position estimation. By sharing pseudorange measurements, i.e. the raw GNSS distance measurements to the satellites in view [28], over V2V communication, each vehicle can subtract the neighbor's pseudoranges from its own and compute a relative position. At the same time, correlated GNSS errors, common to both vehicles, are reduced. The concept of relative localization on the basis of the exchange of GNSS pseudorange data has been presented in [120]. In [121], an integration approach, where pseudorange observations from two vehicles are subtracted from each other, is presented and the theoretical potential is shown through simulations. Later [122], this is tested in a mainly sub-urban environment, yielding a standard deviation error of 3.4 m for a 12 minute run. Using a Weighted Least Squares algorithm and weighting each pseudorange according to the received carrier-to-noise ratio (CN0) the relative position between two GNSS antennas is estimated in [123]. Experimental results with static 3 m and 8 m inter-antenna distance on a rooftop yield baseline length errors of up to 40 m.

Differential Carrier Phase Ambiguity Resolution A number of groups have addressed the relative positioning problem of vehicles by solving differenced carrier phase ambiguities rather than using differenced pseudorange techniques [124–127]. The potential of this approach is derived from the fact that noise in the Phase-lock Loop (PLL) of the GNSS receiver is smaller than the noise in the Delay-lock Loop (DLL) by several orders of magnitude [38]. In order to determine the range towards the satellite, the integer number of cycles has to be resolved. This task is especially difficult in vehicular environments due to signal disturbances, satellite blockage and multipath, which lead to cycle slips that will reset the resolution algorithm [28].

A test platform for relative positioning yielding range errors of less than 1 m 99 % of the time in open sky and 90 % on obscured roads was built in [127]. In [128], a particle filter that samples from the relative position domain to solve the carrier phase ambiguity was designed. The use case was relative positioning of low orbit satellites. The duplication of a trajectory using carrier phase based relative positioning was inspected in [129, 130]. Cooperative relative positioning exchanging Real Time Kinematics (RTK) position solutions between vehicles was analyzed in [131]. Later, integrity concepts based on the same method was explored in [132]. In [133], a novel algorithm for solving the integer ambiguity for low-cost single-frequency receivers based on multiple hypothesis and weighting each according to its residual is presented. The approach yielded encouraging results in open-sky environments, providing a robust relative position with centimeter accuracy and partial

immunity to cycle slips.

GNSS carrier phase-based relative positioning approaches offer extremely accurate full three-dimensional relative position and relative velocity at the output rate of a GNSS receiver. If coupled with on-board inertial sensors, the update rate can be increased up to 15 to 20 Hz in order to meet the requirements of safety-critical applications (see Section 2.1). The main disadvantage is its sensitivity and, consequently, the limited continuity in its performance. Trees, bridges and highway gantries cause momentary drops in the signal level, loss of lock on the carrier phase and cycle slips. Low cost receivers are specially sensitive, and a continuous tracking of the carrier phase is extremely challenging in usual scenarios [133].

2.4. Discussion

As a conclusion to this chapter, Table 2.1 summarizes all presented relative positioning techniques. The requirements reviewed in Section 2.1 are added in each row to allow to evaluate each of the techniques according to the analysis of the previous sections. Three symbols ($+$, $\circ$, $-$) are used to symbolize if a ranging system performs positively, neutral or negatively in a certain category.

On-board ranging sensors, as radar sensors and laser scanners, offer a high accuracy in their range estimation. While radar sensors have poor lateral resolution, laser scanners can calculate the lateral distance with higher accuracy. Both have an acceptable update rate for safety-critical applications (above 10 Hz), but only radar sensors offer a direct estimation of the relative velocity. Vision-based systems, based on stereo cameras, are only able to estimate the distance to vehicles in near range and have to use additional information about objects and context to estimate the distance to more distant vehicles. Relative speed can be estimated by looking at consecutive images. Radar sensors, eventually supported by laser scanner or cameras, are a very suited approach for relative positioning for safety-critical advanced driver assistance systems. Radar sensors and vision-based solutions correctly complement each other regarding longitudinal and lateral performance.

Regarding cost, radar sensors have dropped in price in the last decade. The same is expected for vision-based systems, since camera technology has found its place in consumer market and the technology has matured for introduction into the automotive segment. Laser scanners, with its mechanical parts, will need probably some more time to be cheap enough to find market introduction.

All non-cooperative approaches have LoS characteristics and are easily obstructed by obstacles, such as other vehicles, or have a limited range in bends and crests. This is considered an important drawback, when range information to other vehicles is required in non-highway environments. Rural roads are often curvy and a foregoing vehicle might often leave the sensing range of the device. In urban environments, approaching vehicles might hide behind other vehicles or buildings.

These are situations where ranging sensors have important limitations.

Therefore, cooperative approaches can offer a real and safety-relevant benefit. While transponder based approaches based on RSS and RTD measurements exhibit too large errors, solutions based on ToA require synchronized clocks on radio transponders in each vehicle. Thus, the exchange of positioning information between vehicles seams to be the most suitable solution for a cooperative approach. Here, different solutions compete with each other and it has to be considered which is best to meet the requirements of advanced driver assistance applications. Standalone GNSS solutions currently do not meet the requirements on accuracy on relative position and relative speed. Further on, continuous operation for stand alone GNSS is an important issue.

An "intelligent" approach is to take advantage of the complementary nature of on-board ranging sensors and cooperative approaches based on GNSS and V2V communication. For instance, researchers have worked on augmenting the capabilities of radar sensors with absolute positions exchanged over V2V communication in [57]. This approach was proved in various simulated road environments.

Realizing the important drawbacks of on-board sensors, this thesis focuses on a cooperative approach for relative positioning using V2V communication. It builds on the concept of differential GNSS and the raw GNSS measurement exchange proposed in [120]. Additionally, this thesis will incorporate the advances in sensor fusion in order to increase the availability, continuity and robustness of the relative positioning approach. In order to provide the required confidence, a probabilistic approach, which considers the propagation of the uncertainty, will be followed. Since cost is an important variable in automotive industry, care will be taken in conducting a research bounded by the limitations of low-cost and mass-market sensors.

Table 2.1.: Relative Positioning Techniques

Relative Positioning Technique	**RSS Ranging**	**Radar**	**Laser Scanner**	**ToF Camera**	**Vision Based**	**RTD**	**GNSS only**	**GNSS +INS**	**GNSS Carrier Phase**
Cooperative	No	No	No	No	No	Yes	Yes	Yes	Yes
Accuracy	−−	++	++	++	−	−	○	+	+
Availability	○	○	○	−	○	+	−	○	−−
Reliability	○	++	○	○	○	○	○	○	○
Range FoV	○	○	○	−−	−	++	++	++	++
Dimension	−−	○	○	+	+	−−	○	○	○
Target Resolution	−−	○	○	+	+	++	++	++	++
Price	++	○	−	−−	+	++	++	−	−

Chapter 3.

Theoretical Background for Cooperative Relative Positioning

This chapter will introduce the background theory as required to understand the concepts in this thesis. First, Global Navigation Satellite Systems (GNSS) will be introduced. Along with an introduction to the basic operation and functionality, the GNSS raw measurements will be regarded in detail. The second section will introduce inertial navigation systems. Inertial sensors and sensor platforms will be presented, different coordinate systems and coordinate transformations will be reviewed, and the usage of inertial information for positioning will be explained. Finally, a review on estimation theory and Bayesian filters will be given. Basic principles on estimators are introduced, Bayesian filter theory and its optimal implementation, the Kalman filter, is explained.

3.1. Global Navigation Satellite Systems

The basic idea behind GNSS positioning is that a receiver is able to locate itself by measuring the distance towards a set of satellites. Currently, the only fully deployed GNSS constellation is the American Global Positioning System (GPS) [134]. Other countries have started launching their own navigation satellites, as for instance the Russian system GLONASS [92] or the Chinese Compass/Beidou-2 [135]. To maintain independence from foreign (military) navigation systems, the European Union and the European Space Agency are currently deploying the global navigation system Galileo [36]. GNSS is usually divided in three segments, the space segment, the user segment and the control segment. In GPS, for instance, the space segment is composed by 32 satellites orbiting the Earth in medium Earth orbit at an altitude of about 20.000 km. The control segment is composed by several monitoring stations and antennas. The user segment are the GNSS receivers in smartphones, cars, airplanes, agricultural machines or traffic lights.

By knowing the distance or *range* towards three or more satellites, the transmitter is in principle able to determine its three-dimensional position by trilateration [38]. The range towards a single satellite is estimated by measuring the Time of Arrival (ToA) of the satellite signal, which travels

through the atmosphere at nearly the speed of light and arrives at the receiver antenna. To distinguish the signals from different satellites, a code division multiplexing scheme is used, i.e. each satellite modulates its carrier signal with a different spreading sequence. The control segment is in charge of determining the satellite's position and clock offset. The later is of uttermost importance, since the ranging problem is in fact a synchronization problem between the receiver and the satellite clocks. For this purpose, satellites carry highly precise atomic clocks. The offset due to the free-running inexpensive (and thus imprecise) user clock remains as an unknown to all measured ranges. These "falsely" measured ranges are also called *pseudoranges* [38]. Therefore, the range towards an additional satellite is needed to resolve the user clock bias in addition to the position. In this way, GNSS is able to provide global positioning and time information.

GNSS signals The signals transmitted by the GNSS satellites have special characteristics, so that a receiver is able to track them. They consist of three parts, the carrier wave, the spreading sequence and the navigation data [136]. The carrier wave of GPS, for example, is transmitted at L1 and L2 frequency [134]. The spreading sequence on L1 is called Coarse Acquisition (C/A) code, a predefined 1023 chip sequence transmitted at a chipping rate of 1.023 MHz. The navigation data is Binary Phase Shift Keying (BPSK) modulated binary data at 50 bits per second on top of the C/A code that carries satellite orbit, satellite clock and atmospheric information.

Receiver Operation A GNSS receiver has to perform a series of sequential tasks in order to compute its position. In the acquisition stage, the receiver has to find new satellite signals and estimate their delay. These can be signals from satellites that have been lost momentarily or from newly visible satellites. After the acquisition stage, in the tracking stage the receiver follows dynamic variations of the delay of each satellite over time. This is done in so-called tracking loops. At the same time, the navigation message bits are decoded and interpreted. When a stable tracking of at least four satellites is possible, the navigation computer inside the receiver is able to solve the user position, velocity and time.

Next, the signal tracking stage is explained. Figure 3.1 shows the classical structure for a ToA estimator based on a Phase-lock Loop (PLL)/Delay-lock Loop (DLL) architecture. The analogue processing stage amplifies the signal from the antenna and does the bandpass filtering and the down-conversion to intermediate frequency. The analogue signal is then sampled, so that the following tracking stages are performed in the digital domain. The intermediate frequency signal is down converted to base band by mixing it with a replica of the carrier wave. This process is called carrier wipe-off and is normally done on both the in-phase and quadrature signals. If the replica of the carrier wave is phase-aligned with the incoming signal, the quadrature components is zero and the PLL is said to be "locked in phase". The in-phase signal s_{I} is now multiplied by three C/A code replicas: Early $s_{\mathrm{R,E}}$, Prompt $s_{\mathrm{R,P}}$ and Late $s_{\mathrm{R,L}}$. The three replicas are nominally generated

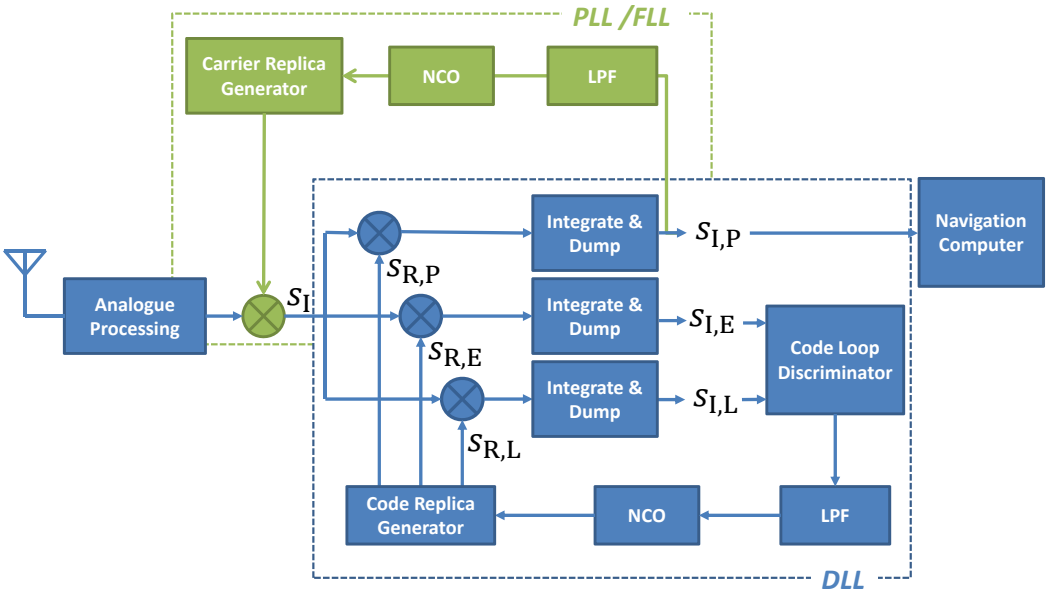

Figure 3.1.: Block diagram of a classic PLL/DLL tracking loop architecture inside a GNSS receiver.

with a spacing of ± 0.5 chip. The "integrate and dump" block outputs a value proportional to the correlation of the incoming signals to each of the replica codes.

The DLL will steer the code replica delay to get the highest correlation at the prompt value $s_{I,P}$ by comparing $s_{I,E}$ and $s_{I,L}$. The delay of the replica code is adjusted so that the values in $s_{I,E}$ and $s_{I,L}$ are equal. This happens inside the code loop discriminator. The loop dynamics are given by the bandwidth of the DLL low pass filter (LPF), which will be a design trade-off between noise and allowed user dynamics. The pseudorange measurement is equal to the adjusted delay to the satellite.

Above, a coherent code tracking loop was introduced, that requires a perfect phase match between incoming and replica carrier signal. Non-coherent tracking loops, on the other hand, do not require a perfect lock on the phase, but only on the frequency. In this case, the PLL is replaced by a Frequency-lock Loop (FLL) and also the quadrature components $s_{Q,E}$, $s_{Q,E}$ and $s_{Q,E}$ have to be taken into account in the code loop discriminator. Different discriminator designs that make different use of the three in-phase components and additional three quadrature components exist. For a deeper understanding on the code and carrier tracking loops, different discriminator configurations and different loop filters, the reader is referred to [38, 93].

Pseudorange, Doppler and Carrier Phase While in the tracking stage, a receiver has a lock on the code delay and on the carrier frequency. The code delay corresponds to the pseudorange measurement and the carrier frequency to the Doppler measurement provided by a GNSS receiver. If the receiver uses a PLL instead of an FLL, the receiver will lock on the phase of the signal and

a third measurement, the *carrier phase*, becomes available.

The pseudorange ρ is the delay of the signal estimated by the DLL and denoted in meters. This measurement is biased by the offset due to the satellite and user clocks. A pseudorange measurement from a receiver r to a satellite s can be expressed as

$$\rho_{\mathsf{r}}^{\mathsf{s}} = r_{\mathsf{r}}^{\mathsf{s}} + c \cdot (\delta t_{\mathsf{r}} - \delta t^{\mathsf{s}}) + \epsilon_{\rho}, \tag{3.1}$$

where $r_{\mathsf{r}}^{\mathsf{s}}$ is the geometric range from the receiver antenna to the satellite antenna, δt_{r} and δt^{s} are the receiver and satellite clock offsets measured in seconds, respectively and c is the speed of light in meters per second. ϵ_{ρ} contains all ranging errors due to atmospheric delays, satellite position errors, relativistic effects and noise. A deeper discussion follows in Section 5.1.

The Doppler measurement $\dot{\Phi}$ is the Doppler shift of the signal estimated by the PLL/FLL and given in meters per second [137]. The signal from the satellites experiences this Doppler shift because of the relative movement of satellite and receiver [38]. Additionally, the measurement is subjected to a bias resulting from the drifts of the satellite and user clocks. The Doppler measurement can be expressed as

$$\dot{\Phi}_{\mathsf{r}}^{\mathsf{s}} = \dot{r}_{\mathsf{r}}^{\mathsf{s}} + c \cdot (\dot{\delta t}_{\mathsf{r}} - \dot{\delta t}^{\mathsf{s}}) + \epsilon_{\dot{\Phi}}, \tag{3.2}$$

where $\dot{r}_{\mathsf{r}}^{\mathsf{s}}$ is the change in geometric range due to the movement of user and satellite. $\dot{\delta t}_{\mathsf{r}}$ and $\dot{\delta t}^{\mathsf{s}}$ are the receiver and satellite clock drifts in seconds per second, while $\epsilon_{\dot{\Phi}}$ contains the combined error due to changes in the satellite clock and the atmosphere and measurement noise.

Finally, the carrier phase measurement Φ is the difference between the phases of the receiver generated carrier replica and the received carrier signal measured in meters. The carrier phase can be measured by the receiver very precisely, up to sub-centimeter level accuracy [28]. However, as one cycle cannot be differentiated from the previous or the next one, the carrier phase measurement comes along with an intrinsic ambiguity term. The carrier phase measurement can be expressed in the following way:

$$\Phi_{\mathsf{r}}^{\mathsf{s}} = r_{\mathsf{r}}^{\mathsf{s}} + c \cdot (\delta t_{\mathsf{r}} - \delta t^{\mathsf{s}}) + \lambda \cdot N + \epsilon_{\Phi}, \tag{3.3}$$

where ϵ_{Φ} incorporates the ranging errors associated to the carrier phase measurement. Here, it is worth mentioning that the ionospheric delay of the carrier phase measurement is of equal magnitude and opposed sign than in the case of the pseudorange measurement and that the noise components is about two orders of magnitude less for the carrier phase measurement as compared to the pseudorange [38]. λ is the L1 wavelength in meters and N the integer number of cycles between the satellite and the receiver. As long as the PLL keeps a lock on the carrier phase, the integer ambiguity remains constant. Momentary signal loss causes the PLL to loose the lock and the integer ambiguity number to reset. This event is called a "cycle slip" and is one of the reasons why using the carrier phase measurements for positioning is still a challenging task [28].

3.2. Inertial Navigation

Inertial navigation deals with the problem of continuously estimating the position, velocity and orientation of a moving object by using motion sensors and rotation sensors via a process called *dead reckoning*. Dead reckoning dates back to ancient time of marine navigation [138]. Starting from a known position, a ship was continually monitoring the covered distance by measuring its speed with the ship log and its heading with a compass. The current vessel's position is determined from the previous fix and advancing the covered distance in a certain direction. As measurement errors in dead reckoning accumulate over time, the availability of anchor points, such as a lighthouse, or other reference information, such as the longitude angle estimated with a sextant, are of high importance for accurate navigation.

In principle, the basic idea behind inertial navigation and the integrative nature of the problem has stayed the same. Today's inertial navigation sensors are accelerometers and gyroscopes, while the reference information for reducing the error growth is mainly GNSS. Modern inertial navigation has been effectively implemented in a wide range of applications such as ships, submarines, aircrafts, unmanned aerial vehicles, guided missiles and spacecraft.

Different types of gyroscopes exist. Ring laser gyroscopes and fiber optic gyroscopes are based on the Sagnac effect [98]. In both sensors, the phase or frequency difference created by the interference of two counter-propagating laser beams is detected in order to measure the turn rate of the sensor. These sensors are extremely precise and have small drifts. Recent advances in the production of Microelectromechanical Systems (MEMS), have made it possible to construct lightweight and small inertial platforms that can cost-effectively be integrated in commercial platforms, such as vehicles. Thus, modern driver assistance systems as Electronic Stability Program (ESP) already rely on the availability of cheap accelerometers and gyroscopes in today's cars.

An Inertial Navigation System (INS) is a system that estimates the position, attitude and velocity of a moving object. It consist of the inertial navigation sensors and the navigation computer. A so-called *strapdown system* contains three orthogonally mounted accelerometers and three orthogonally mounted gyroscopes, measuring linear acceleration and angular velocity respectively [98]. This sensor assembly is called Inertial Measurement Unit (IMU). The navigation computer processes the information of the sensors in order to compute position, attitude and velocity.

3.2.1. Coordinate Frames

Point positioning is the problem of determining the coordinates of a single point, representing an object, and referring it to a certain *coordinate frame*. A coordinate frame is defined as a system that assigns numbers or coordinates to determine the position of each point in space. In a three-dimensional euclidean space, three mutually orthogonal axis span a cartesian coordinate

system. Such a coordinate frame is defined with a reference point and the directions of each of the axis in the space. A general knowledge of the coordinate systems usually used in navigation is essential for understanding the concepts explained in this thesis.

Inertial Reference Frame In order to express force, acceleration, velocity and position vectors in accordance with Newton's laws, an inertial coordinate system must be defined stationary in space, or moving with a constant velocity [16]. In the context of this thesis, this frame is the coordinate frame in which the satellite's position, velocity and acceleration are given and in which inertial sensors on the Earth measure rotations and accelerations. The Earth-Centered-Inertial (ECI) is an inertial coordinate system located at the center of gravity of the Earth but not rotating with it [28]. The z-axis z^i coincides with the Earth's rotation axis and points towards the North pole. The x-axis x^i lies on the equatorial plane and points towards vernal equinox. The y-axis y^i completes the right-handed system, also on the equatorial plane [28].

ECI is fixed to the stars and it is the favored coordinate system for the near-Earth environment, specially suitable to the analysis of satellite motion. Although ECI is not rotating with the Earth, it is constantly accelerating due to the translation movement of the Earth around the sun, and, therefore, strictly speaking it does not meet the requirements of an inertial reference system.

Earth Coordinate Frame A global coordinate frame is needed for representing the position of a point on the Earth. For that purpose, a coordinate system is needed that is fixed to the Earth and rotates with it, so that the coordinates of a stationary object remain fixed over time. The Earth-Centered-Earth-Fixed (ECEF) is such a frame, located at the center of gravity of the Earth and rotating with it. The z-axis of ECEF, z^e, coincides with z^i in the coordinate system ECI. Its x-axis x^e lies in the equatorial plane pointing toward the Earth's prime meridian and its y-axis y^e completes the right-handed system, also on the equatorial plane.

Vehicle Coordinate Frame The vehicle coordinate frame, in the literature often referred to as *body frame*, is fixed to the vehicle, moving and rotating with it. It is usually located at the center of mass of the object, or, in the special case of land vehicles, it is located at the rotating point in the center of the rear axle. In this work, and for practical reasons, the origin is located at the vehicle's foremost point. Horizontal rotations have to be corrected by the distance from the rotation point to the origin of the vehicle coordinate frame. Axes conventions typically depend on the particular vehicle. As shown in Figure 3.2, x^v points in the forward driving direction of the vehicle, y^v points in the left direction and z^v completes the right-handed system pointing in up direction.

The *sensor frame* is the frame in which the 3-axes gyroscopes and accelerometers of the IMU measure angular velocities and accelerations. In the frame of this work, the IMU sensor is assumed

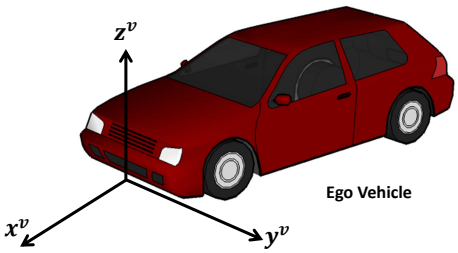

Figure 3.2.: The figure shows the vehicle coordinate frame. Its origin is at the foremost center point of the vehicle. Its x-axis points in forward driving direction, the z-axis perpendicular in up direction, and the y-axis to the left to complete the right-hand rule.

to be perfectly aligned and co-located with the vehicle frame. Hence, the vehicle frame and the *sensor frame* coincide. In cases where a misalignment is desired, it will be explicitly pointed out.

Navigation Coordinate Frame For navigation purposes, it is convenient to define a local coordinate system fixed to the Earth frame. A typical navigation frame is the East-North-Up (ENU) coordinate system, which is obtained by fitting a tangent plane to the geodetic reference ellipse at a certain point. The East-axis points in East direction, the North-axis points in North direction and the Up-axis is perpendicular to the East-North tangent plane completing the right-handed system. Figure 3.3 shows a schematic view of the Earth and all four coordinate systems: ECI, ECEF, vehicle and navigation coordinate frame.

The attitude of the vehicle is given by the attitude of the vehicle frame in the navigation frame. Attitude, therefore refers to how the vehicle frame system needs to be rotated in order to orient its axis in parallel to the navigation frame (this definition of attitude is valid for the other coordinate systems as well). The *Euler angles* are the three rotations around the x-, y- and z-axis that rotate the vehicle frame into the navigation frame. The angle by which the vehicle frame is rotated around the x-axis is the roll angle ϕ. The rotation angles around the y- and z-axis are called pitch θ and yaw ψ respectively. These three rotations are shown in Figure 3.4. To transform the coordinates of a vector in vehicle frame to navigation frame the Euler angles are used by building the Direction Cosine Matrix (DCM) $\mathbf{C}_v^n$ according to:

$$\mathbf{C}_v^n = \begin{bmatrix} \cos\theta\cos\psi & -\cos\phi\sin\psi + \sin\phi\sin\theta\cos\psi & \sin\phi\sin\psi + \cos\phi\sin\theta\cos\psi \\ \cos\theta\sin\psi & \cos\phi\cos\psi + \sin\phi\sin\theta\sin\psi & -\sin\phi\cos\psi + \cos\phi\sin\theta\sin\psi \\ -\sin\theta & \sin\phi\cos\theta & \cos\phi\cos\theta \end{bmatrix}. \quad (3.4)$$

An acceleration vector in vehicle frame $\mathbf{a}^v$ can be transformed to a vector in navigation frame $\mathbf{a}^n$ by multiplying it with $\mathbf{C}_v^n$ as in

$$\mathbf{a}^n = \mathbf{C}_v^n \cdot \mathbf{a}^v. \quad (3.5)$$

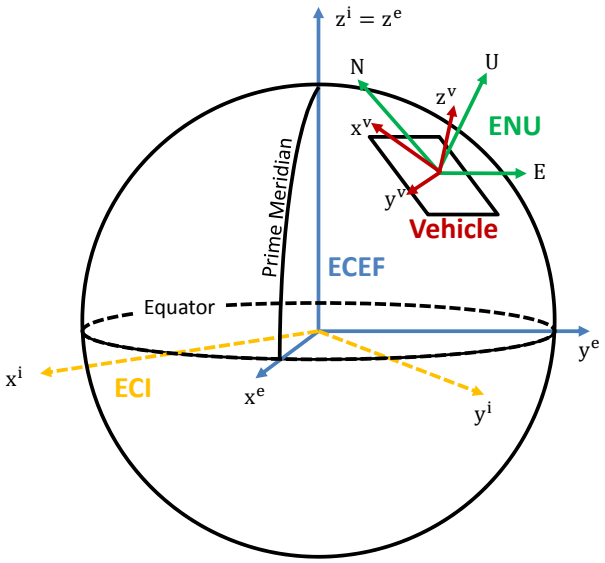

Figure 3.3.: The figure displays the coordinate frames relevant to inertial navigation: the inertial frame ECI (x^i,y^i,z^i), the Earth frame ECEF (x^e,y^e,z^e), the local navigation frame ENU (E,N,U) and the vehicle frame (x^v,y^v,z^v).

Further information on other forms to express the attitude of an object, such as orientation vectors and quaternions, can be found in [98].

3.2.2. Navigation

An IMU provides the measurements to determine the user's position, attitude and velocity. The *strapdown algorithm* is the key to calculate these values from acceleration and turn rate measurements. The basic idea is to integrate once the turn rates in order to continually estimate the object's attitude. Knowing the attitude of the object, the Earth gravitational force can be subtracted from the accelerometer measurements. Then, the resulting acceleration is integrated once to get the velocity and integrated twice to get the position [139]. Figure 3.5 shows the schematic diagram of the strapdown algorithm.

The output of the strapdown algorithm are the position of the vehicle frame in the Earth frame expressed in Earth frame coordinates $\mathbf{p}^e_{e,v}$, the velocity of the vehicle frame in the Earth frame expressed in navigation frame coordinates $\mathbf{v}^n_{e,v}$ and the attitude of the vehicle frame in the navigation frame $\mathbf{C}^n_v$.

The gyroscopes measure the turn rate of the vehicle frame with respect to the inertial frame in vehicle frame coordinates $\boldsymbol{\omega}^v_{i,v}$. The turn rate of the Earth frame in the inertial frame $\boldsymbol{\omega}^n_{i,e}$ is due to the Earth rotation and is dependent on the latitude of the vehicle. The movement of the vehicle in north and east direction makes it necessary to turn the navigation frame with respect to the

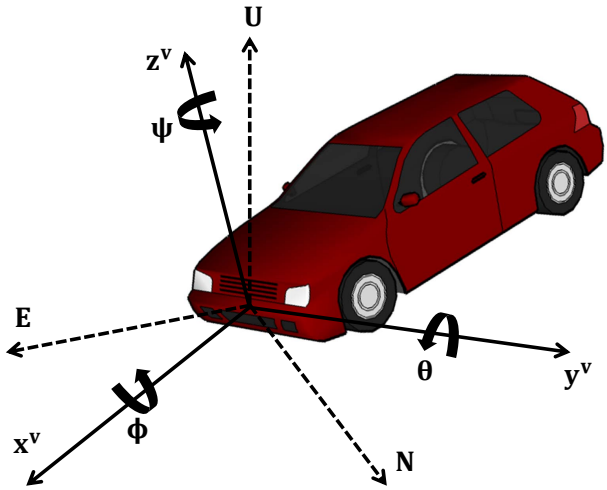

Figure 3.4.: The figure shows the three rotations around the x-, y- and z-axis of the vehicle frame to align it with the navigation frame. The three rotation angles roll, pitch an yaw define the attitude of the vehicle frame with respect to the navigation frame.

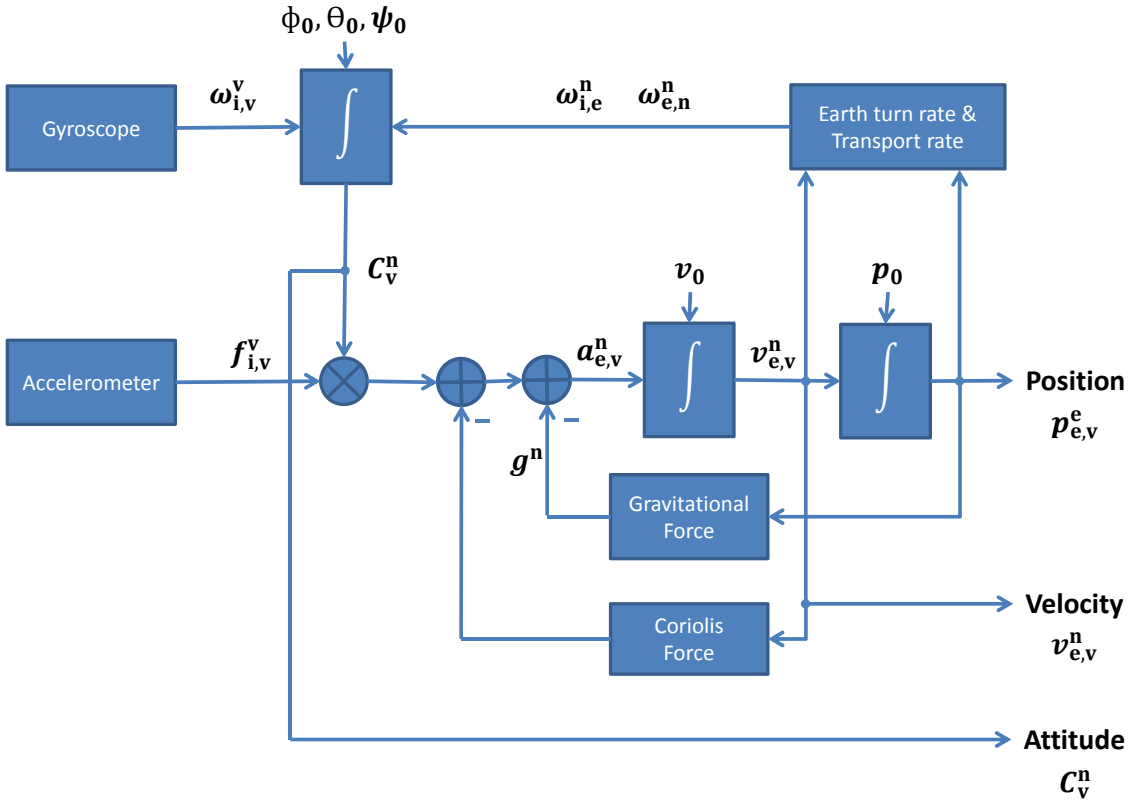

Figure 3.5.: Schematic block diagram of the strapdown algorithm [139]. The gyroscope measurements are integrated once to determine the attitude of the vehicle with respect to the navigation frame. The attitude is used to compensate for the gravity vector in the specific force measurements of the accelerometers. After compensating for the gravity and for the Coriolis force, the acceleration vector is integrated once to get a velocity and twice to get a position.

Earth frame. This is called the transport rate $\boldsymbol{\omega}^{\mathsf{n}}_{e,n}$. These two components can be neglected for short navigation periods and for relatively low velocities [98]. Along with the initial attitude, expressed by the Euler angles ϕ_0, θ_0 and ψ_0, the integration of the turn rates yields the current attitude of the vehicle frame in the navigation frame $\mathbf{C}^{\mathsf{n}}_{\mathsf{v}}$. In a strapdown computer, the attitude at time $t+\tau$ is calculated using the attitude at time t by [98]:

$$\mathbf{C}^{\mathsf{n}}_{\mathsf{v}}(t+\tau) = \mathbf{C}^{\mathsf{n}}_{\mathsf{v}}(t)(\mathbf{I} + \frac{\sin(\sigma)}{\sigma} \cdot [\boldsymbol{\sigma}\times] + \frac{1-\cos(\sigma)}{\sigma^2} \cdot [\boldsymbol{\sigma}\times]^2), \tag{3.6}$$

where $\mathbf{I}$ is the identity matrix, and σ and $[\boldsymbol{\sigma}\times]$ are the norm and the skew symmetric matrix representation of $\boldsymbol{\sigma}$, respectively. $\boldsymbol{\sigma}$ represents the three micro-rotations around the three axes and can be approximated with:

$$\boldsymbol{\sigma} = \boldsymbol{\omega}^{\mathsf{v}}_{\mathsf{i,v}} \cdot \tau, \tag{3.7}$$

with τ being the time between two samples of the inertial sensor. Equation 3.6 and Equation 3.7 are numerical approximations of a time continuous integral in order to be implemented in a time discrete system. A sufficiently high sampling rate is assumed, so that small angular rotations are performed in every integration step [139]. Only under the assumption of small angular rotations, the non-commutativity error due to the chain of rotations is maintained low [98].

The accelerometers, on the other hand, measure the specific force $\mathbf{f}^{\mathsf{v}}_{\mathsf{i,v}}$ of the vehicle frame in the inertial frame expressed in vehicle frame coordinates. To find the velocity $\mathbf{v}^{\mathsf{n}}_{\mathsf{e,v}}$ the acceleration $\mathbf{a}^{\mathsf{n}}_{\mathsf{e,v}}$ is integrated over time. For this, the specific force has to be corrected for the gravitational force of the Earth, the centrifugal force due to the Earth rotation, both depending on the position on the Earth, and the Coriolis force, due to the vehicle's movement in the Earth rotating frame, according to

$$\dot{\mathbf{v}}^{\mathsf{n}}_{\mathsf{e,v}} = \mathbf{a}^{\mathsf{n}}_{\mathsf{e,v}} = \mathbf{C}^{\mathsf{n}}_{\mathsf{v}}\mathbf{f}^{\mathsf{v}}_{\mathsf{i,v}} - (2\boldsymbol{\omega}^{\mathsf{n}}_{\mathsf{i,e}} + \boldsymbol{\omega}^{\mathsf{n}}_{e,n}) \times \mathbf{v}^{\mathsf{n}}_{\mathsf{e,v}} + \mathbf{g}^{\mathsf{n}}, \tag{3.8}$$

where $\mathbf{C}^{\mathsf{n}}_{\mathsf{v}}\mathbf{f}^{\mathsf{v}}_{\mathsf{i,v}}$ is the specific force projected from the vehicle to the navigation frame, $(2\boldsymbol{\omega}^{\mathsf{n}}_{\mathsf{i,e}} + \boldsymbol{\omega}^{\mathsf{n}}_{e,n}) \times \mathbf{v}^{\mathsf{n}}_{\mathsf{e,v}}$ is the Coriolis compensation and $\mathbf{g}^{\mathsf{n}}$ is the gravitation compensation. The Coriolis effect has to be compensated only in long-term navigation periods, e.g. in auronautical navigation for aircraft, and has a marginal effect in road vehicle applications [98]. The differential equation 3.8 is integrated to get the velocity of the vehicle on the Earth in local navigation frame coordinates and taking the initial speed as integrating constant.

Finally, the position $\mathbf{p}^{\mathsf{e}}_{\mathsf{e,v}}$ is obtained by integrating $\mathbf{v}^{\mathsf{n}}_{\mathsf{e,v}}$, transforming it from the navigation to the Earth frame, and taking the initial position $\mathbf{p}_0$ into account. Further details on the strapdown algorithm can be found in [139].

3.2.3. Aided Navigation

The strapdown algorithm is able to compute position, velocity and attitude out of turn rate and specific force measurements. However, inertial navigation is accurate only for short-term computations. Without taking action, the navigation errors will grow rapidly over time. The limited sampling rate, errors in the initial values of attitude, velocity and position, an inaccurate model of the gravity field and measurement errors of the sensors are responsible for this behavior [139]. While systematic errors in the acceleration sensors propagate to the position quadratically over time, attitude estimation errors will propagate cubically into a position error [139]. The error models for both, gyroscopes and accelerometers, will be regarded in detail in Section 5.2.

A commonly used countermeasure against the ever-increasing positioning errors in inertial navigation is to incorporate absolute positioning information from GNSS. The complementary characteristic of both information sources makes it especially suitable to use one system to compensate the drawbacks of the other system. INS cannot be perturbed by external interference sources and, thus, has a continuous availability. Although GNSS has relatively larger position errors due to noise and ranging biases and is prone to being jammed, it is long-term stable with bounded errors.

The most straightforward approach is a so-called *loosely coupled* integration, where inertial information is coupled with position and speed measurements from a GNSS receiver (see Figure 3.6a). A non-linear Kalman filter is usually used to estimate the navigation errors instead of estimating the navigation solution itself [97]. This is called an error state Kalman filter and it is particularly beneficial since the errors have smaller and rather constant dynamics compared to the vehicle's position or velocity. However, the main drawback of a *loosely coupled* approach is that a position and speed solution is required. This is only given if more than four satellites are visible to the GNSS receiver. A system that performs a fusion of inertial sensors with GNSS pseudorange and Doppler measurements directly, rather than with positions and speed values, is said to be a *tightly coupled* system (see Figure 3.6b). Here, navigation is still possible with less than four tracked satellites. Additionally, in a *deeply coupled* system pseudorange and carrier tracking loops inside the GNSS receiver are supported by the inertial integration [97]. Tracking loops can thus be designed with smaller loop bandwidth and, therefore, be more precise due to the smaller errors [38].

3.3. Bayesian Estimation Theory

Relative positioning of vehicles can be considered an estimation problem. Certain parameters, as for instance the relative position or the relative speed, need to be *estimated* from measured data, that might be corrupted by random errors. Examples of estimation processes are the following: (a) A GNSS receiver measures the distance to a satellite by estimating the ToA of a transmitted

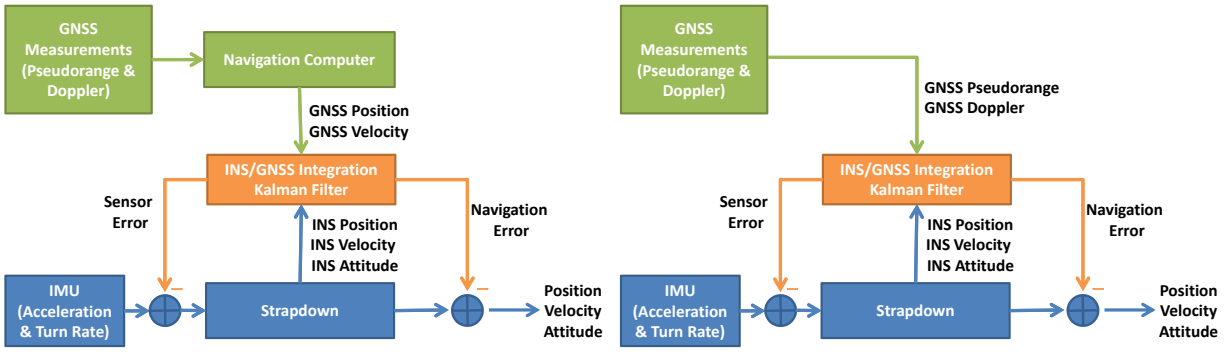

(a) Loosely Coupled System (b) Tightly Coupled System

Figure 3.6.: Loosely and tightly GNSS/INS coupled system architectures.

signal. The weak signal at the receiver is corrupted by noise, has been delayed by the atmosphere, and is biased by the unknown receiver clock time. Noise, delays and biases have random nature. (b) The acceleration and turn rate signals from an IMU are also noisy and have a time varying bias with certain random characteristics. (c) An automotive radar is a device that estimates the relative position of another vehicle by measuring the round trip delay of a transmitted radio frequency signal. The received signal is embedded in noise and corrupted by additional reflected echoes, both being randomly distributed.

In general, an *estimator* attempts to approximate the unknown parameters using available measurements. In Bayesian estimation, the a priori knowledge that is available on the stochastic parameters will be included into the estimator, in order to enhance its performance. Hence, in this section principles of statistics and Bayesian estimation theory that are of importance for the rest of the thesis will be reviewed.

3.3.1. Estimation Theory

The branch of statistics dealing with the estimation or approximation of an unknown *parameter* is called estimation theory. The estimation process is based on *measured* or *observed* data. An estimator $\hat{\theta}$ aims at approximating the unknown parameter θ using the measurements available. The bias of an estimator $\hat{\theta}$ is the deviation of its expected value from the true value θ of the parameter and can be expressed as:

$$Bias(\hat{\theta}) = E\left[\hat{\theta} - \theta\right] = E\left[\hat{\theta}\right] - \theta = \bar{\theta} - \theta, \tag{3.9}$$

where $\bar{\theta}$ is the mean of the estimator θ. It is desirable that an estimator is unbiased, so that its mean coincides with the parameter value. The variance of an estimator gives a measure on how much the estimated value spreads around its mean. In case of an unbiased estimator, the

estimated value will spread around the true value. The smaller the variance, the more compact are the estimated values around the mean value. If the variance is zero, all estimations are identical. The variance is defined as expectation of the quadratic distance of the estimated value $\hat{\theta}$ to the mean value $\bar{\theta}$ according to:

$$Var(\hat{\theta}) = E\left[(\hat{\theta} - \bar{\theta})^2\right]. \tag{3.10}$$

In the case of θ being a vector parameter, the variance is generalized to the variance-covariance matrix, which includes not only the variance of each parameter composing θ, but also the cross-correlation between them. The mean squared error (MSE) of an estimator $\hat{\theta}$ measures the average of the squares of the error of the estimator as:

$$MSE(\hat{\theta}) = E\left[(\hat{\theta} - \theta)^2\right]. \tag{3.11}$$

The MSE incorporates both, the variance and the bias of the estimator, in one single term. The relationship is given by

$$MSE(\hat{\theta}) = Var(\hat{\theta}) + (Bias(\hat{\theta}))^2. \tag{3.12}$$

In estimation theory, an estimator is called optimal when it allows to estimate a parameter without bias and with minimum variance [140]. As will be regarded next, the minimum possible variance for an estimator is given by the Cramér-Rao Lower Bound (CRLB) [141].

Cramér-Rao Lower Bound The variance of an estimator provides a metric on its performance. In estimation theory the CRLB gives a lower bound on the variance of estimators of a deterministic parameter. The best possible unbiased estimator will have, thus, a variance equal to the CRLB.

Given an estimator $\hat{\boldsymbol{\theta}}$ that estimates a set of parameters $\boldsymbol{\theta}$ out of a set of measurements $\mathbf{z}$ with the conditional probability density function $p(\mathbf{z}|\boldsymbol{\theta})$, the CRLB states that the covariance of the estimates $Var(\hat{\boldsymbol{\theta}})$ is lower-bounded by the inverse of the Fisher Information Matrix (FIM) $F(\boldsymbol{\theta})$ [24], according to

$$Var(\hat{\boldsymbol{\theta}}) \geq F(\boldsymbol{\theta})^{-1}, \tag{3.13}$$

where the inequality is satisfied by $Var(\hat{\boldsymbol{\theta}}) - F(\boldsymbol{\theta})^{-1}$ being positive-semidefinite and where each position (k, l) in the FIM is given by

$$[F(\boldsymbol{\theta})]_{k,l} = E\left\{\left[\frac{d}{d\theta_k} ln(p(\mathbf{z}|\boldsymbol{\theta}))\right]\left[\frac{d}{d\theta_l} ln(p(\mathbf{z}|\boldsymbol{\theta}))\right]\right\}. \tag{3.14}$$

The conditional probability density function $p(\mathbf{z}|\boldsymbol{\theta})$ gives a measure on how much the measurements $\mathbf{z}$ correlate with parameter $\boldsymbol{\theta}$. Measurements are better suited if they have a high sensitivity to changes in the parameter $\boldsymbol{\theta}$. This is denoted by the differentiation $\frac{d}{d\boldsymbol{\theta}}$. Incorporating better observables of $\boldsymbol{\theta}$ into an estimator will yield a higher Fischer information and, consequently, a smaller

estimator variance. The rather complex equation for the Fischer Information can be simplified for the case of measurements with additive Gaussian errors:

$$z_i = s_i(\boldsymbol{\theta}) + n_i \quad \text{with } i = 1, \ldots, m, \tag{3.15}$$

where s_i is the observed signal that is function of $\boldsymbol{\theta}$. n_i is white Gaussian noise with equal variance σ^2 and mutually independent for different i. In this case the multivariate Gaussian distribution $p(\mathbf{z}|\boldsymbol{\theta})$ can be written as the product of individual Gaussian Probability Density Functions (PDFs) with variance σ^2 and centered at $s_i(\boldsymbol{\theta})$ according to

$$p(\mathbf{z}|\boldsymbol{\theta}) = \prod_{i=1}^{m} p(z_i|\boldsymbol{\theta}) = \frac{1}{(2\pi\sigma^2)^{\frac{m}{2}}} exp\left\{-\frac{1}{2\sigma^2}\sum_{i=1}^{m}(z_i - s_i(\boldsymbol{\theta}))^2\right\}. \tag{3.16}$$

In this case, the FIM components are simplified to

$$[F(\boldsymbol{\theta})]_{k,l} = \frac{1}{\sigma^2}\sum_{i=1}^{m}\frac{d}{d\theta_k}s_i(\boldsymbol{\theta})\frac{d}{d\theta_l}s_j(\boldsymbol{\theta}) \tag{3.17}$$

As expected, the resulting CRLB will be proportional to the measurement noise variance σ^2. The smaller the variation of s_i and s_j with $\boldsymbol{\theta}$, the less information the measurements carry, and the greater the estimator's covariance. The CRLB will be used in Section 5.1 to compute the minimum variance of different relative position estimators. For a complete derivation of the CRLB, the reader is referred to [24].

Least Squares Estimation In regression analysis, the Least Squares (LS) method is widely used to find the set of function parameters that make the function best fit a set of points. The problem can be set up as a system of equations with the function parameters as unknowns. If more points than parameters exist, the system of equations will be over-determined. As the set of points are usually drawn from a stochastic process, a unique solution to the problem does not exist. The criteria by which the "best solution" is found is the one that minimizes the sum of the squares of the errors. The remaining error is called the residual. Supposing a linear measurement model according to

$$\mathbf{z} = \mathbf{H}\cdot\boldsymbol{\theta} + \boldsymbol{\epsilon}, \tag{3.18}$$

where $\mathbf{z}$ is the measurement vector, $\boldsymbol{\theta}$ is the unobservable state vector, $\mathbf{H}$ is a transformation matrix of the state vector into the measurement vector, and $\boldsymbol{\epsilon}$ is the mutually independent error vector with zero mean and equal variance. The aim is to estimate the state vector $\hat{\boldsymbol{\theta}}$ that minimizes the error residual. This is commonly expressed as

$$\hat{\boldsymbol{\theta}} = \arg\min_{\boldsymbol{\theta}} \|\boldsymbol{\epsilon}\|^2 = \arg\min_{\boldsymbol{\theta}} \|\mathbf{z} - \mathbf{H}\cdot\boldsymbol{\theta}\|^2. \tag{3.19}$$

For the linear case in Equation 3.18, the Ordinary LS solution to the problem is given in closed form by the equation:

$$\hat{\boldsymbol{\theta}} = (\mathbf{H}^T\mathbf{H})^{-1}\mathbf{H}^\intercal\mathbf{z}. \tag{3.20}$$

In the frame of this work the LS method is used, for example, to estimate the baseline vector from a set of pseudorange double difference measurements. As will be shown in Chapter 5, this is an over-determined system of linear equations and the LS algorithm, under certain circumstances that apply in this context, will find the best possible solution. Equation 3.18 presents a linear relationship between state vector and measurement vector. The LS solution can also be found for non-linear problems. Then, however, a closed form as in Equation 3.20 does not exist. The basis for the non-linear LS is to approximate the model by a linear one and to refine the solution found with an Ordinary LS by successive iterations [140].

3.3.2. Bayesian Estimation

The previous methods considered a static solution for the estimation problem. The estimated parameter was assumed to be unknown and deterministic. However, often the parameter θ to be estimated is a random variable and certain information on its stochastic properties, such as its probability distribution, are known. In this case, this *a priori* information should be incorporated into the estimation process to obtain a better estimate. Relative position or relative velocity are random quantities and a priori information might be available and should be included into the estimation process. In a Bayesian approach the observations are supplemented with additional a priori information about their state. To infer the state vector $\mathbf{x}$ from a measurement vector $\mathbf{z}$ the following definitions are useful:

- The probability $p(\mathbf{x})$ is the a priori probability distribution which includes all knowledge, or belief, on the state $\mathbf{x}$ prior to incorporating the measurement $\mathbf{z}$.
- The probability $p(\mathbf{x}|\mathbf{z})$ is called the posterior probability distribution and includes the knowledge regarding $\mathbf{x}$ after incorporating the measurement $\mathbf{z}$.
- The probability $p(\mathbf{z}|\mathbf{x})$ is called the measurement probability distribution and specifies the probability of the measurement $\mathbf{z}$ occurring, given the state $\mathbf{x}$.

Bayes rule offers a convenient way to compute the posterior probability distribution $p(\mathbf{x}|\mathbf{z})$ out of the available prior probability distribution $p(\mathbf{x})$ and the measurement probability distribution $p(\mathbf{z}|\mathbf{x})$ [142]. Bayes rule is expressed as:

$$p\left(\mathbf{x}|\mathbf{z}\right) = \frac{p\left(\mathbf{z}|\mathbf{x}\right)p\left(\mathbf{x}\right)}{p\left(\mathbf{z}\right)} = \kappa \cdot p\left(\mathbf{z}|\mathbf{x}\right)p\left(\mathbf{x}\right), \tag{3.21}$$

where $p(\mathbf{z})$ is the same for any value $\mathbf{x}$ in the posterior $p(\mathbf{x}|\mathbf{z})$ and, thus, can be seen as a

normalizing constant κ. Bayes rule is the center piece of Bayesian dynamic state estimation.

In a dynamic system, the state at a certain point in time is usually not independent from the state in previous instants. For instance, the position and the velocity of road vehicles are correlated over time. The same holds for the position of GNSS satellites, the propagation delays of atmosphere or even the multipath propagation error. The information of the evolution of the state can be used to obtain prior information on its current state. In general, the state at time k, $\mathbf{x}^k$, is generated stochastically from all past states $\mathbf{x}^{0:k-1}$. This probabilistic relationship is given by:

$$p\left(\mathbf{x}^k \middle| \mathbf{x}^{0:k-1}\right). \tag{3.22}$$

A state $\mathbf{x}$ is said to be *complete* when $\mathbf{x}^k$ is the best predictor of future states. This is also known as the *Markov Assumption* [143]. This means that $\mathbf{x}^k$ is a sufficient summary of all that happened in previous time steps [143]. This is expressed as:

$$p\left(\mathbf{x}^k \middle| \mathbf{x}^{0:k-1}\right) = p\left(\mathbf{x}^k \middle| \mathbf{x}^{k-1}\right), \tag{3.23}$$

where $p(\mathbf{x}^k|\mathbf{x}^{k-1})$ is the *state transition probability* and specifies the evolution of states over time and its conditional dependencies. The system state $\mathbf{x}$ should include all relevant states with memory in order to make it complete. The state $\mathbf{x}$ is often called *hidden state*, as it is not directly measurable or observable. Only $\mathbf{z}$ can be observed through measurements or observations.

If $\mathbf{x}^k$ is complete, the probability of a measurement $\mathbf{z}^k$ will only be stochastically dependent of the state $\mathbf{x}^k$. The knowledge of past states and past measurements is not relevant. This can be expressed as:

$$p\left(\mathbf{z}^k \middle| \mathbf{x}^{0:k}, \mathbf{z}^{1:k-1}\right) = p\left(\mathbf{z}^k \middle| \mathbf{x}^k\right), \tag{3.24}$$

where $p(\mathbf{z}^k|\mathbf{x}^k)$ is the *measurement probability* that describes the probabilistic relationship between the measurements and the states. Equation 3.24 implies that measurements are mutually independent of each other. Consequently, any memory in the measurements, such as a constant bias, has to be modeled by the system and included in the system state $\mathbf{x}$ [143].

The state transition probability in Equation 3.23 and the measurement probability in Equation 3.24 together describe the dynamic stochastic system. The state at time k stochastically depends on the state at time $k-1$ through the state transition probability. The measurement at time k stochastically depends on the state at time k through the measurement probability. Such a model is known as Hidden Markov Model (HMM) or Dynamic Bayesian Network (DBN) [143]. The DBN is a network diagram representing the variation of the states and measurements over time and their conditional dependencies as depicted in Figure 3.7.

A DBN is a time discrete model of a possibly time continuous system. The problems regarded in the frame of this thesis are time continuous in nature. Sensors, such as IMU and GNSS measure

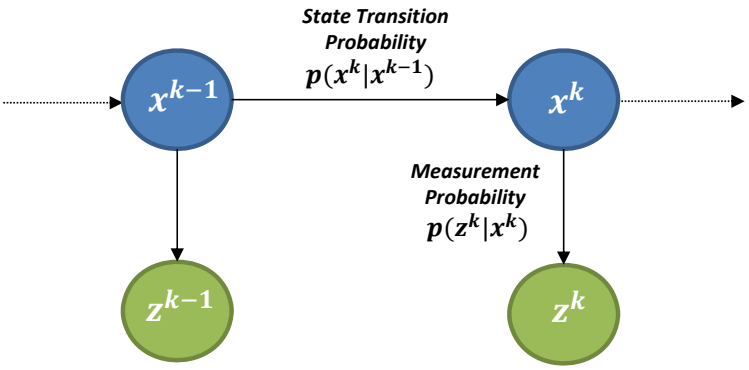

Figure 3.7.: The figure shows two subsequent time steps of a Dynamic Bayesian Network. The state $\mathbf{x}$ at time k is stochastically related to the state in time $k-1$ through the state transition probability $p(\mathbf{x}^k|\mathbf{x}^{k-1})$. The measurement $\mathbf{z}$ and the state $\mathbf{x}$ at time k are stochastically related through the measurement probability $p(\mathbf{z}^k|\mathbf{x}^k)$.

a physical quantity (specific force, turn rate and signal delay) continuously and the real-world processes, such as the movement of the vehicle, are, as well, time continuous. However, since the sensors deliver its measurements in periodic time intervals and, given that the real-world processes is sampled at a sufficient rate, a DBN is a suited approach to model the problems in the frame of this thesis.

The Bayes Filter Algorithm

For dynamic state estimation the Bayes filter tracks the posterior probability density function over time. Bayes filters assume that the state vector $\mathbf{x}$ is complete, and, thus, the posterior PDF contains all available statistical information on the state. The filtering algorithm is divided in two stages and repeated recursively:

- **Prediction**: the *state transition model* is used to propagate the posterior PDF over the state $\mathbf{x}^{k-1}$ to obtain a prior PDF over the state $\mathbf{x}^k$. Since the state is usually subjected to unknown disturbances, the prediction step generally deforms and spreads the state PDF. The computation of the prior PDF can be expressed Chapman-Kolmogorov equation [144] as follows:

$$p\left(\mathbf{x}^k\middle|\mathbf{z}^{1:k-1}\right) = \int p\left(\mathbf{x}^k\middle|\mathbf{x}^{k-1}\right) p\left(\mathbf{x}^{k-1}\middle|\mathbf{z}^{1:k-1}\right) d\mathbf{x}^{k-1}, \tag{3.25}$$

  where $p(\mathbf{x}^k|\mathbf{z}^{1:k-1})$ is the prior PDF over the state $\mathbf{x}^k$, $p(\mathbf{x}^k|\mathbf{x}^{k-1})$ is the state transition probability, and $p(\mathbf{x}^{k-1}|\mathbf{z}^{1:k-1})$ is the posterior PDF over the state $\mathbf{x}^{k-1}$.

- **Measurement Update**: the *measurement model* is used to modify the prior PDF over

the state $\mathbf{x}^k$ obtained in the prediction step to retrieve its posterior PDF. Usually the measurement update step shrinks again the state PDF that was widen through the prediction step, since new information is gained on the state. To compute the posterior PDF, the Bayesian filter algorithm uses the Bayes rule Equation 3.21:

$$p\left(\mathbf{x}^k\middle|\mathbf{z}^{1:k}\right) = \kappa \cdot p\left(\mathbf{z}^k\middle|\mathbf{x}^k\right) p\left(\mathbf{x}^k\middle|\mathbf{z}^{1:k-1}\right), \tag{3.26}$$

where $p(\mathbf{x}^k|\mathbf{z}^{1:k})$ is the posterior PDF over the state $\mathbf{x}^k$, $p(\mathbf{x}^k|\mathbf{z}^{1:k-1})$ is the prior PDF over the state $\mathbf{x}^k$, $p(\mathbf{z}^k|\mathbf{x}^k)$ is the measurement probability, and κ is the normalization constant of the Bayes rule.

The posterior PDF of Equation 3.26 is used as the input to the next prediction step in time step $k+1$. The solution to the estimation problem can either be given by the parameter that maximizes the posterior distribution, the so-called maximum a posteriori (MAP), or the expectation, which would yield the minimum mean squared error (MMSE). Both are given in the following equations:

$$\hat{\mathbf{x}}^k_{\text{MAP}} = \arg\max_{\mathbf{x}^k} \quad p\left(\mathbf{x}^k\middle|\mathbf{z}^{1:k}\right), \tag{3.27}$$

$$\hat{\mathbf{x}}^k_{\text{MMSE}} = \int_{\mathbf{x}^k} \mathbf{x}^k p\left(\mathbf{x}^k\middle|\mathbf{z}^{1:k}\right) d\mathbf{x}^k. \tag{3.28}$$

A practical implementation of the Bayesian filter requires to solve Equations 3.25 and 3.26. Finding the solution to the integral in Equation 3.25 is usually a difficult task [143]. Only if certain restrictions on the state transition model in Equation 3.23 and the measurement model in Equation 3.24 are imposed and certain prior and posterior distributions are assumed, the integral becomes solvable. One of these implementations is introduced in the following section. A second possibility to solve the integral is by following a numerical approach. Particle filters belong to the family of so-called sequential Monte Carlo filters [145]. Here, the prior and posterior distributions are not described analytically, but are described by weighted samples of the state, so-called particles. Therefore, the particle filter is an approximation to the optimal Bayesian filter. For further information on particle filters the reader is referred to [145].

3.3.3. Gaussian Filters

In a Gaussian filter, all prior and posterior beliefs are assumed to be represented by multivariate normal distributions according to:

$$\mathbf{x} \sim \mathcal{N}\left(\overline{\mathbf{x}}, \mathbf{P}\right) = |2\pi\mathbf{P}|^{-\frac{1}{2}}\, exp\left\{-\frac{1}{2}(\mathbf{x}-\overline{\mathbf{x}})^{\intercal}\mathbf{P}^{-1}(\mathbf{x}-\overline{\mathbf{x}})\right\}. \tag{3.29}$$

Thus, the belief PDF over a state $\mathbf{x}$ is fully characterized by a mean vector $\overline{\mathbf{x}}$ and a variance-covariance matrix $\mathbf{P}$.

Kalman Filters The Kalman filter is a technique for estimation in linear Gaussian systems named after Rudolf E. Kálmán who worked on the development of its theory [146]. In a Kalman filter, the prediction and measurement update equations take a linear form with additive white Gaussian noise. The prediction equation is

$$\mathbf{x}^k = \mathbf{F} \cdot \mathbf{x}^{k-1} + \mathbf{B} \cdot \mathbf{u}^k + \boldsymbol{\nu}^{k-1}, \tag{3.30}$$

where $\mathbf{x}^k$ represents the unobserved state vector of the system at time step k, $\mathbf{x}^{k-1}$ is the state vector in the previous time step $k-1$, $\mathbf{F}$ is a linear vector-valued function expressed in matrix form representing the state transition model. The control vector $\mathbf{u}^k$ is mapped to the sate by the control matrix $\mathbf{B}$. The uncertainty in the prediction is modeled by adding the process noise $\boldsymbol{\nu}^{k-1}$. The measurement update equation is

$$\mathbf{z}^k = \mathbf{H} \cdot \mathbf{x}^k + \boldsymbol{\eta}^k, \tag{3.31}$$

where $\mathbf{z}^k$ is the observed data or measurements, $\mathbf{H}$ is the linear measurement model that relates the state vector to the measurements, and $\boldsymbol{\eta}^k$ is the vector representing the measurement noise. Both, $\boldsymbol{\nu}^{k-1}$ in Equation 3.30 and $\boldsymbol{\eta}^k$ in Equation 3.31 are zero-mean mutually independent white Gaussian noise.

It is sufficient that the stated properties of linearity and Gaussianness hold, to ensure that the posterior PDF of the state vector $\mathbf{x}^k$ is always Gaussian. Under this assumption, the Kalman filter represents the optimal solution to the estimation problem [143]. This implies that no algorithm can ever do better than a Kalman filter in this linear Gaussian environment. The Kalman filter, as the LS algorithm, estimates the state process in a way that minimizes the mean of the squared error [147].

Next, the algorithm to solve recursively the state estimation problem using a Kalman filter is presented. The input of the Kalman filter is the posterior PDF from the previous step represented by a mean vector $\widehat{\mathbf{x}}^{k-1}$ and a variance-covariance matrix $\mathbf{P}^{k-1}$. The prediction stage computes the mean vector $\widetilde{\mathbf{x}}^k$ and covariance matrix $\widetilde{\mathbf{P}}^k$ for the prior distribution $p(\mathbf{x}^{k-1}|\mathbf{z}^{1:k-1})$ according to:

$$\widetilde{\mathbf{x}}^k = \mathbf{F} \cdot \widehat{\mathbf{x}}^{k-1} + \mathbf{B} \cdot \mathbf{u}^k, \tag{3.32}$$

$$\widetilde{\mathbf{P}}^k = \mathbf{F} \cdot \mathbf{P}^{k-1} \cdot \mathbf{F}^\intercal + \mathbf{V} \cdot \mathbf{Q}^{k-1} \cdot \mathbf{V}^\intercal, \tag{3.33}$$

where $\mathbf{F}$ is a known matrix defining the linear system function, $\mathbf{V}$ is a known matrix that maps the process noise in the state domain, and $\mathbf{Q}^{k-1}$ is the covariance matrix of the process noise random variables. The resulting prior distribution $p(\mathbf{x}^k|\mathbf{z}^{1:k-1})$ is the Gaussian function $\mathcal{N}\left(\widetilde{\mathbf{x}}^k, \widetilde{\mathbf{P}}^k\right)$.

Then, the measurement stage computes the mean vector $\widehat{\mathbf{x}}^k$ and covariance matrix $\mathbf{P}^k$ of the

posterior distribution $p(\mathbf{x}^k|\mathbf{z}^{1:k})$ incorporating the measurement vector $\mathbf{z}^k$ according to:

$$\widetilde{\mathbf{y}}^k = \mathbf{H} \cdot \widetilde{\mathbf{x}}^k \tag{3.34}$$

$$\mathbf{K}^k = \widetilde{\mathbf{P}}^k \cdot \mathbf{H}^\intercal \cdot (\mathbf{H} \cdot \widetilde{\mathbf{P}}^k \cdot \mathbf{H}^\intercal + \mathbf{R}^k)^{-1} \tag{3.35}$$

$$\widehat{\mathbf{x}}^k = \widetilde{\mathbf{x}}^k + \mathbf{K}^k \cdot (\mathbf{z}^k - \widetilde{\mathbf{y}}^k) \tag{3.36}$$

$$\mathbf{P}^k = (\mathbf{I} - \mathbf{K}^k \cdot \mathbf{H}) \cdot \widetilde{\mathbf{P}}^k \tag{3.37}$$

where $\mathbf{I}$ is the identity matrix, $\mathbf{H}$ is the matrix defining the linear measurement equation and $\mathbf{R}^k$ is the covariance matrix of the measurement noise random vector. The posterior distribution $p(\mathbf{x}^k|\mathbf{z}^{1:k})$ is a Gaussian function $\mathcal{N}\left(\widehat{\mathbf{x}}^k, \mathbf{P}^k\right)$. The *Kalman gain* matrix $\mathbf{K}^k$ specifies the degree to which the measurement is incorporated into the new state estimate. The Kalman gain controls the addition of the *innovation term* $\mathbf{z}^k - \widetilde{\mathbf{y}}^k$ to the prior estimate of the state. This innovation term is the difference between the current measurement $\mathbf{z}^k$ and the predicted measurement $\widetilde{\mathbf{y}}^k$.

In many situations, the linearity assumptions made for the Kalman filter do not hold. Inertial navigation systems, for instance, include highly non-linear equations. In such cases, the Kalman filter cannot be used, and, thus, approximations are necessary in order to deal with non-linearities. Equation 3.30 and Equation 3.31 can be written in a general form as:

$$\mathbf{x}^k = f(\mathbf{x}^{k-1}, \boldsymbol{\nu}^{k-1}), \tag{3.38}$$

$$\mathbf{z}^k = h(\mathbf{x}^k, \boldsymbol{\eta}^k), \tag{3.39}$$

where $f(\cdot)$ and $h(\cdot)$ are non-linear vector-valued functions. When transforming a Gaussian distributed random variable through a non-linear function the result is, in general, a non-Gaussian distributed variable. In fact, performing the belief update exactly is usually impossible for non-linear functions and the Bayes filter does not possess a closed-form solution [143]. Non-linear Kalman filters calculate a Gaussian approximation to the true belief PDF. Depending on the linearization approach, there are several options for obtaining an approximate estimation solution of the non-linear problem. Two well-known approximations to the non-linear Kalman filter are the Extended Kalman Filter (EKF) [145] and the Unscented Kalman Filter (UKF) [148]. In the EKF, the non-linear function is linearized with a first-order Taylor approximation and the Gaussian distributions are propagated through this linear approximation identically as in the Kalman filter. In the UKF, a set of discrete points of the state space, so-called sigma points, are transformed by the non-linear functions and are converted back to a Gaussian distribution. Further information on the EKF and UKF algorithms can be found in [145] and in [148], respectively.

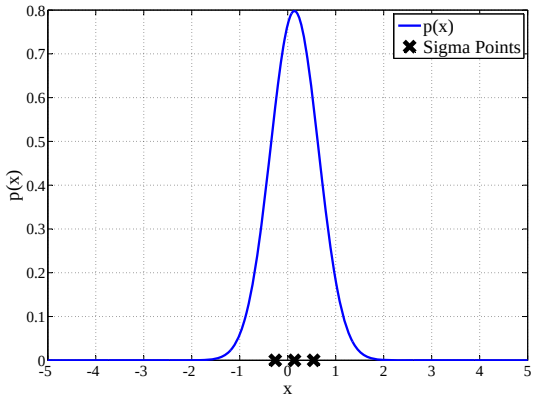

(a) Input PDF

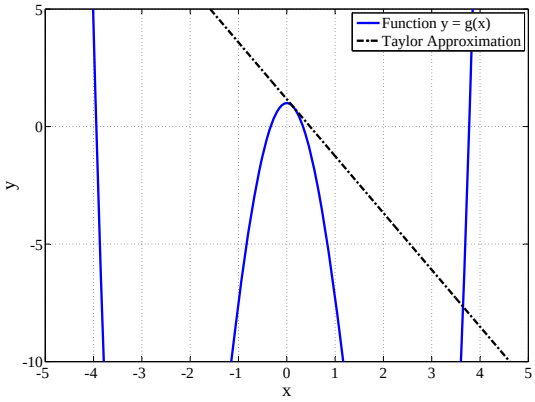

(b) Transformation

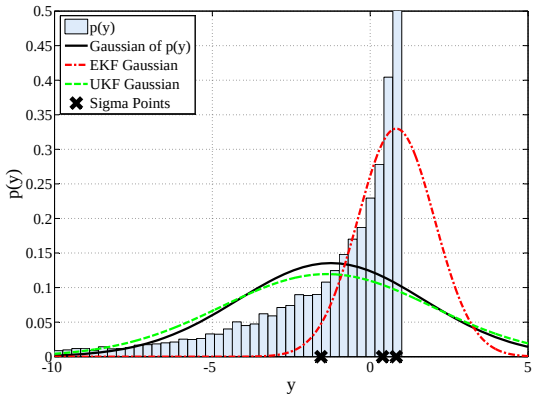

(c) Output PDF

Figure 3.8.: Figure 3.8a shows the PDF $p(x)$ of a random variable x. Also the Sigma points for that distribution are depicted in black. The non-linear transformation $y = g(x)$ is shown in 3.8b along with its first order linear approximation at the mean of x. Figure 3.8c depicts the output PDF $p(y)$ after the transformation of x through the non-linear function g. In blue the normalized histogram for 10,000 samples of y is shown. In black, the Gaussian PDF corresponding to the histogram is depicted. The output of an EKF is represented by the red curve, which corresponds to the transformation of $p(x)$ through the linear approximation of $g(x)$. The black crosses are the three sigma points transformed by g and which result in the green Gaussian PDF for the UKF.

3.3.4. Modeling

The performance of each implementation of a Bayesian Filter depends on the amount of non-linearity in both, the prediction and measurement equation, and prior and posterior variances. Figure 3.8 illustrates this effect for a Gaussian distribution $p(x)$ (Figure 3.8a) passed through a non-linear function $g(x)$ (Figure 3.8b). This is analogous to the propagation of the posterior PDF through a non-linear system model in the prediction step or the propagation of the prior PDF through a non-linear measurement model in the update step. Both output distributions, with EKF (red) and UKF (green), are compared to the true distribution (back) determined through Monte Carlo estimation (Figure 3.8c).

Evidently, after transformation through a non-linear equation, the previous Gaussian distribution is no longer Gaussian (blue histogram). However, a Gaussian distribution that best models the output distribution can be built (black). It can be observed, that the output of the EKF (red) fails to model correctly the output distribution. The quality of the EKF approximation depends on the amount of non-linearity of $g(x)$ and the initial uncertainty, i.e. the width of $p(x)$. The UKF (green distribution), on the other hand, has a better result and, in fact, it can be shown that the Unscented Transform (UT) is accurate up to the second order of the Taylor expansion of $g(x)$ [143].

However, even in the case that linearity and Gaussianess are given, the Kalman filter might perform suboptimal due to model mismatch [149]. Bayesian estimators are only as good as the used system and measurement models reflect the real-world process. The system state $\mathbf{x}$ has to include all relevant hidden states with memory and to satisfy the completeness assumption. The measurements need to be independent one from the other and any bias needs to be included into the system state. In practice, there will always be a certain mismatch between the real world and the models chosen to mirror it. If the mismatch is kept small, by trying to adapt the model as much as possible, the Bayesian filter will converge to the correct solution [149].

Chapter 4.

Theoretical Model for Cooperative Relative Positioning

4.1. Situation Awareness

Situation awareness of the driver and the in-vehicle systems is extremely important in safety-critical advanced driver assistance systems. Any assistance system requires a correct perception of the environment in order to have an accurate picture of the real world and to make the correct decisions upon the available information. Endlsey defines situation awareness as "the perception of the elements in the environment within a volume of time and space, the comprehension of their meaning, and the projection of their status in the near future" [150]. However, perception is by far not trivial. Sensor measurements are corrupted with errors and, additionally, there is not always a suitable sensor for every relevant element of the environment. As perception is inaccurate and incomplete under real-world conditions, situational information is inherently uncertain [151].

The conceptual system decomposition related to situational awareness is depicted in Figure 4.1. This model can be applied for both, a human driver and an advanced driver assistance system. The world is perceived through sensors. This data has to be interpreted to extract evidence on the surrounding environment. The processed data is fitted into a world model. If both, the sensing system and the data interpreter are adequate, this representation describes the relevant surrounding with sufficient accuracy. A controlling system, based on a defined mission or goal, will make a decision on whether to take action and perform a control command. This actuation feeds back into the real world.

In Intelligent Transportation Systems (ITS), each station keeps an updated copy of its knowledge on the surrounding environment. This copy is known as the Local Dynamic Map (LDM) [152]. It comprises a complex database where events and information are classified in different layers depending on its nature. Static and dynamic information, including the map of the environment, the road topology, other vehicles and relevant events, are part of the LDM [153]. The LDM should, as well, provide means to represent degrees of certainty about the stored objects [152].

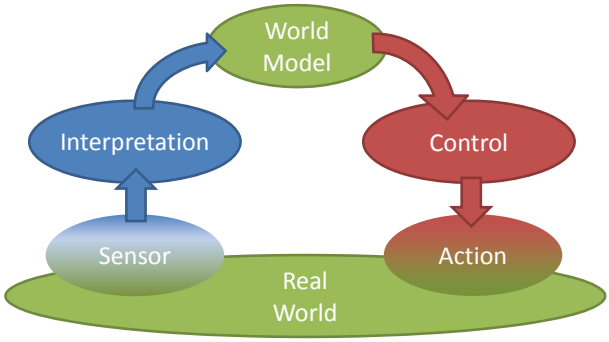

Figure 4.1.: The figure displays the classic sensor/actuator control loop including a local, incomplete, inaccurate representation of the real world.

The structure and the interfaces of an LDM are standardized by European Telecommunications Standards Institute (ETSI) [154]. Figure 4.2 displays selected attributes that are included in an LDM. Hence, this local database represents a practical way to achieve situation awareness in ITS.

One possible metric to quantify awareness quality for collision avoidance applications is based on the ratio of detected vehicles to all vehicles in a certain range and the age of received forwarded information [155]. Another metric is given by the probability of having received one beacon from one neighbor in the last second [156]. Here, also the distance between the transmitter-receiver pair is taken into account, as the required awareness is dependent on the distance between the vehicles. While [155] and [156] focus on communication aspects and disregard the content of the communication packet, in [151] the value of information is considered. Here, Cooperative Situation Awareness is defined as "the concept of utilizing distributed information and treating the information with its actual worth for all entities in the cooperation". The entropy of a random variable is used as a measure of its uncertainty. The uncertainty or entropy of a variable decreases when new evidence, i.e. information or measurements, are incorporated into the system. Thus, the value of information for each evidence can be obtained. In this way, the necessity of transmitting a certain evidence can be related to its value of information.

The situation awareness of the ego vehicle is given by the completeness and accuracy of the attributes it has on its environment (see Figure 4.2). Attributes include surrounding vehicles, pedestrians or cyclists, the status of traffic lights or the own geographical and topological position on the road. This information is, in general, not accurately known, either because it is not directly observable or because the sensors employed have errors in their measurements. A vehicle will not know precisely its own location due to positioning errors. The topological map might be

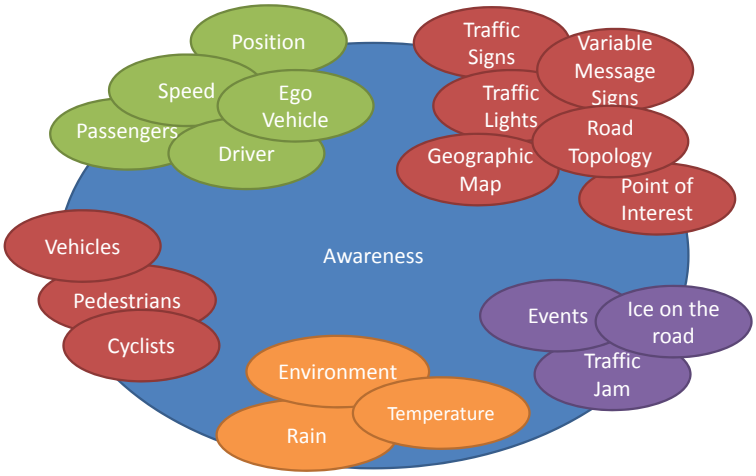

Figure 4.2.: The figure shows exemplary attributes that comprise the awareness in the ITS domain. A Local Dynamic Map stores these attributes along with their certainty.

outdated. The location and dynamics of surrounding vehicles is only known to the extent that they are perceived by local on-board sensors. The intention of other drivers is difficult to observe and can only be partially inferred by, for example, using information on turning or braking lights. Consequently, the awareness has to include these intrinsic uncertainties into account.

From the attributes that comprise the awareness of a vehicle, in this thesis the focus will be on the information concerning the relative position and the relative velocity towards road vehicles. Although the proposed cooperative approach for relative position estimation could be extended to pedestrians, the sensors and equipment proposed in this work are not expected to be carried by a person. Furthermore, due to the motion models used in this thesis, the range of perceived vehicles has to be further limited to cars, vans and non-articulated trucks. The relative position towards other traffic participants, such as motorbikes, bicycles or pedestrians, lie beyond the scope of this work. Further on, and for simplicity, only the relative position and relative velocity towards *one* other vehicle will be considered in the models, simulations and real-world experiments. In this way, the challenges related to classification, association and identification can be disregarded. The underlying assumption is that the relative position of a pair of vehicles is independent of other vehicles. This, however, is not true and cross-correlations between pairs of vehicles can provide further information. The analysis of relative position in clusters of vehicles falls out of the scope of this thesis and is proposed as future work in Chapter 8. Relative position, as will be explained in the following section, will involve related attributes, such as time, absolute position, speed, acceleration, turn rate or heading of each vehicle.

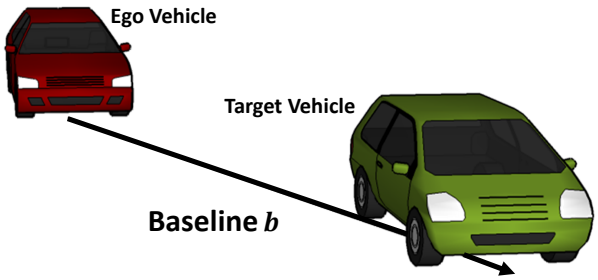

Figure 4.3.: The baseline vector $\mathbf{b}$ is the three-dimensional vector pointing from the foremost center point on the ground of the ego vehicle to the foremost center point on the ground of the target vehicle.

4.2. Definition of the Baseline between two Vehicles

As introduced in the previous section, this thesis focuses on the concrete aspect of relative positioning between vehicles. The ego vehicle is the vehicle at which the driver assistance system requiring information on relative position of surrounding vehicles is running. The target vehicle is one surrounding vehicle, whose relative position towards the ego vehicle is to be estimated.

It is not assumed that ego and target vehicle drive in a certain configuration. In the scope of this thesis, it is not assumed that both vehicles are following each other, although, for the experimental setup in Chapter 7, they are placed in this configuration. While in a platooning application both vehicles follow each other, for other applications, as for instance a forward collision warning application, the target vehicle might be approaching from the front or from the side, while in a blind spot warning application the target vehicle might be driving in the same direction behind to the ego vehicle on the lane next to it.

The aim of a relative positioning system in the ego vehicle is to provide precise, accurate and continuous knowledge about the relative position of the target vehicle. In general, and specially for safety-critical applications, the awareness of nearby vehicles is of higher relevance, since they represent a greater risk. The relative position information about the target vehicle is required in real-time, meaning that the delay caused by the relative positioning system should be small and bounded. However, not only the current relative position information is of importance, but also a prediction of the future trajectory of the target vehicle can be used by the driver assistance system.

The relative position of a target vehicle, as seen from the ego vehicle, is described by a three-dimensional vector. This vector will be named the *baseline* $\mathbf{b}$. The origin of the baseline vector is at the foremost center point on the ground of the ego vehicle, while the end point is at the foremost center point on the ground of the target vehicle. This baseline vector between two vehicles is displayed in Figure 4.3.

The baseline vector is defined in an ego vehicle coordinate frame, following the recommendation of the Society for Automotive Engineers (SAE) for surface vehicle coordinate frames and frame rotations [157]. The x-axis points in forward direction of the vehicle, while the y-axis points to the left and the z-axis, completing the right hand rule, points up (see Figure 3.2). The baseline vector between two vehicles will be denoted as

$$\mathbf{b} = \begin{bmatrix} b_{\mathrm{x}} \\ b_{\mathrm{y}} \\ b_{\mathrm{z}} \end{bmatrix}. \tag{4.1}$$

The longitudinal component of the baseline will be denoted b_{x}, while the lateral or transverse component will be denoted b_{y}. In certain applications, the baseline vector in space can be reduced to a two-dimensional vector on the ground, disregarding the z component b_{z}. Since vehicles usually move on the same plane and larger height differences on short distances are uncommon, this is a valid assumption. A numerical example shows the error in relative position made by disregarding the vertical component. The relative position of a target vehicle at a distance of 100 m, would be incorrectly estimated to 100.5 m on a road with 10 % grade. This corresponds to less than 1 % range error. In vehicular applications, the z component is of interest e.g. in multi-stack highway interchanges to differentiate off-road traffic or in highly inclined roads.

The *baseline velocity* $\dot{\mathbf{b}}$ is equal to the relative velocity between the vehicles. It is given by a three-dimensional vector in space pointing in the direction in which the baseline is varying over time, according to

$$\dot{\mathbf{b}} = \frac{d\mathbf{b}}{dt}. \tag{4.2}$$

The baseline velocity is therefore the derivative of the baseline vector and it is calculated by differentiating each of its components. The magnitude of the baseline velocity is equal to the relative speed between ego and target vehicles. The baseline velocity is important as it quantifies the rate of change of the baseline and, therefore, will enhance the performance of the driver assistance application.

Safety-critical assistance applications use the information of the relative position of another vehicle in form of the baseline and the baseline velocity in order to adapt the speed to an in-front driving car, warn the driver of vehicles in their blind spot or activate the brakes, when the baseline gets critically small. Figure 4.4 shows an overtaking and an intersection scenario for three consecutive time steps. A red baseline velocity vector indicates a shrinking baseline, i.e. a potentially hazardous situation, while a green one indicates a growing baseline vector and, therefore, a safe situation.

In this thesis both, baseline and baseline velocity, are not treated as deterministic quantities whose values are known with infinite accuracy, but are random variables representing their stochastic nature. A random variable is not described by a single value but by a probability distribution

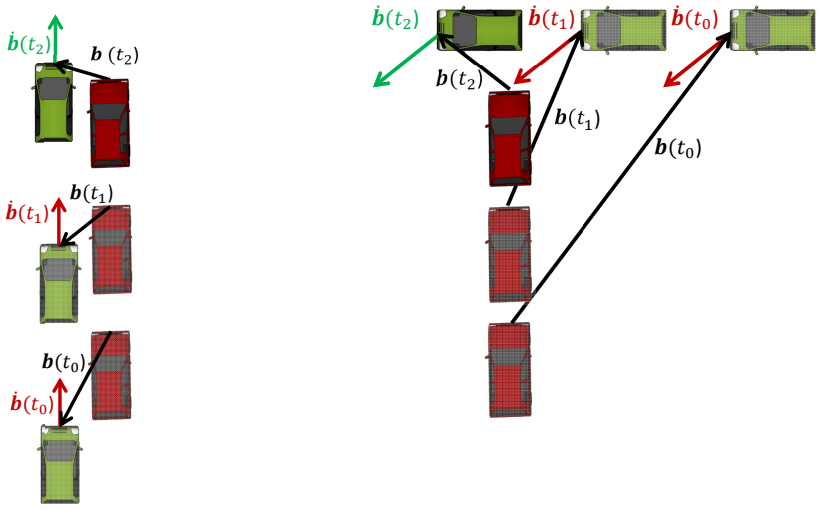

(a) Overtaking (b) Intersection

Figure 4.4.: Evolution of the baseline vector over time for two possible scenarios: On the left picture an overtaking maneuver is displayed, while the right picture displays an intersection scenario. The risk of a maneuver between two vehicles increases when the baseline vector decreases in magnitude. The baseline velocity points in the direction in which the the baseline vector is changing.

over its sample space. Each three-dimensional point in relative positioning space has a probability assigned, corresponding to the probability of the target vehicle being at that position. The same holds for the relative velocity space. The spread of these probabilities over the sample space at a given point in time gives a measure of the uncertainty in the baseline and baseline velocity estimates.

This uncertainty stems from various sources. A ranging sensor, for instance, could have a different precision in its longitudinal and lateral coordinates or a changing accuracy with the opening angle or the ranging distance. A cooperative solution, as the one presented in this thesis, which is based on the exchange of information through a wireless communication channel, has a baseline and baseline velocity accuracy that is dependent e.g. on the communication update rate or the packet error rate. The sensors on board of each of the vehicles have errors, such as random noise and unknown biases, that will propagate into the baseline estimate. A changing constellation of GNSS satellites, both in number and position, will have an immediate impact on the position accuracy. Using incomplete and erroneous models to describe the real world introduces further uncertainty into the estimates.

Figure 4.5 represents the relative position from the ego vehicle towards two vehicles by their probability distribution. In this case, the depicted uncertainty follows a Gaussian distribution over

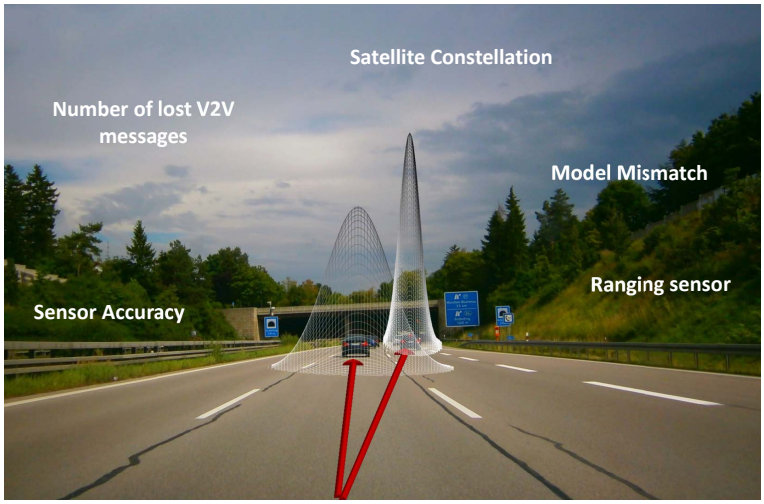

Figure 4.5.: Representation of the baseline vectors towards two vehicles by spatial random variables. In this example, the knowledge of the relative position of the right vehicle is more precise than that of the left vehicle.

space. In general, any other function is possible, but it turns out, that Gaussian distributions are particularly well suited to work with [143]. By means of a probabilistic approach, such as a Bayesian filter, this uncertainty can be modeled over time [143]. The key idea is that, if the uncertainty in the system models and the sensor models is correctly quantified, its propagation to the final baseline and baseline velocity estimates can be correctly tracked over time. Hence, uncertainty shall be described and actively taken into account.

4.3. Bayesian Relative Positioning

Bayesian networks, or belief networks, present, by using a graphical model, the conditional dependencies of a set of random variables [143]. Bayesian networks that model a time sequence of variables are called dynamic Bayesian networks [143]. In Chapter 3, the theoretical concepts of Bayesian estimation were reviewed. In this section it will be shown that the continuous estimation of the relative position of another vehicle is a problem that, if certain conditions are met, can be modeled using a dynamic Bayesian network. The baseline vector from an ego vehicle to a target vehicle is a hidden state that can only be observed through certain evidences or measurements. These can be, for instance, the detected objects of a radar sensor or the baseline measurement from subtracting two GNSS positions. Both examples are noisy measurements of the baseline.

In order to model the problem as a dynamic Bayesian network, the first order Markov assumptions have to be met [143]. The first one, given in Equation 3.23, states that the state estimate in time step k has a single causal relationship to the state estimate in $k-1$ and is independent to any previous estimate in time steps $\{0 \dots k-2\}$. This requires that the state estimate contains the

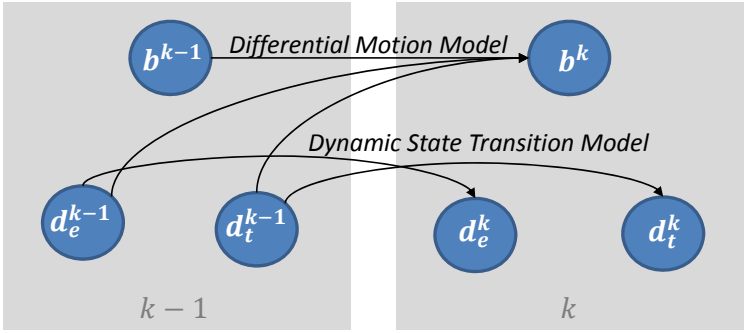

Figure 4.6.: The picture shows the baseline transition model. The baseline $\mathbf{b}^k$ is dependent on the previous baseline $\mathbf{b}^{k-1}$ and the dynamic states of the ego vehicle $\mathbf{d}_\mathrm{e}^{k-1}$ and the target vehicle $\mathbf{d}_\mathrm{t}^{k-1}$. This relationship is given by the differential motion model. The dynamic state of each vehicle in each instant k only depends on the dynamic state in the previous instant $k-1$. This relationship is given by the Dynamic State transition model.

full information and, consequently, is memory-less [143].

If the state estimate would only include the baseline vector $\mathbf{b}$ this requirement is not fulfilled, since the baseline at k does not contain all information to do a prediction for the baseline in $k+1$. Assuming a constant change in the baseline vector over time, the baseline in k will depend on the baseline in both $k-1$ and $k-2$. To overcome this issue and fulfill the Markov assumption, either the relative velocity or the speed and heading of each of the vehicles is require to correctly predict the baseline vector in the next time step. If a linear acceleration is assumed, this Bayesian network would again not fulfill the Markov assumption, if the state is not extended to carry information on the vehicle's acceleration. The kinematic variables are introduced in the dynamic state vectors in time step k, $\mathbf{d}_\mathrm{e}^k$ for the ego vehicle, and $\mathbf{d}_\mathrm{t}^k$ for the target vehicle. Figure 4.6 shows the resulting dynamic Bayesian network for the baseline vector estimate.

The baseline $\mathbf{b}^k$ is said to be dependence-separated or d-separated of $\mathbf{d}_\mathrm{e}^k$ and $\mathbf{d}_\mathrm{t}^k$ if $\mathbf{d}_\mathrm{e}^{k-1}$ and $\mathbf{d}_\mathrm{t}^{k-1}$ are observed respectively [158]. The joint transition probability of the three states $p\left(\mathbf{b}^k, \mathbf{d}_\mathrm{e}^k, \mathbf{d}_\mathrm{t}^k \middle| \mathbf{b}^{k-1}, \mathbf{d}_\mathrm{e}^{k-1}, \mathbf{d}_\mathrm{t}^{k-1}\right)$ can therefore be factorized according in the following way:

$$p\left(\mathbf{b}^k \middle| \mathbf{b}^{k-1}, \mathbf{d}_\mathrm{e}^{k-1}, \mathbf{d}_\mathrm{t}^{k-1}\right) \cdot p\left(\mathbf{d}_\mathrm{e}^k \middle| \mathbf{b}^{k-1}, \mathbf{d}_\mathrm{e}^{k-1}, \mathbf{d}_\mathrm{t}^{k-1}\right) \cdot p\left(\mathbf{d}_\mathrm{t}^k \middle| \mathbf{b}^{k-1}, \mathbf{d}_\mathrm{e}^{k-1}, \mathbf{d}_\mathrm{t}^{k-1}\right). \tag{4.3}$$

The previous equation can further be simplified by accounting for the conditional independence of $\mathbf{d}_\mathrm{e}^k$ from $\mathbf{b}^{k-1}$ and $\mathbf{d}_\mathrm{t}^{k-1}$ and of $\mathbf{d}_\mathrm{t}^k$ from $\mathbf{b}^{k-1}$ and $\mathbf{d}_\mathrm{e}^{k-1}$(see Figure 4.6):

$$p\left(\mathbf{b}^k \middle| \mathbf{b}^{k-1}, \mathbf{d}_\mathrm{e}^{k-1}, \mathbf{d}_\mathrm{t}^{k-1}\right) \cdot p\left(\mathbf{d}_\mathrm{e}^k \middle| \mathbf{d}_\mathrm{e}^{k-1}\right) \cdot p\left(\mathbf{d}_\mathrm{t}^k \middle| \mathbf{d}_\mathrm{t}^{k-1}\right). \tag{4.4}$$

Chapter 5 will dig deeper into relative motion models and baseline prediction models, while this

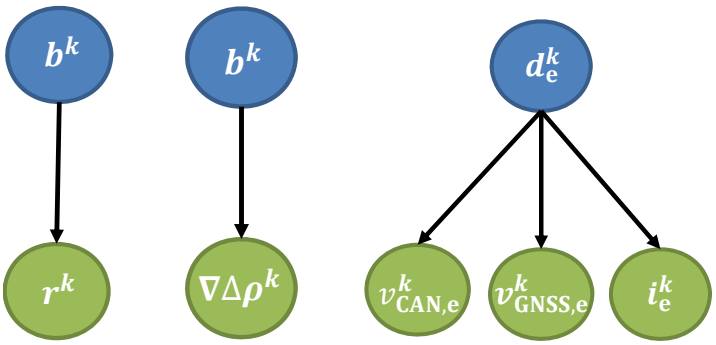

Figure 4.7.: The figures display the causal relationship between hidden states (blue) and observations (green). Figure (a) displays the relationship between the baseline and a radar sensor measurement, while Figure (b) shows the relationship between the baseline and pseudorange double differences. Figure (c) displays the influence of the dynamic state of the vehicle on the CAN bus speed measurement, the GNSS velocity measurements and the measurements of an inertial sensor.

section aims at presenting the causal relationship among the states and the evidences.

The baseline $\mathbf{b}^k$ is a hidden state and, consequently, not directly observable. Instead, measurements from ranging sensors $\mathbf{r}^k$ are influenced by the baseline vector and give evidence on its state as in Figure 4.7a. A cooperative approach based on Vehicle-to-Vehicle (V2V) communication will use the positions of ego and target vehicle estimated in each of the vehicles, to have an estimate of the relative position of both vehicles. In this thesis a novel approach, also based on the exchange on GNSS data, is pursued. However, not the estimated positions in each of the vehicles are exchanged, but the raw pseudoranges $\boldsymbol{\rho}$. As explained in Chapter 3, the pseudoranges are biased and corrupted measurements towards each of the GNSS satellites. These measurements can be differenced twice, as will be explained in more detail in Chapter 5, to give, so-called double differences $\boldsymbol{\nabla\Delta\rho}^k$ that are evidences of the baseline state $\mathbf{b}^k$ as in Figure 4.7b. Their probabilistic dependency is given by the likelihood function

$$p\left(\boldsymbol{\nabla\Delta\rho}^k \middle| \mathbf{b}^k, \mathbf{d}_e^k\right). \tag{4.5}$$

As explained in Chapter 3, this function describes how likely a measurement $\boldsymbol{\nabla\Delta\rho}^k$ is, given the states $\mathbf{b}^k$ and $\mathbf{d}_e^k$. The dependency of the pseudorange double differences with $\mathbf{d}_e^k$ stems from the fact that the baseline vector $\mathbf{b}^k$ needs to be transformed from the ego vehicle coordinate frame to the local navigation coordinate frame by using the orientation of the ego vehicle.

The dynamic state of each vehicle $\mathbf{d}_e^k$ and $\mathbf{d}_t^k$, including its longitudinal speed, heading, turn rate and acceleration, influence the on-board sensors on each vehicle. Their dependency is shown in Figure 4.7c. The speed of the vehicle will influence the speedometer readings $v_{CAN,e}^k$ from the

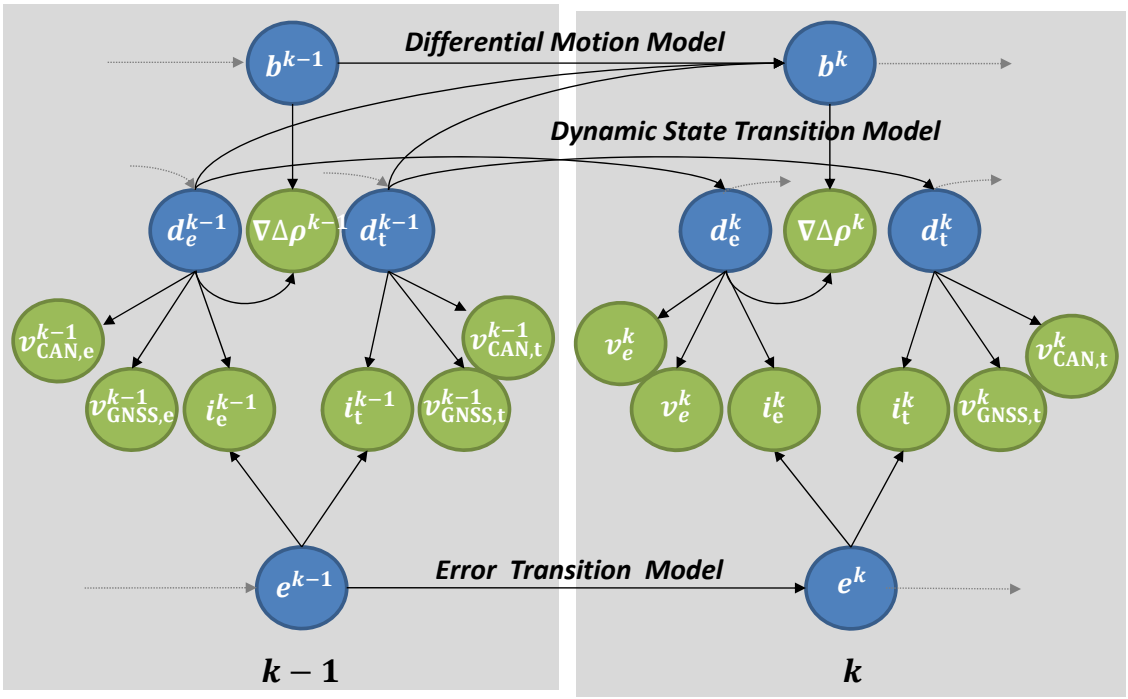

Figure 4.8.: The figure shows the full dynamic Bayesian network for continuous estimation of the baseline between two vehicles in a probabilistic way. The directed graph shows the conditional dependencies between the different random variables.

vehicle's CAN bus. The speed and the heading of the vehicle will have a causal relationship on the velocity measurements from the on-board GNSS receiver, $\mathbf{v}_{\text{GNSS,e}}^{k}$. The acceleration, heading and the turn rate of the vehicle influence the measurements of an Inertial Measurement Unit (IMU), $\mathbf{i}_{\text{e}}^{k}$. Hence, these stochastic relationships can be summarized in the following probabilistic representation for the ego vehicle:

$$p\left(v_{\text{CAN,e}}^{k}, \mathbf{v}_{\text{GNSS,e}}^{k}, \mathbf{i}_{\text{e}}^{k} \middle| \mathbf{d}_{\text{e}}^{k}\right). \tag{4.6}$$

The representation for the target vehicle is analogous. In this model, and complying with the Markov assumption in Equation 3.24, all three evidences in time step k are assumed to be independent from their previous values in time steps $\{1 \dots k-1\}$. This, however, is not true for certain sensors. For instance, the vehicle speedometer, might have a systematic offset or bias caused by a change in the wheel diameter. Also the IMU's accelerometers and gyroscopes have biases as will be explained in Chapter 5. Biases in the measurements are problematic, as they violate the Markov assumption. Consequently, they need to be included in the estimated state. The state $\mathbf{e}^{k}$ includes the biases of all observations that need to be modeled.

All presented Bayesian "pieces" are connected in the complete Bayesian network that models the problem of continuous probabilistic baseline estimation. Figure 4.8 shows the complete Bayesian

network for two consecutive time steps $k-1$ and k. The hidden states are marked in blue, while the observations are marked in green (dark and light in a gray scale printing). The overall joint posterior distribution at time step $k-1$ gives the probability of all hidden states at time step $k-1$ given all observations up to time step $k-1$ (see Chapter 3). This is denoted as:

$$p\left(\{\mathbf{b},\mathbf{d}_\mathsf{e},\mathbf{d}_\mathsf{t},\mathbf{e}\}^{k-1}\middle|\boldsymbol{\nabla\Delta\rho}^{1:k-1},\{v_\mathsf{CAN},\mathbf{v}_\mathsf{GNSS},\mathbf{i}\}_{\mathsf{e,t}}^{1:k-1}\right) \tag{4.7}$$

where the nomenclature $\{\cdot\}_{\mathsf{e,t}}$ expresses observations at both the ego and target vehicle. The joint prior distribution at time step k gives the probability off all states at time step k after performing the prediction step from time step $k-1$ and before incorporating new measurements (see Chapter 3).

$$p\left(\{\mathbf{b},\mathbf{d}_\mathsf{e},\mathbf{d}_\mathsf{t},\mathbf{e}\}^{k},\{\mathbf{b},\mathbf{d}_\mathsf{e},\mathbf{d}_\mathsf{t},\mathbf{e}\}^{k-1}\middle|\boldsymbol{\nabla\Delta\rho}^{1:k-1},\{v_\mathsf{CAN},\mathbf{v}_\mathsf{GNSS},\mathbf{i}\}_{\mathsf{e,t}}^{1:k-1}\right). \tag{4.8}$$

By applying the chain rule [158], Equation 4.8 can be described as the product of:

$$\begin{aligned}
&p\left(\mathbf{b}^k\middle|\{\mathbf{d}_\mathsf{e},\mathbf{d}_\mathsf{t},\mathbf{e}\}^{k},\{\mathbf{b},\mathbf{d}_\mathsf{e},\mathbf{d}_\mathsf{t},\mathbf{e}\}^{k-1},\boldsymbol{\nabla\Delta\rho}^{1:k-1},\{v_\mathsf{CAN},\mathbf{v}_\mathsf{GNSS},\mathbf{i}\}_{\mathsf{e,t}}^{1:k-1}\right)\cdot\\
&p\left(\mathbf{d}_\mathsf{e}^k\middle|\{\mathbf{d}_\mathsf{t},\mathbf{e}\}^{k},\{\mathbf{b},\mathbf{d}_\mathsf{e},\mathbf{d}_\mathsf{t},\mathbf{e}\}^{k-1},\boldsymbol{\nabla\Delta\rho}^{1:k-1},\{v_\mathsf{CAN},\mathbf{v}_\mathsf{GNSS},\mathbf{i}\}_{\mathsf{e,t}}^{1:k-1}\right)\cdot\\
&p\left(\mathbf{d}_\mathsf{t}^t\middle|\mathbf{e}^k,\{\mathbf{b},\mathbf{d}_\mathsf{e},\mathbf{d}_\mathsf{t},\mathbf{e}\}^{k-1},\boldsymbol{\nabla\Delta\rho}^{1:k-1},\{v_\mathsf{CAN},\mathbf{v}_\mathsf{GNSS},\mathbf{i}\}_{\mathsf{e,t}}^{1:k-1}\right)\cdot\\
&p\left(\mathbf{e}\middle|\{\mathbf{b},\mathbf{d}_\mathsf{e},\mathbf{d}_\mathsf{t},\mathbf{e}\}^{k-1},\boldsymbol{\nabla\Delta\rho}^{1:k-1},\{v_\mathsf{CAN},\mathbf{v}_\mathsf{GNSS},\mathbf{i}\}_{\mathsf{e,t}}^{1:k-1}\right)\cdot\\
&p\left(\{\mathbf{b},\mathbf{d}_\mathsf{e},\mathbf{d}_\mathsf{t},\mathbf{e}\}^{k-1}\middle|\boldsymbol{\nabla\Delta\rho}^{1:k-1},\{v_\mathsf{CAN},\mathbf{v}_\mathsf{GNSS},\mathbf{i}\}_{\mathsf{e,t}}^{1:k-1}\right).
\end{aligned} \tag{4.9}$$

Considering the conditional relationships from Figure 4.8, Equations 4.8 and 4.9 can be simplified to yield the joint prior distribution of the state according to:

$$\begin{aligned}
&p\left(\{\mathbf{b},\mathbf{d}_\mathsf{e},\mathbf{d}_\mathsf{t},\mathbf{e}\}^{k},\{\mathbf{b},\mathbf{d}_\mathsf{e},\mathbf{d}_\mathsf{t},\mathbf{e}\}^{k-1}\middle|\boldsymbol{\nabla\Delta\rho}^{1:k-1},\{v_\mathsf{CAN},\mathbf{v}_\mathsf{GNSS},\mathbf{i}\}_{\mathsf{e,t}}^{1:k-1}\right)=\\
&p\left(\mathbf{b}^k\middle|\{\mathbf{b},\mathbf{d}_\mathsf{e},\mathbf{d}_\mathsf{t}\}^{k-1}\right)\cdot p\left(\mathbf{d}_\mathsf{e}^k\middle|\mathbf{d}_\mathsf{e}^{k-1}\right)\cdot p\left(\mathbf{d}_\mathsf{t}^k\middle|\mathbf{d}_\mathsf{t}^{k-1}\right)\cdot\\
&p\left(\mathbf{e}^k\middle|\mathbf{e}^{k-1}\right)\cdot p\left(\{\mathbf{b},\mathbf{d}_\mathsf{e},\mathbf{d}_\mathsf{t},\mathbf{e}\}^{k-1}\middle|\boldsymbol{\nabla\Delta\rho}^{1:k-1},\{v_\mathsf{CAN},\mathbf{v}_\mathsf{GNSS},\mathbf{i}\}_{\mathsf{e,t}}^{1:k-1}\right).
\end{aligned} \tag{4.10}$$

Hence, the joint prior distribution can be written as a function of the posterior distribution of the previous time step $k-1$, and the transition probabilities from $k-1$ to k of each of the states. In Equation 4.10, the probability of the random variables $\{\mathbf{b},\mathbf{d}_\mathsf{e},\mathbf{d}_\mathsf{t},\mathbf{e}\}^{k-1}$ is not required. These are so-called nuisance variables. Therefore, by integrating over the nuisance variables using Chapman-Kolmogorov equation [158] the prior distribution for the states $\{\mathbf{b},\mathbf{d}_\mathsf{e},\mathbf{d}_\mathsf{t},\mathbf{e}\}^{k-1}$ at time

step k is obtainend. This process is called marginalization:

$$p\left(\{\mathbf{b},\mathbf{d}_\mathsf{e},\mathbf{d}_\mathsf{t},\mathbf{e}\}^k\middle|\boldsymbol{\nabla\Delta\rho}^{1:k-1},\{v_\mathsf{CAN},\mathbf{v}_\mathsf{GNSS},\mathbf{i}\}_{\mathsf{e,t}}^{1:k-1}\right)=$$
$$\int\int\int\int p\left(\{\mathbf{b},\mathbf{d}_\mathsf{e},\mathbf{d}_\mathsf{t},\mathbf{e}\}^k,\{\mathbf{b},\mathbf{d}_\mathsf{e},\mathbf{d}_\mathsf{t},\mathbf{e}\}^{k-1}\middle|\boldsymbol{\nabla\Delta\rho}^{1:k-1},\{v_\mathsf{CAN},\mathbf{v}_\mathsf{GNSS},\mathbf{i}\}_{\mathsf{e,t}}^{1:k-1}\right)$$
$$d\mathbf{d}_\mathsf{e}^{k-1}d\mathbf{d}_\mathsf{t}^{k-1}d\mathbf{b}^{k-1}d\mathbf{e}^{k-1}. \tag{4.11}$$

In the update step, the new measurements at time step k are incorporated to the prior distribution to obtain the new posterior by using Bayes Rule. The update equation for the pseudorange double difference measurements $\boldsymbol{\nabla\Delta\rho}^k$ is:

$$p\left(\{\mathbf{b},\mathbf{d}_\mathsf{e},\mathbf{d}_\mathsf{t},\mathbf{e}\}^k\middle|\boldsymbol{\nabla\Delta\rho}^{1:k},\{v_\mathsf{CAN},\mathbf{v}_\mathsf{GNSS},\mathbf{i}\}_{\mathsf{e,t}}^{1:k-1}\right)=\kappa\cdot$$
$$p\left(\boldsymbol{\nabla\Delta\rho}^k\middle|\{\mathbf{b},\mathbf{d}_\mathsf{e}\}^k\right)\cdot p\left(\{\mathbf{b},\mathbf{d}_\mathsf{e},\mathbf{d}_\mathsf{t},\mathbf{e}\}^k\middle|\boldsymbol{\nabla\Delta\rho}^{1:k-1},\{v_\mathsf{CAN},\mathbf{v}_\mathsf{GNSS},\mathbf{i}\}_{\mathsf{e,t}}^{1:k-1}\right), \tag{4.12}$$

where all κ are normalization constants related to Bayes equation as explained in Chapter 3. The update equation for the CAN speed measurements at the ego vehicle $v_{\mathsf{CAN,e}}$ is:

$$p\left(\{\mathbf{b},\mathbf{d}_\mathsf{e},\mathbf{d}_\mathsf{t},\mathbf{e}\}^k\middle|\boldsymbol{\nabla\Delta\rho}^{1:k},v_{\mathsf{CAN,e}}^{1:k},v_{\mathsf{CAN,t}}^{1:k-1},\{\mathbf{i},\mathbf{v}_\mathsf{GNSS}\}_{\mathsf{e,t}}^{1:k-1}\right)=\kappa\cdot$$
$$p\left(v_{\mathsf{CAN,e}}^k\middle|\{\mathbf{d}_\mathsf{e},\mathbf{e}\}^k\right)\cdot p\left(\{\mathbf{b},\mathbf{d}_\mathsf{e},\mathbf{d}_\mathsf{t},\mathbf{e}\}^k\middle|\boldsymbol{\nabla\Delta\rho}^{1:k},\{v_\mathsf{CAN},\mathbf{v}_\mathsf{GNSS},\mathbf{i}\}_{\mathsf{e,t}}^{1:k-1}\right). \tag{4.13}$$

The update equation for the GNSS derived velocity measurements at the ego vehicle $\mathbf{v}_{\mathsf{GNSS,e}}$ is:

$$p\left(\{\mathbf{b},\mathbf{d}_\mathsf{e},\mathbf{d}_\mathsf{t},\mathbf{e}\}^k\middle|\boldsymbol{\nabla\Delta\rho}^{1:k},\{v_\mathsf{CAN},\mathbf{i}\}_\mathsf{e}^{1:k},\{v_\mathsf{CAN},\mathbf{i}\}_\mathsf{t}^{1:k-1},\mathbf{v}_{\mathsf{GNSS,e,t}}^{1:k-1}\right)=\kappa\cdot$$
$$p\left(\mathbf{i}_\mathsf{e}^k\middle|\{\mathbf{d}_\mathsf{e},\mathbf{e}\}^k\right)\cdot p\left(\{\mathbf{b},\mathbf{d}_\mathsf{e},\mathbf{d}_\mathsf{t},\mathbf{e}\}^k\middle|\boldsymbol{\nabla\Delta\rho}^{1:k},v_{\mathsf{CAN,e}}^{1:k},v_{\mathsf{CAN,t}}^{1:k-1},\{\mathbf{i},\mathbf{v}_\mathsf{GNSS}\}_{\mathsf{e,t}}^{1:k-1}\right). \tag{4.14}$$

Finally, the update equation for the inertial measurements in the ego vehicle $\mathbf{i}_\mathsf{e}$ is:

$$p\left(\{\mathbf{b},\mathbf{d}_\mathsf{e},\mathbf{d}_\mathsf{t},\mathbf{e}\}^k\middle|\boldsymbol{\nabla\Delta\rho}^{1:k},\{v_\mathsf{CAN},\mathbf{v}_\mathsf{GNSS},\mathbf{i}\}_\mathsf{e}^{1:k},\{v_\mathsf{CAN},\mathbf{v}_\mathsf{GNSS},\mathbf{i}\}_\mathsf{t}^{1:k-1}\right)=\kappa\cdot$$
$$p\left(\mathbf{v}_{\mathsf{GNSS,e}}^k\middle|\mathbf{d}_\mathsf{e}^k\right)\cdot p\left(\{\mathbf{b},\mathbf{d}_\mathsf{e},\mathbf{d}_\mathsf{t},\mathbf{e}\}^k\middle|\boldsymbol{\nabla\Delta\rho}^{1:k},\{v_\mathsf{CAN},\mathbf{i}\}_\mathsf{e}^{1:k},\{v_\mathsf{CAN},\mathbf{i}\}_\mathsf{t}^{1:k-1},\mathbf{v}_{\mathsf{GNSS,e,t}}^{1:k-1}\right). \tag{4.15}$$

The update equations for the target measurements $v_{\mathsf{CAN,t}}^k$, $\mathbf{v}_{\mathsf{GNSS,t}}^k$ and $\mathbf{i}_\mathsf{t}^k$ are analogous.

Given an initial prior probability distribution $p\left(\{\mathbf{b},\mathbf{d}_\mathsf{e},\mathbf{d}_\mathsf{t},\mathbf{e}\}^0\right)$ for time step $k=0$, the joint posterior distribution for the baseline can be estimated applying the proposed equation for prediction 4.11 and update 4.12 to 4.15 sequentially for every time step k. These equations represent the optimal solution for the estimation of the baseline given the proposed dependency model. In Chapter 5, assumptions on the proposed distributions will be made. These assumptions will, in general, lead to a sub-optimal estimation of the baseline.

4.4. Vehicle Relative Positioning Metrics

Chapter 2 has presented the requirements for relative positioning systems. These requirements were used to judge the suitability of the subsequently presented state-of-the-art approaches for relative positioning that can be found both, installed in modern vehicles or still in development or research phase. In order to evaluate the proposed relative positioning approach based on a Bayesian estimation method, with exchanged GNSS pseudoranges and on-board sensors over a V2V communication link, objective metrics need to be defined.

The *accuracy* of the system will be determined by calculating the error in the estimated baseline and baseline velocity compared to the baseline and baseline velocity measured with a suited reference system. Since planar relative positioning is regarded in the scope of this thesis, this error is given by a two-dimensional vector, which can be decomposed in its longitudinal and lateral component. The accuracy is assessed by performing a statistical analysis on the magnitude of each of these components and synthesizing their distribution in a Cumulative Distribution Function (CDF) plot. In this way, not only mean error values, but also peak errors and the complete distribution can be analyzed.

The *reliability* will be analyzed by looking at the instants when the mean estimation in the relative position exceeds the stated 3σ bound. This bound states, that the correct value lies inside with around $99.77\,\%$ probability. If the baseline and baseline velocity errors stay inside the bound it means that a high reliability can be expected from the system, while estimations that often or strongly exceed the bound unveils an unreliable system.

The *availability* is defined as the ratio of satisfactory operational time to total time [159]. For the proposed relative positioning system, satisfactory operation will be defined as the time the estimation uncertainty of the relative position and relative velocity is below a certain bound. The idea behind is that a relative positioning system providing the driver assistance application an estimation with a large associated uncertainty will, in practice, make the estimation useless and, consequently, the relative positioning system appear unavailable. With this definition, an artificially increase in the stated uncertainty to meet a reliability requirement is avoided.

An ideal relative positioning system will be characterized by a) having a small estimation error in the relative position and relative speed, b) by offering an estimation of the relative position and relative speed that will never exceed the stated uncertainty and c) by always being available, providing an estimation uncertainty smaller than a predefined value required by the driver assistance application.

4.5. Summary

This chapter has motivated the problem of relative vehicle localization through the increasing need of *situational awareness* in ITS. Specially for safety-related applications, vehicles require knowledge of the position of other surrounding vehicles. The problem of relative vehicle localization is equal to estimating the *baseline vector* accurately and continuously over time.

This chapter has introduced the theoretical model for the problem of probabilistic and cooperative relative positioning between two vehicles by using the information from GNSS, inertial sensors and speedometer. The *fusion* of these information sources has been achieved through the design of a *Bayesian filter* in which the baseline and the baseline velocity are estimated over time. The causal relationships have been represented by means of a *Dynamic Bayesian Network*. The states have been chosen to meet the requirements of the problem and fulfill the *first-order Markov assumptions*.

Accuracy, *availability* and *reliability* are the evaluation metrics that have been identified for evaluating the proposed approach in the evaluation chapters.

Chapter 5.

Cooperative Relative Position Estimation through Sensor Fusion

The previous chapter introduced a probabilistic approach to solve the problem of estimating the baseline between two vehicles using a dynamic Bayesian network. The baseline is an unknown or hidden state and sensors represent the information sources that give evidence on this hidden state.

The aim is to find the probability density function of the baseline given the past baseline and the current sensor readings. This probability density function is called the posterior density function and, as explained in the previous chapter, can be written as the recursive product of the prior probability distributions and the sensor likelihoods. In this chapter, the aim is to define each of the probability density functions that are required to estimate the baseline posterior probability distribution.

5.1. GNSS-based Baseline Estimation

The aim of relative positioning is to find the baseline vector $\mathbf{b}$ between two points. In the special case of road transport, the baseline represents the relative position of two vehicles. The cooperative relative positioning approach in this thesis is based on the use of Global Navigation Satellite Systems (GNSS) measurements taken in two vehicles to estimate the baseline. A GNSS receiver is able to measure the distance between its antenna and each of the tracked satellites. A pseudorange is an estimation of the range between the antenna of the satellite orbiting the Earth and the receiver's antenna on the vehicle. The range is attained by measuring the propagation time through the atmosphere of a signal transmitted by the satellite. Since a receiver is usually equipped with an inexpensive, inaccurate and unsynchronized oscillator, the measured distance is offset by an unknown amount. Additionally, the pseudorange is also corrupted by a series of errors produced at the satellite, the atmosphere and the receiver. The measured pseudorange ρ_{e}^{l} of a

receiver e towards a satellite l can be modeled as follows:

$$\rho_{\mathsf{e}}^{l} = r_{\mathsf{e}}^{l} + c \cdot \delta t_{\mathsf{e}} + \epsilon_{\mathsf{e}}^{l} \tag{5.1}$$

where r_{e}^{l} is the true receiver-to-satellite geometric range, c is the speed of light constant in vacuum, δt_{e} is the receiver clock offset and $\epsilon_{\mathsf{e}}^{l}$ is the pseudorange error. The pseudorange errors are divided in different terms corresponding to the different error sources:

$$\epsilon_{\mathsf{e}}^{l} = \epsilon_{\mathsf{sat,e}}^{l} + \epsilon_{\mathsf{eph,e}}^{l} + \epsilon_{\mathsf{trop,e}}^{l} + \epsilon_{\mathsf{ion,e}}^{l} + \epsilon_{\mathsf{mp,e}}^{l} + \epsilon_{\mathsf{n,e}}^{l}, \tag{5.2}$$

where:

- **Satellite Clock Error** ($\epsilon_{\mathsf{sat,e}}^{l}$): this term represents the error in the signal transmission time due to the atomic clock on-board of the satellite. Although atomic clocks are highly accurate, their errors are large enough to require correction and must be taken into account.
- **Ephemeris Error** ($\epsilon_{\mathsf{eph,e}}^{l}$): to calculate the receiver position the position of each satellite needs to be known. The calculation of the satellite's position is made by using orbital parameters broadcasted in the ephemeris data. Errors in satellite position when calculated from the ephemeris data are represented as an additional delay error term in the measured pseudorange.
- **Tropospheric Error** ($\epsilon_{\mathsf{trop,e}}^{l}$): the lower part of the Earth's atmosphere is composed of dry gases and water vapor which produce a delay error in the GNSS signal's propagation time in comparison to a vacuum environment. Thus, the measured pseudorange is larger than the correct value. This error depends on the path the signal has to travel through the atmosphere.
- **Ionospheric Error** ($\epsilon_{\mathsf{ion,e}}^{l}$): the ionosphere consists of gases that are ionized by solar radiation. The ionization produces clouds of free electrons that act as a dispersive medium for GNSS signals in which propagation velocity is a function of frequency. Ionospheric delay error varies over time on a daily cycle and, just as well as the tropospheric error, depends on the path the signal travels through the atmosphere.
- **Multipath Error** ($\epsilon_{\mathsf{mp,e}}^{l}$): objects in the vicinity of the receiver antenna may cause reflections of electromagnetic signals resulting in one or more secondary propagation paths. The signals on these secondary paths always have a longer propagation time and can significantly distort the amplitude and phase of the direct-path signal. In case the Line-of-Sight (LoS) component is blocked by the environment the correlators might track a secondary path causing a large error in the estimation.
- **Noise Error** ($\epsilon_{\mathsf{n,e}}^{l}$): this term collects the remaining non-modeled errors, such as instrumental delays and white noise.

By measuring the ranges towards a set of satellites, it is possible for a GNSS receiver to estimate its absolute position through a process known as trilateration. Hence, two different strategies can be formulated that make it possible to estimate the relative position between two GNSS receivers. On one hand, the straight forward approach consists in subtracting the absolute positions of each of the two receivers. This approach will be called *absolute position differencing* and will be analyzed in Section 5.1.2. The second approach consists in differencing the pseudoranges from each other and forming so-called single and double differences and, in a second step, estimate the baseline using a set of differences. In this thesis, this strategy will be named *pseudorange differencing* and will be explained in Section 5.1.3. Certainly, the aforementioned error sources will impact in one way or the other the performance of both *absolute position differencing* and *pseudorange differencing* techniques. Therefore, before presenting both approaches, analyzing their benefits and drawbacks and comparing their performance in estimating the baseline, the error sources of GNSS signals will be carefully analyzed in the following section.

5.1.1. Common Errors

In this section the errors on the pseudorange measurements will be regarded more carefully. Opposed to the classic description of error sources that can be found in the literature [28, 38], a dedicated analysis is performed taking into account the problem description. On one hand, the spatial correlation of the errors will be regarded. Vehicles that share GNSS measurements over a direct Vehicle-to-Vehicle (V2V) communication link are necessarily in a distance below 2 km [41]. This will be regarded as the maximum correlation distance between the GNSS signals at the antennas of both vehicles in the following assessment. As the GNSS receivers are independent from each other they also measure the range towards the satellites at different time instants. Although GNSS receivers tend to synchronize their measurement instants to GPS time, their increasing clock bias will make them drift from the intended measuring instant until the internal clock is reset. 16 ms will be used as reference value for the divergence of measurement instants in two receivers, since this is the maximum accumulated clock bias in the Ublox LEA 4T receivers used in this thesis until clock reset is performed. Therefore, along with the spatial correlation, also the temporal correlation between the errors will be regarded. Specifically, the correlation between a certain pseudorange error ϵ at two receivers e and t is of interest. Correlated errors at both receivers are foreseen to cancel out by differentiation and will not contribute to the overall error budget, while errors completely uncorrelated and errors that are partially correlated cannot be expected to cancel out when performing a difference.

Satellite Ephemeris and Clock Errors The GPS Operation Control Segment (OCS) is responsible of predicting the future satellite position and clock offset and entering these values into the navigation message. A Kalman filter estimates the current satellite's position, velocity, solar radi-

ation pressure coefficients, clock offset, clock drift and clock drift rate and uses this parameters to propagate the satellite position and clock offset into the future [160]. These parameters inside the navigation message are used by the receivers to compute the satellite's location at transmission time. Any error in the broadcasted ephemerides will directly impact the range estimation done by the receiver.

The broadcasted satellite clock bias is used to correct the signal transmit time at the receiver. Any error in the estimated satellite clock bias automatically traduces to an error in the estimated pseudorange by creating a virtual delay of the signal. The ephemeris error is usually decomposed into three components. The radial component of the error vector points in direction of the Earth center. The along and across track components point in the orbiting direction and perpendicular to the orbiting direction of the satellite. Mainly the radial component of the ephemeris error vector influences the ranging measurements, while the along and across error have a smaller impact depending on the user-satellite geometry. Fortunately the radial component is nearly by one order of magnitude smaller [161]. The Signal In Space Range Error (SISRE) gives a measure of the fidelity of the broadcast navigation message including both, the ephemeris prediction and the satellite clock prediction [160].

The newest generation of GPS satellites currently in orbit are the GPS Block IIF satellites. The overall control segment error, containing both satellite clock and ephemeris error, has been tightened to 3 m for these satellites [162]. According to [28], the SISRE is about 1.5 m (rms), while according to [160] as of 2003 the SISRE was 1.1 m (rms). A short quantification of the satellite position and satellite clock error is performed by comparing broadcasted ephemerides to postprocessed precise satellite positions and satellite clock offsets. The International GNSS Service (IGS) offers post-fitted precise ephemeris that are generated with two weeks delay from the data acquired by its network of more than 200 base stations. The stated accuracy of IGS' final products is around 2.5 cm in position and 75 ps in clock bias (rms). Figure 5.1a shows the radial component of the satellite ephemeris error and Figure 5.1b the satellite clock errors for a set of satellites. It can be observed how the satellite position error contributes up to 1 m (the offset at some of the satellites is due to the uncorrected displacement between the antenna and the satellite's center-of-mass). The satellite clock error has values above 2 m of error on the pseudorange.

The satellite clock error is completely correlated between the receivers, since the offset creates a constant bias on all tracking receivers on the Earth. The ephemeris error, on the other hand, will be slightly different for each receiver on the Earth, due to the different distribution of the radial, across-track and along-track components as seen from each receiver. A conservative bound for the different ephemeris error is given in [163]:

$$\Delta\epsilon_{\text{eph}} \leq \frac{b \cdot \delta r}{r}, \tag{5.3}$$

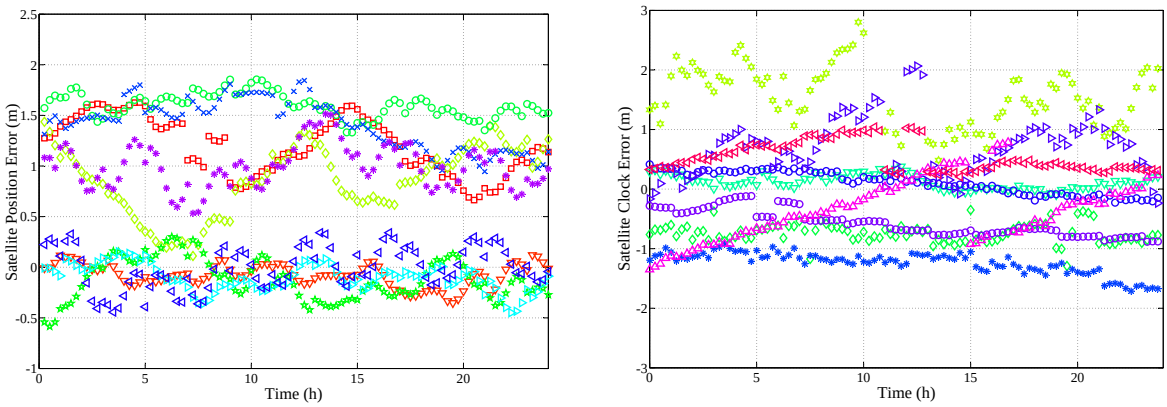

(a) Satellite Ephemeris Error

(b) Satellite Clock Error

Figure 5.1.: The figures show the satellite position error and satellite clock error for ten satellites in a 24 hour period. Both, the satellite position and satellite clock errors were computed by comparing broadcasted to precise ephemerides.

where r is the range to the satellite, δr the ephemeris error and b the separation between both receivers. The large range towards the satellites of approximate 20.000 km is responsible for the small angular separation of the unitary error vectors towards the satellites and, consequently, a small difference in the projection of the ephemeris error vector. At a separation of 2 km, an ephemeris error of 10 m has a difference of less than 1 cm between both receivers. According to Figure 5.1a, the error due to wrong ephemeris is usually much smaller than 10 m and, hence, can be assumed to be completely correlated between two receivers at this separation.

The delayed measurement instants will also slightly influence the correlation of the satellite clock and ephemeris errors. The atomic clock on-board of the satellite is freely running and its clock offset will change according to the drift of the clock. The Block IIF satellites feature high-quality rubidium frequency standards with clock drifts between $10^{-12}\,\frac{\mathrm{s}}{\mathrm{s}}$ [164]. These highly stable clocks yield a negligible clock offset difference in 16 ms of far below 1 mm. From Figure 5.1b variations of 1.5 m in one hour can be seen, which result in a negligible ephemeris error variation in 16 ms.

While the residual error in the ephemeris data is quite small for two unsynchronized receivers, a further magnitude related to the satellite position has to be regarded. The pseudorange measurements in two receivers e and t are estimates of different ranges r_{e}^{l} and r_{t}^{l}. These ranges are not only different because of the different position of the receivers, but also because of the different satellite positions at the transmit instants. The GNSS satellites move at a speed of around 1000 $\frac{\mathrm{m}}{\mathrm{s}}$ with respect to the user on the Earth [28]. Consequently, in 16 ms the satellite travels up to 15 m distance. The radial component of this figure directly impacts the difference in the pseudoranges. In Section 5.1.5, a method for compensating for this amount is presented.

Tropospheric Error The non-dispersive sections of the atmosphere with a refractive index slightly larger than unity cause a delay in the propagation of radio frequency signals. This so-called tropospheric error in the GNSS error budget is caused by water vapor in the low troposphere up to 12 km and dry gases, mainly O_2 and N_2, in the lower atmosphere up to a few hundreds of kilometers above see level [93]. The tropospheric delay depends on the temperature, pressure and humidity along the propagation path [93]. Since this information is usually not available, tropospheric models that use a standard atmosphere model can be used to estimate the delay caused by the troposphere. The Saastamoinen model [165] or the Modifed Hopfield model [166] are such examples. The tropospheric delay ranges from 2 m in zenith direction to 25 m for low satellite elevations of 5°. Fortunately, the tropospheric delay can be predicted with good accuracy. The residual tropospheric error after applying the model is of a few centimeters for zenith satellites, but can sum up to 0.5 m to 1 m for low elevation satellites [28].

The wet delay, the part of the tropospheric delay caused by water vapor in the lower troposphere, is highly variable. Two receivers separated by 2 km might have, in principle, different weather conditions. It has been recognized that horizontal tropospheric variations due to weather fronts could adversely affect Local Area Augmentation Systems [167]. With short baseline measurements (2 km to 3 km), the relationship between the increase in carrier phase double difference residuals and the advance of storm fronts was identified in [168]. Residuals were found to increase up to 0.18 cycles (3.4 cm) because of the difference in tropospheric delay at each antenna. This value, is relevant to Real Time Kinematics (RTK) positioning, but can be safely disregarded for the purposes of this thesis. Regarding the time correlation in 16 ms, the tropospheric delay is regarded as being equal for two different receivers. The dry gases in the atmosphere which account for 90 % of the tropospheric delay are rather stable [28]. Variations of 3 cm observed in one hour [93], have a insignificant impact on the time decorrelation of the tropospheric error.

Ionospheric Error The ionosphere is a region of ionized gases containing free electrons and ions that extends from a height of about 50 km to about 1000 km above the Earth's surface. As the ionization of gases is produced by the radiation of the sun, the effect of the ionosphere on GNSS signals varies widely between night and day. At the same time, the changing solar activity causes the impact of the ionosphere to vary from one day to the next. The parameter used to quantify the effect of the ionosphere on GNSS signals is the Total Electron Content (TEC), which measures the number of free electrons in the path from the satellite to the receiver in a tube of 1 m^2 of cross section [28]. The TEC is measured in Total Electron Content Unit (TECU) which are defined as 10^{16} free electrons per m^2. Solar flares and the resulting magnetic storms create large and sudden changes in the TEC, which affect the delay of GNSS signals.

The amount of the ionospheric delay on the pseudorange estimate, depending on the user latitude, the time of the day, the satellite elevation and the solar activity, varies between several meters and

several tens of meters. Eight parameters of the Klobuchar model [169] are broadcasted by the American Global Positioning System (GPS) system for the receivers to estimate and compensate for the ionospheric delay. According to [170], the residual error after applying the Klobuchar ionospheric model is approximately 50 % of the total ionospheric error. At mid-latitudes the remaining ionospheric error can be up to 10 m.

TEC walls are geographical changes of the ionospheric TEC value. The ionospheric gradient is used to describe the spatial decorrelation rate of ionosphere delay. A large ionospheric gradient means that the ionosphere decorrelates quickly with the increase of the spatial separation. Typical values for a gradient is 1 $\frac{\text{mm}}{\text{km}}$ to 2 $\frac{\text{mm}}{\text{km}}$ [28], with values raising to 400 $\frac{\text{mm}}{\text{km}}$ when the ionosphere is active [171]. Hence, an extreme decorrelation of 80 cm could happen for a 2 km baseline during strong ionospheric activity.

The change in the TEC content in one day with regular solar activity is of about 20 TECU in six hours [125]. However, during a solar flare sudden changes in the TEC content can happen. During the solar burst occurred on October 28^{th} 2003, the TEC content changed as much as 17 TECU in a period of five minutes [172]. This corresponds to a change in delay of 2.7 m in five minutes. Consequently, even the strongest ionospheric events have contributions of less than 1 cm in 16 ms and, thus, the assumption of time correlation of ionospheric errors can safely be made.

Relativistic Error Both, Albert Einstein's General Law of Relativity and the Special Law of Relativity influence strongly the clocks on board of the satellite. On the one hand, the clock on the satellite is at a weaker gravitational potential than the reference clocks on the surface of the Earth. According to the General Relativity, a clock at a lower gravitational potential will run faster than a clock at a stronger potential. This effect is called red shift and will cause that, on average, the satellite clock ticks 45 µs faster every day [173]. On the other hand, the satellites move faster in the inertial frame than a user on the ground. The General Relativity states that a clock traveling at a higher speed will run slower than a stationary clock. This effect known as time dilation accounts on average for 7 µs every day [173]. Both these effects compensate partly. To account for the net effect the satellite clocks are set to run 38 µs slower per day prior to launch. This is known as the factory compensation.

However, these effects are not constant but depend on position of the satellite in its orbit and the position of the user. The residual eccentricity in the satellite orbit causes periodic variations in the time dilation and red shift observed by a user. The receiver has to account for this residual error that can amount to 45 ns or 13.5 m at eccentricities of only 2 % [93]. The amount of the residual relativistic effect due to second order effects such as the Earth oblateness contribution to the gravitational red shift or the tidal potentials of Moon and Sun can account for up to 40 ps or 12 cm [173].

The relativistic effect can be considered as a satellite clock bias and, consequently, is correlated in all receivers tracking the same satellite. The time variation of the relativistic induced error in 16 ms is negligible taking into account the small change in gravitational potential and in satellite velocity in the 15 m the satellite traveled on its orbit. Therefore, this error can be assumed as being completely correlated in two unsynchronized receivers.

The Sagnac effect is a further relativistic component that is caused by the Earth rotation during the signal propagation time from the satellite to the receiver. Although its amount is rather large and can be as high as 133 ns or 40 m, it is easily modeled and it is corrected before computing the absolute position of a receiver [173]. In relative positioning using pseudoranges of two receivers, this effect also needs to be taken into account. This will be presented in a novel synchronization approach in Section 5.1.5.

Noise Error The random noise error on the pseudorange measurements is a consequence of receiver noise originated in different stages of the GNSS signal reception process. In starts with in-band radio frequency noise at the receiver antenna and the noise introduced by the radio frequency front end. The analogue-to-digital converter introduces quantization noise into the digital signal. These effects are all uncorrelated between two receivers, both in space and in time [28]. Therefore, noise cannot be expected to be canceled out by a differentiation procedure.

The magnitude of the pseudorange noise depends on the carrier-to-noise ratio of the incoming signal. This value is usually between 38 dBHz for low-elevation satellites and 45 dBHz for zenith satellites. For a classic Delay-lock Loop (DLL) architecture as introduced in Chapter 3, the pseudorange noise will also depend on its design parameters. If the input to the DLL is assumed to be the ranging Coarse Acquisition (C/A) code plus white Gaussian noise, the following equation gives the standard deviation σ_ρ of the pseudorange noise [38]:

$$\sigma_\rho = c \cdot T_c \sqrt{\frac{d \cdot B_\rho}{4 \cdot T \cdot \frac{C}{N_0}}}, \tag{5.4}$$

where T_c is the chip width, d is the correlator spacing, B_ρ the loop bandwidth, T the DLL integration time, $\frac{C}{N_0}$ the carrier-to-noise ratio of the signal and c the speed of light. The chip width is constant and its value for the C/A code is 1 µs. The correlator spacing d is a design parameter. The smaller the chip width, the more precise the tracking of the delay. However, a small spacing increases the risk of loosing track of the prompt correlation peak when the signal is weak or the risk of tracking a neighboring peak caused by multipath propagation. The integration or averaging time T is designed according to the dynamics of the platform. By increasing the averaging, the noise in the pseudorange gets filtered out. However, longer averaging yields a lower loop bandwidth and a worse response to variations in the signal. Typical values for loop bandwidth B_ρ in vehicular environments are between 1 Hz and 4 Hz [28].

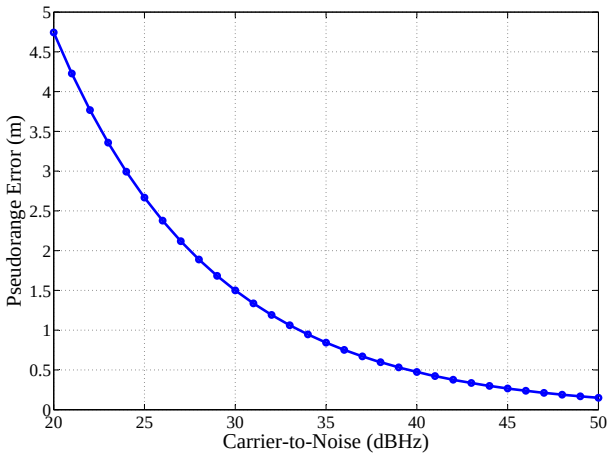

Figure 5.2.: This figures shows the pseudorange error due to noise in a C/A code DLL with a 0.1 chip spacing and 1 Hz loop bandwidth in dependance of the carrier-to-noise ratio of the incoming signal.

The pseudorange error due to noise is depicted in Figure 5.2 and can be considered around 0.2 m for good carrier-to-noise ratio (45 dB Hz) and 2.5 m for bad satellite reception (25 dB Hz).

Multipath Error Besides the direct LoS signal transmitted from the GNSS satellite, objects in the vicinity, as well as the ground, can cause reflections that reach the user antenna. These multipath components are delayed and attenuated replicas of the original LoS signal. Inside the DLL, the multipath components distort the correlation peak, making early and late correlator samples not being centered on the true arrival time of the direct path. Consequently, the pseudorange is biased by an amount that can be either positive or negative. The amount of multipath error depends on the DLL correlator spacing, the time and phase delay, the phase-rate and the attenuation of the multipath components [38]. As an example, pseudorange errors due to multipath for a receiver with 0.5 chip correlator spacing in the presence of a -12 dB attenuated multipath signal can produce errors up to 20 m [28]. In vehicular environments, pseudorange errors of more than 100 m were measured in urban environments [100]. In this cases the LoS component of the signal is blocked and the DLL is tracking a reflected component.

The multipath components are strongly related to the surrounding objects causing them and, therefore, are not correlated in space [93]. The components arriving at two receivers separated by short distances have different phases and therefore another interference pattern at the DLL. The impact of the receiver unsynchronization in multipath environments will be subject of analysis in Chapter 6.

Discussion The different contributions to the pseudorange errors have been analyzed. The second column in Table 5.1 summarizes the expected amount of these errors. A relative position

Table 5.1.: Summary on GNSS Errors

Error Source	**Potential Error**	**Decorrelation for a 2 km baseline**	**Decorrelation for a 16 ms unsynchronization**
Satellite Clock & Satellite Ephemeris	1.5 m	1 cm	negligible
Tropospheric Error	0.5 m to 1 m	5 cm	negligible
Ionospheric Error	2 m to 10 m	2 mm to 4 mm 80 cm during high activity	$<$ 1 cm
Relativistic Error	0 cm to 12 cm	correlated	negligible
Noise Error	0.2 m to 2.5 m	0.2 m to 2.5 m	0.2 m to 2.5 m
Multipath Error	0 m to 20 m	0 m to 20 m	0 m to 20 m

technique as the one followed in this thesis aims at eliminating their contribution. The third and fourth column describe the amount of decorrelation of the common errors, once when the two receivers are spaced 2 km apart from each other, and once when both receivers make the measurements delayed 16 ms from each other.

Table 5.1 reveals that by using a differential approach on GNSS pseudoranges an amount of several meters can be potentially canceled out. Specially the cancellation of the ionosphere induced error for lower elevation satellites will have a major impact on the baseline estimation. Further on, Table 5.1 shows that the correlation between two receivers in two different vehicles also holds in the case of a 2 km separation distance and 16 ms unsynchronization. The largest uncorrelation could be due to a difference in the residual ionospheric error after compensation at two distant vehicles during a strong solar burst.

The pseudorange noise error still remains, since it is uncorrelated between the receivers, but if correctly tackled, its contribution can be minimized as will be presented in the following sections. Multipath is the great problem to vehicular positioning. It is uncorrelated and, consequently, not removable through differentiation and can contribute with large errors. Multipath must be tackled by other methods. One possibility will be addressed in Section 5.6.4.

5.1.2. Absolute Position Differencing

After acquiring and tracking the GNSS signal of at least four satellites, a GNSS receiver e is able to compute an estimate of its three-dimensional absolute position vector $\mathbf{p}_\mathsf{e} = \begin{bmatrix} x_\mathsf{e} & y_\mathsf{e} & z_\mathsf{e} \end{bmatrix}^\mathsf{T}$. This position is usually expressed in an Earth-fixed coordinate frame, as for instance, the Earth-Centered-Earth-Fixed (ECEF). The process of determining the position by measuring the Time of Arrival (ToA) to a set of known transmitters using the geometry of circles or spheres is called *trilateration*. The straightforward approach consists in solving the position $\mathbf{p}_\mathsf{e}$ and the receiver clock error δt_e in a non-linear system of equations that takes L available pseudorange measurements into account:

$$\rho_\mathsf{e}^l = r_\mathsf{e}^l + c \cdot \delta t_\mathsf{e} + \epsilon_\mathsf{e}^l, \tag{5.5}$$

with $l = \{1, \ldots, L | L > 4\}$ and where the range between receiver e and satellite l, r_e^l, can be expressed as:

$$r_\mathsf{e}^l = \|\mathbf{p}^l - \mathbf{p}_\mathsf{e}\| = \sqrt{(x^l - x_\mathsf{e})^2 + (y^l - y_\mathsf{e})^2 + (z^l - z_\mathsf{e})^2}, \tag{5.6}$$

where $\mathbf{p}^l = \begin{bmatrix} x^l & y^l & z^l \end{bmatrix}^\mathsf{T}$ is the known satellite position. Consequently, Equation 5.5 has four unknowns and, by taking $L = 4$ measurements, a solution can be found in the ideal case. In general, and due to the noise ϵ_e^l, a solution to the resulting system of equations does not exist. Therefore, the best solution in the sense of minimizing the mean squared error is found using the Least Squares (LS) method explained in Chapter 3. A standard algorithm to solve the system of non-linear equations is the Gauss-Newton method [174]. The method linearizes the system model at an initial user position $\mathbf{p}_\mathsf{e}^0 = \begin{bmatrix} x_\mathsf{e}^0 & y_\mathsf{e}^0 & z_\mathsf{e}^0 \end{bmatrix}^\mathsf{T}$ and clock bias δt_e^0. The range from receiver e to satellite l at iteration 0 is

$$r_\mathsf{e}^l \approx \|\mathbf{p}^l - \mathbf{p}_\mathsf{e}^0\| + \frac{x^l - x_\mathsf{e}^0}{\|\mathbf{p}^l - \mathbf{p}_\mathsf{e}^0\|}\delta_\mathsf{x} + \frac{y^l - y_\mathsf{e}^0}{\|\mathbf{p}^l - \mathbf{p}_\mathsf{e}^0\|}\delta_\mathsf{y} + \frac{z^l - z_\mathsf{e}^0}{\|\mathbf{p}^l - \mathbf{p}_\mathsf{e}^0\|}\delta_\mathsf{z}, \tag{5.7}$$

where $\delta_\mathsf{x} = x_\mathsf{e}^0 - x$, $\delta_\mathsf{y} = y_\mathsf{e}^0 - y$ and $\delta_\mathsf{z} = z_\mathsf{e}^0 - z$ are the position offsets to the solution. The offset in the position and clock, $\boldsymbol{\delta} = \begin{bmatrix} \delta_\mathsf{x} & \delta_\mathsf{y} & \delta_\mathsf{z} & \delta t \end{bmatrix}^\mathsf{T}$, is found by solving the resulting system of linear equations

$$\boldsymbol{\delta\rho}_\mathsf{e} = \mathbf{G}_\mathsf{u} \cdot \boldsymbol{\delta}, \tag{5.8}$$

where

$$\mathbf{G}_{\mathsf{u}} = \begin{bmatrix} u_{\mathsf{x}}^1 & u_{\mathsf{y}}^1 & u_{\mathsf{z}}^1 & 1 \\ \vdots & \vdots & \vdots & 1 \\ u_{\mathsf{x}}^L & u_{\mathsf{y}}^L & u_{\mathsf{z}}^L & 1 \end{bmatrix} = \begin{bmatrix} \frac{x^1 - x^0}{\|\mathbf{p}^1 - \mathbf{p}_{\mathsf{e}}^0\|} & \frac{x^1 - x^0}{\|\mathbf{p}^1 - \mathbf{p}_{\mathsf{e}}^0\|} & \frac{x^1 - x^0}{\|\mathbf{p}^1 - \mathbf{p}_{\mathsf{e}}^0\|} & 1 \\ \vdots & \vdots & \vdots & 1 \\ \frac{x^L - x^0}{\|\mathbf{p}^L - \mathbf{p}_{\mathsf{e}}^0\|} & \frac{x^L - x^0}{\|\mathbf{p}^L - \mathbf{p}_{\mathsf{e}}^0\|} & \frac{x^L - x^0}{\|\mathbf{p}^L - \mathbf{p}_{\mathsf{e}}^0\|} & 1 \end{bmatrix}, \tag{5.9}$$

$$\boldsymbol{\delta\rho}_{\mathsf{e}} = \begin{bmatrix} \rho_{\mathsf{e}}^1 - r_1^0 \\ \vdots \\ \rho_{\mathsf{e}}^L - r_L^0 \end{bmatrix}. \tag{5.10}$$

$\mathbf{G}_{\mathsf{u}}$ is the geometry matrix containing the unitary vectors $\mathbf{u}^l$ to the L satellites in view as row vectors and a last column filled with ones. As explained in Chapter 3, the least squares solution to Equation 5.8 is given by:

$$\boldsymbol{\delta} = (\mathbf{G}_{\mathsf{u}} \cdot \mathbf{G}_{\mathsf{u}}^{\mathsf{T}})^{-1} \cdot \mathbf{G}_{\mathsf{u}}^{\mathsf{T}} \cdot \boldsymbol{\delta\rho}_{\mathsf{e}}. \tag{5.11}$$

In every iteration i the offset $\boldsymbol{\delta}$ is added to the previous position estimate according to $\mathbf{p}_{\mathsf{e}}^{i+1} = \mathbf{p}_{\mathsf{e}}^{i} + \boldsymbol{\delta}$. While the offset becomes smaller, the method will eventually converge to the solution $\begin{bmatrix} \hat{\mathbf{p}}_{\mathsf{e}} & \delta\hat{t}_{\mathsf{e}} \end{bmatrix}^{\mathsf{T}}$ that minimizes the root mean squared error to all pseudoranges. In general, the position computation converges quickly in two to four steps, even when choosing a null vector as initial position and clock bias [28]. For the subsequent performance analysis, the geometry matrix for *absolute position differencing* is defined as:

$$\mathbf{G}_{\mathsf{APD}} = (\mathbf{G}_{\mathsf{u}} \cdot \mathbf{G}_{\mathsf{u}}^{\mathsf{T}})^{-1} \cdot \mathbf{G}_{\mathsf{u}}^{\mathsf{T}}. \tag{5.12}$$

Several approaches exist to improve the absolute position estimated in this way. A Weighted Least Squares (WLS) approach can be used to give different weights to the measurements according to their noise variance. If the magnitude of the noise variance is unknown, the weighting matrix can be designed in dependance of the elevation of the satellite or the carrier-to-noise ratio of the received signal. Other epoch-wise methods to solve the absolute positioning problem that offer greater robustness and faster convergence are the steepest descent algorithm and the Levenberg-Marquardt algorithm [24]. In a Kalman filter, the absolute position may be estimated making use of the temporal relationship of the unknowns and the biases and use these to increase the accuracy of the position estimate [38].

In the case that the pseudoranges adhere to the model in Equation 5.5, the estimation of the absolute position is unbiased. However, as explained in the previous section, certain errors might bias the pseudorange measurements, and, consequently, bias the absolute position estimate. Some of the error sources can be modeled and be partially subtracted to the pseudorange measurements in order to decrease their impact on the final position estimate. Other biases as, for instance, the ionospheric delay, can be modeled and canceled up to a certain amount. The residual stays as a bias in the pseudorange measurement, and biases the position estimate.

In *absolute position differencing* the estimate $\hat{\mathbf{b}}_{\text{APD}}$ of the baseline $\mathbf{b}$ between two receivers e and t is calculated by subtracting their absolute positions as in

$$\hat{\mathbf{b}}_{\text{APD}} = \hat{\mathbf{p}}_{\text{t}} - \hat{\mathbf{p}}_{\text{e}}. \tag{5.13}$$

Cramér-Rao Lower Bound for *absolute position differencing* Recalling Chapter 3.3, the Cramér-Rao Lower Bound (CRLB) for an unbiased estimator defines a performance lower bound on the variance of parameter estimation algorithms. Now, the CRLB for the baseline estimated with *absolute position differencing* will be derived. Equation 3.17 gives the Fisher Information Matrix (FIM) for a vector estimator that uses observations corrupted by additive white Gaussian noise of variance σ^2. The measurements z_i in Equation 3.17 are now the pseudoranges ρ_e^l. To compute the FIM the derivative of the measurements with respect to the state is required. In this case, this is equal to the geometry matrix $\mathbf{G}_{\text{u}}$ from the Gauss-Newton method. The resulting FIM for the absolute position estimator $\hat{\mathbf{p}}_{\text{e}}$ at receiver e is

$$\mathbf{J}_{\hat{\mathbf{p}}_{\text{e}}} = \frac{1}{\sigma^2}\mathbf{G}_{\text{u}}^{\intercal}\mathbf{G}_{\text{u}}, \tag{5.14}$$

The corresponding CRLB is given by the inverse of the FIM:

$$Cov(\hat{\mathbf{p}}_{\text{e}}) = \sigma^2(\mathbf{G}_{\text{u}}^{\intercal}\mathbf{G}_{\text{u}})^{-1}. \tag{5.15}$$

In the case that the pseudorange are corrupted with additive noise of varying variance given by the diagonal matrix $\mathbf{R}_{\rho}$, the previous equation is written as:

$$Cov(\hat{\mathbf{p}}_{\text{e}}) = (\mathbf{G}_{\text{u}}^{\intercal}\mathbf{R}_{\rho}^{-1}\mathbf{G}_{\text{u}})^{-1}. \tag{5.16}$$

Now, assuming uncorrelated estimators in both receivers, the variances add to give the lowest bound for the baseline estimation with *absolute position differencing*:

$$Cov(\hat{\mathbf{b}}_{\text{APD}}) = 2\sigma^2(\mathbf{G}_{\text{u}}^{\intercal}\mathbf{G}_{\text{u}})^{-1}. \tag{5.17}$$

In the general case of different satellites in receivers e and t and different noise variances on the pseudoranges to different satellites from different receivers, the CRLB yields:

$$Cov(\hat{\mathbf{b}}_{\text{APD}}) = (\mathbf{G}_{\text{u,e}}^{\intercal}\mathbf{R}_{\rho,\text{e}}^{-1}\mathbf{G}_{\text{u,e}})^{-1} + (\mathbf{G}_{\text{u,t}}^{\intercal}\mathbf{R}_{\rho,\text{t}}^{-1}\mathbf{G}_{\text{u,t}})^{-1}, \tag{5.18}$$

where the different satellite geometries are expressed in $\mathbf{G}_{\text{u,e}}$ and $\mathbf{G}_{\text{u,t}}$, and the different pseudorange covariances the matrices $\mathbf{R}_{\rho,\text{e}}$ and $\mathbf{R}_{\rho,\text{t}}$.

5.1.3. Pseudorange Differencing

A second approach is proposed for the direct estimation of the baseline $\mathbf{b}$. Instead of computing the absolute position of each vehicle, the *pseudorange differencing* approach for relative positioning of vehicles relies on the double differentiation of GNSS pseudorange measurements. In a first step, a single difference measurement $\Delta\rho^l_{\mathsf{et}}$ is obtained by subtracting the pseudorange measurements from two different receivers e and t referred to the same satellite l:

$$\Delta\rho^l_{\mathsf{et}} = \rho^l_t - \rho^l_e = \Delta r^l_{\mathsf{et}} + c \cdot \Delta\delta t_{\mathsf{et}} + \Delta\epsilon^l_{\mathsf{et}}, \tag{5.19}$$

where $\Delta\delta t_{\mathsf{et}}$ is the differenced receiver clock biases and the differenced pseudorange error is equal to

$$\begin{aligned}\Delta\epsilon^l_{\mathsf{et}} =& \epsilon^l_{\mathsf{sat,t}} + \epsilon^l_{\mathsf{eph,t}} + \epsilon^l_{\mathsf{ion,t}} + \epsilon^l_{\mathsf{trop,t}} + \epsilon^l_{\mathsf{mp,t}} + \epsilon^l_{\mathsf{n,t}} \\ & - \epsilon^l_{\mathsf{sat,e}} - \epsilon^l_{\mathsf{eph,e}} - \epsilon^l_{\mathsf{ion,e}} - \epsilon^l_{\mathsf{trop,e}} - \epsilon^l_{\mathsf{mp,e}} - \epsilon^l_{\mathsf{n,e}}.\end{aligned} \tag{5.20}$$

As analyzed in Section 5.1.1, under a close proximity assumption, the terms ϵ_{ion}, ϵ_{trop}, ϵ_{sat} and ϵ_{eph} can be assumed to be equal in both receivers and are canceled out with the single difference operation yielding

$$\Delta\epsilon^l_{\mathsf{et}} \approx \epsilon^l_{\mathsf{mp,t}} + \epsilon^l_{\mathsf{n,t}} - \epsilon^l_{\mathsf{mp,e}} - \epsilon^l_{\mathsf{n,e}}. \tag{5.21}$$

Hence, the single difference in Equation 5.19 is still biased by the user clocks at e and t and by the uncorrelated noise and multipath. By subtracting two single differences towards two different satellites l and m, a double difference measurement $\nabla\Delta\rho^{lm}_{\mathsf{et}}$ is computed. With this procedure, the common errors to both satellites are canceled out. This is the case for the differenced receiver clock error $\Delta\delta t_{\mathsf{et}}$. A double difference pseudorange measurement is expressed in the following way:

$$\nabla\Delta\rho^{lm}_{\mathsf{et}} = \nabla\Delta r^{lm}_{\mathsf{et}} + \nabla\Delta\epsilon^{lm}_{\mathsf{et}}, \tag{5.22}$$

where the symbol $\nabla\Delta$ denotes the difference between the corresponding terms in the two single differences. $\nabla\Delta r^{lm}_{\mathsf{et}}$ is the projection of the baseline in the differenced direction to satellites l and m. The error term $\nabla\Delta\epsilon^{lm}_{\mathsf{et}}$ represents the remaining differential error term between two receivers and two satellites:

$$\nabla\Delta\epsilon^{lm}_{\mathsf{et}} \approx \nabla\Delta\epsilon_{\mathsf{mp}} + \nabla\Delta\epsilon_{\mathsf{n}}. \tag{5.23}$$

As reported in [175], the remaining errors are mainly multipath and non-modeled errors like thermal noise and interference. It should be noticed that, while common errors terms are nearly canceled out by differencing, uncorrelated error terms increase the noise variance within this operation likewise.

Figure 5.3 shows the geometric relationship between the vehicles and the satellites. The baseline

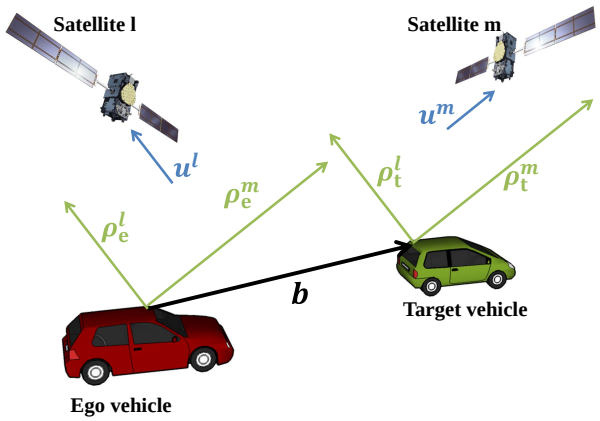

Figure 5.3.: Geometric relationship between the baseline between two vehicles and the pseudorange double difference measurements. For simplicity the baseline has to be put equal to the distance between the GNSS antennas. In general, the displacement vectors from the antenna position to the vehicle reference point defined in Chapter 4 has to be added.

$\mathbf{b}$ between two vehicles, ego and target, is a vector in space expressed in an Earth-fixed coordinate frame, such as ECEF. Each double difference measurement $\nabla\Delta\rho_{\mathrm{et}}^{lm}$ is a projection of the baseline vector $\mathbf{b}$ in the direction of the differenced satellite unitary vector $\mathbf{u}^{lm} = \mathbf{u}^l - \mathbf{u}^m$. By taking three or more double difference measurements the baseline coordinates can be computed by solving a system of linear equations. Here is an example for three pseudorange double differences:

$$\begin{bmatrix} \nabla\Delta\rho_{\mathrm{et}}^{lm} \\ \nabla\Delta\rho_{\mathrm{et}}^{ln} \\ \nabla\Delta\rho_{\mathrm{et}}^{lo} \end{bmatrix} = \begin{bmatrix} u_{\mathrm{x}}^{lm} & u_{\mathrm{y}}^{lm} & u_{\mathrm{z}}^{lm} \\ u_{\mathrm{x}}^{ln} & u_{\mathrm{y}}^{ln} & u_{\mathrm{z}}^{ln} \\ u_{\mathrm{x}}^{lo} & u_{\mathrm{y}}^{lo} & u_{\mathrm{z}}^{lo} \end{bmatrix} \begin{bmatrix} b_{\mathrm{x}} \\ b_{\mathrm{y}} \\ b_{\mathrm{z}} \end{bmatrix} \tag{5.24}$$

where b_{x}, b_{y} and b_{z} are the three baseline coordinates, and u_{x}^{lm}, u_{y}^{lm} and u_{z}^{lm} the three differenced unitary vector coordinates, both in the same navigation frame. The three double differences in this example are computed by subtracting the single differences to satellite m, n and o from the single difference to satellite l. Although any combination of double differences is possible, the approach of selecting one satellite as the *common satellite* is a common procedure [28]. Usually, the common satellite is chosen to be the one near the zenith, since it is more unlikely that this satellite is obstructed and therefore has a better signal strength and, consequently, less noise. This is important since the noise error of the common satellite is introduced in all double differences. The compact representation for the linear system of equations in Equation 5.24 is given by:

$$\boldsymbol{\nabla\Delta\rho}_{\mathrm{et}} = \mathbf{G}_{\mathrm{uu}} \cdot \mathbf{b}, \tag{5.25}$$

where $\boldsymbol{\nabla\Delta\rho}_{\mathrm{et}}$ is the vector containing all double differences and $\mathbf{G}_{\mathrm{uu}}$ is the geometry matrix containing differenced unitary vectors to the satellites in view. Usually, the system of linear

equations in Equation 5.25 is overdetermined. The solution $\hat{\mathbf{b}}_{\text{PRD}}$ that minimizes the squared error to this system of equations is given by [174]:

$$\hat{\mathbf{b}}_{\text{PRD}} = (\mathbf{G}_{\text{uu}}^{\intercal} \cdot \mathbf{G}_{\text{uu}})^{-1} \cdot \mathbf{G}_{\text{uu}}^{\intercal} \cdot \boldsymbol{\nabla\Delta\rho}_{\text{et}}. \tag{5.26}$$

For future analysis the definition of the geometry matrix for *pseudorange differencing* is given:

$$\mathbf{G}_{\text{PRD}} = (\mathbf{G}_{\text{uu}} \cdot \mathbf{G}_{\text{uu}}^{\intercal})^{-1} \cdot \mathbf{G}_{\text{uu}}^{\intercal}. \tag{5.27}$$

Each double difference noise component $\nabla\Delta\epsilon$ in Equation 5.23 includes the noise contributions from four pseudorange measurements, ρ_{e}^{l}, ρ_{t}^{l}, ρ_{e}^{m} and ρ_{t}^{m}. As subtraction cancels any common noise component out (e.g.noise at the antenna's amplifier), the assumption holds, that the noise of the different pseudoranges is statistically mutually independent of each other. The next equations present the noise variance-covariance matrix for the pseudorange double differences for two receivers e and t and three common satellites, l, m and n. The $\mathbf{L}$ matrix represents the linear relationship between the the pseudorange vector $\boldsymbol{\rho}$ and the double difference vector $\boldsymbol{\nabla\Delta\rho}_{\text{et}}$:

$$\boldsymbol{\nabla\Delta\rho}_{\text{et}} = \begin{bmatrix} \nabla\Delta\rho_{\text{et}}^{lm} \\ \nabla\Delta\rho_{\text{et}}^{ln} \end{bmatrix} = \mathbf{L} \cdot \boldsymbol{\rho} = \begin{bmatrix} 1 & 1 \\ -1 & 0 \\ 0 & -1 \\ -1 & -1 \\ 1 & 0 \\ 0 & 1 \end{bmatrix}^{\intercal} \begin{bmatrix} \rho_e^l \\ \rho_e^m \\ \rho_e^n \\ \rho_t^l \\ \rho_t^m \\ \rho_t^n \end{bmatrix} \tag{5.28}$$

Assuming equal noise with variance σ_ρ^2 on all pseudoranges in both receivers e and t, the noise covariance matrices for the pseudoranges yield $\mathbf{R}_{\rho,\text{e}} = \mathbf{R}_{\rho,\text{t}} = \sigma_\rho^2 \cdot \mathbf{I}$. Hence, the noise covariance matrix for the double differences is

$$\mathbf{R}_{\nabla\Delta\rho} = \mathbf{L} \begin{bmatrix} \mathbf{R}_{\rho,\text{e}} & \mathbf{0}_{3\times3} \\ \mathbf{0}_{3\times3} & \mathbf{R}_{\rho,\text{t}} \end{bmatrix} \mathbf{L}^{\intercal} = 2\sigma_\rho^2 \begin{bmatrix} 2 & 1 \\ 1 & 2 \end{bmatrix} \tag{5.29}$$

Equation 5.29 reveals that the noise variance for a double difference measurement is four times the noise variance of each pseudorange measurement (assuming equal variance on all pseudorange measurements). Further on, it should be noticed that the resulting double differenced observations involving a common satellite are statistically dependent. Therefore, the calculated remaining noise covariance matrix $\mathbf{R}_{\nabla\Delta\rho}$ is not diagonal, but has off-diagonal components of twice the noise variance of the pseudorange measurement.

Cramér-Rao Lower Bound for pseudorange differencing *Pseudorange differencing* is a unbiased estimator of the baseline between the vehicles. Therefore the CRLB of $\hat{\mathbf{b}}$ using the measurements $\boldsymbol{\nabla\Delta\rho}$ is derived next. As a measurement model, additive white Gaussian noise is added to the pseudorange double differences. The resulting measurement model is

$$\boldsymbol{\nabla\Delta\rho} = \mathbf{G}_{\mathsf{uu}}\mathbf{b} + \boldsymbol{\nabla\Delta\epsilon}, \tag{5.30}$$

with $\boldsymbol{\nabla\Delta\epsilon}$ being white additive Gaussian noise with zero mean and mutually correlated with covariance matrix $\mathbf{R}_{\nabla\Delta\rho}$. Consequently the measurement likelihood $p(\boldsymbol{\nabla\Delta\rho}|\mathbf{b})$ is a multivariate Gaussian with mean $\mathbf{G}_{\mathsf{uu}}\mathbf{b}$ and covariance $\mathbf{R}_{\nabla\Delta\rho}$:

$$p(\boldsymbol{\nabla\Delta\rho}|\mathbf{b}) = \frac{1}{\sqrt{(2\pi)^{N-1}\|\mathbf{R}_{\boldsymbol{\nabla\Delta\rho}}\|}} exp\left\{-\frac{1}{2}(\boldsymbol{\nabla\Delta\rho} - \mathbf{G}_{\mathsf{uu}}\mathbf{b})^{\mathsf{T}}\mathbf{R}^{-1}_{\nabla\Delta\rho}(\boldsymbol{\nabla\Delta\rho} - \mathbf{G}_{\mathsf{uu}}\mathbf{b})\right\} \tag{5.31}$$

where N is the number of measured pseudoranges and $\|\cdot\|$ denotes the determinant operation. Note that having correlated noise between the measurements, the assumptions that lead to Equation 3.17 are not valid anymore. The Fischer Information Matrix of Equation 3.17 for this case is simplified to

$$\mathbf{J}_{\hat{\mathbf{b}}} = \mathbf{G}^{\mathsf{T}}_{\mathsf{uu}}\mathbf{R}^{-1}_{\nabla\Delta\rho}\mathbf{G}_{\mathsf{uu}}, \tag{5.32}$$

and the corresponding CRLB for the pseudorange differencing baseline estimator is

$$Cov(\hat{\mathbf{b}}_{\mathsf{PRD}}) = (\mathbf{G}^{\mathsf{T}}_{\mathsf{uu}}\mathbf{R}^{-1}_{\nabla\Delta\rho}\mathbf{G}_{\mathsf{uu}})^{-1}. \tag{5.33}$$

As in the case of the CRLB out of the measurement model for *absolute position differencing* (see Equation 5.18), this CRLB for *pseudorange differencing* is a function of the measurement errors and the constellation geometry. For a given satellite geometry, $\mathbf{G}_{\mathsf{u}}$ or $\mathbf{G}_{\mathsf{uu}}$, and a given measurement errors, $\mathbf{R}_{\rho}$ or $\mathbf{R}_{\nabla\Delta\rho}$, both CRLB yield the same value. This is intuitive, since the CRLB gives the covariance of the best possible estimator.

Figure 5.4a to Figure 5.4f show the skyplot, i.e. the position of the satellites on a polar plot, for different satellite constellations. The concentric circles represent satellite positions with same elevation. The central point is the zenith (90°), while the outer circle represents the horizon (0°). A horizontal baseline between two vehicles of 100 m in north direction is simulated. All pseudorange measurements were simulated with equal standard deviation of $\sigma_{\rho} = 1\,\mathrm{m}$. The red ellipse represents the horizontal CRLB of the estimation of the relative position. Table 5.2 summarizes the variances in east, north and up direction of each of the plots.

For the chosen baseline direction, north-south variance corresponds to the uncertainty in the longitudinal component of the baseline, while the east-west variance represents the uncertainty in the lateral component of the baseline. The up-component of the the CRLB mirrors directly the

uncertainty in the height component of the baseline, which, usually plays a subordinate role in vehicle relative positioning.

Figure 5.4a shows the optimal satellite configuration that minimizes the geometric errors. A wide open configuration with orthogonal satellites yields a small error in all three baseline components. In practice, low satellite elevations are not convenient, as the signals are easily obstructed and, consequently, have a lower signal strength and more noise. Usually an elevation mask between 5° and 15° is chosen [38]. The vertical baseline error is larger than the horizontal components due to the geometry of the problem, having only satellites located on one side of the celestial hemisphere (see second row in Table 5.2). When only high-elevation satellites are visible (see Figure 5.4b), the uncertainty in the vertical component increases strongly. A special case is when both vehicles drive along an urban canyon. Here, low elevation satellites in lateral direction to the baseline are blocked due to high buildings, while satellites in canyon-direction are available at low elevation. The result is a low lateral baseline accuracy as pictured in Figure 5.4c.

Thus, in order to have a good longitudinal accuracy satellites distributed along the semicircle *in-line with the baseline* and through the zenith are needed. Lateral accuracy is improved by satellites distributed along the semicircle *perpendicular to the baseline* and through the zenith. For good vertical baseline accuracy, low elevated satellites are of advantage.

In case of equal measurement errors, the choice of the common satellite is irrelevant. Figure 5.4d has the same constellation than Figure 5.4a but choosing a different common satellite and, thus, the same baseline errors can be appreciated. In practice, however, the highest located satellite near zenith is chosen, which is usually the satellite suffering less obstruction, higher signal power and is the more often available. In Figure 5.4e and 5.4f, extended constellations with 8 and 12 satellites can be observed. The last two rows in Table 5.2 reveal how the horizontal error can be reduced the more satellites are available.

5.1.4. Comparison: Absolute Position Differencing and Pseudorange Differencing

The previous sections introduced two different techniques to estimate the baseline vector between two vehicles, namely, the subtraction of absolute positions and the differentiation of GNSS pseudoranges. In this section, a systematic analysis of both approaches is performed. To simplify this analysis, a single epoch view is assumed, where a temporal relationship of the errors is neglected. The metric used is the mean squared error (MSE), which includes both, the variance and the bias of the estimator. The MSE for the relative positioning problem is defined as $\epsilon_{\hat{b}} = E[\|\hat{\mathbf{b}} - \mathbf{b}\|^2]$. The input to the estimators are the pseudoranges ρ_{e}^l and ρ_{t}^l with $l = \{1 \dots L\}$ and L being the number of tracked satellites. The error model considered for the pseudoranges of e and t are the

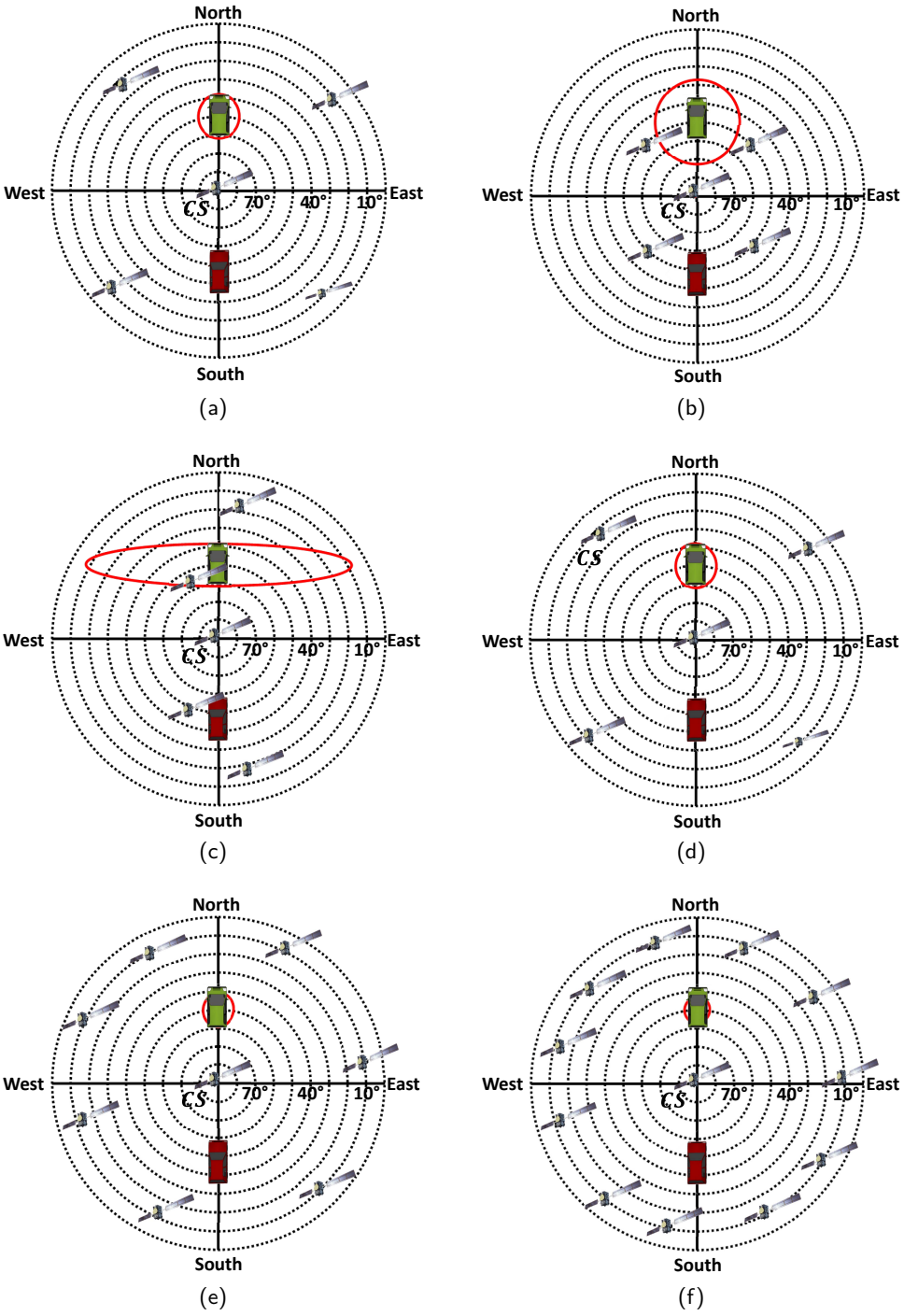

Figure 5.4.: The red ellipsoid represents the horizontal components of the CRLB for different satellite geometries and pseudorange measurements with white Gaussian noise of equal variance. Table 5.2 contains the values for the ellipsoids.

Table 5.2.: Cramér-Rao Lower Bound (CRLB) values for different satellite geometries

Figure	**East Error**	**North Error**	**Up Error**
Figure 5.4a	1.1338 m	1.1213 m	2.9383 m
Figure 5.4b	2.2772 m	2.2766 m	15.5557 m
Figure 5.4c	7.1751 m	1.1298 m	6.3145 m
Figure 5.4d	1.1338 m	1.1213 m	2.9383 m
Figure 5.4e	0.8250 m	0.9068 m	2.8223 m
Figure 5.4f	0.6841 m	0.7047 m	2.9087 m

following:

$$\epsilon_{\mathrm{e}}^{l} = C^{l} + n_{\mathrm{e}}^{l}, \tag{5.34}$$

$$\epsilon_{\mathrm{t}}^{l} = C^{l} + n_{\mathrm{t}}^{l}, \tag{5.35}$$

where C^l is the common error to the pseudoranges of both receivers e and t to the same satellite l. For simplicity, it is assumed that the common error is uniformly distributed in the interval $[0, c]$, where c is the common error limit. The statistical properties of C^l are summarized next:

$$C_{\mathrm{e}}^{l} = C_{\mathrm{t}}^{l}, \tag{5.36}$$

$$E[C^{l}] = \frac{c}{2}, \tag{5.37}$$

$$E[(C^{l})^{2}] = \frac{c^{2}}{3}, \tag{5.38}$$

$$E[C^{l} \cdot C^{m}] = E[C^{l}] \cdot E[C^{m}] = \frac{c^{2}}{4}. \tag{5.39}$$

Whereas, n_{e}^{l} and n_{t}^{l} in Equation 5.34 and Equation 5.35 are noise components following a Gaussian distributions with zero mean and equal variance σ_{ρ}^{2} on all satellites, and mutually independent between satellites and between receivers. Its statistical properties are summarized next:

$$E[n_{\mathrm{e}}^{l}] = 0, \tag{5.40}$$

$$E[(n_{\mathrm{e}}^{l})^{2}] = \sigma_{\rho}^{2}, \tag{5.41}$$

$$E[n_{\mathrm{e}}^{l} \cdot n_{\mathrm{t}}^{l}] = 0, \tag{5.42}$$

$$E[n_{\mathrm{e}}^{l} \cdot n_{\mathrm{e}}^{m}] = 0. \tag{5.43}$$

Since this is a snapshot analysis, no assumptions on the time correlation of the errors is made. In general, common errors and noise are not white but have a certain time correlation. The common error is to a certain extend static due to the limited dynamic of the satellite position, the dynamic of the atmosphere or the behavior of the atomic clocks on the satellite. The noise component on the pseudoranges is colored by the tracking loops in the receivers. Next, the propagation of these errors from the pseudoranges to both baseline estimators will be regarded for *absolute position differencing* and *pseudorange differencing*. On the one hand, the baseline estimate $\hat{\mathbf{b}}_{\mathsf{APD}}$ has a mean squared error $\epsilon_{\hat{b},\mathsf{APD}}$. It can be mathematically derived that the MSE for *absolute position differencing* is given by:

$$\begin{aligned}\epsilon_{\hat{b},\mathsf{APD}} &= E[\|\hat{\mathbf{b}}_{\mathsf{APD}} - \mathbf{b}\|^2] = \\ &= \mathbf{G}_{\mathsf{APD,e}} \cdot \mathbf{R}_\rho \cdot \mathbf{G}_{\mathsf{APD,e}}^{\mathsf{T}} + \mathbf{G}_{\mathsf{APD,t}} \cdot \mathbf{R}_\rho \cdot \mathbf{G}_{\mathsf{APD,t}}^{\mathsf{T}} \\ &\quad - 2 \cdot \mathbf{G}_{\mathsf{APD,e}} \cdot \mathbf{R}_{\mathsf{C}} \cdot \mathbf{G}_{\mathsf{APD,e}}^{T}. \end{aligned} \tag{5.44}$$

The geometry matrices at the ego receiver, $\mathbf{G}_{\mathsf{APD,e}}$, and at the target receiver, $\mathbf{G}_{\mathsf{APD,t}}$, transform the pseudorange errors given by the covariance matrices $\mathbf{R}_\rho$ and $\mathbf{R}_{\mathsf{C}}$ into an error in the baseline. Both are defined as:

$$\mathbf{R}_\rho = \begin{bmatrix} \sigma^2 + \frac{c^2}{3} & \frac{c^2}{4} & \cdots & \frac{c^2}{4} \\ \frac{c^2}{4} & \sigma^2 + \frac{c^2}{3} & \cdots & \frac{c^2}{4} \\ \vdots & & \ddots & \vdots \\ & \cdots & & \end{bmatrix}, \tag{5.45}$$

$$\mathbf{R}_{\mathsf{C}} = \begin{bmatrix} \frac{c^2}{3} & \frac{c^2}{4} & \cdots & \frac{c^2}{4} \\ \frac{c^2}{4} & \frac{c^2}{3} & \cdots & \frac{c^2}{4} \\ \vdots & & \ddots & \vdots \\ & \cdots & & \end{bmatrix}. \tag{5.46}$$

On the other hand, the baseline estimate $\hat{\mathbf{b}}_{\mathsf{PRD}}$, whose mean squared error is given by:

$$\epsilon_{\hat{b},\mathsf{PRD}} = E[\|\hat{\mathbf{b}}_{\mathsf{PRD}} - \mathbf{b}\|^2] = \mathbf{G}_{\mathsf{PRD}} \cdot \mathbf{R}_{\nabla\Delta\rho} \cdot \mathbf{G}_{\mathsf{PRD}}^{\mathsf{T}}, \tag{5.47}$$

where $\mathbf{G}_{\mathsf{PRD}}$ is the transformed geometry matrix from Equation 5.27 and $\mathbf{R}_{\nabla\Delta\rho}$ is the error covariance matrix for the double differences from Equation 5.29. $\mathbf{R}_{\nabla\Delta\rho}$ incorporates only the contribution from the noise terms n_{e}^l and n_{t}^l, since the common error C^l has canceled out through differentiation.

Finally, with Equations 5.44 and 5.47, an expression for the mean squared error for both estimators in dependence of the geometry of the satellite constellation used in each receiver, the common error limit c and the noise standard deviation σ_ρ has been found.

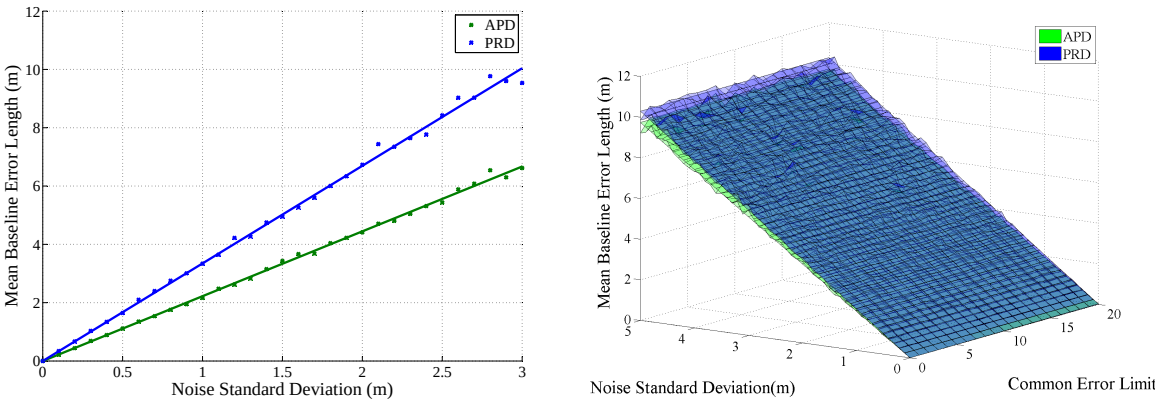

(a) Noise (b) Noise & Common Errors

Figure 5.5.: Mean baseline error with *absolute position differencing* (green) and *pseudorange differencing* (blue) with pseudoranges corrupted by noise (left figure) and noise and common errors uniformly distributed between zero and the common error limit (right figure).

Given a fixed arbitrary constellation of 12 GNSS satellites and two antenna positions separated 100 m from each other, a series of Monte-Carlo simulations have been performed using MATLAB in order to determine the performance of each of the methods. For this purpose, multiple runs with varying random errors on the pseudoranges have been simulated. The pseudorange of each receiver to each satellite is the true range, plus a bias term due to the user clock and an error term. In *absolute position differencing*, each receiver estimates its position and user clock bias by solving iteratively the non-linear least squares problem. In a second step, the positions in the navigation frame are subtracted from each other to retrieve the baseline. In *pseudorange differencing*, first the common set of pseudoranges are subtracted twice to calculate the pseudorange double differences. The baseline using all double differences is estimated using a least squares algorithm. The mean squared error vector over all simulations is computed in order to compare both methods against each other.

First, a simulation adding a random Gaussian error n_{e}^{l} with a certain standard deviation σ_ρ on each of the pseudoranges has been performed. The resulting baseline's mean squared error is shown in Figure 5.5a. The dots in the figure are the result from the Monte-Carlo simulation with 2000 realizations, whereas the solid line represents the theoretical result from Equation 5.44 and Equation 5.47. Their resemblance proves that the theoretical derived equations correctly describe the errors in the scenario. It can be seen that *absolute position differencing* yields a better solution than *pseudorange differencing* when using the same set of 12 satellites. This is due to the fact that the estimate of *pseudorange differencing* is subjected to four times the pseudorange noise on the code double differences. If the number of satellites is decreased, the solutions of *absolute position differencing* and *pseudorange differencing* tend to be similar and are exactly the same when using the same four satellites.

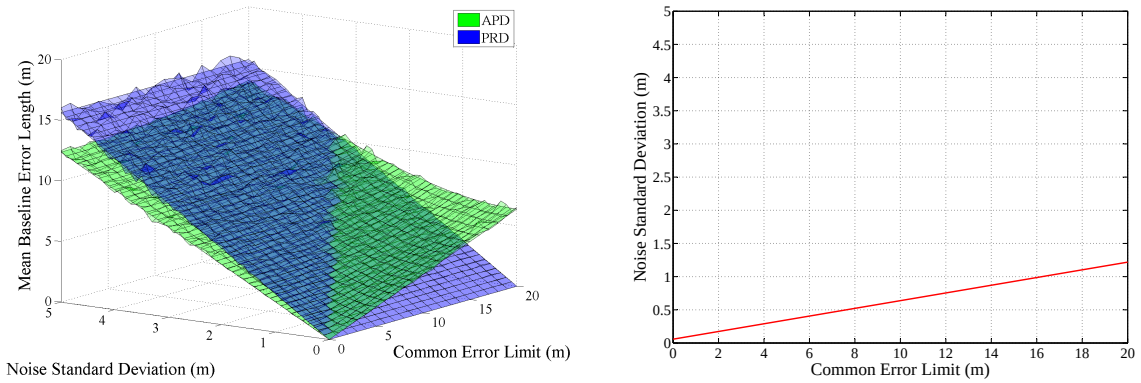

(a) Mean Baseline Error (b) Threshold

Figure 5.6.: The figure shows the baseline error of *absolute position differencing* and *pseudorange differencing* with pseudoranges corrupted by noise and common errors. For *absolute position differencing* the receivers use each 11 satellites where ten are common. *Pseudorange differencing* uses ten common satellites. It can be noticed how the common errors degrade *absolute position differencing*'s baseline estimate. The right figure shows the performance threshold of both approaches, resulting from the projection of the intersection between both planes onto the error plane.

In the following simulation common errors are added on the pseudoranges of ego and target receiver. The 3-D plot in Figure 5.5b displays the baseline mean squared error in dependance of both, the noise standard deviation σ_ρ and the common error limit c. It can be seen how, independently on the magnitude of the common error, *absolute position differencing* performs better than *pseudorange differencing*. When the same satellites are used at both receivers, the bias in $\hat{p}_\mathsf{e}$ and $\hat{p}_\mathsf{t}$ is equal and cancels out. In this case, both estimators, *absolute position differencing* and *pseudorange differencing*, are able to cancel out common errors, but *absolute position differencing* achieves a lower MSE. This is however not the case when a different subset of satellites is used in each receiver. Figure 5.6a shows the baseline error when using nine common and two different satellites in each receiver. The result is a baseline error of several meters in *absolute position differencing*. This leads to the conclusion that, depending on the magnitude of the noise and the magnitude of the common errors on the pseudoranges, *absolute position differencing* or *pseudorange differencing* will give a better result for the estimation of the baseline. The red line on the error plane is the *absolute position differencing-pseudorange differencing* performance threshold that shows the limit at which noise and common errors compensate and the *absolute position differencing* and the *pseudorange differencing* planes intersect.

The presented results were simulated taking a fixed constellation of satellites. Since the GPS satellite constellation repeats approximately every day, the simulation has been extended over 24 hours in order to attain for all possible positions of the satellites. In the same way, the performance of both approaches using different number of satellites in every receiver has been

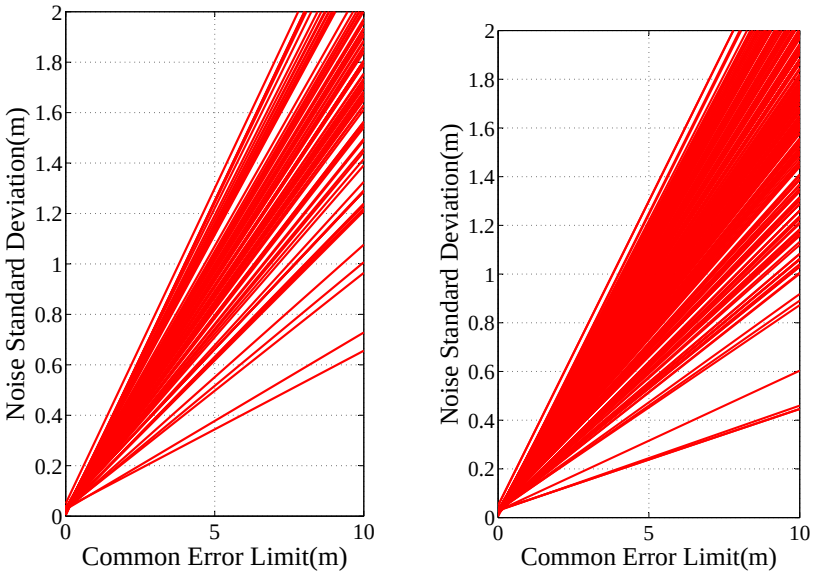

(a) Satellite Geometry (b) Number of Satellites

Figure 5.7.: The performance threshold in dependence of the pseudorange noise standard deviation and the common error limit is shown. The left figure shows the results for 10 common satellites during one whole day. The right figure are the results for combinations of 6 to 11 out of 12 satellites in each receiver.

tested. The resulting displacement of the *absolute position differencing-pseudorange differencing* performance threshold is shown in Figure 5.7. The figure reveals that indeed the performance of both approaches depends on the constellation geometry and on the number of used satellites. There areas of the error plane where *pseudorange differencing* outperforms *absolute position differencing* and vice versa. For example, when the noise standard deviation is below 0.5 m and the common errors are distributed between 0 m and 10 m *pseudorange differencing* yields a better baseline estimate than *absolute position differencing* when using more than 6 satellites.

This performance analysis reveals that, in the case of white Gaussian noise errors, *absolute position differencing* approach yields smaller baseline estimate errors than *pseudorange differencing*. This comes from the fact that the subtraction of pseudoranges in the *pseudorange differencing* approach doubles the variance of the errors in the measurements that are used in the baseline least square problem. When looking at the common errors, it can be observed that when using the same set of satellites at both receivers, the *absolute position differencing* solution also cancels out common errors at both receivers. When using different satellites at each receiver, *absolute position differencing*'s performance decreases with increasing common errors. The performance of each of the estimators will ultimately depend on the working point of the receiver in the scenario. While in an open sky environment with good GNSS signal coverage, the errors due to noise will be small, signals blockage might cause a drop in the received signals strength.

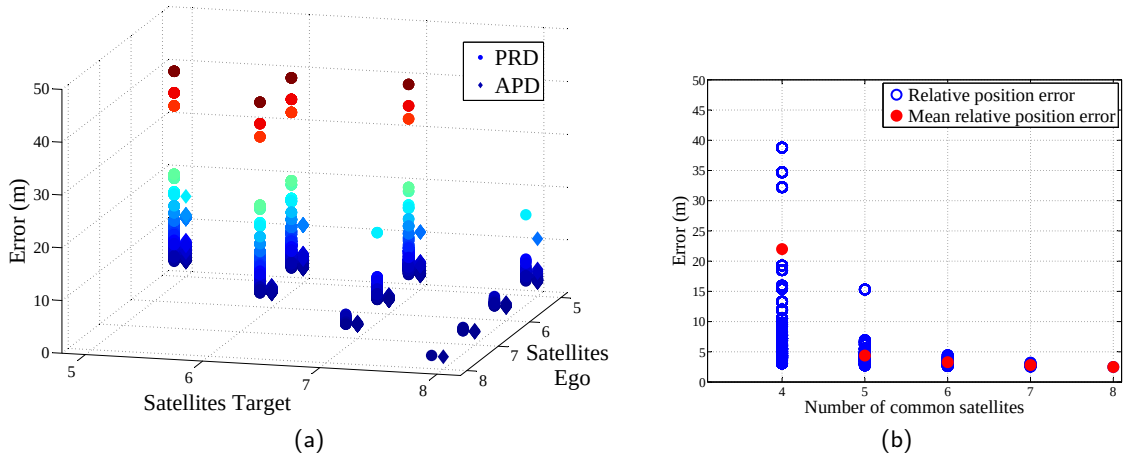

Figure 5.8.: The left figure compares the relative positioning error of *absolute position differencing* and *pseudorange differencing* with a fixed constellation of eight satellites in an only-noise scenario. The right figure shows the error of PRD in dependance of the number of common satellites.

To better understand the dependance of the error of both relative positioning techniques with respect to the constellation, the used satellites in each receiver and the magnitude of the noise and the common errors, a simulation with a fixed 8 satellites constellation is performed. The constellation corresponds to that seen the 4th of June 2013 at 18:30 from the Wessling, south-west of Munich (Germany). In Annex A, a skyview plot is displayed. The noise on the pseudoranges is equal to 1 m (1σ) and the common error is equal to the Klobuchar ionospheric delay model with the parameters of that day, which result in a satellite-dependent pseudorange errors between 2 and 10 m. Figure 5.8a and Figure 5.9a show the error (1σ) in the relative positioning estimate for both, *absolute position differencing* and *pseudorange differencing*, with varying number of satellites tracked by each receiver for the cases of only-noise and only-common errors respectively. The number of satellites in ego and target receiver is switched between 5 and 8 satellites and all combinations of satellites in each receiver are considered. The resulting maximum, minimum and mean values for the relative positioning errors can be found in Annex A.

The situations more prone to happen in practice are with the receivers tracking eight or seven satellites (cells 8-8, 8-7 and 7-7). This yields up to two satellites that are not common between receivers. Situations where the receivers track six satellites are less likely to happen (cells 8-6, 7-6 or 6-6). In these cases up to four satellites could be different. It is improbable that receivers track less than six satellites, especially under consideration that in future multiple satellite constellations will be available (cells 8-5, 7-5, 6-5 or 5-5).

In Figure 5.8, only white Gaussian noise is considered to corrupt the pseudoranges. For both receivers tracking eight satellites (cell 8-8), *absolute position differencing* yields a slightly smaller error than *pseudorange differencing* (2.38 m and 2.49 m respectively). When decreasing the num-

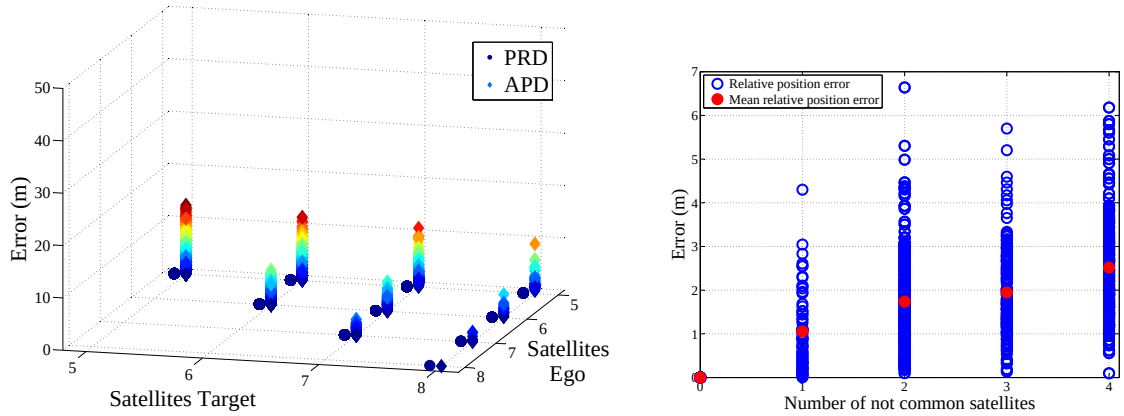

Figure 5.9.: The figures compare the relative positioning error of *absolute position differencing* and *pseudorange differencing* with a fixed constellation of eight satellites in an only common error scenario. The right figure shows the error of APD in dependance of the number of the satellites that are not common to both receivers.

ber of satellites the difference in error between both approaches also increases. For instance, when each receiver tracks seven satellites (cell 7-7), *absolute position differencing* has a maximum error of 3.10 m as opposed to 4.42 m of *pseudorange differencing* (mean errors of 2.70 m as opposed to 3.22 m respectively). Figure 5.8b shows the error of *pseudorange differencing* depending on the number of common satellites. For eight to six satellites the maximum error is below five meters. Below that number, the error strongly increases. When the number of common satellites is equal to four and for cases of bad geometry the maximum error of *pseudorange differencing* is of several hundreds of meters (the plot is cut at 50 m).

In Figure 5.9, only common errors are considered. The relative position estimation with *pseudorange differencing* yields zero error for all combinations (see Figure 5.9a). For *absolute position differencing* the minimum error is zero, which correspond to the cases when both receivers track the same satellites. When tracking one different satellite (e.g. cell 8-7) the error is at worst 1.93 m and the mean over all possible combinations yield 0.77 m. The situation is worse when two satellites are not common (e.g. cell 7-7 or cell 8-6). Here the error is at most 4.47 m and in mean 1.51 m.

Figure 5.9b shows the relative positioning error in dependance of the number of satellites which are not tracked by both receivers and that bias the estimation of the relative position. In order to not consider cases with bad geometry, only the situations when the receivers tracked more than 5 satellites are considered. For one or two different satellites, the maximum error is 4.30 m and 6.64 m and the mean error over all combination of satellites is 1.05 m and 1.73 m, respectively.

With this analysis it has been shown that it is worth to exchange GNSS raw measurements and to only use common pseudoranges to estimate the relative position between vehicles. This is

convenient when at least six common satellites are available. In this way, errors performed by differencing the absolute positions in the order of several meters can be avoided. In general it is more convenient to have an increase in noise, which averages out over time when applying a filtering technique, as for instance the Kalman filter, than having a bias in the measurements, which shifts the relative position by a constant offset.

5.1.5. Receiver Synchronization

When computing double differences, the pseudorange measurements are assumed to be taken at the same time instant. Usually, GNSS receivers perform measurements at every whole second according to GPS time or a given fraction of a second according to its measurement rate. However, the receiver clock has a certain bias with respect to GPS time and this offset changes according to the clock drift of the internal oscillator. This means that measurements taken at two different receivers will usually have an offset of a few milliseconds, causing a potential uncorrelation of common errors [176]. The impact of this time offset on the decorrelation of common error in GNSS was subject of analysis in Section 5.1.1. The pseudorange double difference computation with this explicit time offset is:

$$\begin{aligned}\nabla\Delta\rho_{\mathsf{et}}^{lm}(t_0) &= \nabla\rho_{\mathsf{e}}^{lm}(t_0) - \nabla\rho_{\mathsf{t}}^{lm}(t_0+\Delta t)\\ &= \rho_{\mathsf{e}}^{l}(t_0) - \rho_{\mathsf{t}}^{l}(t_0+\Delta t) - \rho_{\mathsf{e}}^{m}(t_0) + \rho_{\mathsf{t}}^{m}(t_0+\Delta t)\\ &= r_{\mathsf{e}}^{l}(t_0) - r_{\mathsf{t}}^{l}(t_0+\Delta t) - r_{\mathsf{e}}^{m}(t_0) + r_{\mathsf{t}}^{m}(t_0+\Delta t)\\ &+ \epsilon_{\mathsf{e}}^{l}(t_0) - \epsilon_{\mathsf{t}}^{l}(t_0+\Delta t) - \epsilon_{\mathsf{e}}^{m}(t_0) + \epsilon_{\mathsf{t}}^{m}(t_0+\Delta t),\end{aligned} \tag{5.48}$$

where t_0 is used to denote the measurement instant at receiver e and Δt is the offset to the measurement instant at receiver t. Recalling the analysis from Section 5.1.1, the term $\epsilon_{\mathsf{e}}^{l}(t_0) - \epsilon_{\mathsf{t}}^{l}(t_0+\Delta t)$ will effectively cancel out the contributions towards satellite l coming from the atmosphere and the satellite given both, the proximity assumption and the assumption that these errors change slowly with respect to Δt. The same holds for satellite m. The receiver clock biases at ego and target receiver, $\delta t_{\mathsf{e}}(t_0)$ and $\delta t_{\mathsf{t}}(t_0+\Delta t)$, are not included in Equation 5.48, since they are canceled by the differentiation to satellites l and m. Multipath errors, on the other hand, in general remain unsubtracted due to their low spatial and temporal correlation. Satellite, receiver, reflector or scatter movement cause the multipath characteristics to be time variant [177]. The initial assumption that $\nabla\Delta\epsilon_\rho \approx \nabla\Delta\epsilon_{multipath} + \nabla\Delta\epsilon_{noise}$ holds in the case of unsynchronized receivers.

The third line in Equation 5.48 contains the geometric ranges to the satellites l and m from

receivers e and t. These could be rewritten as:

$$\begin{aligned}&\Delta r^{l}_{\mathrm{et}}(t_0) - \delta\Delta r^{l}_{\mathrm{et}}(\Delta t) - \Delta r^{m}_{\mathrm{et}}(t_0) + \delta\Delta r^{m}_{\mathrm{et}}(t_0+\Delta t) = \\ &\nabla\Delta r^{lm}_{\mathrm{et}}(t_0) - \delta\Delta r^{l}_{\mathrm{et}}(\Delta t) + \delta\Delta r^{m}_{\mathrm{et}}(t_0+\Delta t)\end{aligned} \tag{5.49}$$

The first term in the second line, $\nabla\Delta r^{lm}_{\mathrm{et}}(t_0)$, is the actual desired quantity, representing the projection of the baseline at time t_0 towards satellites l and m. The second and the third term represent the change in geometric range in Δt. During the offset time, the movement of the satellites, the displacement of the receivers due to the Earth rotation and the displacement of each of the receivers due to its movement creates a systematic error that has to be accounted for. The maximum relative movement between receiver and satellite is about 1000 $\frac{\mathrm{m}}{\mathrm{s}}$, leading to a double difference error of about one meter per every millisecond offset. The equatorial rotation rate is about 465.1 $\frac{\mathrm{m}}{\mathrm{s}}$, producing a displacement of the receivers of up to 0.5 m every millisecond offset. A relative movement of the vehicles on the surface Earth of 60 $\frac{\mathrm{m}}{\mathrm{s}}$ amounts to 6 cm for every millisecond receiver time offset.

A technique to synchronize the measurements taken by different receivers at different time instants is proposed [176]. By taking the pseudorange rate or Doppler measurement at the receiver as a measure of the relative speed between receiver and satellite, $\frac{dr^{l}_{\mathrm{e}}}{dt}$, a linear extrapolation of the pseudoranges is performed:

$$\rho(t_0+\Delta t) = \rho(t_0) + \Delta t \cdot \lambda \cdot \dot{\phi}(t_0), \tag{5.50}$$

where λ is the L1 wavelength. The Doppler measurement at t_0, $\dot{\phi}(t_0)$, gives an estimate of the pseudorange change rate and can therefore be used to predict the pseudorange in $t_0+\Delta t$. The extrapolation assumption holds as long as the relative movement between receiver and satellite is constant for this short period of time. The apparent Doppler shift caused by the receiver's clock drift is common to all satellites and will cancel out when double differencing.

In order to be able to perform this adjustment, the exact time t_0 when the measurement has been performed has to be known. The receiver will output the GPS timestamp at which the measurement is taken. This has to be corrected by the receiver clock offset, which the receiver is able to estimate by solving the navigation equations. The extrapolation time Δt is the difference to the next measurement epoch. All measurements in the next chapters have been synchronized using this method.

Any change in speed, i.e. acceleration in vehicle and/or satellite, will cause an erroneous extrapolation. Considering maximum vehicle acceleration of around 8 $\frac{\mathrm{m}}{\mathrm{s}^2}$, the range error due to a change in the vehicle's speed during 10 ms is in the order of micrometers and can be neglected. The change of the satellite's speed is below 1 $\frac{\mathrm{m}}{\mathrm{s}^2}$ [178] and is, thus, also neglected. Finally, due to the large radius of the Earth the change in rotational velocity in such a short time frame can be disre-

garded. In the same way, second order variations in the ionosphere and troposphere delays could cause modeling errors. However, as explained in Section 5.1.1, changes in the TEC distribution, even during solar flares, are in the order of minutes and will not introduce additional errors. The satellite elevation and the changes of water concentration in the atmosphere are, as well, slow processes that will not influence the outcome of the extrapolation. Therefore, extrapolating using the Doppler measurement seems to be reasonable.

5.2. Inertial Sensors

The fusion of GNSS and inertial information has the great advantage that both sensors complement each other, making it possible to obtain accurate and continuous position, velocity and orientation estimates. The coupling of Inertial Measurement Unit (IMU) and GNSS will be extended within this work to relative positioning of vehicles. IMUs were introduced in Chapter 3. A typical model for the gyroscope measurements $\hat{\boldsymbol{\omega}}$ is, according to [139]:

$$\hat{\boldsymbol{\omega}} = \mathbf{M}_\omega \cdot \boldsymbol{\omega} + \mathbf{b}_\omega + \mathbf{n}_\omega, \tag{5.51}$$

where $\boldsymbol{\omega}$ is the 3D turn rate of the sensor in inertial frame, $\mathbf{M}_\omega$ is the remaining axis misalignment after factory compensation, $\mathbf{b}_\omega$ is the gyroscope bias and $\mathbf{n}_\omega$ is sensor noise. The gyroscope bias is given in degrees per second ($\frac{^\circ}{\mathrm{s}}$) or degrees per hour ($\frac{^\circ}{\mathrm{h}}$). The bias of the gyroscope is not constant, but wanders over time. Its time variation is the bias stability and it is commonly described stochastically as a first-order Gauss-Markov process. The noise of the gyroscope is commonly assumed to be zero-mean, white and Gaussian distributed [139]. As seen in Chapter 3, the turn rates are integrated to compute the orientation. Consequently, the integration of the noise in the gyroscopes will create an error in the orientation. Therefore, the noise in a gyroscope is often expressed by the angle random walk in $^\circ/\sqrt{\mathrm{h}}$. This describes the average deviation of the angle after integrating the turn rates [179]. It can be shown that standard deviation in the angle grows with the square root of time [180]. An angular random walk of $15\,^\circ/\sqrt{\mathrm{h}}$ means that after one hour the standard deviation of the orientation error will be 15°. The noise can also be defined in terms of its Fast Fourier Transform (FFT) density in $^\circ/\mathrm{s}/\sqrt{\mathrm{Hz}}$.

Accelerometers measure specific force. According to [139], the following model can be assumed for the accelerometer measurements $\hat{\mathbf{f}}$:

$$\hat{\mathbf{f}} = \mathbf{M}_a \cdot \mathbf{f} + \mathbf{b}_a + \mathbf{n}_a, \tag{5.52}$$

where $\mathbf{f}$ is the specific force experienced by teh sensor, $\mathbf{M}_a$ is again the axis misalignment, $\mathbf{b}_a$ is the accelerometer bias and $\mathbf{n}_a$ is accelerometer noise. In this case, the bias of the sensor is given in $\frac{\mathrm{m}}{\mathrm{s}^2}$ and the noise can be quantified by the velocity random walk in $\mathrm{m/s}/\sqrt{\mathrm{s}}$ or directly by the

FFT noise density in $\mathrm{m/s^2/\sqrt{Hz}}$.

The misalignment will be considered zero and, thus, the matrices $\mathbf{M}_\omega$ and $\mathbf{M}_a$ are equal to the identity matrix. An Allan variance analysis makes it possible to obtain the characteristic values for the bias stability and the noise variance for a particular sensor [180]. This tool is usually used to measure the stability of oscillators, such as crystal oscillators, atomic clocks or lasers [181]. In the frame of this thesis it is applied to characterize the stability of gyroscopes and accelerometers sensors used in the scope of this work.

A long sequence of data samples is divided in intervals of the increasing length. Each of the intervals is averaged and the difference of averages of successive intervals is squared and averaged for all intervals. This is performed for all averaging times possible without loosing significance in the statistics. The resulting Allan variances (or Allan deviation if taken the squared root) are plotted as function of the averaging time in a log-log graph, as shown in Figure 5.10a and Figure 5.10b for the accelerometers and the gyroscopes.

The first section of both, the acceleration and the gyroscope curves, shows the impact of white noise and thus has a slope of -0.5. If the averaging time is quadrupled, the noise power is halved. By looking at an averaging time of 1 s the angle random walk can easily be read [182]. This yields a value of $5 \times 10^{-4}\,\mathrm{rad/\sqrt{s}} = 0.03\,^\circ/\sqrt{\mathrm{s}} = 0.03\,^\circ/\mathrm{s}/\sqrt{\mathrm{Hz}}$ for the gyroscope and $9 \times 10^{-4}\,\mathrm{m/s/\sqrt{s}} = 0.05\,\mathrm{m/s^2/\sqrt{Hz}}$ for the accelerometer noise. The stability of the bias of the sensor is read in the Allan deviation chart by looking at the minimum of the curves. Here the values of $14\,\frac{^\circ}{\mathrm{h}}$ at 500 s for the gyroscope and of $2.5 \times 10^{-4}\,\frac{\mathrm{m}}{\mathrm{s}^2}$ at 100 s for the accelerometer are read.

The data sheet for the Xsens MTx inertial sensors[1] states the following values for the gyroscopes: a bias stability of $20\,\frac{^\circ}{\mathrm{h}}$ and a noise density of $0.05\,^\circ/\mathrm{s}/\sqrt{\mathrm{Hz}}$. For the accelerometer a bias stability of $4 \times 10^{-6}\,\frac{\mathrm{m}}{\mathrm{s}^2}$ and a noise density of $0.003\,\mathrm{m/s/^2\sqrt{Hz}}$ are specified. While the parameters for the turn rate sensors pretty well match the data sheet specifications, the parameters for the accelerometers show important deviations. For this reason, the more pessimistic values from the presented Allan variance study will be used for the experiments in the following chapters.

By dividing the FFT noise spectral density by the sample rate of the sensor it is possible to compute a standard deviation for the turn rate and acceleration noise. This can be used to model the likelihood of measurements in the update step of a Bayesian filter as explained Section 3.3. The bias stability parameter can be used to model the time variation of the turn rate and accelerometer biases in the prediction step of a Bayesian filter using a random walk model:

$$\mathbf{b}_\omega^{k+1} = \mathbf{b}_\omega^k + \mathbf{n}_{\mathbf{b}_\omega}, \tag{5.53}$$

[1] Xsens MTi10 series URL: http://www.xsens.com/products/mti-10-series/

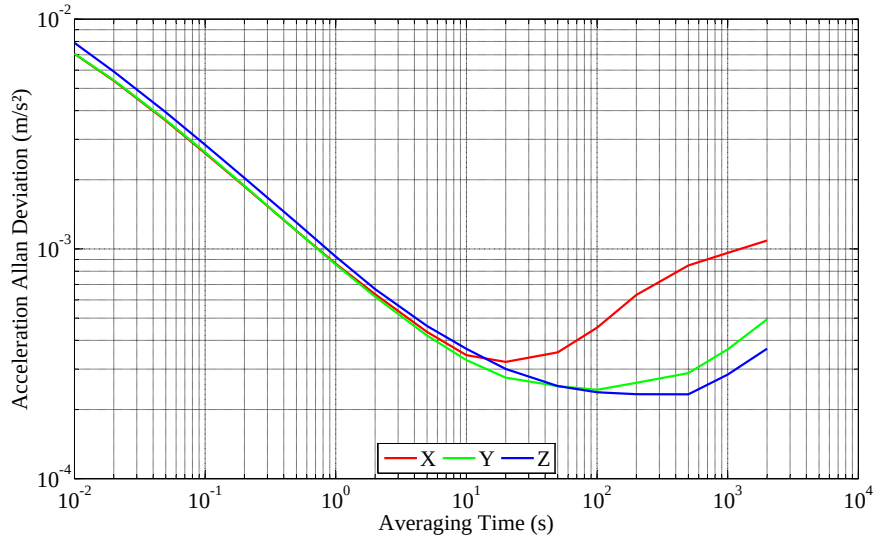

(a) Accelerometer

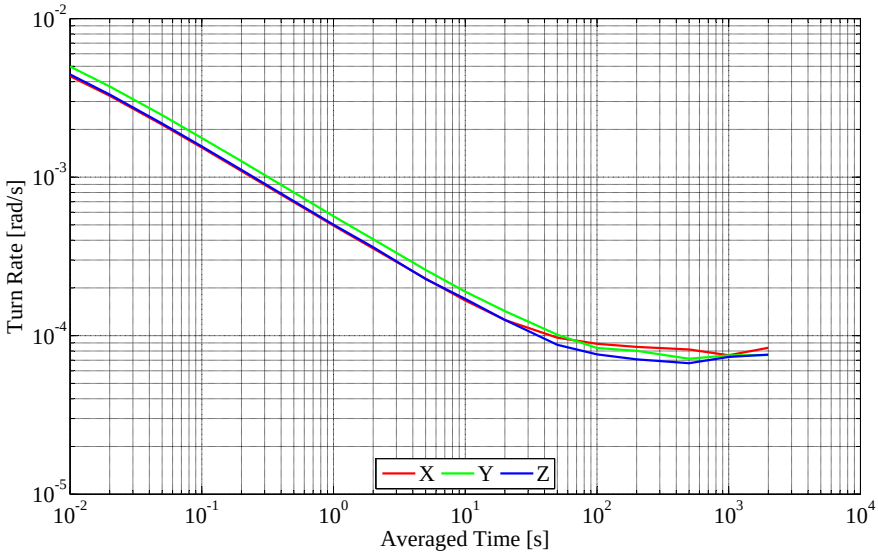

(b) Gyroscope

Figure 5.10.: Allan deviation plots for the Xsens MTx accelerometers and gyroscopes used in the scope of this thesis.

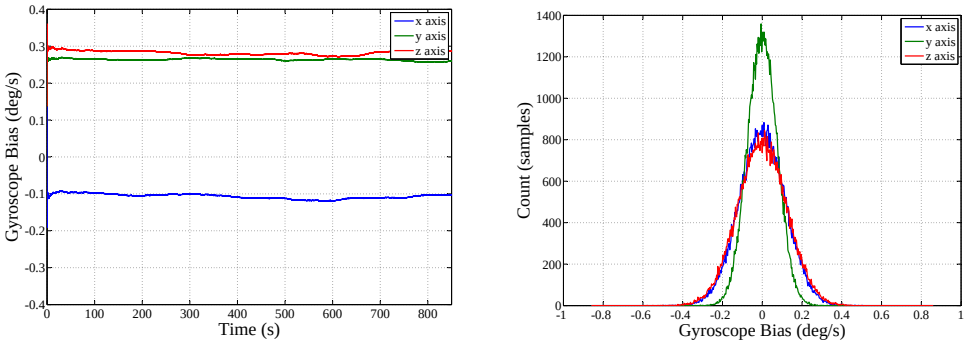

(a) Bias (b) Noise

Figure 5.11.: The left figure shows the gyroscope biases for the sensors used in this work. A 500 s window was used to average the input samples from each of the gyroscopes. The right figure shows the noise distribution using a histogram on the biased-free samples. A normality test yields that the distribution of the errors is well approximated with a Gaussian distribution.

and choosing for the random walk noise $\mathbf{n}_{\mathbf{b}_\omega}$ standard deviation a value equal to:

$$\sigma = \sqrt{\frac{\delta t}{t}} \cdot B_{\mathsf{s}}, \tag{5.54}$$

where δt is the sampling time, t is the averaging time used to find the bias stability and B_{s} is the bias stability measured in $\frac{^\circ}{\mathsf{s}}$ [180]. Figure 5.11a shows the gyroscope biases over a period of 800 seconds, that have been computed by averaging with a time window equal to the bias stability value. The biases for the used Xsens MTx IMUs have values in the order of $\pm 0.5\,\frac{^\circ}{\mathsf{s}}$. If left uncompensated their integration would yield an angular error above 10° in less than one minute. Figure 5.11b shows the distribution of the errors for the three axis gyroscope in form of a histogram. Their nearly Gaussian shape is confirmed by applying a Kolmogorov-Smirnov (KS) test. This test compares the cumulative distribution function of the empirical data with the cumulative distribution function of a normal distribution. The KS test does not reject the null-hypothesis at a $5\,\%$ significance level, meaning that the gyroscope noise Probability Density Function (PDF) resembles a Gaussian distribution. The accelerometer sensors, which are not shown here, yield the same results for the Kolmogorov-Smirnov test. Additionally, the skewness and the kurtosis values for the distribution have similar values as a normal distribution. Hence, the assumption that the noise on gyroscopes and accelerometers of the Xsens MTx is white and Gaussian is correct and they can be used in a Gaussian Bayesian filter.

Sensor Placement and Alignment Each of the vehicles in this thesis is equipped with an IMU. The placement of the IMU on the vehicle is important for navigation purposes. The center of the yaw rotation of a four wheel vehicle is in the center of the rear axle [97]. If the IMU is not

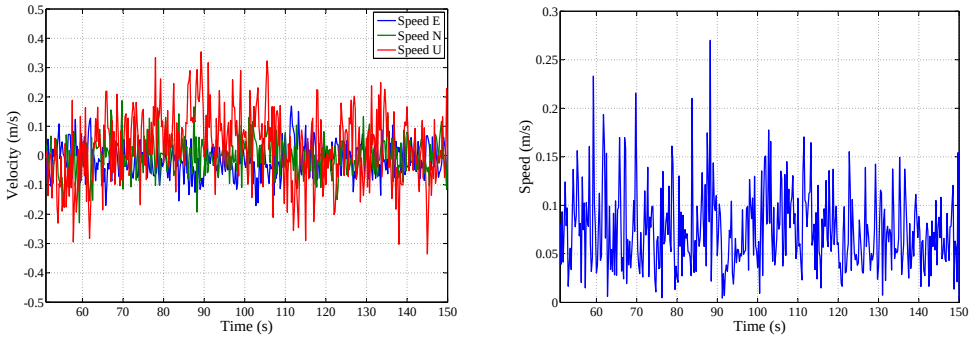

(a) Velocity ENU (b) Horizontal Speed

Figure 5.12.: The left figure shows the ENU velocity error components for a Ublox LEA 4T in a test environment with good carrier to noise ratio. The velocity was computed using a tightly coupled processing of Doppler measurements. The right figure is the corresponding horizontal speed measurement.

placed at this location, it is not measuring exactly the rotation of the vehicle and the amount has to be corrected by the displacement vector between the IMU and the center of rotation. This, so-called "lever-arm effect" has also to be compensated when the GNSS antenna is not located at same location than the IMU [183]. Besides the mounting point of the IMU, also the alignment is crucial for navigation. The ideal case is to have the sensor frame and the vehicle frame aligned with each other. A calibration step is assumed after the placement of the IMU inside the vehicle prior to the experiments.

5.3. GNSS Doppler Measurements

By measuring the Doppler shift towards the GNSS satellites in view, and by knowing their orbital speed, a receiver is able to solve for its own 3D velocity and its clock drift. The procedure is analogous to 3D position calculation by taking Doppler measurements instead of pseudoranges, satellite velocity instead of satellite position and computing receiver velocity and clock drift instead of receiver position and clock bias.

The computation of the satellite's velocity is easily accomplished by differencing subsequent satellite positions computed out of the broadcasted navigation messages, thus achieving satellite velocity accuracy of $\pm 1 \frac{mm}{s}$ [178]. Figure 5.12a shows the Doppler derived velocity error in the ENU frame for a static receiver. The standard deviation of the single velocity components are $6.0 \frac{cm}{s}$, $6.3 \frac{cm}{s}$ and $13.5 \frac{cm}{s}$. As expected the Up component has a larger error due to the hemispherical satellite constellation. Figure 5.12b shows the error of the norm of the velocity vector, i.e. the speed, processed using a Kalman filter.

An alternative that offers higher accuracy is to use time differenced carrier phase measurements.

These, due to higher integration times within the GNSS receiver, are less noisy than Doppler measurements [184]. The inherent integer ambiguity associated to carrier phase measurements is canceled through time differentiation. The drawback is their lower availability in situations with low carrier-to-noise ratio and the occurrence of cycle slips. Again, both the velocity ENU component errors and the speed error is shown in Figure 5.13a and Figure 5.13b, respectively. The standard deviation in the velocity components are 1.9 $\frac{\text{cm}}{\text{s}}$, 1.1 $\frac{\text{cm}}{\text{s}}$ and 5.8 $\frac{\text{cm}}{\text{s}}$. When available, the GNSS velocity is used twofold. On the one hand, it is used for updating the speed of the vehicle by taking the magnitude of the velocity vector. On the other hand, the planar components of the velocity will yield the east-north direction or heading of the vehicle.

It has to be noted that, when the single velocity components follow Gaussian distributions, the distribution of the speed estimation follows a Ricean distribution, that can only be approximated to a Gaussian distribution at higher speed. At zero speed, the speed error is Rayleigh distributed. Nevertheless, a Gaussian distribution will be considered when including the speed into a Bayesian filter.

The accuracy of the heading estimate is dependent on the magnitude of the measured velocity. At zero speed the heading is undetermined. The higher the speed of the vehicle is, the better the heading estimate can be done. Its standard variation can be approximated with:

$$\sigma_h \approx \arctan \frac{\sigma_v}{\|v\|}, \tag{5.55}$$

with σ_h and σ_v being the standard deviations of the heading and the velocity component, respectively, and $\|v\|$ being the norm of the velocity vector. This results in heading errors of 0.4°, 0.08° and 0.04° when driving at 10 $\frac{\text{km}}{\text{h}}$, 10 $\frac{\text{km}}{\text{h}}$ and 100 $\frac{\text{km}}{\text{h}}$ respectively. The resulting PDF for the heading estimate has a Gaussian shape, and is confirmed performing a KS test at different speed from 2 $\frac{\text{m}}{\text{s}}$ to 40 $\frac{\text{m}}{\text{s}}$. The heading estimate from GNSS is the sole source of absolute heading information that is available. Therefore, its correct incorporation into the filter and fusion with gyroscope data is highly important and will be discussed in Section 5.6.2.

5.4. Speed Sensors

A speed sensor inside the vehicle is able to determine the rotation speed of the wheels by means of measuring the fluctuating magnetic field disturbed by a toothed ring mounted at the wheel or differential [29]. Speed sensors are part of active safety systems in modern vehicles, as the Anti-lock Braking System (ABS) or Electronic Stability Program (ESP) [29]. Not all wheels rotate at the same speed. Especially in turns the inner wheels rotate less than the outer wheels. Due to wheel slip and skids, both wheels might have different speed and, thus, will provide false vehicle speed measurements [97]. The on-board control unit, takes an average speed of the four wheels

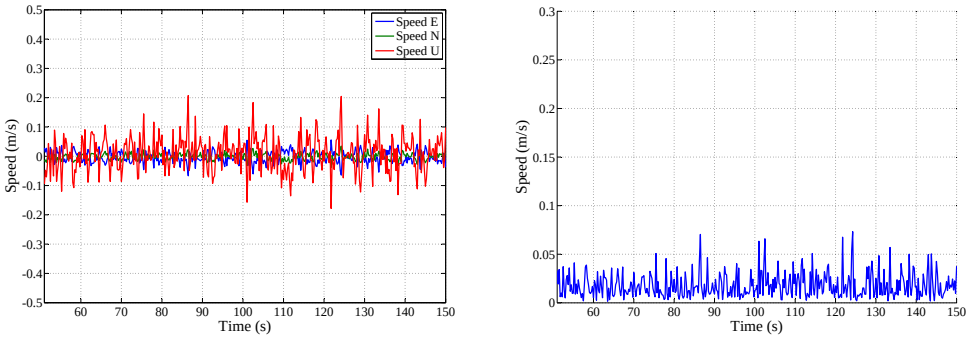

(a) Velocity ENU (b) Horizontal Speed

Figure 5.13.: The left figure shows the ENU velocity error components for a Ublox LEA 4T in the same test conditions as in Figure 5.12. Instead of using GNSS Doppler measurements, the more accurate carrier phase measurements are used as updates of the Kalman Filter.

to calculate the speed of the vehicle. A scale factor error due to the uncertainty of the wheel radii is an additional and predominant error source. Usually, the speed values are quantized to the next whole $\frac{\text{km}}{\text{h}}$ prior to deliver it through the On-board Diagnostics (OBD) interface. Hence, this processed information is less accurate than the speed information available to ABS or ESP. Therefore, a model for the available speed measurement is assumed next. The speed sensor inside the vehicle gives a biased and noisy measure $\hat{v}$ of the forward speed of the vehicle:

$$\hat{v} = A \cdot v + b_{\text{v}} + \epsilon_{\text{v}}, \tag{5.56}$$

where v is the actual speed of the vehicle, A is a scale factor due to the unknown wheel radii, b_{v} is an offset in the speed sensor and n_{v} is quantization noise. The distribution of the noise component depends on the quantization method. Rounding or truncation have an impact on its mean. However, this is taken into account by the offset parameter b_{v}. Quantization noise is uniformly distributed with standard deviation $\sigma_{\text{v}} = 1/\sqrt{12}\ \frac{\text{km}}{\text{h}}$. The sensor fusion architecture, which will be introduced in the next section, is based on a Kalman filter. This implementation of a Bayesian filter assumes white Gaussian distributed noise. Consequently, the colored and uniformly distributed noise of the speed sensor will cause a non-optimal behavior of the Bayesian estimator.

Parameter b_{v} can be determined through a calibration procedure, since it is likely that it stays constant over the duration of the measurements. The wheel radii, on the other hand, suffer changes over time and it is convenient to design a calibration procedure for parameter A. As discussed in Section 5.3, GNSS receivers offer a second source of speed information of the vehicle. Figure 5.14 compares both sources of speed information. In Figure 5.14a the speed of a vehicle on a section of highway is shown. The offset and the quantization of the speedometer values can be appreciated. These sections can be used to automatically learn the parameters A and b_{v} of the

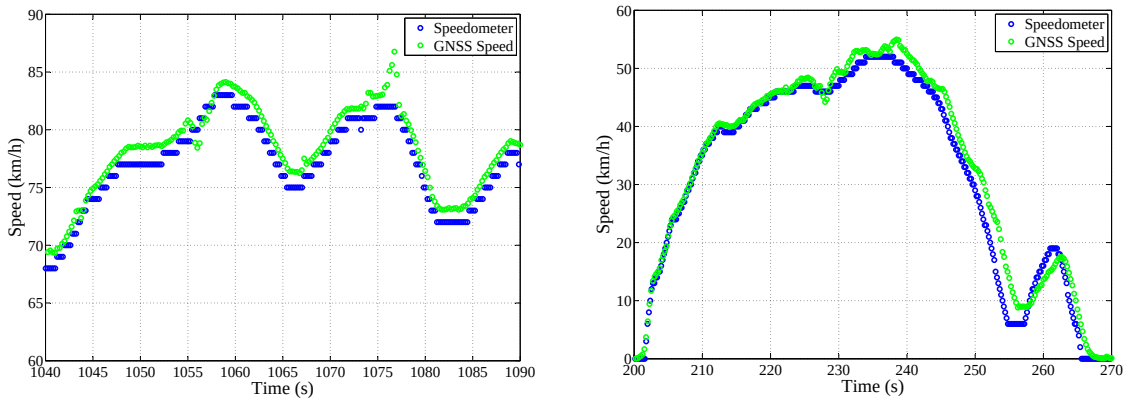

(a) Highway (b) Urban

Figure 5.14.: Comparison of vehicle speed from GNSS and on-board speedometer in highway and in urban scenario.

sensor. However, around second 1055 and 1075 the influence of multipath and low signal strength on the GNSS speed estimation occurs. Figure 5.14b shows a drive through an urban canyon. Low signal strength and multipath cause the filtered output of the velocity estimate to give an incorrect and biased information on the speed of the vehicle. Luckily, multipath is a transitory effect and will average out in a long-term estimation of the speedometer parameters.

5.5. Vehicle Relative Motion Models

In Chapter 3, the Bayesian filter, along with its prediction and update steps, has been presented. When estimating the relative position of a target vehicle in a Bayesian filter, a system model, that predicts the baseline coordinates in $k+1$ from the baseline coordinates in time step k, is required. Numerous publications propose filter designs that use such full 3D models, such as [183, 185]. While aircraft, missiles and submarines move freely in all directions, special constraints that hold for ground vehicles can be exploited to simplify the problem. So-called non-holonomic constraints are based on the fact that land vehicles are not able to move sideways, up-wards nor downwards [186].

In the literature, planar motion models for vehicles are divided in either kinematic or dynamic models. Kinematics studies the motion of objects, their position, velocity and acceleration, without considering their cause of motion. On the other hand, dynamic models include the effect of force and torque vectors on the motion of the vehicles.

The bicycle model is a dynamic model often considered in the literature for vehicle positioning [187–189]. With the help of this model, the position and the heading of the vehicle are estimated. As control inputs, usually the wheel speed, the steering angle and the yaw rate from the ESP

sensors are used. The bicycle model is parametrized by including the mass of the vehicle and the distances from the center of mass to the front and rear axles. An improvement to this model is the Ackermann motion model, which considers a four wheel vehicle [190]. The advantage of this model over the commonly used bicycle model is that here the speed of every single wheel is used to compute the speed of the vehicle [191].

In this thesis, the more simpler kinematic models are considered. Kinematic models are non-parametric models that consider the vehicle as a point mass. They are reasonable for low-speed scenarios, without sharp driving maneuvers and obviate the lateral displacement of the vehicle [192].

If the relative position is assumed to be given in a two-dimensional vehicle coordinate frame as explained in Chapter 3, the function $f(\cdot)$ transforms the baseline in time step k, $\begin{bmatrix} b_{\mathsf{x}}^k & b_{\mathsf{y}}^k \end{bmatrix}^\mathsf{T}$, into the baseline in time step $k+1$, $\begin{bmatrix} b_{\mathsf{x}}^{k+1} & b_{\mathsf{y}}^{k+1} \end{bmatrix}^\mathsf{T}$. Ideally, this function is linear, so that the Kalman filter is applied. If this is not the case, the approximations to the optimal filter given by the Extended Kalman Filter (EKF) and Unscented Kalman Filter (UKF) need to be implemented.

One simple kinematic model is a rectilinear constant speed model. Here the baseline $\mathbf{b}$ is predicted using the baseline velocity $\dot{\mathbf{b}}$, which represents the relative speed between the vehicles. The prediction equations are:

$$\begin{bmatrix} b_{\mathsf{x}} \\ b_{\mathsf{y}} \\ \dot{b}_{\mathsf{x}} \\ \dot{b}_{\mathsf{y}} \end{bmatrix}^{k+1} = \begin{bmatrix} b_{\mathsf{x}} + \Delta t \cdot \dot{b}_{\mathsf{x}} \\ b_{\mathsf{y}} + \Delta t \cdot \dot{b}_{\mathsf{x}} \\ \dot{b}_{\mathsf{x}} \\ \dot{b}_{\mathsf{y}} \end{bmatrix}^{k} + \begin{bmatrix} n_{\mathsf{x}} \\ n_{\mathsf{y}} \\ n_{\dot{\mathsf{x}}} \\ n_{\dot{\mathsf{y}}} \end{bmatrix}^{k}, \tag{5.57}$$

where Δt is the prediction time. The noise terms n_{x}, n_{x}, $n_{\dot{\mathsf{x}}}$ and $n_{\dot{\mathsf{y}}}$ model the uncertainty in the prediction of each of the states. The baseline velocity $\dot{\mathbf{b}}$ is, at the same time, also part of the estimated state vector. It can either be, that the baseline velocity is directly observed, for example through a ranging sensor or from a differential GNSS Doppler measurement. If, on the contrary, the relative velocity remains unobserved, it will be inferred from the relative position observations in the filter. The relative velocity can also be predicted by incorporating the velocity of both vehicles. The equations of the resulting Constant Velocity (CV) model are:

$$\begin{bmatrix} b_{\mathsf{x}} \\ b_{\mathsf{y}} \\ \dot{b}_{\mathsf{x}} \\ \dot{b}_{\mathsf{y}} \end{bmatrix}^{k+1} = \begin{bmatrix} b_{\mathsf{x}} + \Delta t \cdot (v_{\mathsf{t}} \cdot \cos(\Delta\psi) - v_{\mathsf{e}}) \\ b_{\mathsf{y}} - \Delta t \cdot v_{\mathsf{t}} \cdot \sin(\Delta\psi) \\ v_{\mathsf{t}} \cdot \cos(\Delta\psi) - v_{\mathsf{e}} \\ -v_{\mathsf{t}} \cdot \sin(\Delta\psi) \end{bmatrix}^{k} + \begin{bmatrix} n_x \\ n_y \\ n_{\dot{x}} \\ n_{\dot{y}} \end{bmatrix}^{k}, \tag{5.58}$$

where $\Delta\psi = \psi_{\mathsf{t}} - \psi_{\mathsf{e}}$ is the difference in heading angles towards north of the ego and target vehicle and v_{e} and v_{t} are the longitudinal speed of ego and target vehicle respectively. The speed

and heading of the target vehicle are also estimated quantities and form part of the state vector. The speed and heading values from the ego vehicle are used as control input in the prediction step. This model assumes that both the ego and the target vehicle move with constant speed and constant heading. It will however, perform poorly when the vehicles accelerate or brake or when they change the driving direction. Only if the time step length Δt is infinitesimally small, this model can be used to approximate an accelerated or curvilinear movement. One possibility is to absorb these situations by designing the prediction models with increased system noise. The result is a relative position estimate with a higher uncertainty. To overcome this problem, the previous CV model is extended to the Constant Acceleration (CA) model by incorporating the accelerations of each of the vehicles:

$$\begin{bmatrix} b_{\mathrm{x}} \\ b_{\mathrm{y}} \\ \dot{b}_{\mathrm{x}} \\ \dot{b}_{\mathrm{y}} \end{bmatrix}^{k+1} = \begin{bmatrix} b_{\mathrm{x}} + \Delta t \cdot ((v_{\mathrm{t}} + 0.5 \cdot \Delta t \cdot a_{\mathrm{t}}^2) \cdot \cos(\Delta\psi) - (v_{\mathrm{e}} + 0.5 \cdot \Delta t \cdot a_{\mathrm{e}}^2)) \\ b_{\mathrm{y}} + \Delta t \cdot ((v_{\mathrm{t}} + 0.5 \cdot \Delta t \cdot a_{\mathrm{t}}^2) \cdot \sin(\Delta\psi) \\ (v_{\mathrm{t}} + 0.5 \cdot \Delta t \cdot a_{\mathrm{t}}^2) \cdot \cos(\Delta\psi) - (v_{\mathrm{e}} + 0.5 \cdot \Delta t \cdot a_{\mathrm{e}}^2) \\ (v_{\mathrm{t}} + 0.5 \cdot \Delta t \cdot a_{\mathrm{t}}^2) \cdot \sin(\Delta\psi) \end{bmatrix}^{k} + \begin{bmatrix} n_{\mathrm{x}} \\ n_{\mathrm{y}} \\ n_{\dot{\mathrm{x}}} \\ n_{\dot{\mathrm{y}}} \end{bmatrix}^{k}, \tag{5.59}$$

where a_{e} and a_{t} are the longitudinal accelerations of the ego and target vehicle respectively. The acceleration of the target vehicles is added to the state vector, whereas the acceleration of the ego vehicle is used as a control input.

The rectilinear models, however, fail to track the relative position when the vehicles are turning. Therefore, the rectilinear CV model is extended to include the turn rates of both vehicles in the prediction of the baseline [193]. The equations for the curvilinear Constant Turn Rate and Velocity (CTRV) model are shown next:

$$\begin{bmatrix} b_{\mathrm{x}} \\ b_{\mathrm{y}} \\ \dot{b}_{\mathrm{x}} \\ \dot{b}_{\mathrm{y}} \end{bmatrix}^{k+1} = \begin{bmatrix} \mathbf{C}_{k-1}^{k} & 0 \\ 0 & \mathbf{C}_{k-1}^{k} \end{bmatrix}^{k} \mathbf{B}^{k} + \begin{bmatrix} n_{\mathrm{x}} \\ n_{\mathrm{y}} \\ n_{\dot{\mathrm{x}}} \\ n_{\dot{\mathrm{y}}} \end{bmatrix}^{k}, \tag{5.60}$$

where $\mathbf{C}_{k-1}^{k}$ is the rotation matrix for the rotation that the ego vehicle has performed during Δt:

$$\mathbf{C}_{k-1}^{k} = \begin{bmatrix} \cos(\Delta t \cdot \dot{\psi}_{\mathrm{e}}^{k-1}) & -\sin(\Delta t \cdot \dot{\psi}_{\mathrm{e}}^{k-1}) \\ \sin(\Delta t \cdot \dot{\psi}_{\mathrm{e}}^{k-1}) & \cos(\Delta t \cdot \dot{\psi}_{\mathrm{e}}^{k-1}) \end{bmatrix}, \tag{5.61}$$

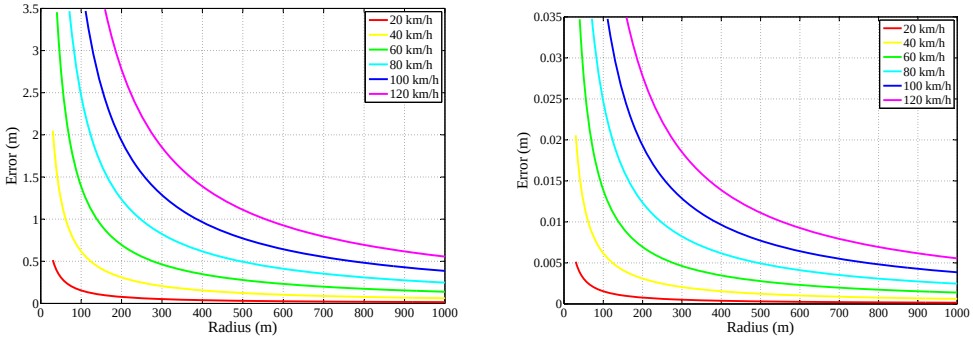

(a) $1Hz$ (b) $10Hz$

Figure 5.15.: Baseline error for target vehicle driving in curve and predicted with rectilinear movement model. The prediction error increases with decreasing curve radius or increasing speed.

and $\mathbf{B}^k$ is the prediction of the baseline in the ego vehicle frame at k:

$$\mathbf{B}^k = \begin{bmatrix} b_x - \frac{v_e}{\dot{\psi}_e} \cdot \sin(\Delta t \cdot \dot{\psi}_e) + \frac{v_t}{\dot{\psi}_t}(\sin(\Delta\psi + \Delta t \cdot \dot{\psi}_t) - \sin(\Delta\psi)) \\ b_y + \frac{v_e}{\dot{\psi}_e} \cdot (\cos(\Delta t \cdot \dot{\psi}_e) - 1) - \frac{v_t}{\dot{\psi}_t}(\cos(\Delta\psi + \Delta t \cdot \dot{\psi}_t) - \cos(\Delta\psi)) \\ v_t \cdot \cos(\Delta\psi) - v_e \\ v_t \cdot \sin(\Delta\psi) \end{bmatrix}^k . \tag{5.62}$$

The factors $\frac{v_e}{\dot{\psi}_e}$ and $\frac{v_t}{\dot{\psi}_t}$ yield the radius of the curve performed by the ego and the target vehicle, respectively. In case a vehicle is not turning, i.e. driving on a curve with sufficiently large radius, this term tends to infinity and the corresponding model for the vehicle is substituted for a rectilinear model. The CTRV model of Equation 5.60 can be extended to include linear accelerations in the same way as in Equation 5.59. The resulting equations of the Constant Turn Rate and Acceleration (CTRA) model are not shown here.

Figure 5.15 shows the prediction error with the rectilinear model for a turning target vehicle in dependance of the curve radius and the speed of the vehicle. Figure 5.15a and 5.15b show the curves for 1 Hz and 10 Hz update rate, respectively. The baseline is predicted for 1 s and 0.1 s, respectively, and then an measurement update for the state is performed. For 1 Hz update rate, large baseline errors occur even for large curve radii. Such a low update rate is only suited for a highway environment. At 10 Hz update rate, tight curves exhibit errors in the order of centimeters. In this thesis a curvilinear model with an update rate of at least 10 Hz is chosen.

Figure 5.16a shows the results for the baseline estimation error using the constant velocity and the constant acceleration kinematic models during a typical acceleration maneuver. The target vehicle has accelerated with 2 $\frac{m}{s^2}$ away from the ego vehicle. The resulting estimation error is always lower for the CA model (red) compared to the CV model (blue). If the update rate is sufficiently increased, the CV model can have an equal performance than the CA model. At an update rate of

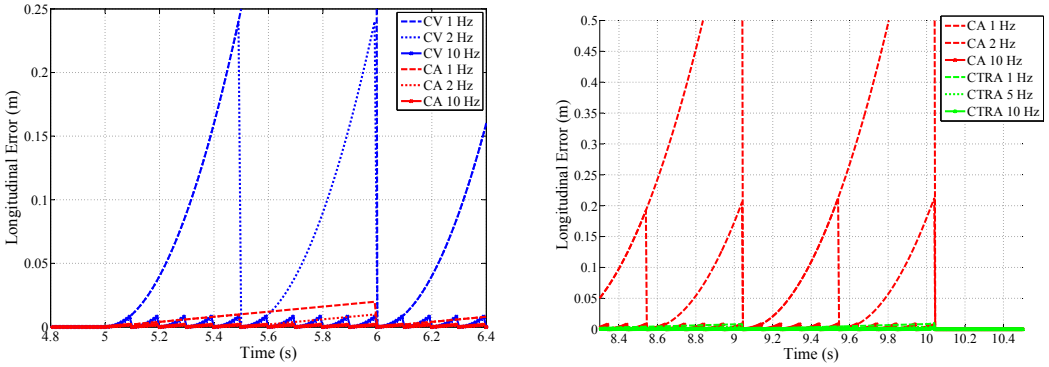

(a) Uniform Rectilinear Acceleration

(b) Constant Turn Rate

Figure 5.16.: Baseline prediction error during a $2\,\frac{\mathrm{m}}{\mathrm{s}^2}$ rectilinear acceleration maneuver (left) and during a $20\,\frac{^\circ}{\mathrm{s}}$ turn at $5\,\frac{\mathrm{m}}{\mathrm{s}}$ (right).

10 Hz and accelerations in the order of the ones encountered in vehicular environments, the error is maintained below 2 cm using a CV model.

Figure 5.16b shows the baseline estimation error with a CTRA and a CA model while performing a $20\,\frac{^\circ}{\mathrm{s}}$ turn at $5\,\frac{\mathrm{m}}{\mathrm{s}}$. During the turning maneuver, the CTRA model (green) is able to properly predict the baseline and yields a smaller error than the rectilinear CA model (red). At an update rate of 1 Hz, errors of nearly 1 m can be appreciated. With increasing update rate, the rectilinear model is, as well, able to predict the baseline. At 10 Hz both models have sub-centimeter accuracy.

The rectilinear motion model has been extensively used in various forms for absolute and relative positioning of vehicles by many research groups as for instance [103, 194–196]. Several research groups have used the constant turn rate model, for example for vehicle positioning [112, 196–198] or for tracking objects detected with on-board ranging sensors [82]. The use of a certain motion model will heavily depend on the road environment. In scenarios with slow and linear changes in the speed and heading, a rectilinear constant velocity model is a suited approach. In an urban scenario, however, vehicles accelerate and decelerate in short periods of time and perform often 90° turns at intersections. In this scenario, a curvilinear constant acceleration model yields better results [199].

The noise components in Equations 5.58 through 5.60 represent the uncertainty in the prediction step using each of the models. There are two sources of this uncertainty. On the one hand, the inaccurate estimate of the speed, acceleration, heading and turn rate of each vehicle will propagate in every prediction step to the baseline estimate. The noise on the acceleration should accommodate possible jerks of the vehicle. On the other hand, also the uncertainty due to model mismatch, i.e. the fact that the vehicles might not displace according to these models, or other sources, as for example the error due to the GNSS antenna position on the roof of the vehicle, need to be taken into account.

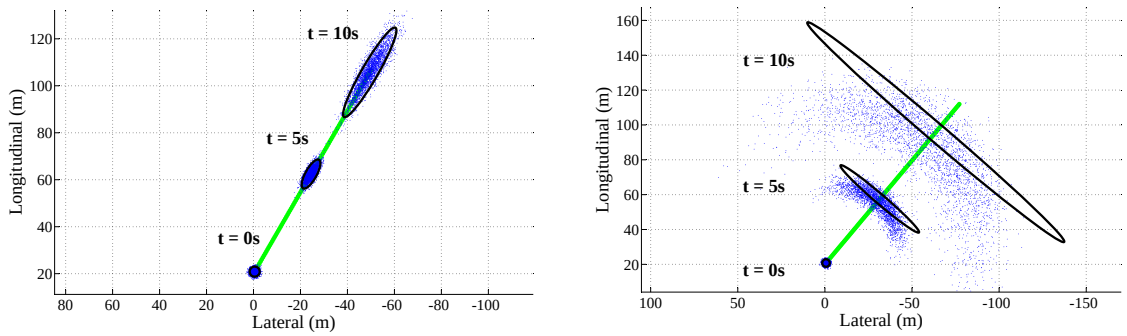

(a) Small Heading Error

(b) Large Heading Error

Figure 5.17.: Baseline uncertainty during a ten second prediction period. The blue cloud is the Monte Carlo approximation with 3000 particles. The black ellipse is the Gaussian approximation performing a linearization of the otherwise non-linear relative motion model.

As introduced in Chapter 4, for a probabilistic relative positioning approach the baseline transition probability $p\left(\mathbf{b}^k \middle| \mathbf{b}^{k-1}, \mathbf{d}_\mathrm{e}^{k-1}, \mathbf{d}_\mathrm{t}^{k-1}\right)$ is needed. This probability density results from the relative motion models presented in Equations 5.58 through 5.60. However, due to the non-linearity of these equations, Gaussian probability functions for all components of $\mathbf{b}^{k-1}$, $\mathbf{d}_\mathrm{e}^{k-1}$ and $\mathbf{d}_\mathrm{t}^{k-1}$ do not result, in general, in a Gaussian distribution of the baseline $\mathbf{b}^k$. By performing a first order linearization, an approximation to this function can be found.

Figure 5.17 shows the approximated Gaussian distribution of $p\left(\mathbf{b}^k \middle| \mathbf{b}^{k-1}, \mathbf{d}_\mathrm{e}^{k-1}, \mathbf{d}_\mathrm{t}^{k-1}\right)$ for three time steps as a black ellipse and the actual distribution computed with a Monte Carlo method as a blue cloud of points. In green, the true relative position of the target vehicle, which follows a rectilinear constant velocity motion, is shown. Figure 5.17a assumes a small uncertainty in the headings ψ_e and ψ_t, yielding a lower non-linearity in the constant velocity motion models. Consequently, the Gaussian PDF correctly approximates the true relative position distribution. In Figure 5.17b, however, the uncertainty in the heading is larger to absorb possible rotations of the target vehicle. The result is a poorer approximation of the true distribution.

The heading estimation of the ego vehicle and its associated uncertainty have a special impact on the estimate of the relative position. Relative positioning estimation through GNSS information (both by differencing absolute positions or through pseudorange differencing) is performed in an Earth-fixed coordinate system. To translate this estimation into the ego vehicle coordinate frame a rotation using the ego vehicle heading has to be performed. The uncertainty in the ego vehicle heading will translate in an uncertain rotation of one frame into the other and into an increased uncertainty in the relative position of the target vehicle. When the target vehicle is driving in front of the ego vehicle, it is the lateral coordinate of the baseline which will be mainly affected. Figure 5.18 displays the uncertainty of a 30 m and a 50 m long baseline in navigation frame

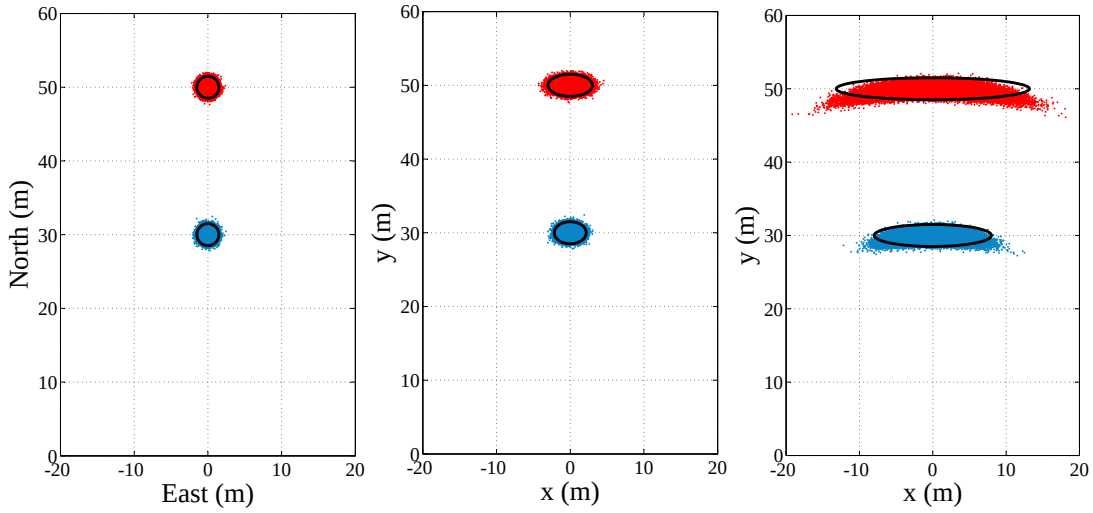

Figure 5.18.: The figures show the uncertainty of a 30 m and a 50 m baseline. The red and blue dots are the particle clouds and the black ellipses are the linearized Gaussian uncertainty. The left figure shows the baseline in navigation frame coordinates with a 1 m (1σ) error in north and east direction. After rotating this baseline into the ego vehicle frame by the ego vehicle's heading angle with an uncertainty of 1° (1σ) in the middle figure and 5° (1σ) in the right figure, the uncertainty in the baseline has increased.

(5.18a) and how a heading uncertainty of 1° (1σ) in Figure 5.18b, and of 5° (1σ) in Figure 5.18c, impact the baseline estimate in the vehicle frame. The uncertainty is widen by applying the transformation matrix in Equation 3.5. Again, due to the linearization errors, a Gaussian filter will yield an erroneous estimate for higher heading errors.

To sum up, it can be stated that the use of a more complex model as the constant acceleration from Equation 5.59 or the constant turn rate model from Equation 5.60 has a benefit when longer prediction periods need to be bridged during accelerations or turning maneuvers. This can happen, for example, during communication outage phases. All models are highly non-linear in the heading of the vehicles. Consequently, the more accurate these parameters are estimated, the less linearization error is performed by using a parametric Bayesian filter as the EKF or the UKF. In Chapter 6, the rectilinear and the constant turn rate models will be tested in a vehicle simulator.

5.6. Multisensor Fusion

The multisensor fusion approach to estimate of the relative position of a target vehicle towards an ego vehicle is based on a probabilistic filtering technique to incorporate in an optimal way the

building blocks that have been introduced in the previous sections. The direct baseline measurements from differential GNSS measurements will be fused with on-board inertial information from both, ego and target vehicles. The motion models from the previous section will be used to predict the prior distribution of the baseline between the vehicles before incorporating new measurements or when GNSS measurements are not available, as for instance in tunnels.

Figure 5.19 shows the overall multisensor fusion architecture, which follows a cascaded decentralized fusion concept. This architecture is given by two main constraints to the system. On the one hand, due to the limited communication bandwidth, the message update rate is limited to 10 Hz. On the other hand, as explained in Chapter 3, the inertial computation has to be done at a high update rate in order to maintain a low error due to skew matrix approximation and numerical integration. For this reason, the kinematic measurements from the IMU are processed independently in the *kinematic filter* and supported by the speed information from the vehicle's Controller Area Network (CAN) bus and velocity measurements from the GNSS receiver. The outputs of this filter are the speed and the acceleration in forward direction, the yaw angle or heading of the vehicle with respect to the north and the yaw rate or turn rate around the up axis.

In the case of the target vehicle, the kinematic information is packed together with the GNSS measurements of the tracked satellites into a Cooperative Awareness Message (CAM) and broadcasted over V2V communication. In the *relative positioning filter*, the kinematic information is used to predict the baseline and the differenced pseudorange measurements are used to update the baseline prediction.

The output of the filter is the estimation of the baseline and the baseline velocity. Both are two-dimensional quantities given in the ego vehicle frame. Along with both estimates, the current uncertainties in the baseline and baseline velocity are output by the upper relative positioning filters. These are given as 4×4 variance-covariance matrices that represent the Gaussian confidence ellipses around the mean baseline and baseline velocity estimate. The design of both filters is described in the following sections. Hence, the cooperative relative positioning unit can be regarded as a further ranging sensor from the driver assistance application's point of view, the same way as a radar or a stereo vision sensor.

5.6.1. Relative Positioning Filter

To track the relative position of two vehicles, a probabilistic filtering technique based on a Bayesian filter has been chosen. As presented in Chapter 3, the Kalman filter is one possible technique to implement a dynamic Bayesian filter. Here, the posterior probability distribution of the baseline and baseline velocity at time step k is given by their mean vector $\mathbf{x}^k$ and their variance covariance matrix $\mathbf{P}^k$. The state vector contains both, the estimates of the two-dimensional baseline and the

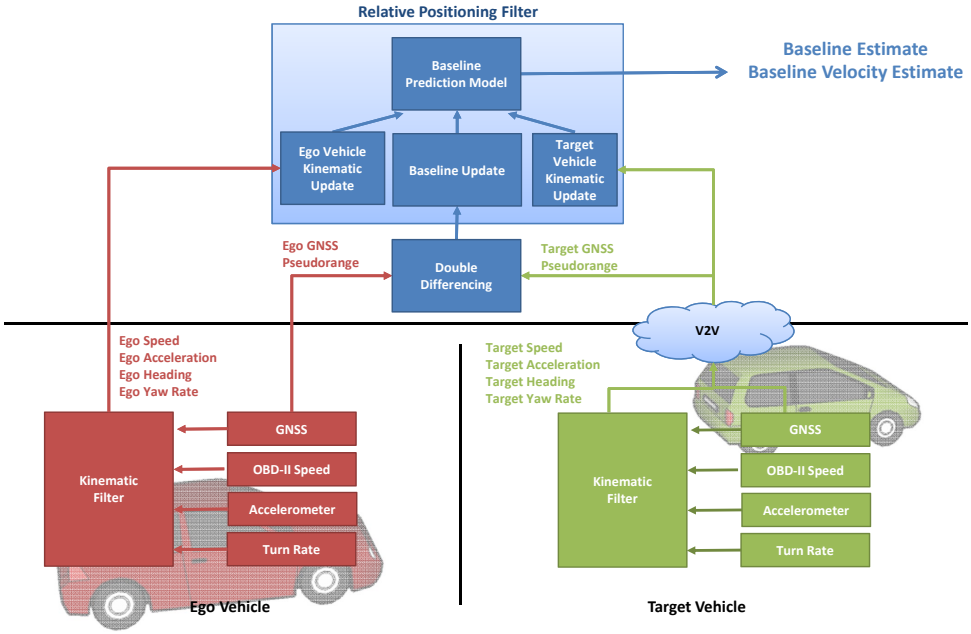

Figure 5.19.: Multisensor fusion architecture for cooperative relative position estimation. A cascaded decentralized approach solves the communication and inertial measurements constraints.

baseline velocity in vehicle coordinates according to

$$\mathbf{x}^k = \begin{bmatrix} b_\mathrm{x} & b_\mathrm{y} & \dot{b}_\mathrm{x} & \dot{b}_\mathrm{y} \end{bmatrix}^\mathsf{T}. \tag{5.63}$$

To predict the baseline in the next step a probabilistic system model based on the relative motion models presented in Section 5.5 is proposed. Depending on the motion model used to predict the prior distribution in the next step, the state vector $\mathbf{x}^k$ has to be increased with the required kinematic parameters of the target vehicle. In the case of a CTRV model, the state vector additionally includes the speed v_t, the heading ψ_t and the yaw rate $\dot{\psi}_\mathrm{t}$:

$$\mathbf{x}^k = \begin{bmatrix} b_\mathrm{x} & b_\mathrm{y} & \dot{b}_\mathrm{x} & \dot{b}_\mathrm{y} & v_\mathrm{t} & \psi_\mathrm{t} & \dot{\psi}_\mathrm{t} \end{bmatrix}^\mathsf{T}. \tag{5.64}$$

Prediction Model A probabilistic motion model will incorporate the uncertainty of the prediction step into the prior distribution. Through the probabilistic model, not only $\mathbf{x}^k$ is transformed into $\hat{\mathbf{x}}^{k+1}$, but also $\mathbf{P}^k$ is transformed into $\hat{\mathbf{P}}^{k+1}$, by incorporating the uncertainties in the kinematic estimates, such as the speed, headings or yaw rates used to predict the baseline in the next step.

The equations using the rectilinear CV motion model for prediction are

$$\begin{aligned}
b_{\mathsf{x}}^{k+1} &= b_{\mathsf{x}}^{k} + \Delta t \cdot (v_{\mathsf{t}}^{k} \cdot \sin(\psi_{\mathsf{t}}^{k} - \psi_{\mathsf{e}}^{k}) - v_{\mathsf{e}}^{k}) \\
b_{\mathsf{y}}^{k+1} &= b_{\mathsf{y}}^{k} + \Delta t \cdot (v_{\mathsf{t}}^{k} \cdot \cos(\psi_{\mathsf{t}}^{k} - \psi_{\mathsf{e}}^{k})) \\
\dot{b}_{\mathsf{x}}^{k+1} &= v_{\mathsf{t}}^{k} \cdot \sin(\psi_{\mathsf{t}}^{k} - \psi_{\mathsf{e}}^{k}) - v_{\mathsf{e}}^{k} \\
\dot{b}_{\mathsf{y}}^{k+1} &= v_{\mathsf{t}}^{k} \cdot \cos(\psi_{\mathsf{t}}^{k} - \psi_{\mathsf{e}}^{k}) \\
v_{\mathsf{t}}^{k+1} &= v_{\mathsf{t}}^{k} + n_{\mathsf{v}} \\
\psi_{\mathsf{t}}^{k+1} &= \psi_{\mathsf{t}}^{k} + \Delta t \cdot \dot{\psi}_{\mathsf{t}}^{k} \\
\dot{\psi}_{\mathsf{t}}^{k+1} &= \dot{\psi}_{\mathsf{t}}^{k} + n_{\dot{\psi}}
\end{aligned} \tag{5.65}$$

where Δt is the time step at which the Kalman filter is executed. The baseline and the baseline velocity are predicted using the rectilinear constant speed model from Equation 5.58. The speed of the target vehicle is maintained with a random walk model. The current rotation around the up axis, $\dot{\psi}^{k}$, is used to predict the heading of the vehicle ψ^{k+1} in the next time step. The kinematic estimates from the ego vehicle represent the control input:

$$\mathbf{v}^{k} = \begin{bmatrix} v_{\mathsf{e}} & \psi_{\mathsf{e}} & \dot{\psi}_{\mathsf{e}} \end{bmatrix}^{\mathsf{T}}. \tag{5.66}$$

The noise terms n in Equation 5.65 represent the prediction uncertainty in speed and turn rate due to correspondent linear and circular accelerations. These are modeled as mutually independent zero mean Gaussian distributed noise. This noise will propagate in each prediction step to the baseline and baseline velocity state estimates. The more complex movement models, CA, CTRV and CTRA have been introduced in the previous section and can be used instead of the first four lines in Equation 5.65.

Update Model Two measurement update steps are performed to the relative positioning filter. The first update is the kinematic state of the target vehicle, when a CAM is received. The kinematic estimates, i.e. speed, heading and yaw rate from target vehicle, are updated, with the measurement vector:

$$\mathbf{z}_{\mathsf{t}}^{k} = \begin{bmatrix} v_{\mathsf{t}} & \psi_{\mathsf{t}} & \dot{\psi}_{\mathsf{t}} \end{bmatrix}^{\mathsf{T}}, \tag{5.67}$$

which contains the kinematic estimates from the lower kinematic filter of the target vehicle. The update function

$$\mathbf{z}_{\mathsf{t}}^{k} = \mathbf{H} \cdot \mathbf{x}^{k} + \boldsymbol{\eta}, \tag{5.68}$$

relates the state space $\mathbf{x}^{k}$ and the measurement space $\mathbf{z}^{k}$. $\boldsymbol{\eta}$ is zero-mean Gaussian distributed noise that models the measurement likelihood. Its noise variance-covariance directly stems from the output of the lower kinematic filters as will be explained in the following section. The mea-

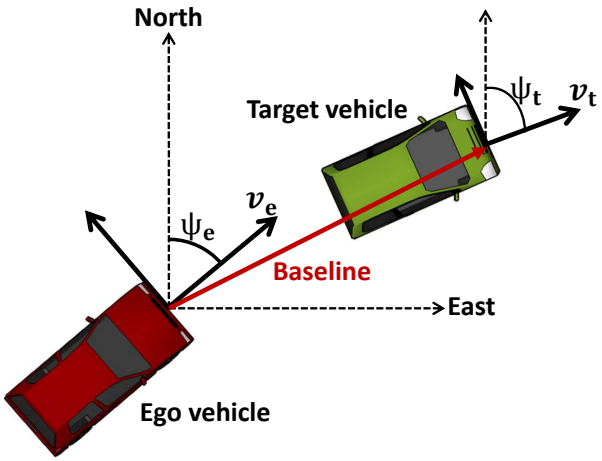

Figure 5.20.: The pseudorange double differences are measured in the local navigation coordinate frame, while the baseline is estimated in the vehicle-fixed coordinate frame. By means of the heading of the ego vehicle, the baseline is rotated from the vehicle-fixed to the local navigation frame.

surement matrix $\mathbf{H}$ is

$$\mathbf{H} = \begin{bmatrix} 0_{3\times4} & I_{3\times3} \end{bmatrix}^{\mathsf{T}}. \tag{5.69}$$

If the received CAM contains GNSS pseudorange measurements, these are differenced from the latest ego pseudoranges to form pseudorange double differences to update the baseline estimate. In a first step, the pseudorange measurements have to be synchronized as explained in Section 5.1.5. A gating procedure discards the measurements that are likely to be corrupted by multipath as will be explained in Section 5.6.4. The pseudorange double differences $\boldsymbol{\nabla\Delta\rho}$ are related to the baseline estimate $\mathbf{b}$ according to

$$\boldsymbol{\nabla\Delta\rho} = \mathbf{G}_{\mathsf{uu}} \cdot \mathbf{C}_{\mathsf{v}}^{\mathsf{n}} \cdot \mathbf{b} + \boldsymbol{\eta}_{\nabla\Delta\rho} \tag{5.70}$$

where $\mathbf{G}_{\mathsf{uu}}$ is the geometry matrix of differenced unitary vectors to the satellites, $\mathbf{C}_{\mathsf{v}}^{\mathsf{n}}$ is the coordinate transformation matrix from vehicle frame to navigation frame as in Equation 3.4. In the two-dimensional case, as depicted in Figure 5.20, this rotation is a function of the ego vehicle's heading. The observation noise $\boldsymbol{\eta}_{\nabla\Delta\rho}$ of the pseudorange double difference measurements is modeled as zero mean Gaussian noise with covariance matrices $\mathbf{R}_{\nabla\Delta\rho}$. This models the remaining error after differentiation, i.e. noise and multipath as explained in Section 5.1.3.

As it can be observed, both, the equations for prediction Equation 5.65 and GNSS update Equation 5.70 are not linear. Consequently, an approximation to the linear and Gaussian Kalman filter has to be done. A UKF implementation has been chosen for the relative positioning filter in the frame of this thesis (see Chapter 3).

5.6.2. Kinematic Filter

The lower kinematic filter estimates the speed and the heading of the vehicle, which are necessary to correctly predict the baseline vector in GNSS impaired or GNSS denied environments (see Equation 5.65). Optionally, also the acceleration and the yaw rate are estimated. For this purpose, the measurements from the IMU are coupled with the speed information from the vehicle's CAN bus and the Doppler-derived speed and heading of the GNSS receiver. GNSS heading and speed estimation are very accurate when favorable constellation, line-of-sight to the satellites and no multipath are given. The velocity vector accuracy is in the order of less than 2 $\frac{\text{cm}}{\text{s}}$ (see Section 5.3). IMU and speed sensor are on board of the vehicle and are not affected by external disturbances. Microelectromechanical Systems (MEMS)-based IMU measurements have good short-term stability if its drifts are correctly estimated. Speed sensors also have biases that require correct calibration or estimation as explained in Section 5.4.

Consequently, the GNSS Doppler related estimations of speed and heading are used to estimate the biases of the on-board IMU and speed sensors, when good GNSS signal quality is given. When this is not the case, the GNSS measurements are disconnected and dead-reckoning kinematic mode is executed.

A kinematic assumption is a valuable source of information that can be integrated into the measurement step of a Bayesian filter like another sensor measurement. Therefore, they are also called pseudo-measurements. For instance, a zero-rotation assumption tells the Bayesian filter that the vehicle is not rotating when it is at a standstill [97, 105]. The assumption of zero-rotation can safely be made, as the vehicle is not able to rotate around any of its axis without moving forward. The idea is that the information of the vehicle not being rotating makes the turn rate biases directly observable.

The estimation of the heading is especially important, since it impacts the linearity of the relative motion models as explained in Section 5.5. Further on, the proposed relative motion models of Section 5.5 also included a rotational term accounting for the uncertainty in the ego heading estimate. Hence, an accurate and reliable estimation of the ego vehicle's heading is of great importance in order to meet the lateral relative position requirements.

The guidelines, constraints and requirements on the kinematic filter can be synthesized as follows:

- The kinematic filter output vector is a random variable with a mean value and a variance-covariance matrix. These are the measurement updates for the upper relative positioning filter.
- The kinematic filter estimates forward speed, acceleration, heading and turn rate of the vehicle.
- The heading of the vehicle needs to be estimated with high accuracy, e.g. less than 0.5°

(1σ). On the one hand, to minimize the linearization error of the relative positioning filter and, on the other hand, to perform a correct rotation from the navigation frame to the ego vehicle frame.

- It is important to correctly estimate the gyroscope biases. They are directly observable at standstill, but need to be continuously estimated over time since they may change over time.
- Estimate the acceleration of the vehicle, in order to use a constant acceleration model instead of a constant velocity model. Constant acceleration models are expected to be beneficial in rural and urban areas where changes in speed occur more often and where the limited update rate of GNSS and CAN might not provide sufficient time resolution.
- The kinematic filter should be able to cope with longer GNSS outages. Outages of around 1 minute are likely to occur in urban tunnels. The longest German tunnel, the Rennsteigtunnel, has a length of nearly 8 km, needing over five minutes to drive through it.
- The processing rate of the kinematic filter is limited by the system on which it is executed. The output at which estimates are given out is limited by the maximum V2V communication update rate of 10 Hz [13].
- It is important to use an IMU based on MEMS technology. This is an important constraint, since it has an impact on the performance of the kinematic filter. MEMS IMUs are less stable and more noisy than Ring Laser Gyroscopes (RLGs) or Fiber Optic Gyroscopes (FOGs).

Two kinematic filter architectures are compared in this thesis. Both use the same sensors and pseudo-measurements to estimate the kinematic parameters speed, acceleration, heading and heading rate. Next, the basic architecture of each of both approaches is presented.

Full 3D Inertial Filter This is the standard Kalman filter for fusing GNSS and Inertial Navigation System (INS) measurements [97, 139]. Originally designed for high precision FOG IMUs, the classic algorithm is applied here to MEMS-based IMUs. In a strapdown algorithm the gyroscope is integrated to obtain the attitude of the vehicle in the navigation frame and the accelerometers are integrated once to obtain the velocity in the navigation frame (see Chapter 3). In an EKF, the errors between the strapdown attitude and velocity outputs and the GNSS velocity are estimated. In a so-called *open-loop configuration* the estimated errors are subtracted from the strapdown's algorithm output. In a *closed-loop configuration* the estimated errors are fed back to the strapdown before starting the next iteration. Thereafter, the state of the EKF is re-initialized to zero. In this work, the later configuration is chosen. The state vector is equal to:

$$\mathbf{x} = \begin{bmatrix} \delta\mathbf{v} & \delta\boldsymbol{\alpha} & \mathbf{b}_\omega & \mathbf{b}_\mathbf{a} \end{bmatrix}^\mathsf{T}, \tag{5.71}$$

including the 3-state velocity error in East-North-Up (ENU) navigation frame $\delta\mathbf{v}$, the 3-state attitude error $\delta\boldsymbol{\alpha}$, the 3-axis gyroscope bias $\mathbf{b}_\omega$ and the 3-axis accelerometer bias $\mathbf{b_a}$. The INS error propagation equations are as follow:

$$\begin{bmatrix} \delta\mathbf{v} \\ \delta\boldsymbol{\alpha} \\ \mathbf{b}_\omega \\ \mathbf{b_a} \end{bmatrix}^{k+1} = \begin{bmatrix} \mathbf{I}_3 & \Delta t \cdot \mathbf{F}_{1,2} & 0 & \Delta t \cdot \mathbf{F}_{1,4} \\ 0 & \mathbf{I}_3 & \Delta t \cdot \mathbf{F}_{2,3} & 0 \\ 0 & 0 & \mathbf{I}_3 & 0 \\ 0 & 0 & 0 & \mathbf{I}_3 \end{bmatrix} \begin{bmatrix} \delta\mathbf{v} \\ \delta\boldsymbol{\alpha} \\ \mathbf{b}_\omega \\ \mathbf{b}_a \end{bmatrix}^{k} + \begin{bmatrix} 0 & \mathbf{G}_{1,2} & 0 & 0 \\ \mathbf{G}_{2,1} & 0 & 0 & 0 \\ 0 & 0 & \mathbf{I}_3 & 0 \\ 0 & 0 & 0 & \mathbf{I}_3 \end{bmatrix} \begin{bmatrix} \boldsymbol{\nu}_\omega \\ \boldsymbol{\nu}_\mathsf{a} \\ \boldsymbol{\nu}_{\mathrm{b}_\omega} \\ \boldsymbol{\nu}_{\mathrm{b_a}} \end{bmatrix}^{k}, \tag{5.72}$$

with

$$\mathbf{F}_{1,2} = \mathbf{C}_\mathsf{v}^\mathsf{n} \cdot [\mathbf{f}\times], \tag{5.73}$$

$$\mathbf{F}_{1,4} = \mathbf{C}_\mathsf{v}^\mathsf{n} \cdot \mathbf{I}_3, \tag{5.74}$$

$$\mathbf{F}_{2,3} = -\mathbf{C}_\mathsf{v}^\mathsf{n}, \tag{5.75}$$

$$\mathbf{G}_{1,2} = \mathbf{C}_\mathsf{v}^\mathsf{n}, \tag{5.76}$$

$$\mathbf{G}_{2,1} = -\mathbf{C}_\mathsf{v}^\mathsf{n}, \tag{5.77}$$

where $\mathbf{f}$ is the current specific force measurement, $\mathbf{C}_\mathsf{v}^\mathsf{n}$ the current attitude computed by the strapdown algorithm, Δt the time interval between two IMU samples, ν_ω and ν_a are the white Gaussian noise on the gyroscopes and accelerometer. Their variances are set according to the Allan variance analysis from Section 5.2. A random walk model is used for the prediction equation of the gyroscope and accelerometer biases with ν_{b_ω} and $\nu_{\mathrm{b_a}}$ being white Gaussian noise. Its variance will be small in order to make it relatively static in accordance to its maximum temporal change according to Section 5.2.

By looking at each row of Equation 5.72, the different contributions to each of the estimated errors can be regarded. The increment in the velocity errors $\delta\mathbf{v}$ is due to the acceleration produced by the incorrect correction of the gravity vector due to an attitude error and the contribution of the accelerometer biases and the noise rotated into the navigation frame. The attitude errors $\delta\boldsymbol{\alpha}$ are accumulated due to the biases in the turn rate sensors and the noise of the turn rate sensors into navigation frame. These are simplified equations of the complete inertial error-state Kalman filter that includes the contributions due to imperfect knowledge of the gravity, Earth turn rate, Coriolis force, incorrect assumptions of the shape of the Earth etc. [98].

The error-state Kalman filter is updated using the GNSS speed $\mathbf{v}_{\mathrm{GNSS}}$ expressed in ENU coordinates.

An alternative would be to perform a tightly coupled integration, where the Doppler measurements from the GNSS receiver are used in the update step (see Figure 3.6b). The latter approach has the advantage that updates to the Kalman filter are also available when less than for satellites are tracked by the GNSS receiver. The filter state is updated using the following equation:

$$\hat{\mathbf{v}} - \mathbf{v}_{\text{GNSS}} = \begin{bmatrix} \mathbf{I}_3 & \mathbf{0}_{3\times 9} \end{bmatrix} \cdot \mathbf{x} + \boldsymbol{\eta}_{\text{v}_{\text{GNSS}}}, \tag{5.78}$$

where $\hat{\mathbf{v}}$ is the computed velocity from the strapdown algorithm and $\boldsymbol{\eta}_{\text{v}_{\text{GNSS}}}$ is the GNSS velocity error which is assumed to be white and Gaussian distributed. Its covariance matrix is output by the least-squares or Kalman filter used to compute the GNSS velocity out of the GNSS Doppler measurements and will include the uncertainties given by the geometry and the quality of the raw measurements. If GNSS measurements are not available, the CAN speedometer readings, v_{CAN}, are used to update the filter velocity error. This is done by creating a velocity vector in vehicle frame, with its x-axis value equal to the CAN speed and the y- and z-axis values equal to zero. The assumption of the vehicle not moving side- nor up-wards is known as non-holonomic assumption. The update equation is:

$$\hat{\mathbf{v}} - \mathbf{C}_{\text{v}}^{\text{n}} \cdot \begin{bmatrix} v_{\text{CAN}} & 0 & 0 \end{bmatrix}^{\text{T}} = \begin{bmatrix} \mathbf{I}_3 & \mathbf{0}_{3\times 9} \end{bmatrix} \cdot \mathbf{x} + \boldsymbol{\eta}_{\text{v}_{\text{CAN}}}, \tag{5.79}$$

where the velocity vector containing the CAN speedometer value is rotated from the vehicle frame to the navigation frame and subtracted from the current velocity computed by the strapdown $\hat{\mathbf{v}}$. The resulting vector represents a measurement update of the first three states of the Kalman filter. The measurement error $\boldsymbol{\eta}_{\text{v}_{\text{CAN}}}$ is modeled as white Gaussian noise with variance-covariance matrix equal to:

$$\mathbf{C}_{\text{v}}^{\text{n}} \cdot \mathbf{R}_{\text{v}_{\text{CAN}}} \cdot \mathbf{C}_{\text{v}}^{\text{n}\text{T}}, \tag{5.80}$$

where $\mathbf{R}_{\text{v}_{\text{CAN}}}$ is the variance-covariance matrix containing in its diagonal the variance of the CAN speedometer and the uncertainties associated to the non-holonomic constraints.

As an information to observe the gyroscope biases a zero-rotation assumption is implemented in the filter. This update is executed when the speed of the vehicle is below 0.1 $\frac{\text{m}}{\text{s}}$, which is regarded as a safe threshold to assume that the vehicle is not rotating. The update equation is:

$$\boldsymbol{\omega} = \begin{bmatrix} \mathbf{0}_{3\times 6} & \mathbf{I}_3 & \mathbf{0}_{3\times 3} \end{bmatrix} \cdot \mathbf{x} + \boldsymbol{\eta}_{\text{nra}}, \tag{5.81}$$

where $\boldsymbol{\omega}$ is the turn rate measurement from the gyroscope and $\boldsymbol{\eta}_{\text{nra}}$ is the noise on the zero-rotation assumption. Its variance is chosen equal to the gyroscope measurement error variance. In order to achieve a fast convergence at the beginning, but still immunity to spurious gyroscope measurements when the vehicle starts moving, a gating procedure of gyroscope measurements is implemented using the Mahalanobis distance including the current estimate covariance of the gyroscope biases. The Mahalanobis distance is later discussed in this chapter (see Section 5.6.4).

Even estimating correctly the gyroscope biases, the roll and pitch attitude angle errors will grow steadily over time due to the integration of noise. Here, the heading measurements from GNSS do not help, since roll and pitch remain unobserved. For this reason a zero-acceleration assumption is implemented. The key idea is that, when the vehicle is not accelerating it only senses the gravity on its three axis. The update equation is as follows:

$$\begin{bmatrix} \hat{\phi} \\ \hat{\theta} \end{bmatrix} - \begin{bmatrix} \arcsin \frac{f_y}{g} \\ -\arcsin \frac{f_x}{g} \end{bmatrix} = \begin{bmatrix} \mathbf{0}_{2\times 3} & \mathbf{I}_2 & \mathbf{0}_{2\times 7} \end{bmatrix} \cdot \mathbf{x} + \boldsymbol{\eta}_{\mathsf{zaa}}, \tag{5.82}$$

where $\hat{\phi}$ and $\hat{\theta}$ are the roll and pitch angle computed by the strapdown algorithm and $\boldsymbol{\eta}_{\mathsf{zaa}}$ is the zero-acceleration measurement noise. The variance of the noise should be high enough to include the sensor noise in the accelerometers, errors in the magnitude of the gravity and attitude errors due to biases in the accelerometers. An accelerometer bias of $0.1\,\frac{\mathsf{m}}{\mathsf{s}^2}$ produces an attitude error of 0.6 degree by using this technique. A time window of three seconds is used to detect that the vehicle is not accelerating by averaging the measurements from the accelerometers and comparing the norm to the magnitude of the gravity vector. The zero-acceleration assumption is applied, if the difference falls below a predefined threshold.

Outside the error-state Kalman filter, the IMU sensor readings are corrected by the current estimations of the biases $\mathbf{b}_\omega$ and $\mathbf{b}_a$ prior to the strapdown computation (see Figure 3.6a). Then, the output of the strapdown algorithm, $\hat{\mathbf{v}}$ and $\hat{\boldsymbol{\alpha}}$ is corrected with the estimated velocity and attitude errors, $\delta\mathbf{v}$ and $\delta\boldsymbol{\alpha}$. Thus, the relevant output of this filter, namely longitudinal speed and acceleration, heading and planar turn rate, are found as follows:

$$v = \|\hat{\mathbf{v}} - \delta\mathbf{v}\|, \tag{5.83}$$

$$a = [\mathbf{C}_{\mathsf{v}}^{\mathsf{n}} \cdot (\mathbf{f} - \mathbf{b}_{\mathsf{a}})]_{\mathsf{x,y}}\,, \tag{5.84}$$

$$\psi = [\hat{\boldsymbol{\alpha}} - \delta\boldsymbol{\alpha}]_{\psi}\,, \tag{5.85}$$

$$\dot{\psi} = \mathbf{C}_{\mathsf{v}}^{\mathsf{n}} \cdot (\boldsymbol{\omega} - \mathbf{b}_\omega). \tag{5.86}$$

The longitudinal speed v is the norm of the velocity output by the strapdown $\hat{\mathbf{v}}$ corrected by the estimated velocity error $\delta\mathbf{v}$ (see Equation 5.83). The longitudinal acceleration a is the planar component of the acceleration in the navigation frame (see Equation 5.84). The heading estimate is the yaw angle from the attitude out of the strapdown algorithm $\hat{\boldsymbol{\alpha}}$ corrected by the attitude error estimation $\delta\boldsymbol{\alpha}$ (see Equation 5.85). Finally, the vehicle frame turn rates $\boldsymbol{\omega}$ are corrected by the bias $\mathbf{b}_\omega$ and transformed to the navigation frame with $\mathbf{C}_{\mathsf{v}}^{\mathsf{n}}$ to compute the heading rate $\dot{\psi}$ (see Equation 5.86).

The advantage of the filter is the estimation of the acceleration out of the IMU measurements. This however involves accurate attitude estimation in order to subtract the high-magnitude gravity vector. Small errors in the attitude estimation will cause large velocity errors. Therefore, correct

estimation of turn rate biases is of uttermost importance.

Full Bayesian Filter This is a completely Bayesian filter to estimate the 3-axis attitude and turn rate, the longitudinal speed and acceleration of the vehicle and the accelerometer and gyroscope biases. Instead of integrating the accelerometer and gyroscope measurements, this approach evaluates how the sensor measurements fit the current vehicle state by updating the state in a Bayesian way. The state vector is

$$\mathbf{x} = \begin{bmatrix} v & a & \phi & \theta & \psi & \dot{\phi} & \dot{\theta} & \dot{\psi} & b_{\omega,\mathrm{x}} & b_{\omega,\mathrm{y}} & b_{\omega,\mathrm{z}} & b_{\mathrm{a,x}} & b_{\mathrm{a,y}} & b_{\mathrm{a,z}} \end{bmatrix}^{\mathsf{T}}, \tag{5.87}$$

where v is the longitudinal speed, a the longitudinal acceleration, ϕ, θ and ψ the Euler angles that transform the vehicle frame to the navigation frame, $\dot{\phi}$, $\dot{\theta}$ and $\dot{\psi}$ the turn rates around the vehicle frame axis and $b_{\omega,\mathrm{x}}$, $b_{\omega,\mathrm{y}}$, $b_{\omega,\mathrm{z}}$ and $b_{\mathrm{a,x}}$, $b_{\mathrm{a,y}}$, $b_{\mathrm{a,z}}$ the three gyroscope and accelerometer biases respectively. Speed and attitude angles are predicted using the previous estimation and the current acceleration and turn rates, respectively, plus noise to model the uncertainty in the prediction. As in the previous filters, a random walk model is used to predict the gyroscope and accelerometer biases of the next time step.

The measurements from accelerometer, gyroscope, CAN speed and GNSS speed and heading, will be used to update the estimates in a Bayesian way. The update equations for the accelerometer are:

$$a_{\mathsf{x}} = a\cos\theta \quad - g\sin\theta \quad + b_{\mathrm{a,x}} \quad + \eta_{\mathsf{ax}}, \tag{5.88}$$

$$a_{\mathsf{y}} = \quad g\sin\phi\cos\theta \quad + v\cdot\dot{\psi}\cos\phi \quad + b_{\mathrm{a,y}} \quad + \eta_{\mathsf{ay}}, \tag{5.89}$$

$$a_{\mathsf{z}} = a\sin\theta \quad + g\cos\phi\cos\theta \quad - v\cdot\dot{\psi}\sin\phi \quad + b_{\mathrm{a,z}} \quad + \eta_{\mathsf{az}}, \tag{5.90}$$

where the accelerometer measurements a_{x}, a_{y} and a_{z} are related to the attitude ϕ, θ and the speed v and acceleration a of the vehicle. The right side of all three equations is written column-wise to highlight the contributions due to the longitudinal acceleration of the vehicle, the gravity and the lateral centripetal force when driving in bends. η_{a} is white Gaussian noise on the accelerometers according to Section 5.2. These update equations include so-called non-holonomic constraints regarding the movement of the vehicle [200]. They assume that the vehicle is only moving along its forward axis and that it is driving on a planar surface. The update equations for the gyroscopes are:

$$\omega_{\mathsf{x}} = \dot{\phi} \quad - \dot{\psi}\sin\theta \quad + b_{\omega\mathrm{x}} \quad + \eta_{\omega\mathrm{x}}, \tag{5.91}$$

$$\omega_{\mathsf{y}} = \dot{\theta}\cos\phi \quad + \dot{\psi}\sin\phi\cos\theta \quad + b_{\omega\mathrm{y}} \quad + \eta_{\omega\mathrm{y}}, \tag{5.92}$$

$$\omega_{\mathsf{z}} = \dot{\psi}\cos\theta\cos\phi \quad - \dot{\theta}\sin\phi \quad + b_{\omega\mathrm{z}} \quad + \eta_{\omega\mathrm{z}}, \tag{5.93}$$

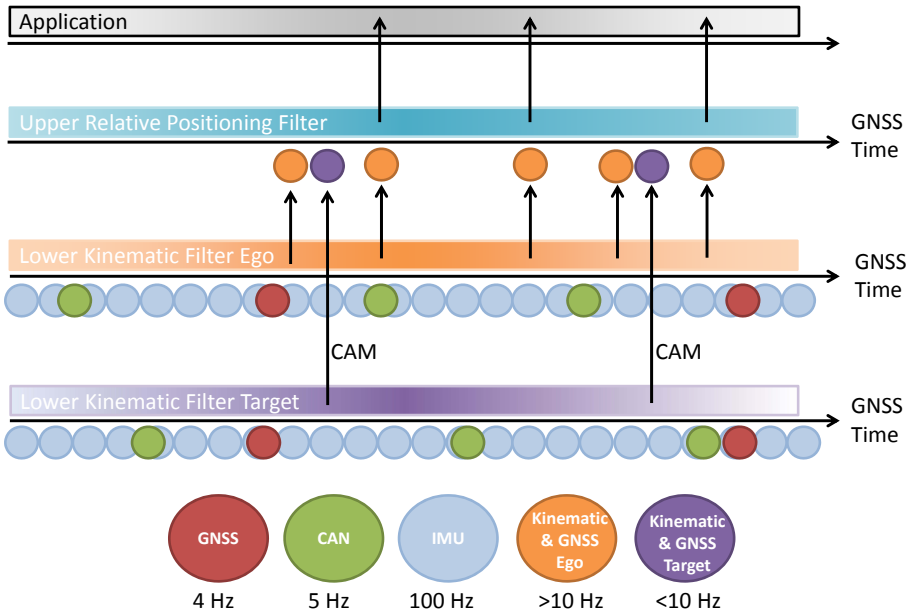

Figure 5.21.: The figure shows a schematic representation of the scheduling mechanism in the upper and lower filter in ego and target vehicle.

where the gyroscope measurements ω_x, ω_y and ω_z are related to the attitude angles ϕ, θ, the turn rates in navigation frame $\dot{\phi}$, $\dot{\theta}$ and $\dot{\psi}$ and the gyroscope biases $b_{\omega x}$, $b_{\omega y}$ and $b_{\omega z}$. η_ω are the gyroscope measurement noise components according to Section 5.2.

The update equations for the speed and the heading map one to one the state to the measurement. At standstill the zero-rotation assumption is applied by updating the turn rates $\dot{\phi}$, $\dot{\theta}$ and $\dot{\psi}$ with values of zero.

In Chapter 6, both kinematic filters are tested in a vehicle simulator. It is part of the analysis to evaluate the performance of each implementation regarding the estimation of the speed, acceleration, heading and heading rate of the vehicles, especially when GNSS velocity measurements are not available or they are corrupted while driving under dense tree canopy or through urban canyons. Special attention is also put on the estimation of the biases, which are hidden states that are observable during standstill phases of the vehicle or partly observable while driving.

5.6.3. Synchronization

When designing a cooperative system timing and synchronization are crucial issues. Vehicles exchange data that need to be measured in the same time scale in order to be correctly incorporated in the estimation filters. Using GNSS-time has the advantage that it is a completely synchronized system. In GPS, for example, ground segment, satellites and ground receivers are all synchronized to GPS time, which is an atomic coordinate time standard [28]. When solving its position, the

receiver is automatically synchronized to GPS time with nanosecond precision.

However, the time instants when the position solutions of two receivers are made, might be offset by a few milliseconds. A time offset of 16 ms creates a relative position error of about 0.8 m for two vehicles driving in opposite directions on a rural road at 100 $\frac{\text{km}}{\text{h}}$! For this reason, in this work it was proposed to synchronize the raw GNSS measurements when forming pseudorange double differences as explained in Section 5.1.5. The analysis is completed here for the fusion with other sensors.

The timing schema for the sensor fusion architecture is shown in Figure 5.21. For the kinematic filters in each of the vehicles (orange and violet squares), the on-board sensors, namely the IMU (blue circle) and the speed sensor (green circle), are required to be accurately synchronized to GPS time. This means that when a speed, acceleration or turn rate measurement sample is taken by the sensor, this is immediately related to GPS time. These measurements are incorporated into the kinematic filter adapting the prediction step according to the time to the last measurement update. At regular intervals the kinematic filter in the target vehicle outputs its current timestamped kinematic estimate to input it into a CAM (violet circles). If a new GNSS measurement is available (red circle), this is also input into the CAM. At the relative positioning filter (turquoise square), the ego vehicle kinematic state (orange circle) is used to predict the current states prior to incorporating the target measurements of the arrived CAM. The ego vehicle kinematic state is also used to predict the baseline states when the application (grey) requires a new relative position estimate.

The communication between the vehicles requires some time, including reading sensor values, composing the CAM, accessing the channel, coding and modulation, transmission and the corresponding actions at the receiver side. According to [201], the mean time to actually access the channel is 1 ms, while [202] presents access times of as high as 10 ms in dense traffic scenarios. The actual transmission time and coding-decoding times are small when compared to these values. The communication over the CAN bus inside the vehicle is also below 10 ms [203]. For the worst case, the assumption of a 30 ms transmission latency is sufficient. Consequently, the relative positioning filter might lag for the short period of the communication delay as seen from the application.

5.6.4. Pseudorange Measurement Quality and Gating

The previously described multisensor fusion approach for relative positioning uses GNSS double differenced pseudorange measurements to update the baseline estimate. This update is done according to the likelihood of the measurements, i.e. how good they match the prior distribution given by the prediction step. Unlike on-board sensors, as for instance speedometer or IMU, where the measurement error statistic is stationary, GNSS measurements have varying statistical properties. Depending on the signal reception and the signal strength at the antenna the amount

of noise on the double differences will vary. Up to some extend, the varying quality of the GNSS measurements can be, and will be, assessed by taking the carrier-to-noise measurements from the GNSS receiver. Unfortunately, multipath errors are difficult to detect, as they do not have an immediate impact on the carrier-to-noise estimate, and can produce large biases in the order of tens of meters [38].

According to D. Hawkins "an outlier is an observation which deviates so much from the other observations as to arouse suspicions that it was generated by a different mechanism" [204]. The approach followed in this thesis to provide certain robustness in the relative position estimate is to discard measurements that are not likely to fit the prediction. This is similar to probabilistic data association as used, for instance, for associating observations to targets in radar sensors and avoid incorrect associations [147]. For this approach, a gate width or tolerance band is defined to prevent faulty measurements to corrupt the estimate. One straightforward possibility is to use a fixed value for the gate width, as for instance in [205]. In this thesis, an alternative method was followed, where the gate width changes over time according to the a priori knowledge, based on the Mahalanobis distance between the predicted and the measured pseudorange double differences. In general, the Mahalanobis distance differs from the Euclidean distance in that it takes the correlation between the measurements into account [206]. The Euclidean distance d_e between the double difference pseudorange measurements $\boldsymbol{\nabla\Delta\rho}$ and the predicted double difference pseudorange measurements $\mathbf{G}_{uu}\cdot\mathbf{C}_v^n\cdot\hat{\mathbf{b}}$, with $\mathbf{G}_{uu}$ being the differenced unitary matrix from Equation 5.25 and $\mathbf{C}_v^n$ the rotation matrix from the vehicle frame to the local navigation frame, is

$$d_e = \sqrt{(\boldsymbol{\nabla\Delta\rho} - \mathbf{G}_{uu}\cdot\mathbf{C}_v^n\cdot\hat{\mathbf{b}})^T(\boldsymbol{\nabla\Delta\rho} - \mathbf{G}_{uu}\cdot\mathbf{C}_v^n\cdot\hat{\mathbf{b}})}. \tag{5.94}$$

On the other hand the Mahalanobis distance d_m is given by:

$$d_m = \sqrt{(\boldsymbol{\nabla\Delta\rho} - \mathbf{G}_{uu}\cdot\mathbf{C}_v^n\cdot\hat{\mathbf{b}})^T((\mathbf{G}_{uu}\cdot\mathbf{C}_v^n)^T\mathbf{P}(\mathbf{G}_{uu}\cdot\mathbf{C}_v^n))^{-1}(\boldsymbol{\nabla\Delta\rho} - \mathbf{G}_{uu}\cdot\mathbf{C}_v^n\cdot\hat{\mathbf{b}})}. \tag{5.95}$$

The Mahalanobis distance does not only take the mean values of measurements and state estimates into account, but also the uncertainty in the prediction and the correlation among the measurements. It can be seen that the a priori uncertainty $\mathbf{P}$ enters in the distance computation. Observations with a Mahalanobis distance above a predefined threshold will be discarded. Common practice reveals that a value of three for the threshold is common [139]. In Chapter 7, the performance of the gating approach in multipath corrupted environments will be analyzed. The same scenario will be run activating and deactivating the gating or using different gate widths for the Mahalanobis distance.

Similarly, GNSS derived measurements, as for instance speed and heading, will also be affected by

an incomplete satellite constellation, low carrier-to-noise values or the occurrence of multipath. In the same way as above, the Mahalanobis distance to the current state estimate is used to detect outliers in the GNSS speed and heading measurements and avoiding the update with a corrupted measurement. When measurements get rejected, the speed is updated with measurements from the CAN bus speedometer and the heading angle is obtained on the basis of the integration of the gyroscopes.

5.7. Impact of Communication

A cooperative approach for relative positioning of vehicles relies on the availability of a V2V communication channel to exchange information between vehicles. Its performance will, consequently, depend on the reliability of the communication link. An overview on the challenges regarding the communication link, the expected performance and related work is given in this section. First, a brief analysis on the required communication load for the proposed cooperative approach is presented.

5.7.1. Communication Load

The amount of transmitted data depends upon the numerical values, the type of data, the limit and the precision of each parameter. Additionally, the used encoding will translate the values to an array of bits. The current V2V communication standard specifies that "encoding and decoding shall be done according to ASN.1 unaligned packet encoding rules" [13]. ASN.1 stands for Abstract Syntax Notation One, and is a standard developed by the International Telecommunication Union (ITU) Telecommunication Standardization Sector that describes the rules to encode and decode data in telecommunications and computer networks.

With this encoding, and considering all mandatory fields and the most prominent optional fields, the current length of CAM messages can be situated between 200 and 500 Byte [207, 208]. This is considered to include, besides the identification and the position of the vehicle, the kinematic filter output, i.e. speed, acceleration, heading, and yaw rate, along with its uncertainties.

The proposed technique for relative positioning of vehicles on behalf of pseudorange differencing requires that the vehicles exchange the pseudoranges measured towards the satellites along with the corresponding satellite identification and the measured carrier-to-noise value. For this analysis, a simple encoding strategy is assumed. Pseudorange measurements are floating point values that need to be traduced to integer values and, finally, to an array of bytes. The pseudorange measurements are rounded to the next mm and encoded with 5 Byte. The satellite number is encoded with 1 Byte to account for different constellations and geostationary satellites. The

Table 5.3.: Communication Load

Relative Positioning Approach	**Communication Load**
CAM with ASN.1 PER	200 - 500 Byte
Pseudoranges (GPS)	95 Byte
Pseudoranges (GPS + GLONASS)	165 Byte
Pseudoranges (GPS + GLONASS + Galileo)	277 Byte

carrier-to-noise ratio is an integer value ranging from 0 dBHz to 50 dBHz, which, thus, can be encoded with 1 Byte.

With the current GPS constellation consisting of 32 satellites, a receiver on the ground at medium latitudes is able to track a maximum of 12 GPS satellites with an elevation mask of 5° [209]. The usage of further GNSS satellites from other constellations, as for instance GLONASS or Galileo, or even geostationary satellites from augmentation systems, as for instance, EGNOS, would increase this number [38]. For this analysis, a mean of 12 visible satellites per constellation is assumed.

The pseudoranges are assumed to be extrapolated by the clock offset to the nearest point in the common time grid. This timestamp has to be exchanged in order to precisely align the pseudoranges in different cars. The time of week consists of the seconds passed since midnight Saturday/Sunday GPS time, i.e. a number increasing from 0 to 604 800. A precision of tens of milliseconds is needed to unambiguously mark the measurement on the time scale. Hence, 4 Byte are sufficient to encode the timestamp.

Table 5.3 shows the amount of data needed to exchange all measured pseudoranges for each of the constellations. The typical size of a CAM message has been added for comparison. The exchange of GPS pseudoranges adds 95 Byte to the original CAM. Including further constellations, into the system might double the size of the original CAM. The transmission of all pseudorange measurements for GPS, GLONASS and Galileo using this simple encoding strategy accounts for a maximum of 277 Byte. This analysis proves that the exchange of pseudorange measurements does not require an extreme amount of communication resources, but could, in principle, be exchanged using the available V2V communication technology.

5.7.2. Communication Link Performance

The cooperative relative positioning system proposed in this thesis relies on the exchange of CAMs. These messages are single-hop messages that are transmitted in broadcast mode to all neighbors and which do not require a network routing strategy to be disseminated [210]. Hence, only the Physical and the Medium Access Layer of the Open Systems Interconnection (OSI) model [211] are required to transmit and receive CAMs.

Physical Layer CAMs are transmitted using the control channel, which is the channel reserved for safety-critical information in the ITS-G5 standard. The communication technology behind V2V is similar to the IEEE802.11 standard used for wireless local area networks, commonly known as WiFi. In Europe, V2V works in the 5.9 GHz communication band, where besides the control channel other five 10 MHz service channels are allocated for Intelligent Transportation Systems (ITS) communication [11]. The default data rate on the physical layer is 6 Mbps, with the possibility of transmitting at higher rates by adapting the modulation and the coding rate. The transmit power is limited to 33 dBm Equivalent Isotropic Radiated Power (EIRP). This will limit the maximum communication range achievable for cooperative relative positioning. Besides of the transmit power, the range will depend on the transmit and receive antenna and on the propagation conditions. While 2 km communication range has been achieved [41], typical communication ranges are expected to be between 500 m and 1000 m [212]. However, messages from neighboring vehicles might still not be received due to physical effects on the wireless channel. Shadowing, blocking, multipath induced fading, Doppler and interference result in some messages being incorrectly received. Field tests have shown that packet error rates of around 50 % can be expected at a range of 300 m [213]. Other work states average V2V availability of 90 % at 200 m and 50 % at 1000 m [131].

However, the probability of packet reception is not a suited metric to quantify awareness in vehicular ad-hoc networks, since only an average value is given and the time distribution of the packet drops remains hidden [214]. Consecutive packet drops, so-called bursts, are specially harmful for mutual awareness, since no measurement updates are received from the target vehicle and, hence, the driver assistance application has to rely solely on a predicted relative position with increasing uncertainty. According to real-world experiments in [215], consecutive package drops of up to 15 messages (1.5 s) occur with a probability of more than 0.1 % in highway environments.

Medium Access Layer The medium access protocol used in V2V communication is Carrier Sense Multiple Access with Collision Avoidance (CSMA-CA) [10]. The key concept of this protocol is that any station, prior transmitting a packet, listens to the channel to determine if it is free. In that case it starts transmitting its packet. However, the problem of CSMA-CA is that, when the channel load is high, the likelihood of packets colliding increases [207]. One possible cause is that two nearby stations sense the channels as idle and start transmitting at the same time and, thus, causing a packet collision. A further reason is that a station is not able to detect a transmission that is going on at a distant location and starts transmitting itself causing a collision at the receiver. This is known as hidden terminal problem and is the cause of most of the collision in vehicular networks [202].

The Update Delay, by quantifying the time between two successful message receptions from the same transmitter, is a suited metric for beacon based ad-hoc networks providing a measure of

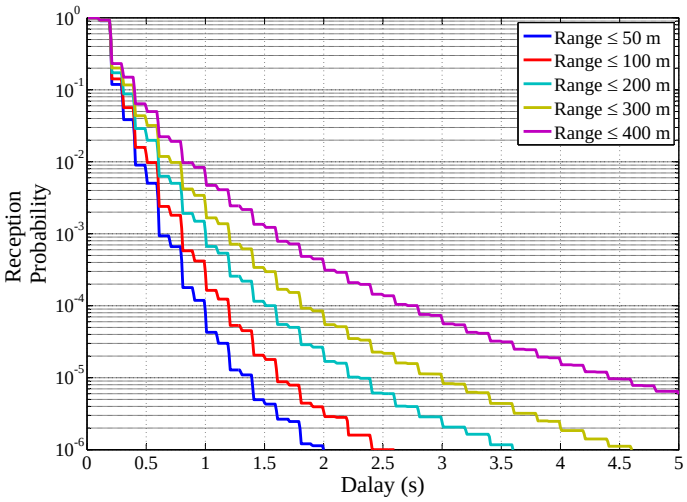

Figure 5.22.: The figure shows the Update Delay curves for a highway scenario with five lanes in each direction. The repetition rate used by the vehicles complies with the trigger conditions described in the standard [13].

the situational awareness [216]. Figure 5.22 displays the probability of reaching a certain Update Delay while driving on a highway with medium traffic consisting of five lanes in each direction. In this environment, for instance, with a probability of 3×10^{-4} a message from a vehicle driving 100 m in front does not reach the ego vehicle in 1 s.

Hence, a reliable prediction model of the baseline is important to be able to bridge the instants in which no GNSS measurements nor kinematic information from the target vehicle is available at the ego vehicle. Especially, taking into account that the driver assistance application requires data continuously. In this regard, "unconsciousness" intervals of a few seconds due to Physical and Medium Access layer should be considered. With this in mind, the following chapters will evaluate the prediction performance of the proposed relative motion models of Section 5.5 and the prediction capability of the cooperative relative positioning approach in terms of accuracy, availability and reliability.

5.8. Summary

This chapter has presented and discussed different components that are used for probabilistic relative positioning of vehicles. An analysis on the errors that affect GNSS yielded that the pseudorange measurements towards the satellites can be biased by an amount of several meters. Some of the error components are common to receivers close by, and, hence, could be eliminated through differencing. Two approaches for estimating the relative position between two receivers using GNSS have been compared to each other. The classic approach of differencing the absolute positions computed by each of the receivers yields a biased relative position estimate when the

receivers do not use the same satellites or they incorporate their measurements in a different way. By exchanging the pseudoranges towards the satellites, only the measurements common to both receivers are used and, thus, an unbiased estimate of the relative position is obtained. The price is a slight increase in the noise and a lower availability if only a small number of satellites is in view. A new technique for synchronizing GNSS measurements taken at different receivers in different vehicles based on Doppler extrapolation has been proposed.

A characterization of MEMS inertial sensors consisting of accelerometers and gyroscopes was performed. The magnitude of the gyroscope biases requires that they are correctly taken into account in the Bayesian filter by tracking their value over time. The sensor noise was proved to be white and Gaussian.

Further on, static measurements indicated that GNSS-derived velocity is accurate up to a few $\frac{\text{cm}}{\text{s}}$ under good GNSS coverage. However, satellite signal blockage and multipath can cause errors up to $1\,\frac{\text{m}}{\text{s}}$. These situations can be bridged by using a correctly calibrated speedometer, at the expense of having correlated quantization noise.

Relative motion models that predict the baseline in the absence of GNSS updates have been presented. It is suggested to use second-order models, such as the constant acceleration and constant turn rate model, in order to keep a small relative positioning error when the message update rate between the vehicles is below 10 Hz. It is important to keep the heading error below $1°$, in order to have a small error due to the linearization of the system model and to decrease the lateral error of the baseline vector when the target vehicle drives at higher distance. The architecture of a two step sensor fusion filter for relative positioning has been proposed, consisting of an upper relative positioning filter and a lower kinematic filter in each of the vehicles.

Last but no least, an analysis on the required V2V communication resources revealed that the amount of additional data for cooperative relative position is a fraction of the current CAM size. A review of the Update Delay metric showed that communication outages between vehicles of one second have to be bridged by the relative positioning filter in real-world environments.

Chapter 6.

Verification under Controlled Conditions

The system and sensor models presented in the previous chapter aim at describing the vehicular environment to get close to the real-world. However, due to the high complexity of each single system, a mismatch between models and real-world is likely to occur. The sensor models for speed sensors and inertial measurement unit assume Gaussian errors and time correlated biases. GNSS pseudorange, Doppler and carrier phase measurements are, as well, assumed to be disturbed by additive white Gaussian noise. The rectilinear and constant turn rate models for the vehicle dynamics are simplified models, whereas the movement of real-world road vehicles might deviate from this behavior.

The next two sections present the results of controlled tests performed using simulations. First, a MATLAB simulation environment is used to create the sensor outputs for two vehicles driving in different configurations. The second section evaluates the GNSS measurements and their impact on the baseline estimation by using a GNSS constellation simulator that generates real GNSS signals which are fed into real GNSS receivers.

6.1. Cooperative Relative Position Simulator

Before testing the cooperative relative positioning system presented in the previous chapter in real-world environments with real-world sensors in real cars, a simulation environment is used for testing and validating the multisensor fusion approach. A simulator is used to generate sensor log files of a controlled environment where two vehicles drive different maneuvers, where all on-board sensors and movement dynamics are modeled. The simulator log files are input into the cooperative relative position filter for the sake of its validation. The proposed approach is verified by checking that the states are correctly estimated and tracked in time by comparing them to the true values given by the simulator. By using a sensor simulation environment, it is possible to have a reference of all estimated parameters, against which the estimation can be compared to. As it will be explained in Chapter 7, the real-world experiments will lack a correct truth for many of the values, as for instance, speed, heading or absolute positions of vehicles or satellites.

From an estimation perspective, the multisensor fusion will perform optimal if the prediction equations exactly model the movement of the simulated vehicles and the measurement likelihoods exactly model the errors on the simulated sensors. In this sense, the simulations will not be able to quantify the performance of the proposed approaches. However, the usage of a simulator has multiple interesting advantages. First of all the mentioned availability of a true value for all states. Next, the possibility of performing multiple realizations of the same experiment and in this way obtaining a statistical evaluation of the performance of the used estimators. In a simulated environment, multiple parameters can be accurately tuned, which are otherwise not controllable in a real-world environment. For instance, the following aspects could be addressed by using a simulated environment:

- Sensor models: different noise levels in speed and inertial sensors can be modeled and it is possible to model ideal noise-free sensors. The impact of quantization noise on the speed sensor can be addressed.
- Inertial Measurement Unit (IMU) misalignment: ideally the IMU on-board of each vehicle would be perfectly aligned with the body frame. The impact of a misalignment between sensor and body frame or the effect of the lever arm between IMU and GNSS antenna can be studied.
- System synchronization: the processing units on-board of each vehicle are not synchronized and run on their own clocks. The impact of not having a fully synchronized system can be inspected.
- Time discretization: the impact of having a time discretized system can be investigated, specially in strong vehicle dynamics, such as high longitudinal and lateral accelerations.
- Observability: Some states are not observable or are only weakly observable. This is the case, for instance, for the gyroscope and accelerometer biases, the attitude of the vehicle or the heading at standstill. How this states can be made observable and how much time it requires can be inspected by using a simulated environment.
- System non-linearity: The impact of non-linearity in the system equations can be analyzed.

Some of these aspects will be regarded in the scope of this work. The Cooperative Relative Position Simulator is composed of two independent and cascaded components: the *True Value Generator* and the *Sensor Simulator*. In Figure 6.1, the two components are displayed. The True Value Generator emulates the vehicle state in ego and target vehicle in a predefined scenario. The vehicle state, in the scope of this work, is reduced to the following values:

- Position $\mathbf{p}$ of the vehicle expressed in local navigation coordinates.
- Attitude $\boldsymbol{\alpha}$ of the vehicle given by its three Euler angles which transform the vehicle coordinate frame into the local navigation coordinate frame.

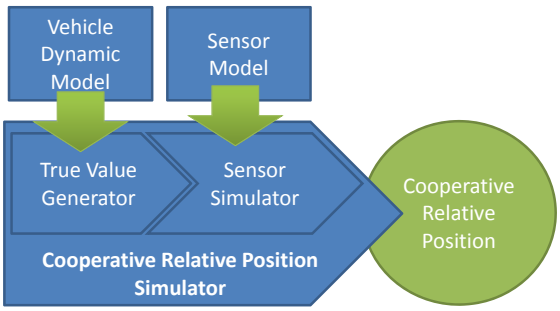

Figure 6.1.: The Cooperative Relative Position Simulator emulates the sensors at ego and target vehicle that are the input for the Cooperative Relative Positioning algorithms. It consists of two steps: first, the True Value Generator creates the dynamic state of both vehicles. Then, the Sensor Simulator, along with the sensor models and its parameters, creates the log files that are fed into the Cooperative Relative Positioning algorithm.

- Velocity $\mathbf{v}$ of the vehicle in local navigation coordinates.
- Acceleration $\mathbf{a}$ of the vehicle expressed in vehicle coordinates.
- Turn rate $\boldsymbol{\omega}$ of the vehicle expressed in vehicle coordinates.
- Clock bias δt and clock drift $\dot{\delta t}$ of the GNSS receiver.

To simplify the complexity of the modeling, certain assumptions are applied in this study. First, the vehicle consists of two rigid bodies which are connected by springs; the one above is called sprung mass and the other one is called unsprung mass. The damping factor of the spring is linear. The vehicles drive exclusively in the east-north plane of the local navigation coordinate system, and thus, the up coordinate is constant. This coordinate system is fixed at time t^0 at the position of the ego vehicle and it does not change during the simulation. This constraint assumes a flat surface of the Earth. The gravity vector is constant over space and always points in negative up direction. The vehicles move only in their forward direction with no skidding or side-slip. The simulator's clock runs at 1 kHz ($\Delta t = 1\,\text{ms}$), which is assumed to be a high enough sampling rate in order to represent accurately the vehicle's dynamics.

In the simulator, a platooning scenario is implemented, where the ego vehicle drives at a varying distance behind the target vehicle. Both vehicles drive on straight paths interrupted by bends of different curvature. The vehicles always start from standstill and accelerate with constant predefined jerk. At the end of the scenario, both vehicles come to a standstill. Each of the vehicles are given initial values for their position $\mathbf{p}_\text{e}^0$ and $\mathbf{p}_\text{t}^0$, attitude $\boldsymbol{\alpha}_\text{e}^0$ and $\boldsymbol{\alpha}_\text{t}^0$, velocity $\mathbf{v}_\text{e}^0$ and $\mathbf{v}_\text{t}^0$, acceleration $\mathbf{a}_\text{e}^0$ and $\mathbf{a}_\text{t}^0$, turn rates $\boldsymbol{\omega}_\text{e}^0$ and $\boldsymbol{\omega}_\text{t}^0$, clock bias δt_e^0 and δt_t^0 and clock drift $\dot{\delta t}_\text{e}^0$ and $\dot{\delta t}_\text{t}^0$. Also the starting date and time are give as initial values.

The input to the simulator are the three-dimensional jerk values $\mathbf{j}^k$ at each time instant. A constant

positive jerk value makes the specific force of the vehicle to increase linearly and, consequently, the speed to increase quadratically. In this way, smooth accelerations and decelerations are achieved. By having the constant jerk segments as control input, both, linear accelerations and decelerations, as well as, constant circular turns can be simulated. The suspension factors in x and y direction, S_{x} and S_{y}, specify the angle by which the vehicle is pitched and banked when accelerating in x and y direction, respectively [217, 218]. Equations 6.1 through 6.9 describe the iteration loop that calculates the kinematic state for each of the vehicles.

$$\boldsymbol{\omega}_{\mathrm{xy}}^{k} = \mathbf{j}_{xy}^{k} \cdot S_{\mathrm{yx}} \tag{6.1}$$

$$\boldsymbol{\omega}_{\mathrm{z}}^{k} = \frac{v_{x}^{k}}{R} \tag{6.2}$$

$$\boldsymbol{\Omega}^{k} = \left[\boldsymbol{\omega}^{k}\times\right] \tag{6.3}$$

$$\mathbf{C}^{k} = \mathbf{C}^{k-1} \cdot (\mathbf{I} + \frac{\sin(\sigma)}{\sigma} \cdot \boldsymbol{\Omega}^{k} \cdot \Delta t + \frac{1-\cos(\sigma)}{\sigma^{2}} \cdot \boldsymbol{\Omega}^{k} \cdot \Delta t) \tag{6.4}$$

$$\mathbf{a}^{k} = \mathbf{a}^{k-1} + \mathbf{j}^{k} \cdot \Delta t \tag{6.5}$$

$$\mathbf{f}^{k} = \mathbf{C}^{k\mathsf{T}} \cdot \mathbf{g} + \mathbf{a}^{k} \tag{6.6}$$

$$\mathbf{v}^{k} = \mathbf{v}^{k-1} + \frac{1}{2} \cdot (\mathbf{C}^{k}\mathbf{a}^{k} + \mathbf{C}^{k}\mathbf{a}^{k-1}) \cdot \Delta t \tag{6.7}$$

$$\mathbf{p}^{k} = \mathbf{p}^{k-1} + \frac{1}{2} \cdot (\mathbf{v}^{k} + \mathbf{v}^{k-1}) \cdot \Delta t \tag{6.8}$$

$$\delta t^{k} = \delta t^{k-1} + \dot{\delta t}^{k-1} \cdot \Delta t \tag{6.9}$$

The simulated vehicles will roll and pitch due to accelerations in lateral and longitudinal direction, respectively. The corresponding angular rates are computed in Equation 6.1. The yaw rate is given by the longitudinal speed and the radius of the curve as in Equation 6.2. Equation 6.3 computes the skew symmetric matrix from the turn rates $\boldsymbol{\omega}^{k}$, which is then integrated in Equation 6.4 to find the new attitude of the vehicle given by its direct cosine matrix $\mathbf{C}^{k}$ (see Equation 3.6). Here, σ is the norm of the turn rate vector times the time step Δt. By integrating the jerk $\mathbf{j}^{k}$ in Equation 6.5 the acceleration of the vehicle in vehicle frame $\mathbf{a}^{k}$ is obtained. The transposed Direction Cosine Matrix (DCM) is used in Equation 6.6 to add the gravity $\mathbf{g}$ projected into the vehicle frame to the acceleration and compute the vehicle's specific force [97]. In Equation 6.7, the velocity of the vehicle in navigation frame $\mathbf{v}^{k}$ is obtained by applying the trapezoidal integration rule on the rotated acceleration of the vehicle [219]. Finally, the new position $\mathbf{p}^{k}$ is calculated from the previous position and the traveled distance by integrating the speed in Equation 6.8. The GNSS receiver clock bias is obtained adding the drift to the previous clock bias in Equation 6.9. The true values for the position of the GNSS satellites, their satellite clock bias and drift are taken from a RINEX ephemeris file that is loaded into the simulator [220]. Once the true values for both

vehicles and the GNSS satellites are generated by True Value Generator, the Sensor Simulator will simulate the sensor outputs for the GNSS receiver, the IMU and speed sensor. All parameters can be introduced to the simulator via a graphical user interface. For each of the sensors a model for their output is described next.

Speed Sensor The speed sensor measures the speed of the vehicle in forward direction. The sensor output v_{CAN} will have a constant bias b_{CAN} added to the true longitudinal speed of the vehicle v_{x} and an additive white Gaussian noise component ϵ_{CAN} according to

$$v_{\text{CAN}} = \lceil v_{\text{x}} + b_{\text{CAN}} + \epsilon_{\text{CAN}} \rceil \,. \tag{6.10}$$

Statistical analysis performed on available sensors yield that the bias of the speed sensor is between $0\,\frac{\text{m}}{\text{s}}$ and $0.3\,\frac{\text{m}}{\text{s}}$. The Gaussian noise is zero mean and standard deviation of around $0.3\,\frac{\text{m}}{\text{s}}$. The Controller Area Network (CAN) bus readings output the value rounded to the next integer.

Inertial Measurement Unit From the simulated attitude $\boldsymbol{\alpha}$, turn rate $\boldsymbol{\omega}$ and accelerations $\mathbf{a}$ of the vehicle the six IMU measurements are generated. The accelerometers inside the IMU measure the specific force $\mathbf{f}_{\text{acc}}$ which is given by

$$\mathbf{f}_{\text{acc}} = \mathbf{M}_a \cdot (\mathbf{a} + \mathbf{C}^{\intercal}\mathbf{g}) + \mathbf{b}_a + \mathbf{n}_a, \tag{6.11}$$

where the misalignment matrix $\mathbf{M}_a$ multiplies the acceleration of the vehicle $\mathbf{a}$ and the rotated gravity vector $\mathbf{g}$ with components $\begin{bmatrix} 0 & 0 & 9.81 \end{bmatrix}^{\intercal}$. The accelerometer biases $\mathbf{b}_a$ are generated by a first order Gauss-Markov model as explained in Chapter 5 and $\mathbf{n}_a$ is mutually independent white Gaussian noise. The misalignment matrix presents the rotation of the sensor frame into the vehicle frame. When the sensor is perfectly aligned with the vehicle this matrix equals the identity matrix. The turn rates measured by the gyroscopes $\boldsymbol{\omega}_{\text{gyr}}$ are given by

$$\boldsymbol{\omega}_{\text{gyr}} = \mathbf{M}_\omega \cdot \boldsymbol{\omega} + \mathbf{b}_\omega + \mathbf{n}_\omega, \tag{6.12}$$

where $\mathbf{n}_\omega$ is mutually independent white Gaussian noise and $\mathbf{b}_\omega$ are the gyroscope biases that are generated by a first order Gauss-Markov model.

In the frame of this work, only the impact of certain sensor errors are analyzed, while other errors are assumed to be nonexistent or compensated by a prior calibration. For instance, the misalignment of the sensor and errors in the estimation of the gravity are assumed to be zero. Additionally, as a first approach, accelerometer biases are set to zero and only the gyroscope biases are considered.

GPS Measurements The pseudorange measurements are simulated by taking the true position of the vehicle $\mathbf{p}^k$ and the true position of the satellite $\mathbf{p}_s^k$ at the time of transmission of the signal. This requires an iterative process analogous to the common positioning problem, since both the transmission time and satellite position are unknown. Starting with the satellite position at reception time as an initial guess and calculating the signal propagation time, a first approximation of the actual transmit time is made. This is used to compute a new satellite position and to enter the next iteration. Once this process converges, the satellite and a user clock bias are added to the propagation time to yield the pseudorange. Additionally, atmospheric errors can be activated. The ionospheric delay is computed from Klobuchar parameters in the Receiver Independent Exchange Format (RINEX) ephemeris file, while the tropospheric delay is calculated using the Modified Hopfield model [221]. The atmospheric parameters for the dry and wet tropospheric delay (temperature, air pressure, etc.) can be configured for each run. For the carrier phase measurements a random number of whole L1 cycles is added to the true range, while the sign of the ionospheric delay is inverted as described in Chapter 3. The Doppler measurements are calculated from the relative speed of satellite and receiver. The speed of the satellite is computed from three consecutive satellite positions. The clock drifts $\dot{\delta t}$ of receiver and satellite clocks are added. All three GNSS measurements are corrupted by Gaussian noise. The variances of pseudorange, carrier phase and Doppler can be set independently for each run. The possibility of adding a constant offset on the pseudoranges has been implemented in order to simulate a multipath induced bias in the pseudorange estimate.

As will be discussed in Section 6.2.1, pseudorange measurements are corrupted by time-correlated noise, thus, violating the first-order Markov assumption in a Bayesian filter. In order to evaluate the impact of a time correlation on the proposed filters, colored noise can be activated within the Cooperative Relative Position Simulator. The time correlation of pseudoranges is correctly modeled with an autoregressive filter of order one according to:

$$\epsilon^k = n^k + \zeta_1 \cdot \epsilon^{k-1}, \tag{6.13}$$

where ζ_1 is the AR(1) model parameter equal to 0.855, which matches the time correlation of the Ublox LEA 4T receivers used in this thesis and n is white Gaussian noise with zero mean and a standard deviation dependent on the simulated Carrier-to-Noise Ratio (CN0).

6.1.1. Movement Model Evaluation

The first test aims at validating the proposed relative motion models from previous chapter. For this purpose, and in order to isolate the problem to exclusively consider movement model errors, the initial baseline and baseline velocities are initialized to true values and all errors in the inertial and speed sensors are deactivated and the GNSS double differenced measurements are disconnected.

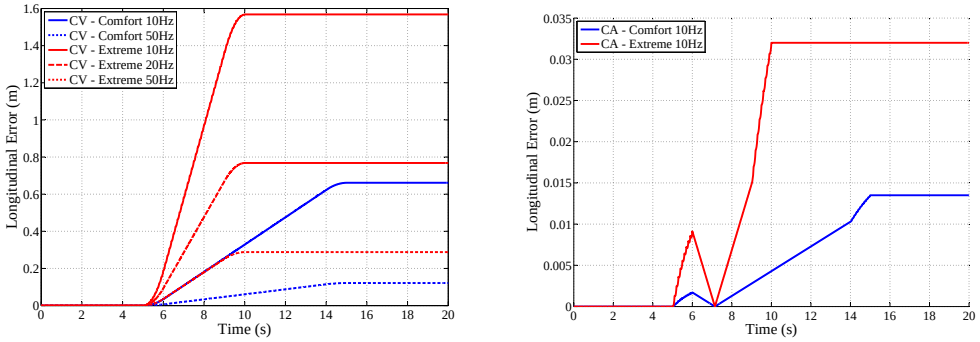

(a) Constant Velocity Model (b) Constant Acceleration Model

Figure 6.2.: The figures show the longitudinal baseline prediction error when performing an acceleration of the target vehicle using a CV and a CA model. The blue curves are comfortable maneuvers (jerk of 1.5 $\frac{m}{s^3}$), while the red curves are extreme maneuvers (jerk of 8 $\frac{m}{s^3}$). In order to get the prediction error below 1 m a higher update rate than 10 Hz is required using the CV model. The CA model yields prediction errors of a few centimeters at 10 Hz update rate.

The baseline will be predicted solely on the basis of the correct values of speed, acceleration, turn rate and heading in each vehicle.

During normal driving, comfortable accelerations that can be encountered range from $-2\,\frac{m}{s^2}$ to $2\,\frac{m}{s^2}$ [222], with acceleration changes below $2\,\frac{m}{s^3}$ [223]. Sports cars have accelerations above $6\,\frac{m}{s^2}$ and emergency braking can reach decelerations up to $10\,\frac{m}{s^2}$ and acceleration changes of $8\,\frac{m}{s^3}$ in periods below 1 s [224].

Typical horizontal turn rates are given by the road topology, which is designed in order to limit the centripetal acceleration and lateral jerk experienced by a vehicle to around $1.5\,\frac{m}{s^2}$ and $1\,\frac{m}{s^3}$, respectively [225]. During normal driving, the horizontal turn rates are below $20\,\frac{°}{s}$. Higher turn rates can be encountered in bends with small radii. In a curve with 10 m radius, a maximum turn rate of $57\,\frac{°}{s}$ can be performed before the wheels slip on the surface.

Longitudinal and lateral jerk produce changes in longitudinal acceleration and changes in turn rate respectively. Since these changes are not contemplated within any of the proposed models, these situations are expected to introduce relative positioning errors. The error stems from the limited update rate for the kinematic estimations of the target vehicle that are made available at the ego vehicle. With an unlimited communication bandwidth and, hence, a sufficiently high update rate, any movement could be approximated with the proposed movement models. The kinematic state estimate of the ego vehicle does not contribute to this error, since it is automatically available for the cooperative position sensor fusion.

Figure 6.2 shows the longitudinal baseline estimation error for both, a comfortable acceleration (blue) and an extreme acceleration (red) of the target vehicle, for different update rates using a

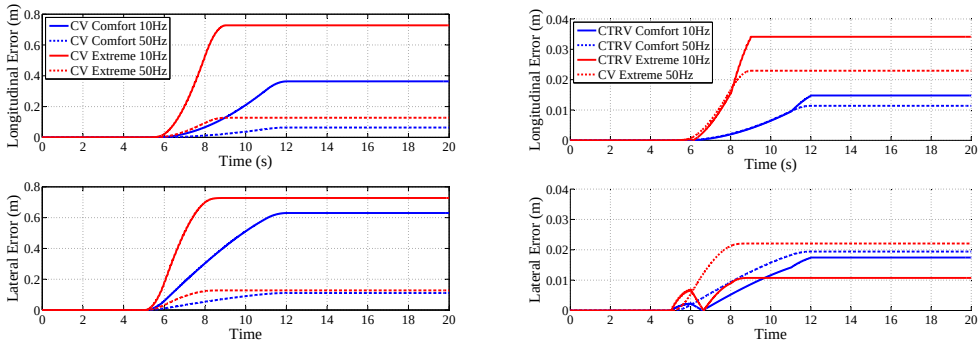

(a) Constant Velocity Model (b) Constant Turn rate and Velocity Model

Figure 6.3.: The figures show the longitudinal and lateral baseline prediction errors using a CV and a CTRV while performing a turning maneuver. The blue curves are comfortable maneuvers (change of 10 $\frac{°}{s}$ in 1 s), while the red curves are extreme maneuvers (change of 30 $\frac{°}{s}$ in 0.1 s). Both target-to-ego update rates of 10 and 50 Hz are displayed.

CV and a CA model. It can be observed that only the CA model is able to produce centimeter-level errors for both, comfortable and extreme acceleration maneuvers using 10 Hz update rate. With a CV model, longitudinal errors above 1 m can be expected.

Figure 6.3 shows the analogous evaluation for a comfortable and an extreme 90° turn of the target vehicle. Only with high update rates of 50 Hz, the CV model is able to produce a relative position error below 10 cm. The Constant Turn Rate and Velocity (CTRV) model yields relative positioning errors below 5 cm even for extreme maneuvers at 10 Hz.

Also the relative velocity between the vehicles is correctly predicted with errors below 5 $\frac{m}{s}$ while performing an extreme acceleration maneuver of the target vehicle using a CA model and an extreme turn maneuver using a CTRV model.

As a conclusion, one can say that, if vehicles adhere to the presented movement models and accurate kinematic updates are available for each vehicle's speed, acceleration, heading and turn rate, the baseline can be tracked with sufficient accuracy over longer periods of time if a Constant Turn Rate and Acceleration (CTRA) model is used. An update rate of 10 Hz is sufficient in order to obtain relative position errors below 5 cm and relative velocity error below 5 $\frac{m}{s}$.

6.1.2. GNSS Evaluation

The impact of the GNSS satellite signals on the baseline estimate is regarded next. For this purpose different tests are executed that focus on how the baseline and the baseline uncertainty vary with changing satellite constellation and with different carrier-to-noise values. Figure 6.4 shows the apparent satellite position in terms of elevation and azimuth.

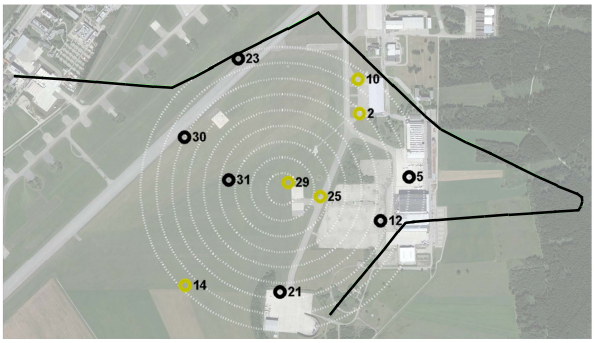

Figure 6.4.: The figure shows the simulated driving path superimposed to an aerial view in Google Maps. A skyplot displays the position of the GNSS satellites during simulated test run.

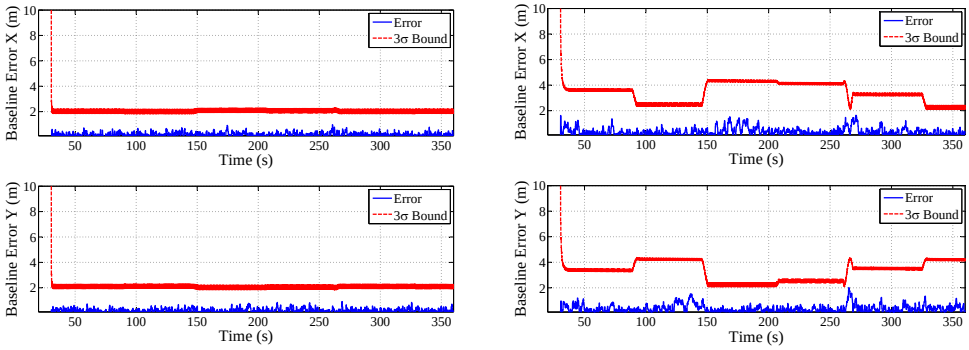

(a) Full Constellation (b) Partial Constellation

Figure 6.5.: The left figure shows the baseline estimation error and its uncertainty during the whole run using the full constellation of satellites. The right figure shows the estimation error when a partial constellation is used. The result is an increase in the estimation uncertainty.

The satellites highlighted in yellow represent a reduced constellation with five satellites (2, 10, 14, 25 and 29 as common satellite) that could be in view when driving on a south-west/north-east urban canyon. This is used to analyze the impact of having only satellites in one direction. Figure 6.5 shows the baseline estimation error and its 3σ-uncertainty in longitudinal and in transverse direction. When using the full constellation of satellites the baseline 3σ-uncertainty is similar in both directions (see Figure 6.5a). However, both uncertainties increase when compared to the full constellation test as less satellites are used (see Figure 6.5b). The longitudinal constellation favors the accuracy of the longitudinal component of the baseline as explained in Section 5.1.3. When taking the turn in second 90 the constellation is parallel to the baseline and consequently the x-variance decreases while the y-variance increases. The turn at second 145 has the opposite impact.

Next, the baseline uncertainty with varying number of satellites is assessed. For this, the number

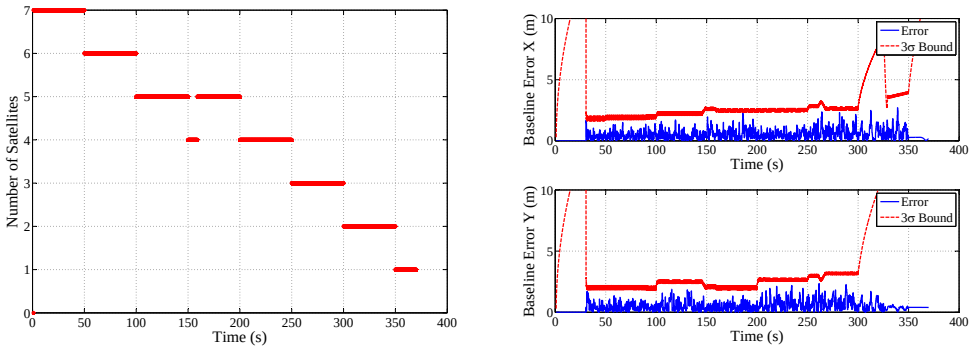

(a) Number of Satellites (b) Baseline Error

Figure 6.6.: Baseline estimate with varying Number of Satellites. The left figure shows the number of double differences used to update the baseline estimate. The right figure shows the longitudinal and lateral baseline error.

of visible satellites is progressively reduced from 7 to 2, ending with one sole double difference that updates the baseline estimate. Figure 6.6 shows the resulting baseline estimation errors and the 3σ uncertainty bound. It can be seen that the estimation uncertainty stays relatively bounded while decreasing the number of satellites. When from second 300 on only two satellites, i.e. one double difference, is available, the uncertainty in the relative position estimate increases without bound in one direction and is loosely bounded in the other after performing the last curve. From second 350 on, no double difference can be formed and the relative position can only be predicted through the movement model.

Pseudoranges have been simulated with a medium carrier-to-noise ratio by adding noise with standard deviation of 1 m. The simulated Doppler noise is set to 5×10^{-5} Hz. The multisensor fusion filter assumes exactly this error in the pseudorange measurements. Consequently, the results are optimal from the point of view of estimating the baseline uncertainty. In real-world scenarios the challenge is to correctly determine the current error on each pseudorange and Doppler measurement.

Time correlation of GNSS measurement noise As previously explained, pseudorange measurement noise is correlated over time due to the GNSS receiver tracking loops. Consequently, also the noise on the pseudorange double differences is time correlated. The impact of this correlation on the baseline estimate within the simulator is regarded next. An acceleration-turn-deceleration scenario is simulated. First, the pseudoranges output by the simulated GNSS receiver are corrupted with white noise and then the pseudoranges are corrupted by noise modeled with AR(1) model with parameter ζ_1 equal to 0.855. This value stems from the investigation performed with the available GNSS receivers as explained in Section 6.2.1. Figure 6.7 shows the error in the baseline estimation for both cases. Figure 6.7b reveals that the incorporation of colored noise

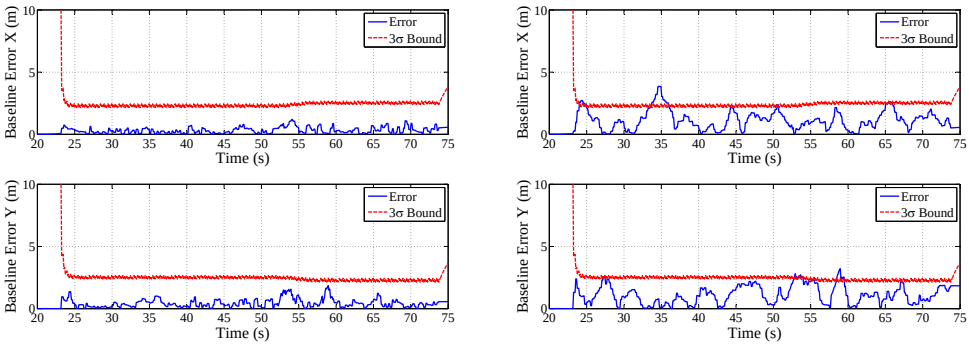

(a) White Noise (b) Colored Noise

Figure 6.7.: The figures show the error in the baseline estimate when using pseudorange measurements corrupted by white (left) and colored noise (right). The unmodeled correlation of the noise in the measurements creates an overconfident baseline estimate.

to the measurements leads to a suboptimal behavior of the filter, producing larger errors and an overconfident estimation of the baseline. Therefore, in the scope of this thesis, the measurement noise has been increased accordingly. Different approaches, such as state augmentation and measurement differencing, exist to cope with the problem of colored noise inside a Kalman filter [226]. A further approach is to implement a shaping filter by augmenting the state space incorporating the autoregressive model of the autocorrelation as a further equation [227].

GNSS Outlier Rejection An offset on some of the pseudoranges in either one of the vehicles is added. The purpose is to validate the outlier rejector presented in Chapter 5. The offset on the pseudorange aims at modeling the effect of a reflected path in a GNSS receiver. The pseudorange error is varied throughout the simulation. Starting from a large offset of 30 m on two satellites, the amplitude is reduced until it reaches 0.2 m.

Figure 6.8a reveals large errors in both the longitudinal and lateral component of the baseline estimate. Since the pseudorange double difference error is not adapted, the baseline uncertainty estimation remains low and the actual error exceeds the 3σ bound leading to a confidence error. In Figure 6.8b the multipath rejector has been activated. The result is a correct suppression of the faulty satellite when the pseudorange offset is 30 m and 20 m. The 10 m offset, however, is incorporated into the estimate, since the Mahalanobis distance falls below the rejection threshold. Further decreasing the rejection threshold has the drawback of suppressing also healthy satellites. The sub-meter pseudorange offsets are correctly averaged out inside the Kalman filter, since their contribution is in the order of the pseudorange noise (1 m).

The rejector will work well for strong multipath offsets that occur over short periods of time in a small number of satellites. It also requires that an accurate baseline with small uncertainty is present before the multipath hits in. The rejector is a suitable approach when many satellites

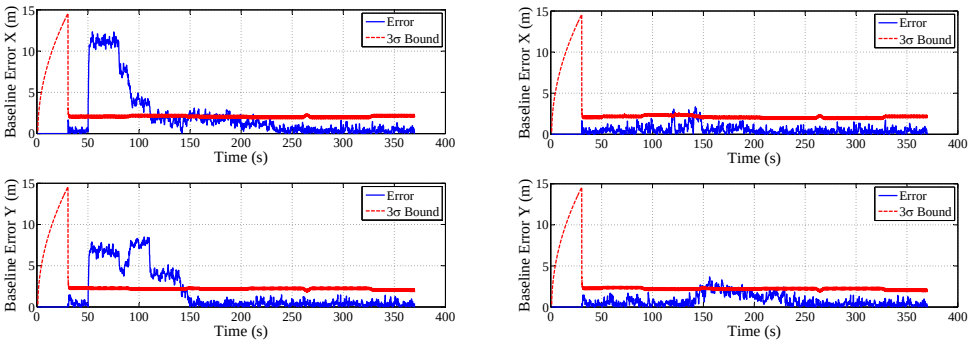

(a) Multipath Rejector Deactivated (b) Multipath Rejector Activated

Figure 6.8.: Baseline estimate in the presence of multipath. The left figure shows the baseline estimate error in longitudinal and lateral direction. The right figure shows the baseline error activating the multipath rejector.

are available and the disadvantage of using less satellites can be assumed. Already today GNSS receivers are able to track multiple constellations of satellites and tracking around 20 satellites is not unusual in open sky environments. In future, with GNSS receivers tracking different constellations, the availability of satellites will greatly increase.

6.1.3. Kinematic Evaluation

This section evaluates the performance of the lower kinematic filter using a 122 s section consisting of both vehicles performing an acceleration, three bends and a deceleration until standstill. The complete parameter list used in the simulation can be found in Table B.1 and Table B.2 in Annex B. Figure 6.9 shows the speed, acceleration, turn rate and attitude profile during the run. The bends of different radius and length create different bank angles and turn rates. As introduced in Chapter 5, the lower kinematic filter estimates the vehicle's longitudinal speed, acceleration, heading and turn rate using an IMU, the vehicle's speedometer and GNSS velocity from Doppler measurements. Further on, assumptions that yield knowledge on the estimated parameters are integrated into the filter as pseudo-measurements. Two different configurations were presented and are evaluated here for their accuracy, robustness and observability of parameters. In order to fairly evaluate the both kinematic filters, the measurement noise variances are set identical. The initial state of each parameter is set to the true value and initial uncertainty values are equal in both filters. The initial gyroscope biases are set to zero. Every time one hundred realizations of the experiment have been performed in order to make a statistical relevant evaluation.

The evaluation of both kinematic filters concentrates on its performance in estimating the four relevant parameters. For this, the estimation error of one of the realizations is displayed over time as a blue line. The gray area represents three times the standard deviation of the estimated

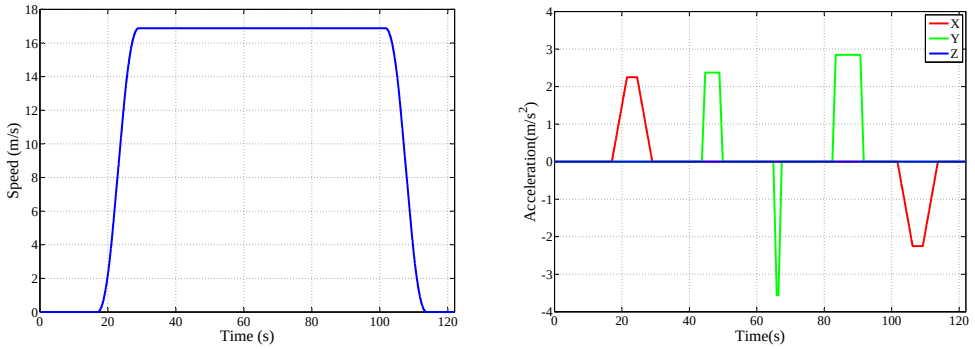

(a) Speed (b) Acceleration

(c) Attitude (d) Attitude Rate

Figure 6.9.: The figure shows the speed, acceleration, attitude rate and attitude profile for one vehicle in the Cooperative Relative Position Simulator. Around second 20, the vehicle starts accelerating from standstill until reaching a speed of 17 $\frac{\text{m}}{\text{s}}$. This acceleration causes the vehicle to pitch back 7°. From second 45 to 50, the vehicle takes a left turn. The lateral acceleration causes the vehicle to roll to the outer side of the curve. After two more bends with different radius to the right and to the left, the vehicle comes to a stop at second 115.

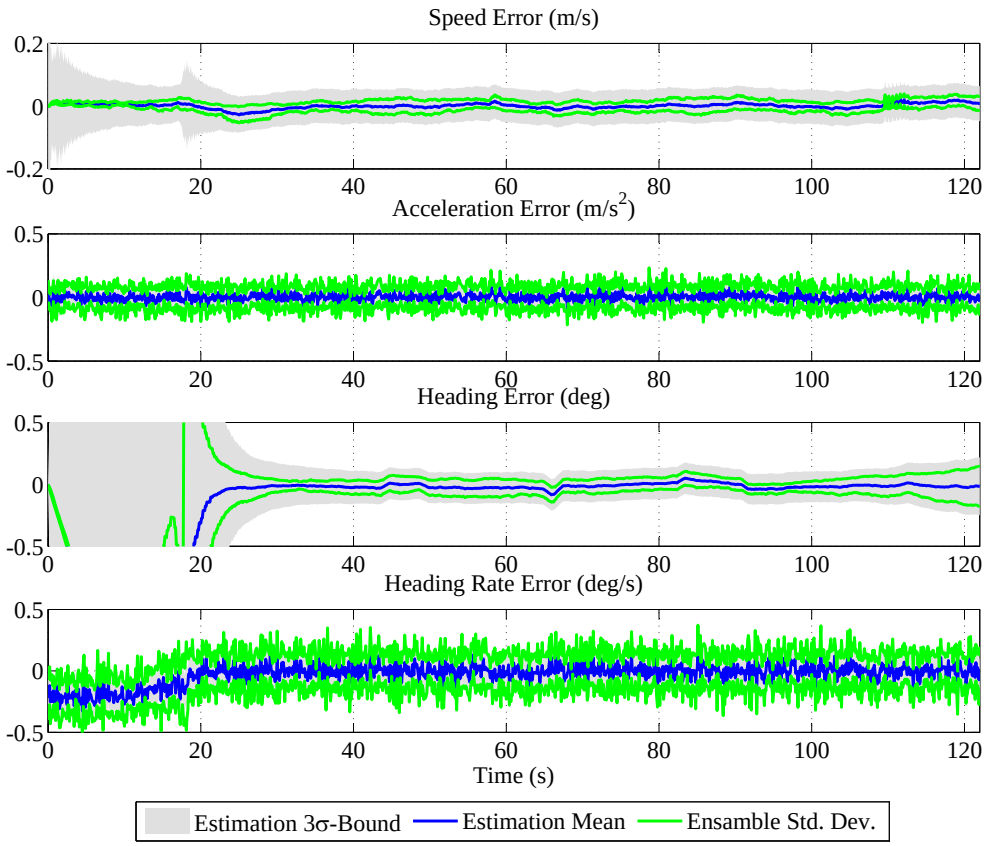

Figure 6.10.: The figure shows the estimation error of the relevant parameters using the Full 3D Inertial Filter with GNSS during the 122 s run. The blue lines correspond to the estimation error of one single realization of the experiment, while the overall 3σ error over all experiments is shown in green. In gray the filter's 3σ-bound is displayed.

parameter (3σ-bound). The green lines represent the actual 3σ-standard deviation over all one hundred realizations. Ideally, the stated uncertainty given by the kinematic filter would match the actual uncertainty of the output. Each filter is evaluated, once activating the GNSS measurements, and once without these measurements.

Full 3D Inertial Filter This filter implements a strapdown algorithm that integrate gyroscope measurements to compute the vehicle's attitude and integrate the accelerometers to compute the velocity. In a Kalman filter, the increasing errors of the strapdown algorithm, along with the gyroscope biases, are estimated by incorporating GNSS information. Starting with the correct orientation, the filter keeps on integrating the gyroscopes to track the attitude of the vehicle. Here, the main problem is the unobservability of roll and pitch angles, which accumulate an error due to the integration of noise over time. The estimation errors, along with the estimation uncertainty (3σ), are shown in Figure 6.10. Vehicle speed and acceleration are correctly estimated over the whole 122 s run. The speed estimate is correctly bounded by the availability of full 3D GNSS

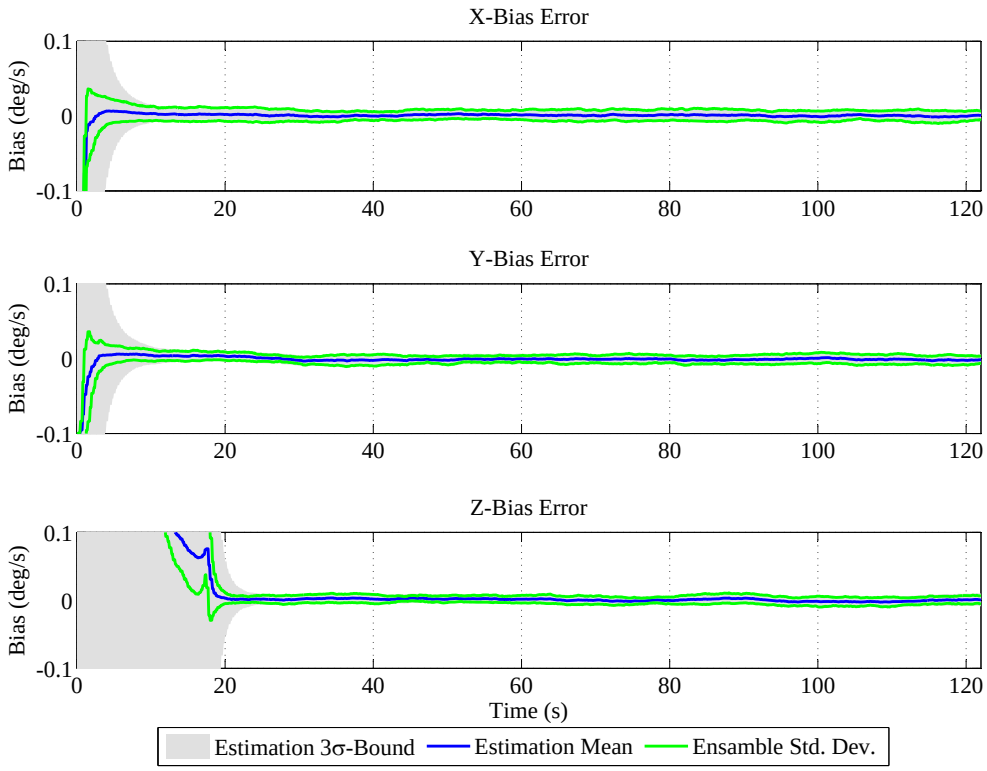

Figure 6.11.: The figure shows the estimation error of the three gyroscope biases with the Full 3D Inertial Filter. The biases in the planar axis converge rapidly to the correct values. Since the zero-rotation assumption is not activated in this example, the z-axis bias is only observable when the vehicles moves and GNSS heading information is available.

velocity. The heading angle of the vehicle stays unobserved during the standstill section of the test run and is correctly updated when the speed of the vehicle increases with the information from GNSS heading. The heading rate stems from the bias-corrected and projected gyroscope measurements from vehicle frame to navigation frame.

In Figure 6.11, the correct estimation of gyroscope biases in the first seconds during standstill can be appreciated. In this run zero-rotation assumption nor zero-acceleration assumptions are activated. The z-axis gyroscope bias is observed later when the vehicles starts accelerating and the heading updates from GNSS start becoming more and more accurate. With the activation of the zero-rotation assumption, all gyroscope bias are observed during standstill. With increasing stopping time the biases can be estimated with increasing accuracy. In this way it is possible to completely eliminate the initial heading and heading rate errors in Figure 6.10.

Figure 6.12 shows the estimation of the four relevant parameters during a GNSS outage between second 40 and 90. The longitudinal speed and heading errors increase and their steadily growing uncertainty are correctly modeled in the filter. Acceleration and heading rate remain bounded due to the information from the accelerometers and gyroscopes respectively. In order to limit the error

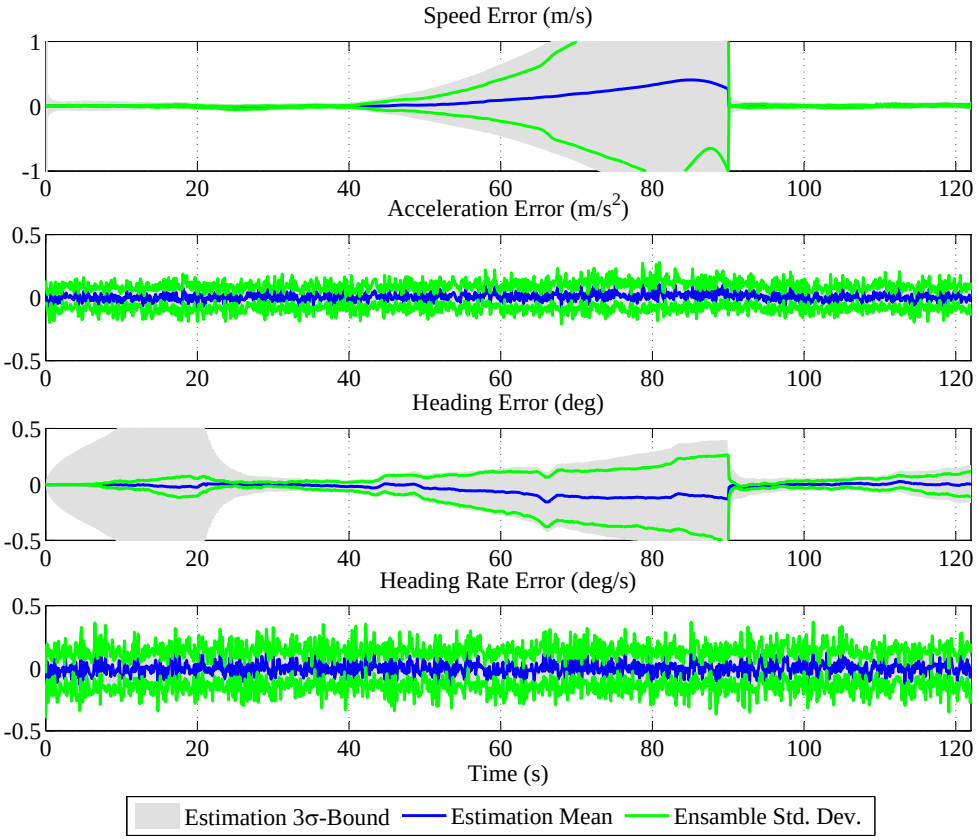

Figure 6.12.: The figure shows the estimation errors in all four relevant parameters using the Full 3D Inertial Filter in the absence of GNSS velocity updates between second 40 and second 90. Longitudinal speed and heading have larger errors when compared to the simulation where GNSS was available. The error in the heading increases steadily due to the absence of a suitable observation. The heading rate, which is equal in this filter to the z-axis turn rate, is bounded.

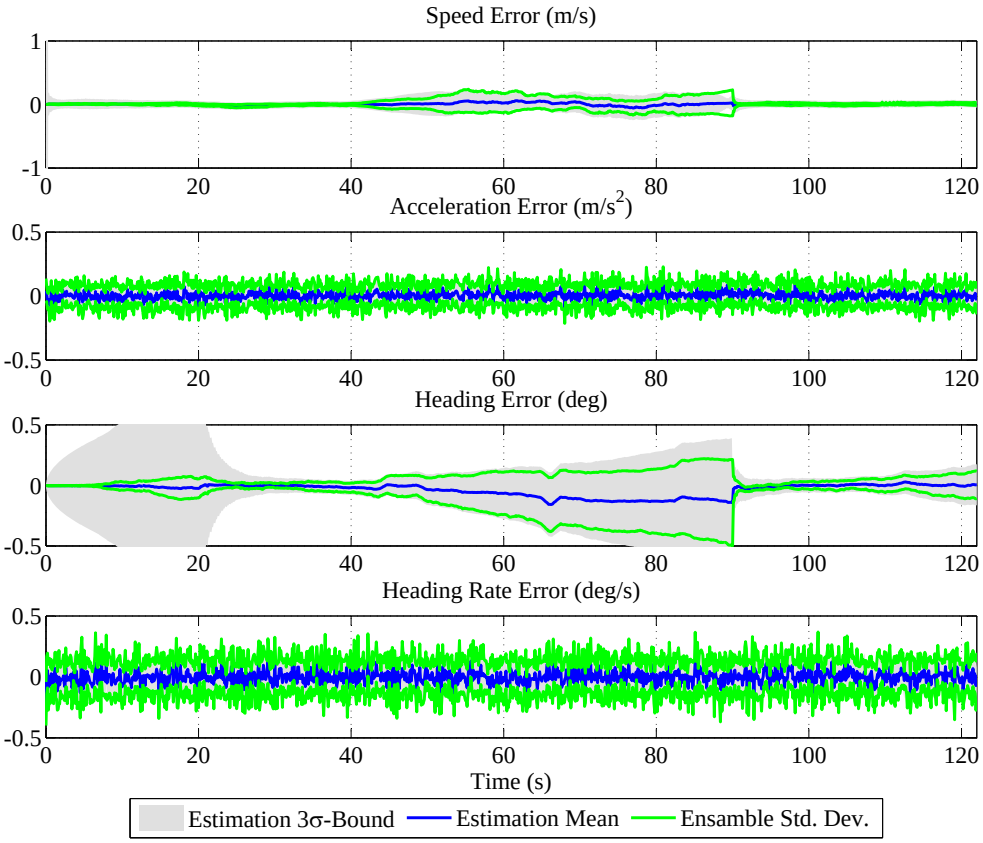

Figure 6.13.: The figure shows the estimation errors in all four relevant parameters using the Full 3D Inertial Filter in the absence of GNSS velocity updates between second 40 and second 90 and using the CAN bus speedometer information instead. This information is able to correctly contain the growth of the longitudinal velocity error in comparison to Figure 6.12.

growth in the velocity component, CAN speed measurements are activated. The CAN speedometer offers an observation of the forward speed of the vehicle without an information of its heading angle. Additionally, the non-holonomic constraints state that the lateral and vertical speed of the vehicle are both zero. Figure 6.13 shows the estimation errors in this case. It can be seen how in the GNSS-denied section the longitudinal speed error increases slightly due to the less certain speed information, but the uncertainty is correctly estimated. The heading error increases, similar than in Figure 6.12. The rate at which this error increases is dependent on the gyroscope noise variance and its correct estimation of the biases.

Full Bayesian Filter In this approach an eleven-state Kalman Filter is used to estimate both longitudinal speed and acceleration, 3D attitude, turn rate and gyroscope biases. Instead of integrating the gyroscopes and accelerometers in a strapdown algorithm, here the measurements of accelerometers and gyroscopes update the state in a Bayesian way. Further updates are a

zero-rotation assumption when the vehicle is at standstill and GNSS heading and speed when this information is available. The estimation errors with GNSS updates available are shown in Figure 6.14.

The Full Bayesian approach implicitly incorporates a zero-acceleration assumption (see Equation 5.90) and, thus, its attitude angles do not drift over time. This makes it possible to have an accurate estimation of the longitudinal acceleration of the vehicle. In general, the estimated uncertainty for speed, acceleration and heading are greater than the actual ensemble standard deviation, meaning that the filter is under-confident. This is related to the fact that the prediction equations do not incorporate any sensor information in order to steer the a priori estimate towards the expected measurement. This fact requires an increased process noise variance in order to react correctly to acceleration and decelerations maneuvers or changes of direction. The effect of a tight process noise variance-covariance matrix can be appreciated in the heading rate estimation error in Figure 6.14. The filter does not correctly follow the changes in heading rate during the three turns and yields small errors in heading rate, which propagate to the heading and the speed estimates.

The filter estimates the gyroscope biases at standstill (see Figure 6.15). If a standstill is not available, the filter correctly learns the z-axis gyroscope bias with the GNSS heading measurements and the x- and y-axis gyroscope biases with the information of the accelerometers.

In Figure 6.16, the GNSS measurements have been disconnected between second 40 and 90. The speed estimate is updated with measurements from the CAN bus speedometer, which is less accurate, resulting in an increased speed and acceleration uncertainty. The uncertainty in the heading estimate grows quickly due to the absence of heading information. However, also here, the filter predicts an under-confident error. The aforementioned errors in the heading rate directly cause biased estimates of the heading.

Discussion The previous comparison between the Full 3D inertial filter and the Fully Bayesian filter yielded that both approaches, in principle, are valid for estimating all four kinematic parameters of interest. The estimation error is for both filters around zero. However, the Fully Bayesian approach yields under-confident estimations, while the Full 3D inertial filter has an optimal behavior by offering an unbiased mean and a covariance that correctly depicts the existing uncertainty. A correct bounding of the uncertainty is important, since it will propagate to the relative position between the vehicles and, possibly, lead to a reliability failure. Further on, the Fully Bayesian approach requires a correct tuning of the system variance-covariance matrix in order to adapt to changing dynamics of the vehicle. For these reasons, in the real-world experiments in Chapter 7, the Full 3D inertial kinematic filter is chosen to estimate the speed, the acceleration, the heading and the heading rate in both the ego and the target vehicle. However, a worse performance is expected in real-world conditions, due to model mismatch and unmodeled effects. Inertial sensor

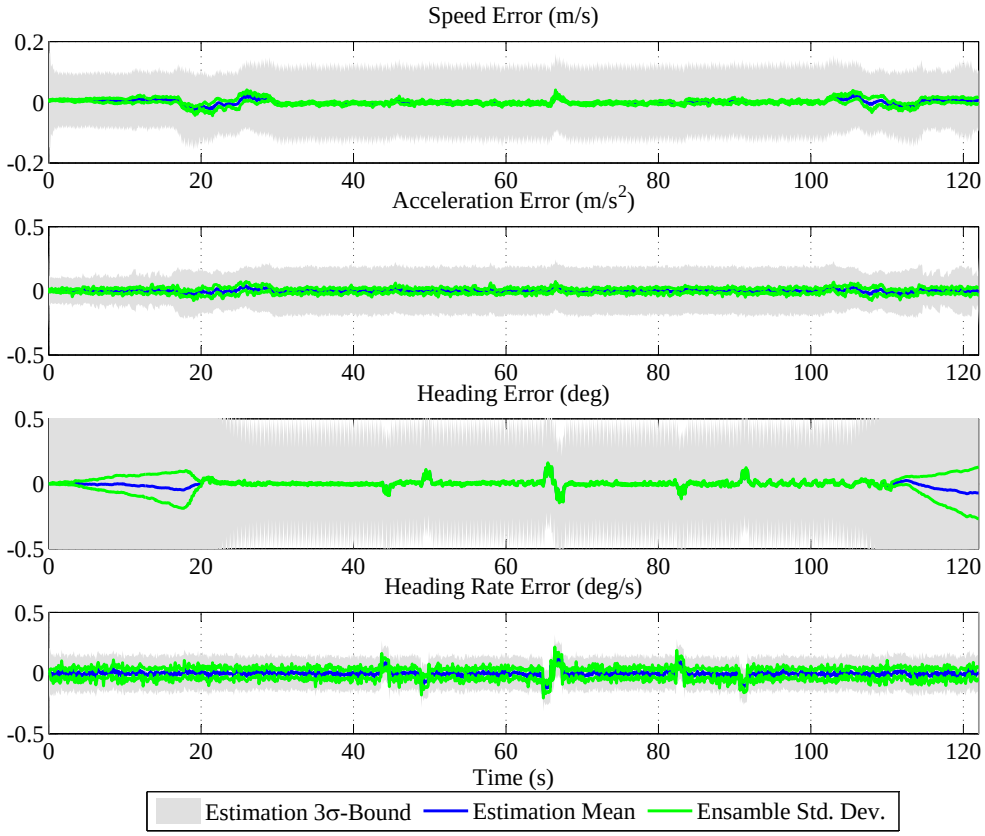

Figure 6.14.: The figure shows the estimation error of the relevant parameters using the Full Bayesian kinematic filter with GNSS during the 122 s run. The blue lines correspond to the estimation error of one single realization of the experiment, while in green the overall error 3σ deviation over all experiments is shown. In gray the filter's 3σ-bound is displayed.

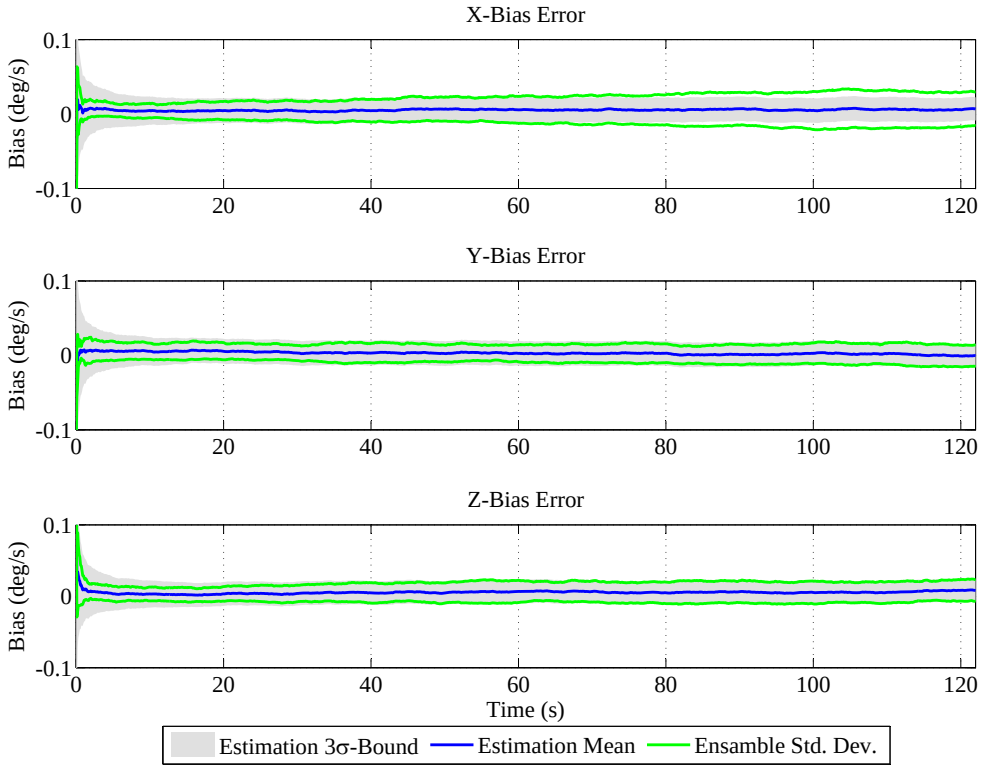

Figure 6.15.: The figure shows the estimation of the three gyroscope biases with the Full Bayesian Filter in the absence of GNSS. By using the zero-rotation assumption the estimate rapidly converges to the true value when the vehicle is at a standstill. While the vehicle is driving the uncertainty in the gyroscope bias slowly increases since no suited observation exists.

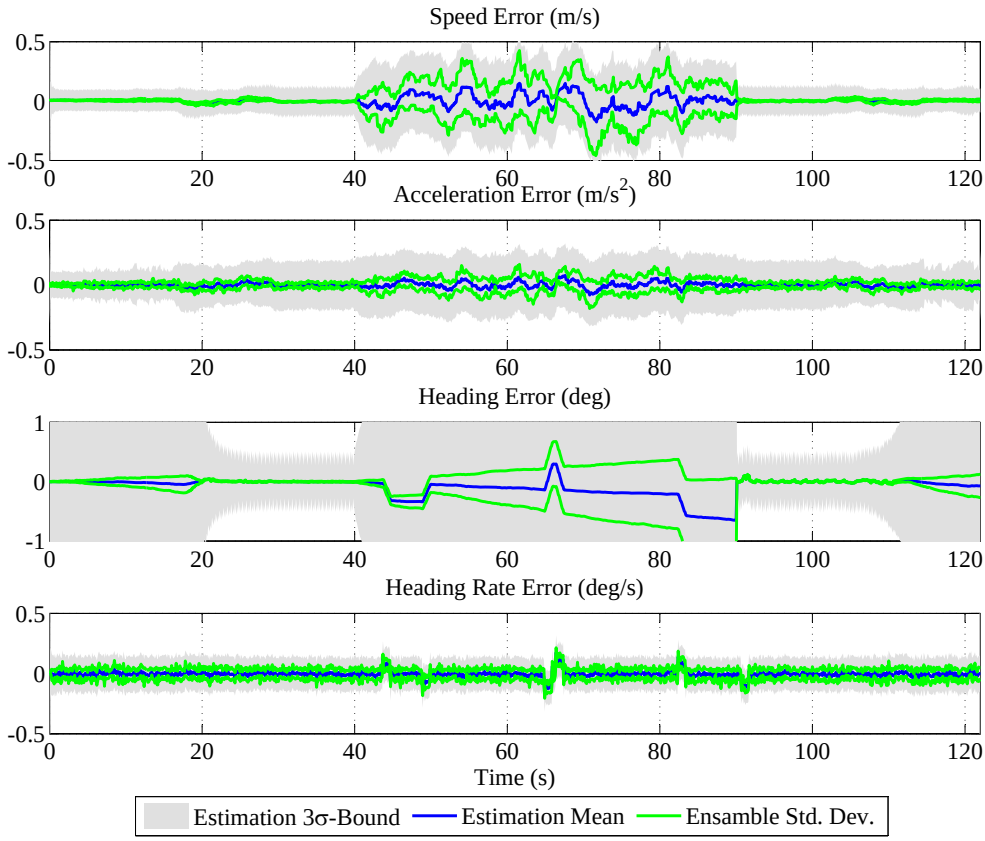

Figure 6.16.: The figure shows the estimation errors in all four relevant parameters using the Full Bayesian Filter in the absence of GNSS speed and heading updates. Longitudinal speed and acceleration have larger error when compared to the simulation where GNSS was available. The error in the heading increases steadily due to the absence of an suitable observation.

misalignment, lever arm effects, deviating measurement models and complex vehicle dynamics will influence the performance of the filter in an unpredicted way.

6.1.4. Speed Quantization

The speed measurement output by the vehicle CAN bus is quantized to a whole number of $\frac{\text{km}}{\text{h}}$. This causes an error on the speed measurements that is uniformly distributed between $\pm 0.14\,\frac{\text{m}}{\text{s}}$. Compared to GNSS derived speed, which was quantified in Chapter 5 with an error of $0.06\,\frac{\text{m}}{\text{s}}$ (1σ), the CAN speedometer error is larger. The second important drawback is that the error does not average to zero but can have a maximum bias of $\pm 0.14\,\frac{\text{m}}{\text{s}}$. This bias amounts to 16.8 m relative positioning error in 60 s.

Therefore, in practice it will be only be possible to bridge short GNSS outages using the quantized CAN speed measurement. The alternative would be to directly use the information from Hall

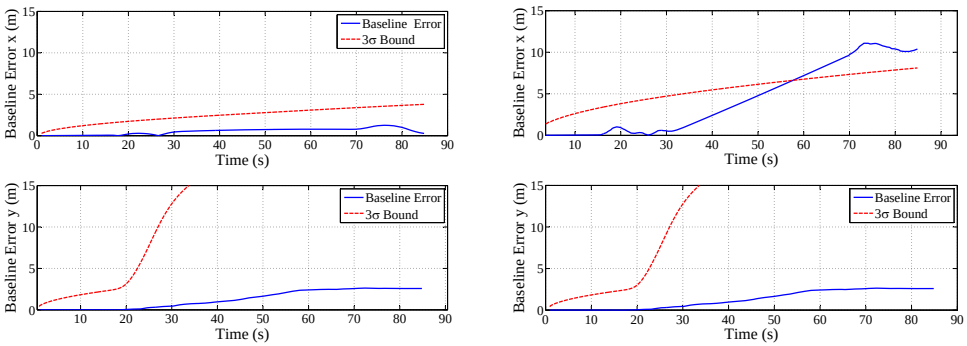

(a) Speed from GNSS (b) Speed from CAN

Figure 6.17.: Baseline estimation error in longitudinal and lateral direction using GNSS based speed estimate (left) and CAN speedometer (right). The speed of ego and target vehicle are chosen to produce the worst case scenario: the rounding of the constant speed in each vehicle produces an ever-inceasing error in the relative position. In this case on the longitudinal component of the baseline.

effect sensors mounted in the wheel and which are used for Anti-lock Braking System (ABS). The resulting speed estimate has a random error with a bias of less than $0.02\,\frac{\mathrm{m}}{\mathrm{s}}$, related to the estimation of the wheel radius [228]. In the worst case this would accumulate to 2.4 m relative positioning error in 60 s.

The impact of not having a Gaussian distributed noise is assessed using the simulator. For this, an acceleration, constant speed, deceleration scenario is simulated. GNSS pseudorange double difference updates are deactivated and the baseline is solely estimated by prediction. Figure 6.17a shows the baseline estimated using the speed derived from the GNSS measurements, which is zero mean and has small error (1σ). The longitudinal and lateral errors are due to time discretization and a small error in the ego vehicle heading estimate, respectively. Figure 6.17b shows the same scenario using the quantized speed measurement from the CAN bus instead. The speed of each vehicle in the constant speed section is set to the worst case, where the target vehicle's speed has a value that is round up, while the ego vehicle's speed if round off to the next lower integer speed. A steadily increasing longitudinal baseline error is the consequence.

In practice, vehicles will not drive at the edge of the rounding threshold for long periods of time. In fact, the rounding error will average out over longer GNSS blockages. Nevertheless, the relative positioning filter is not capable of correctly estimating this behavior. The result is a reliability failure.

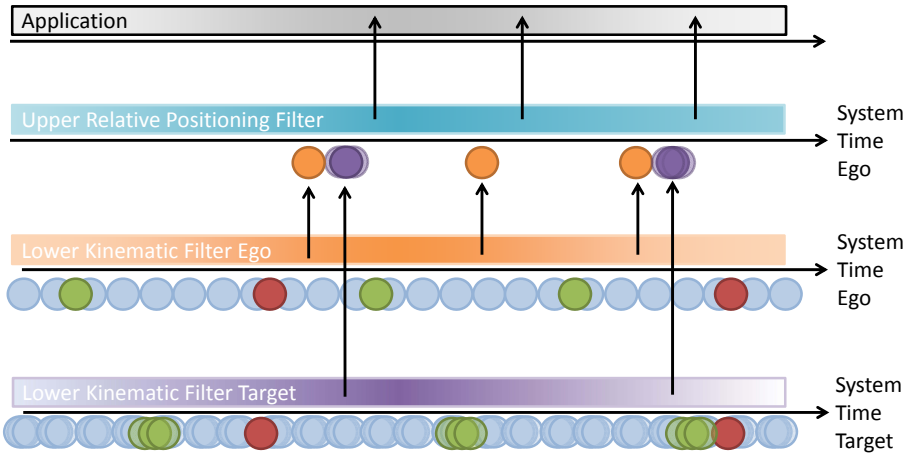

Figure 6.18.: The figure illustrates the "blurring" of the arrival time of sensor data due to an unsynchronized clock in the target vehicle.

6.1.5. Timing Evaluation

For a cooperative approach precise timing is a crucial issue. Recalling Figure 5.21, sensor data from the target vehicle is merged in the upper relative positioning filter with sensor data from the ego vehicle. In order to have a correct estimation of the relative position, the fused sensor data need to be referred to a common clock. For practical reasons this clock is given by GNSS time, which is precise and stable. Consequently, GNSS measurements will per se be synchronized to GNSS time and can be shared without further problem between vehicles.

Unless a dedicated hardware synchronization to GNSS time is performed, system clocks inside ego and target vehicle are biased and will steadily drift away from GNSS time. The timestamps of sensor data, such as IMU and CAN bus speedometer, will, therefore, have an unknown offset. One solution, and the one implemented in this thesis, is to relate system and GNSS time per software synchronization. Each time a GNSS measurement with an accurate GNSS timestamp arrives, the system time is updated. Outages in GNSS are correctly bridged by extrapolating linearly the relationship between system time and GNSS time. Figure 6.18 illustrates the problem of having an unsychronized system clock in the target vehicle. IMU and CAN sensor data will have a remaining random error in their measurement time. This jitter due to unsynchronization for the real-world test setup used in this thesis is shown in Figure 6.19. The $-80\,\text{ms}$ spikes every $102\,\text{s}$ could be related to periodic tasks of the Linux operating system or garbage collection tasks in the Java run-time environment. The two $50\,\text{ms}$ peaks are situations when the vehicle was driving in a tunnel and GPS tracking is momentarily lost. Here the GNSS clock is unreliable and should not be used for updating the system time.

A jitter on the system clock with a standard deviation of $10\,\text{ms}$ will traduce to an error in the sensor magnitude. If, for instance, a vehicle is accelerating with $7\,\frac{\text{m}}{\text{s}^2}$, a $10\,\text{ms}$ uncertainty in the

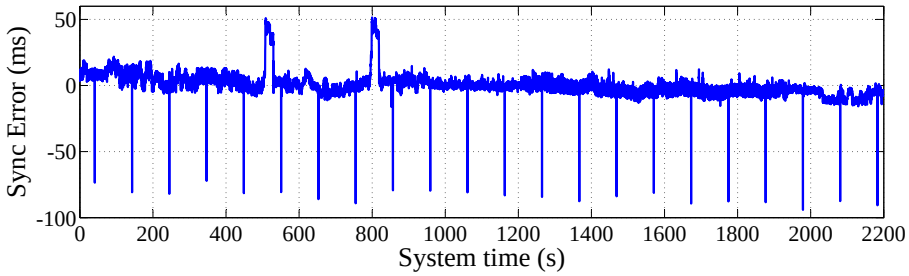

Figure 6.19.: The figure shows the synchronization error between system time and GPS time after software synchronization of the test setup used in this thesis. The synchronization errors are mostly between ± 20 ms.

Table 6.1.: Error due to System Clock Unsynchronization

Sensor Measurement	Maximum Rate of Change	Error due to system clock unsynchronization (1σ)	Error of the sensor (1σ)
Speedometer	$7\ \frac{m}{s^2}$	$0.07\ \frac{m}{s}$	$0.8\ \frac{m}{s}$
Accelerometer	$0.5\ \frac{m}{s^3}$	$0.005\ \frac{m}{s^2}$	$0.01\ \frac{m}{s^2}$
Gyroscope	$20\ \frac{^\circ}{s^2}$	$0.02\ \frac{^\circ}{s}$	$0.29\ \frac{^\circ}{s}$

measuring instant of the vehicle's speedometer will produce a speed error of $0.07\ \frac{m}{s}$. Table 6.1 summarizes the errors due to system clock unsynchronization for all vehicle sensors taking into account the largest expected rate of change of the considered magnitude. It can be seen how all errors are below the expected errors of the sensor itself. Hence, it can be concluded that the proposed software synchronization will not lead to a major performance decrease in the estimation of the kinematic parameters inside of the vehicles.

In the absence of GNSS signals, during first acquisition or during temporary loss of tracking, the clock in each vehicle is drifting freely until lock is reacquired. In this time, sensor data issued in the vehicle has no temporal reference. Quartz clocks exhibit drifts below $10^{-5}\ \frac{s}{s}$, which accumulates to 6 ms in one minute. As long as a GNSS fix is acquired once every minute, no drift above the synchronization error of around 10 ms is expected.

6.2. GNSS Simulator

The previous section described the Cooperative Relative Position simulator where the Cooperative Relative Positioning algorithms are evaluated and validated. Prior to perform measurements in

the "uncontrolled" real world, an intermediate step is performed. The GPS receivers used for this work are connected to a GPS constellation simulator. The GSS7790 from Spirent simulates the L1 radio frequency (RF) signals from a set of GPS satellites as they would be received at an antenna at a certain location at a certain time[1]. The user has full control on the simulated satellite orbits, satellite and atmospheric errors or the user position and movement. The RF signals are fed into the antenna connector of the GPS receiver, which will acquire and track the different satellite signals, decode the navigation message and deliver pseudorange, Doppler and carrier phase measurements to compute a position, velocity and time estimate. First, for the purpose of characterizing the used GPS receivers and in order to validate the differentiation of pseudoranges explained in Chapter 5, a set of experiments in a zero-baseline configuration are performed.

A zero-baseline experiment consists of two receivers which are fed with exactly the same GNSS signals received at one common antenna [175]. By using an RF splitter the output of the antenna is guided to two Ublox LEA 4T receivers. Each antenna input is DC-blocked to prevent the antenna supply component damaging the Spirent simulator. The Ublox receivers were configured with an automotive platform model and were set to output raw GPS measurements at 4 Hz. This setup forces a zero-baseline between the receivers, making it an ideal experiment to validate the presented differencing and synchronization algorithms. At the same time, it represents the best possible solution that can be achieved with two receivers, as the configuration forces all allegedly common errors to be equal (i.e. satellite and atmospheric errors) and therefore canceling out completely. In an ideal case, one could assume that noise and multipath would also cancel out completely, as the same signals are applied to both receivers. Nevertheless, the following deviations from the ideal zero-baseline experiment might have an impact on the resulting baseline not being zero:

- Receiver unsynchronization. As the receivers take pseudorange measurements at different points in time the white noise at the input of each receiver is not correlated and thus not canceling out. Possible multipath contributions are also less correlated the larger the time offset.
- Quantization Noise. After downconversion from RF to intermediate frequency, an analogue to digital converter samples the incoming analogue signals and outputs digital samples. This process involves a quantization step that assigns to each output sample the nearest discrete value, thus producing quantization noise. As both receivers are not synchronized with each other, this noise signal is not correlated and will not cancel out.
- Receiver Response. The receiver automatically adapts the carrier and code loop filters to get the best trade-off between tracking accuracy and signal dynamic response. In some cases, this response can be configured, but in general it is not visible to the user. Two independent

[1] Spirent GSS7790 Advanced Multi-Output, Multi-Channel GPS Simulation System. URL http://www.spirent.com/Products/GSS7790

receivers could respond differently to the same input.

The Spirent's SimGen software has been used to set up different test scenarios. SimGen enables to vary the power level of the signals of single satellites. Errors, including atmospheric delays, satellite ephemeris and satellite clock errors and multipath, can be activated. Also the movement of the receiver antenna can be simulated by using a predefined ground vehicle motion model.

The next sections present the experiments and the results of the performed tests activating and deactivating certain errors. To present the results, both, pseudorange and the pseudorange double differences, are displayed. However, pseudorange signals are not practically displayed. The large variation of the pseudorange measurements due to satellite movement, and satellite and receiver clock drift, cause the measurements change by hundreds of meters every second and, thus, hiding any effect caused by noise, multipath or atmospheric errors. For this reason, the Code Minus Carrier (CMC) signals are displayed. As the name indicates, the CMC observable are computed by subtracting the carrier phase from the code measurement[2][229]. Recalling Equations 3.1 and 3.3, it is possible to define

$$\rho_{\text{cmc}} = \rho - \Phi = N \cdot \lambda + 2 \cdot \epsilon_{\text{ion}} + \epsilon_{\text{mp},\rho} + \epsilon_{\text{mp},\Phi} + \epsilon_{\text{n},\rho} + \epsilon_{\text{n},\Phi}. \tag{6.14}$$

The ρ_{cmc} observable is free from satellite and clock biases, satellite position errors and the tropospheric delay. On the other hand, the ionospheric delay ϵ_{ion} is doubled due to its opposite sign in pseudorange and carrier phase measurement. The unknown number of cycles, or ambiguity, N is a constant offset in the CMC observable. The remaining components are multipath and noise on both the pseudorange ($\epsilon_{\text{mp},\rho}$ and $\epsilon_{\text{n},\rho}$) and the carrier phase ($\epsilon_{\text{mp},\Phi}$ and $\epsilon_{\text{n},\Phi}$). The noise on the carrier phase, as described in Chapter 3, is around two orders of magnitude smaller than on the pseudoranges and the multipath on the carrier phase is smaller than $\lambda/4$.

6.2.1. Static Scenario - No errors

In this scenario, a static position of the receivers with a regular constellation of GPS satellites is simulated. All satellite and atmospheric errors are deactivated, while the power of the signals is maintained at a high value. The aim is validating the double differencing technique with Doppler extrapolation proposed in Chapter 5. Figure 6.20 shows the pseudorange CMC and pseudorange double difference over a period of 200 seconds. Both signals are around zero and have a noisy characteristic. The varying receiver-satellite range is canceled in the CMC signal in Figure 6.20a, and, since the ionospheric delay for the scenario is zero, only the noise of pseudorange and carrier-phase is depicted. The double difference measurement in Figure 6.20b is around zero since the baseline between the antennas is of zero length. Only the noise of four pseudoranges contributes

[2]The code measurement is actually the pseudorange estimate. Both terms are used interchangeably in this section.

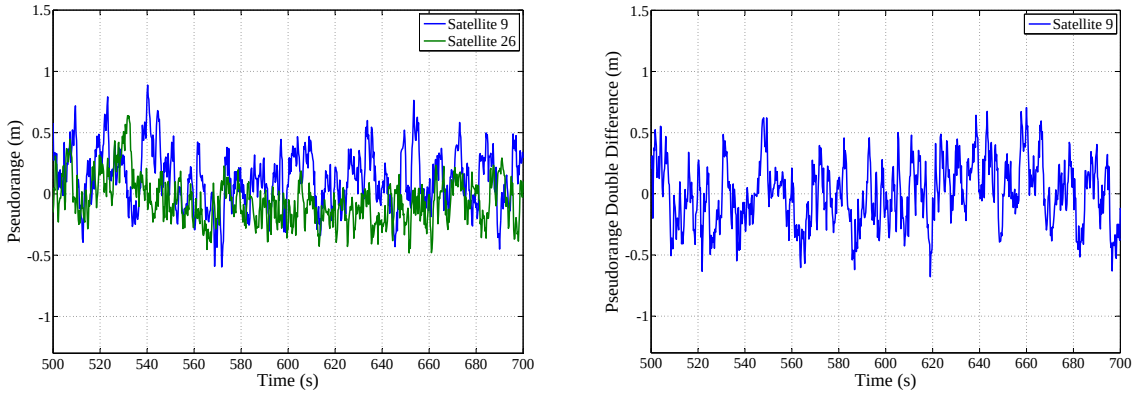

(a) Pseudorange CMC (b) Pseudorange Double Difference

Figure 6.20.: Pseudorange CMC and pseudorange double differences in a zero-baseline test setup for two example satellites.

to the measurement. It can be observed that the noise variance is increased by performing double differences.

Figure 6.21 shows the pseudorange double differences and their mean and standard deviation over a period of 900 seconds. The mean values of the signals are zero for three double difference measurements, as expected in a zero-baseline experiment. A random error corresponding to the noise on all four double differences still remains in the signal. The standard deviation for this error is below 40 cm. To further assess this random error in the pseudorange double differences, the signal power of the satellites was decreased stepwise from 20 dB to -5 dB with respect to -130 dB nominal power. A low carrier-to-noise density leads to a higher variance in the pseudorange measurement. This dependence, as explained in Chapter 5, is receiver dependent and is a function of the bandwidth of code tracking loop, the integration time and the early-late correlator spacing given by:

$$\sigma_\rho = 4 \cdot c \cdot T_c \sqrt{\frac{\gamma}{\frac{C}{N_0}}}, \tag{6.15}$$

where all variables have been summarized in a common parameter γ. Figure 6.22 shows this relationship. A curve fitting of the sample points to the general form yields a value of 7.5×10^{-4} for parameter γ. Hence, a relationship between the carrier-to-noise measurement and the pseudorange double difference noise is found and can be used to adapt the measurement covariance matrix in the relative positioning filter. This relationship is valid for these receivers and under the assumption that the parameters of the tracking loops do not change over time.

In order to incorporate the pseudorange double difference measurements into a Bayesian filter it is important to analyze the statistical distribution of the errors. On the one hand, the time correlation of the double differences is analyzed. Figure 6.23a shows the autocorrelation for the pseudorange double differences in time. The double differences have a time correlation of approximately 4 s,

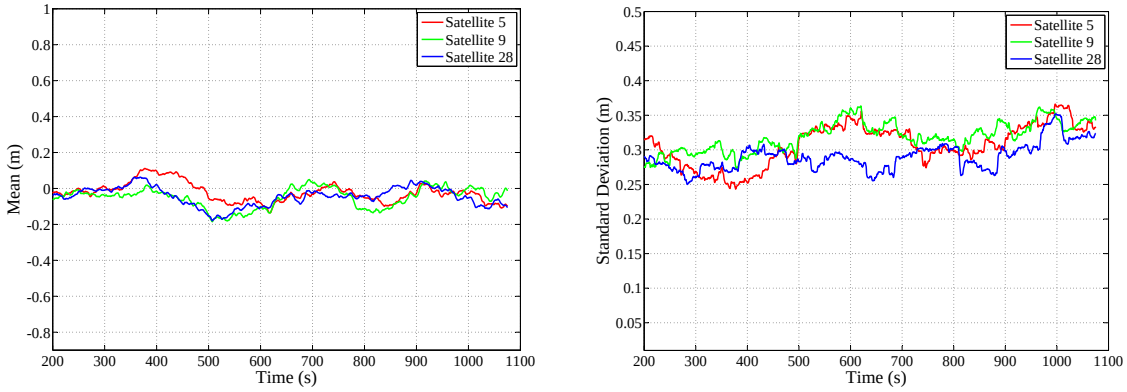

(a) Mean (b) Standard Deviation

Figure 6.21.: The left figure shows the mean of the double differences, which is around zero for all three satellites. The right figure is the standard deviation, which is around 30 cm. The window length is 125 s.

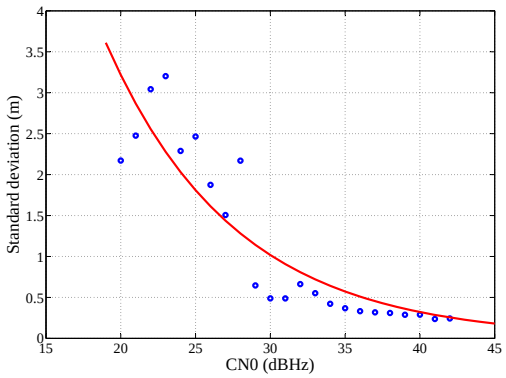

Figure 6.22.: Pseudorange double difference standard deviation over CN0 in a zero-baseline experiment. The error in the double differences grows with decreasing carrier-to-noise ratio in both satellites.

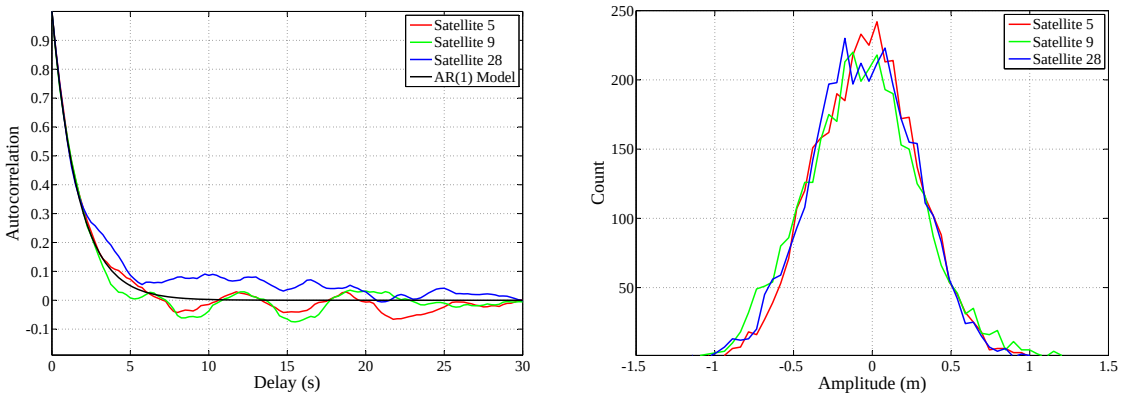

(a) Autocorrelation (b) Histogram

Figure 6.23.: The left figure shows the autocorrelation function of three different pseudorange double differences. A time correlation of about 4 s can be observed in the left figure. The right figure shows a histogram of the amplitude of the pseudorange double differences. A similarity test shows that the shape of the distribution resembles a Gaussian curve.

yielding a Delay-lock Loop (DLL) bandwidth of 0.25 Hz. In black, the autocorrelation of an autoregressive model of order 1, AR(1), with a model parameter ζ_1 equal to 0.855 proofs to match correctly the behavior of the pseudorange double difference noise. Thus, this observation violates the first Markov assumption that measurements in a Bayesian filter shall only depend on the current state and not on previous states or previous measurements. However, in the scope of this work the suboptimal solution is considered and its consequences have been analyzed using the Cooperative Relative Vehicle Simulator. This results were presented in Section 6.1.2.

On the other hand, it is important to know if the assumption of a Gaussian distribution for the noise in the pseudorange double differences holds. Figure 6.23b shows a histogram of the amplitude of the double difference signals. The shape of the histogram suggests that the remaining noise is to be modeled according to a normal distribution. A Kolmogorov-Smirnov normality test confirms the hypothesis of being Gaussian distributed noise at a significance level of 5 %.

6.2.2. Static Scenario - Common errors

To demonstrate the correct cancellation of common errors in the pseudorange double differences, an atmospheric delay has been modeled using the Spirent simulator. This is modeled choosing a set of parameters for the Klobuchar model [169] that are applied on the RF signals. The error is different on each satellite and varies over time. The delay caused by the simulated ionosphere ranges from 2.14 m to 11.25 m. Additionally, a tropospheric delay is simulated using a tropospheric model specified in STANAG 4294 [230]. This causes a delay ranging from 2.7 m to 27.5 m. Figure 6.24a shows the pseudorange CMC signal to three satellites. While the CMC

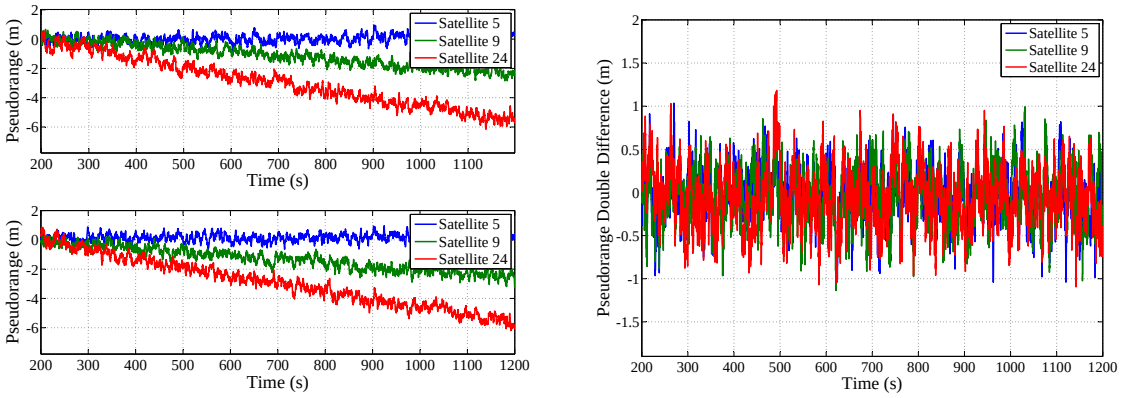

(a) Pseudorange CMC for Ego & Target

(b) Pseudorange Double Difference

Figure 6.24.: The left figure shows the pseudoranges to satellites 5, 9 and 24 at both receivers. The increasing delay is caused by the modeled ionospheric delays. The right figure shows the resulting pseudorange double differences. The ionospheric delay modeled on the SV's signals varies from 2 m to 12 m.

signals in Figure 6.20 were constant around zero, it can be clearly seen how the pseudoranges show now an increasing delay. While the satellite moves, the delay changes due to the different propagation of the signal through the atmosphere. The contribution of the ionosphere is doubled according to Equation 6.14. Unfortunately, the CMC signals hide the effect of the troposphere, as the associated delay is equal on code and carrier signal. The pseudorange double differences in Figure 6.24b, however, do not show any increased error or offset. The variance of the signal and its mean show similar values as in the previous error-free scenario. In this way, it has been verified that a double difference procedure cancels out common errors on the pseudorange measurements.

6.2.3. Static Scenario - Multipath errors

In order to assess the impact of multipath, three different multipath models haven been simulated, namely a *fixed offset multipath model*, a *Doppler offset multipath model* and a *ground reflection multipath model*.

The *fixed multipath model* simulates a second delayed replica of the GNSS signal on a separate channel. The delay of the second signal affects both the code and the phase of the carrier, however, in this model this initial offset stays constant over time. A different phase offset causes a different interference between both paths. Figure 6.25a shows the interference for a phase offset of zero between the direct path (blue) and the a delayed path (red) with 50 m delay and 3 dB attenuation. Figure 6.25b shows the same delayed path but with a phase offset of π. The resulting pseudorange estimation error varies from about 10 m to -10 m. Different time delays for the second path, with different relative phase and different loss have been simulated using the Spirent simulator in order to analyze its impact on the double differences. The hypothesis is

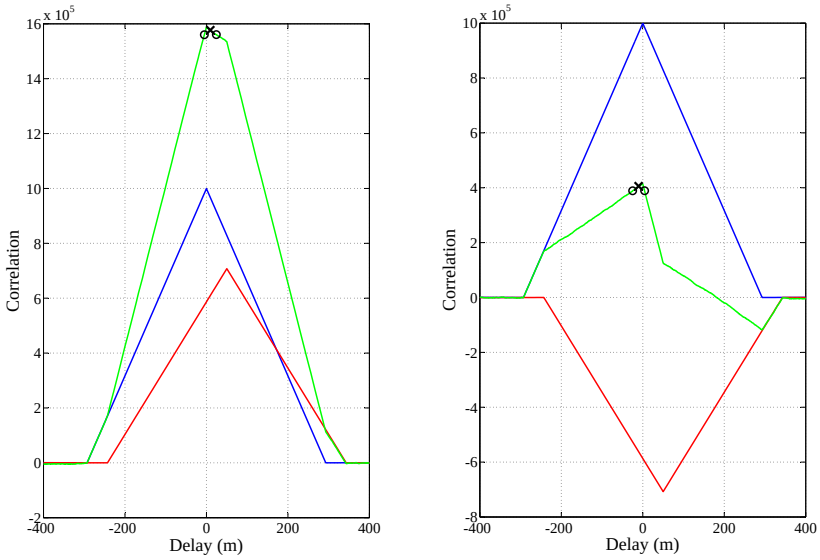

(a) Constructive (b) Destructive

Figure 6.25.: Pseudorange error in the code correlator produced by a second 3 dB attenuated and 50 m delayed path with phase delay zero (6.25a) and π (6.25b). The direct path is represented in blue and the delayed path is represented in red. The green curve represents the code correlator output (early-late spacing is 0.1 chip and integration time is 1 ms.) The estimation error for the left figure is 10.49 m and -10.19 m for the right figure.

that the fixed and time invariant offset will bias in the same way both receivers and will cancel out when performing double differences. Figure 6.26a shows the CMC curves for three satellites at each receiver. Different steps every three minutes correspond to a change in the delay of the second path. From minute 10 to minute 37 an offset of around 10 m and phase delays from 0 to 2π have been simulated. Then, from minute 37 to 55, the delay increases stepwise to approximately 50 m. From minute 55 on, a delay of approximately 10 m and decreasing loss of the second path is simulated. Since ionospheric errors are deactivated and considering Equation 6.14, the offset in the signals is due to multipath and noise in both pseudorange and carrier phase. As the latter can be considered negligible, the offset is mainly a consequence of the multipath on the pseudorange. At first glance, both receivers have similar offsets, which would confirm the hypothesis that multipath is canceled out when performing double differences. Figure 6.26b, however, shows that a remaining offset of 1 m to 2 m is transferred to the pseudorange double differences.

This indicates that the fixed offset is not completely canceled out after differentiation. Nevertheless, the figure shows that this bias is small in relation to the offset of the second path. As a conclusion one could say that, although the receivers are of the same model, each of them gives a slightly different pseudorange estimate in the presence of a reflection. This difference biases the

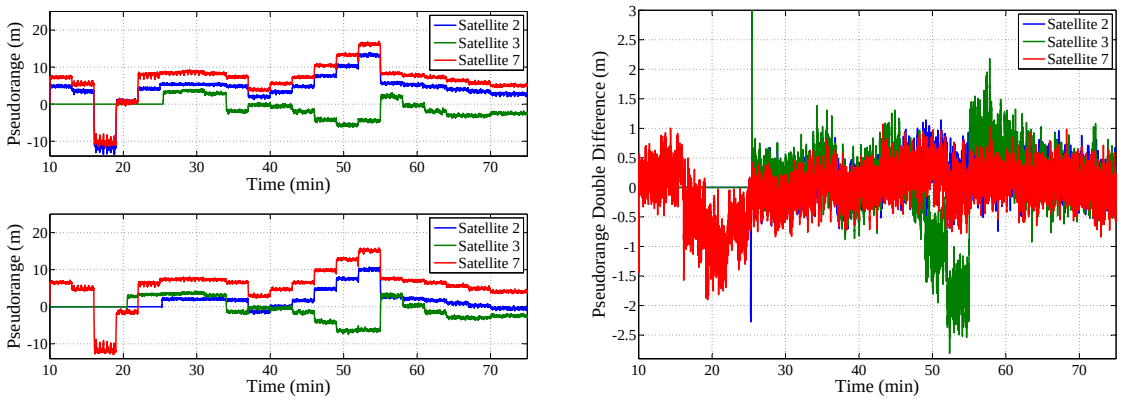

(a) Pseudorange CMC Ego & Target

(b) Pseudorange Double Difference

Figure 6.26.: The left figure shows the CMC for satellites 2, 3 and 7 at ego and target receiver with a fixed multipath offset model. The curves at zero at the beginning of the simulation are satellites that are still not acquired. From minute 10 to 37 a delay of around 10 m and varying phase offset is simulated. From minute 37 to minute 55 the offset is increased stepwise from 1 m to 50 m. From minute 55 an offset around 10 m is decreased in loss from 1 dB to 12 dB. The right figure shows the resulting pseudoranges double differences for satellites 2, 3 and 7.

pseudorange double differences.

The *Doppler multipath model* is an extension of the fixed multipath model, where the delayed and attenuated second path has a Doppler offset with respect to the direct path. The Doppler offset produces a change in the phase of the second path, and this way changes the sign of the interference periodically. Depending on the Doppler offset the tracking loops are able to track this periodic change or might only show an offset in the pseudoranges. Doppler offsets ranging from 0.1 Hz to 200 Hz have been simulated every three minutes starting at minute 10. These values would correspond to the Doppler shift experienced by a receiver moving directly towards a reflector at a speed of 0.07 $\frac{\text{km}}{\text{h}}$ and 137 $\frac{\text{km}}{\text{h}}$ respectively. The second path has a delay of 15 m and an attenuation of 3 dB. Figure 6.27a shows the resulting double differences.

The Doppler offset of 0.1 Hz creates periodic disturbances to the double differences every 10 s. This disturbance is created when both paths interfere negatively and the signal vanishes. This could be verified by looking at the CN0 measurement over time for both receivers, where a periodic interference pattern can be recognized. A Doppler offset of 1 Hz does not seem to be harmful. At 16 minutes, the 5 Hz Doppler is activated and meter disturbances occur to all double differences that get smaller after two minutes. The 10 Hz (minute 19) and 30 Hz (minute 22) Doppler shifts generate errors in Double Differences of up to several tenths of meters. But also here, after a transient phase of approximately one minute, the code loops converge and track the direct path, yielding a double difference value around zero. High Doppler shifts (80, 120, 160 and 200 Hz) do not impact the double differences as the interference pattern changes rapidly and gets averaged

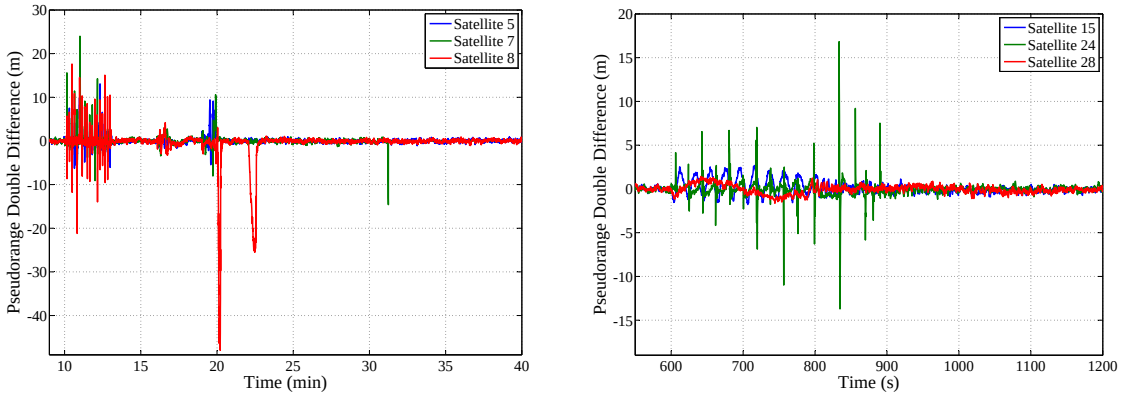

(a) Doppler Offset (b) Reflector

Figure 6.27.: The left figure shows the Pseudorange double differences for several satellites with a Doppler multipath model. Different Doppler offsets ranging from 0.1 Hz to 200 Hz are simulated every three minutes starting from minute 10. The delay of the second path is 15 m and the attenuation 3 dB. The right figure shows the pseudoranges double differences for a movement towards a reflector from 50 m to 0 m. At 600 s the multipath model is activated. At 780 s the movement starts. The variations in speed occur smoothly.

out by the tracking loops.

The *ground reflection model* simulates a second path arriving at the antenna after reflecting on the ground. This test can be regarded as a combination of the previous two tests. In contrast to the fixed offset model, here the delay between the direct and the reflected path changes with the movement of the surrounding. This delay change will create a Doppler offset between both paths. A static receiver at a certain height will experience a relatively slow interference due to the changing elevation of the satellite, which will create a changing interference pattern due to the changing phase offset. In this test the height of the antenna changes from 50 m to 0 m at 0.1 $\frac{\text{m}}{\text{s}}$, which corresponds to Doppler offsets between the paths around 0.5 Hz. Figure 6.27b shows the resulting pseudorange double differences for the descent. At 600 s the ground reflection model is activated, while at 780 s the descent starts.

From 600 s to 780 s a periodic interference can be observed, corresponding to the angular movement of the satellite. Here the Doppler offset is about 0.1 Hz. Errors up to 10 m are possible. The amplitude and the frequency of the error due to the interference is different for each satellite, depending on its elevation. From 780 s to 1250 s, the receivers descend from 50 m to 0 m. The descending speed is changed gradually from 0 $\frac{\text{m}}{\text{s}}$ to 0.1 $\frac{\text{m}}{\text{s}}$ and back to 0 $\frac{\text{m}}{\text{s}}$. This increasing speed creates a increasing Doppler offset between both paths, that produces a faster variation in the pseudorange errors. The delay of the second path gets smaller with decreasing height. The delay is larger for lower elevated satellites, as for instance satellite 24.

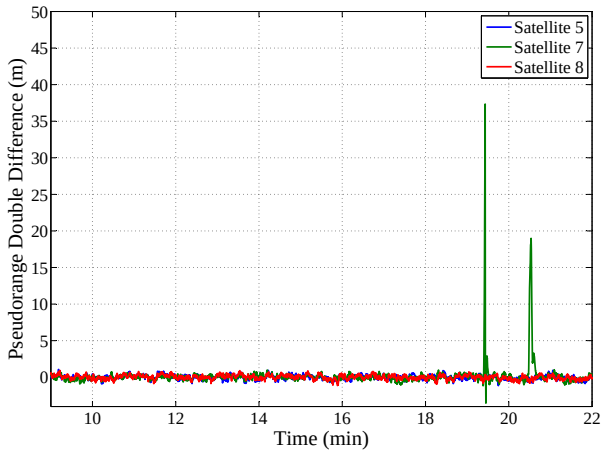

Figure 6.28.: Pseudorange double differences for three satellites in a dynamic test. The receivers experience high speeds up to 80 $\frac{m}{s}$ and high accelerations up to 15 $\frac{m}{s^2}$. The signal towards a low elevation satellite (satellite 7) experiences a loss of lock during the 15 $\frac{m}{s^2}$ acceleration and deceleration.

It can be concluded that static or slowly changing multipath signals (below 5 Hz) produce meter-level errors on pseudorange double differences for a zero-baseline setup. Fast varying multipath components (above 10 Hz Doppler shift) are averaged out in the DLL of each GNSS receiver and have a negligible impact. The zero-baseline setup regarded in this section represents the scenario with highest possible correlation between the receivers. Multipath propagation is a strongly local phenomenon, where the signal interference patterns at two locations can be completely different. Consequently, in a setup with two antennas at different locations (e.g. on two different vehicles), the multipath is expected to impact in a even stronger way the pseudorange double differences.

6.2.4. Dynamic Scenario

A dynamic scenario has been simulated, where the antenna accelerates from standstill to a certain speed, moves at constant speed, decelerates back to zero and holds still for one minute. This maneuver is repeated five times for accelerations of 3, 5, 7, 10 and 15 $\frac{m}{s^2}$, while the speed varies from 14 $\frac{m}{s}$ to 80 $\frac{m}{s}$. The purpose of the test is to verify that high vehicle dynamics do not impact the pseudorange double differences. Figure 6.28 shows the pseudorange double differences for this scenario. It can be observed that no errors occur until minute 19. However, the last acceleration and deceleration of 15 $\frac{m}{s^2}$, pushes the tracking loop of a low elevated satellite (satellite 7) to its limit and causes it to loose the lock. During the 80 $\frac{m}{s}$ constant speed drive, the lock is re-acquired. Since the dynamics found in real-world scenarios are well below these values, it is not expected that the used GNSS receiver will have a limited performance for estimating the relative position.

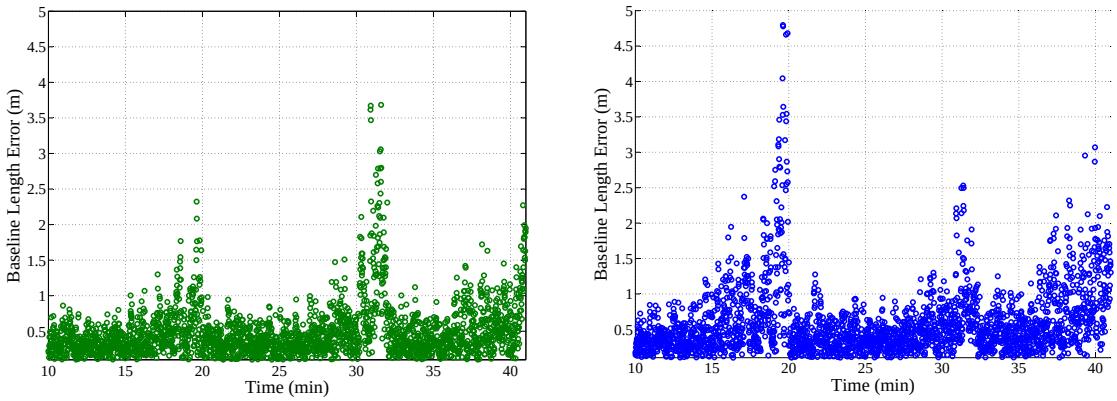

(a) Absolute Position Differencing

(b) Pseudorange Differencing

Figure 6.29.: Baseline error of *absolute position differencing* (left) and *pseudorange differencing* (right) with pseudoranges corrupted by noise. From minute 15 to minute 20 the CN0 of the common satellite decreases stepwise from 40 dB Hz to 30 dBHz. From minute 25 to 32 a set of satellites not including the common satellite are decreased in power accordingly. From minute to 37 to 41 the power of all satellites is decreased together.

6.2.5. Baseline Estimation

The previous analysis has focused on the pseudorange double difference signals. Now, the estimation of the baseline by differencing absolute positions and by pseudorange differentiation as explained in Chapter 5 will be regarded. For this purpose, the previous zero-baseline test setup is used. First, a scenario with only noise is analyzed. A constellation of 11 satellites is simulated for a 42 minute period. The power of the GNSS signals is increased and decreased during the simulation. A nominal value of 44dBHz is set for all satellites at the beginning of the simulation. First, the power of the common satellite is decreased (minute 15 to 20). Then, the power of all satellites but the common satellite is decreased (minute 25 to 32). Finally the power of all satellites together is decreased stepwise (minute 37 to 41). Figure 6.29 shows the magnitude of the baseline error for both the *absolute position differencing* and the *pseudorange differencing* solution using a Least Squares (LS) algorithm. Both epoch-wise solutions yield an unbiased estimate of the baseline. Increasing the errors on the common satellite has a strong impact in *pseudorange differencing*, since it translates to higher errors on all double differences, while for *absolute position differencing* it is averaged out with the other pseudoranges in the LS algorithm. Therefore, it is important to use a satellite with a good Line-of-Sight (LoS) as the common satellite. When all signals are degraded equally, *pseudorange differencing* results in slightly higher errors than *absolute position differencing*.

Next, common errors are activated in the constellation simulator. An ionospheric delay is simulated in the RF signal using one set of Klobuchar parameters, while a different set of Klobuchar

parameters is used for modeling the ionospheric delay before computing the position solution using a LS. The purpose is to cancel only partially the actual ionospheric delay. Table 6.2 shows the set of Klobuchar parameters used for the simulated RF signal and for the model in the LS algorithm[3]. As shown in Table 6.3, the relative error in modeling the ionospheric delay with the second set of Klobuchar parameters ranges between 20 % and 37 %. As explained in Chapter 5, in practice the Klobuchar model cancels approximately half of the ionospheric delay. Thus, these values represent a rather conservative situation.

Figure 6.30a shows how both approaches correctly estimate the baseline. Using the same constellation of satellites in each receiver, *absolute position differencing* correctly cancels out the common errors. Similar behavior of *absolute position differencing* and *pseudorange differencing* is observed for other correlated errors that can be activated in the simulator, as for instance, satellite ephemeris errors or satellite clock errors.

When one of the receivers tracks one different satellite, the residual ionospheric error induces a bias in the baseline estimate using *absolute position differencing*. This is shown in Figure 6.30b. In this case one of the receivers was including the low located satellite 18 in its position computation algorithm, thus obtaining a biased position estimate. Depending on the position of the satellite, the baseline error distributes on the different baseline coordinates. A low located satellite, as in this example, produces a horizontal baseline error, while higher located satellites shift the position in the vertical direction. The different components of the error are displayed for *pseudorange differencing* in Figure 6.31a and for *absolute position differencing* in Figure 6.31b. The horizontal components of the baseline error are always below 0.5 m for *pseudorange differencing*, while the horizontal components reach up to 1.5 m of error for *absolute position differencing*.

This test demonstrates the practical usage of pseudorange double differencing for relative positioning using low-cost GNSS receivers. The numerical values confirm also the theoretical result from Chapter 5. The differentiation of absolute positions can cause biased baseline estimates of over one meter when the vehicles use different satellites for computing the baseline. This value can even be higher when, in exceptional situations, the atmospheric errors are incorrectly modeled in the receiver (e.g. storm fronts or solar bursts) or the GNSS control segment incorrectly estimates the satellite positions and clock biases. With the differentiation of pseudoranges, it is assured that only the satellites common to both receivers are used and that, consequently, common error components always cancel out and thus the resulting baseline estimate is free of any bias.

[3] In Table 6.2, sc stands for the unit semicircles. 1 sc is equal to 180°.

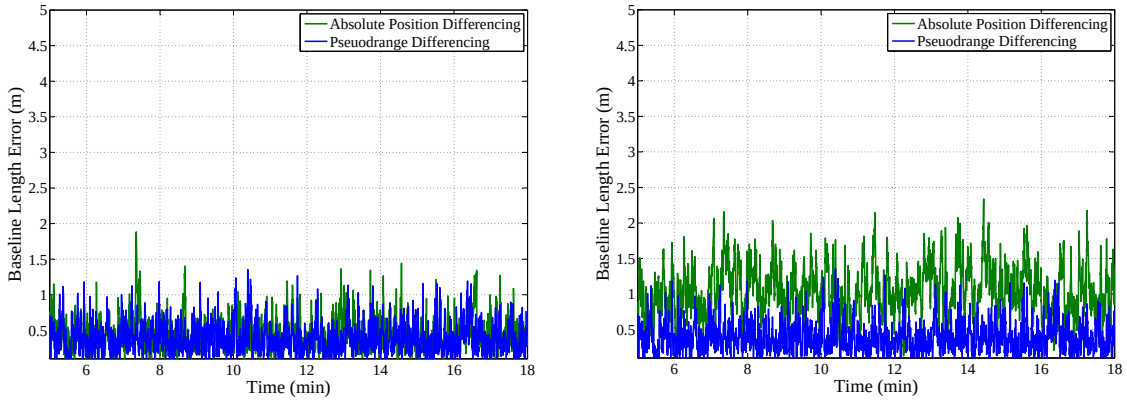

(a) Same Set of Satellites (b) Different Satellites

Figure 6.30.: Baseline error of *absolute position differencing* and *pseudorange differencing* with pseudoranges delayed by the ionosphere. The left figure shows both methods using the same set of pseudoranges, yielding unbiased baseline estimates. In the right figure one of the receivers tracks one additional satellite, yielding a biased estimate of the baseline when using differencing absolute positions. *Pseudorange differencing*, on the other hand, produces an unbiased estimate of the baseline.

Table 6.2.: Klobuchar Parameters

Applied to	**Alpha**	**Beta**
RF-Signal	$0.0168\ \mu s$ $0.0000\ \frac{\mu s}{sc}$ $-0.1192\ \frac{\mu s}{sc^2}$ $0.0596\ \frac{\mu s}{sc^3}$	$122\,900\ s$ $-32\,770\ \frac{s}{sc}$ $-196\,600\ \frac{s}{sc^2}$ $-65\,540\ \frac{s}{sc^3}$
Least Squares	$0.0197\ \mu s$ $0.0000\ \frac{\mu s}{sc}$ $-0.1100\ \frac{\mu s}{sc^2}$ $0.0500\ \frac{\mu s}{sc^3}$	$130\,000\ s$ $-32\,000\ \frac{s}{sc}$ $-196\,000\ \frac{s}{sc^2}$ $-65\,000\ \frac{s}{sc^3}$

Table 6.3.: Ionospheric Error: Simulated vs. Modeled

Satellite	5	13	15	18	24	28	30
RF-Signal (m)	7.35	4.032	5.26	8.39	10.87	4.47	6.75
Least Squares (m)	9.04	5.05	6.65	11.56	13.65	5.58	8.46
Divergence	22 %	25 %	26 %	37 %	25 %	24 %	25 %

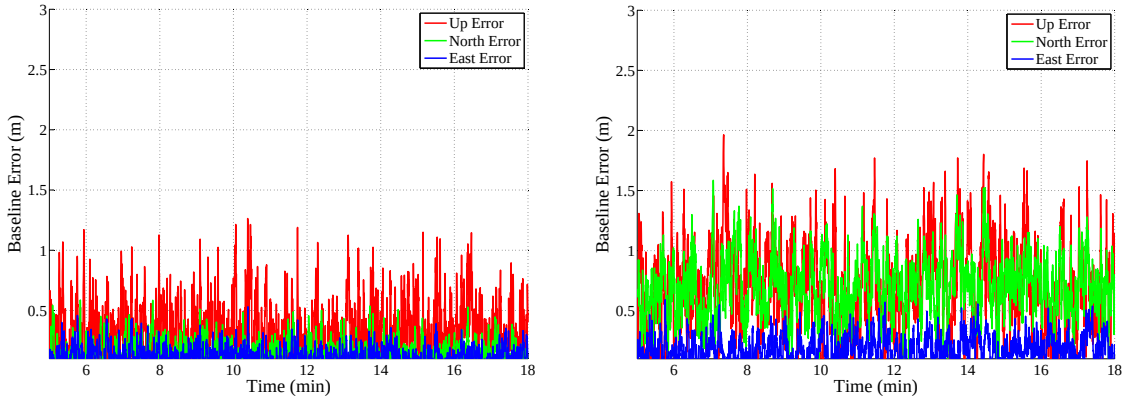

(a) Pseudorange Differencing (b) Absolute Position Differencing

Figure 6.31.: Instead of the norm of the baseline error, all three ENU coordinates of the error are displayed here. It can be observed that the horizontal errors of *pseudorange differencing* are below 0.5 m, whereas, one of the horizontal error components of *absolute position differencing* climbs as high as 1.5 m.

6.3. Summary

This chapter aimed at bridging the gap between the theoretical analysis in Chapters 4 and 5 and the real-world evaluation in Chapter 7. This was achieved by evaluating and verifying the performance of the proposed cooperative relative positioning approach in controlled test environments.

A relative position vehicle simulator has been used to artificially produce a reference position and kinematics of two vehicles and a set of satellites. All sensor outputs inside both vehicles, namely the GNSS measurements, the inertial sensor measurements and the speed measurements have been simulated in both vehicles. It has been verified that the along-baseline constellation in an urban canyon affects the lateral baseline estimate. It could be tested that it is possible to have a bounded relative position estimate with only three orthogonal satellites, i.e. two pseudorange double differences. With only two satellites the relative positioning error increases without bound and its growth can only be reduced by having an appropriate baseline prediction.

It has been demonstrated that it is important to include acceleration and turn rates in the proposed kinematic relative motion models when working at 10 Hz update rate. Sub-centimeter relative positioning errors can be expected during comfortable maneuvers. Extreme maneuvers require higher update rates to keep the prediction relative positioning error below 1 m.

The Full 3D Inertial filter is able to estimate in an optimal way the speed, the acceleration, the heading and the heading rate of the vehicle. In the absence of GNSS measurements, CAN speedometer and non-holonomic constraints make it possible to limit the longitudinal speed error and, with the help of the on-board gyroscopes, maintain the heading error below 1° (3σ) in a

period of one minute. The zero-rotation assumption makes it possible to estimate the biases of the gyroscopes in the first seconds when the vehicle is at a standstill.

With a GPS constellation simulator, the performance of the GNSS pseudorange double differences for relative positioning has been analyzed in a hardware-in-the-loop setup using the receivers, that will also be used in the real-world experiments in the next chapter. The synchronized double differences are verified to have Gaussian errors with zero-mean and a 1σ deviation of 30 cm at high carrier-to-noise ratio. The relationship between carrier-to-noise ratio and noise standard deviation for these receivers has been presented. Further on, it was found, that the noise error on double differences is not uncorrelated, but has a time correlation of 4 seconds. It has been demonstrated that ionospheric and tropospheric delays are correctly canceled out. Multipath, however, was found to cause biased pseudorange double difference estimates in a zero-baseline setup due to the synchronization of pseudorange measurements. The baseline between two antennas can be estimated by using pseudorange double differences with sub-meter accuracy in the horizontal components. The baseline estimated by differencing absolute positions, was found to be biased by over one meter, when each receiver tracked a different set of satellites.

Chapter 7.

Experimental Evaluation in Real World Environments

The sensor fusion concept for cooperative relative positioning of vehicles presented in Chapter 5 will be evaluated in real-world driving conditions in this chapter. First, the test setup consisting of two vehicles with installed GNSS receivers, inertial measurement units and speed sensors and Vehicle-to-Vehicle (V2V) communication transceivers is presented. Next, the reference system used to evaluate the performance of the cooperative relative positioning approach is introduced. The driving scenarios, along with their special characteristics, will be described next. Finally, the performed test runs for assessing the cooperative relative positioning system are presented in detail. On the one hand, GNSS-only tests are performed to analyze the quality of the Global Navigation Satellite Systems (GNSS) measurements in different driving environments and to understand the advantage of subtracting pseudoranges over differencing absolute positions. On the other hand, the cooperative approach based on sensor fusion is evaluated in all three environments with regard to its accuracy, reliability and availability.

7.1. Experimental Setup

The experiments were performed using two test vehicles. The first vehicle, acting as the ego vehicle, was a Mercedes G400. The second vehicle, playing the role of the target vehicle, was a Renault Clio 3. The main difference between the ego and the target vehicle is that the former is equipped with the reference system that will be presented in Section 7.2. In the performed experiments both vehicles drive behind each other, the target vehicle in front of the ego vehicle.

A cooperative system requires that information is exchanged between the participants by means of a suited communication technology. The work presented in this theses requires the ego and target vehicle to exchange sensor measurements with each other. For the experimental evaluation however, all measurements from the sensors are logged on-board on an automotive computer in each vehicle and no information is exchanged in real-time. The data is processed offline and the

(a) Mercedes G400 (b) Renault Clio 3

Figure 7.1.: Test vehicles used in this work to acquire real-world measurement data. The Renault Clio 3 acted as the target vehicle, which is tracked by the Mercedes G400, in the role of the ego vehicle.

algorithms are post-mission evaluated. In this way, the practical challenges related to the use of an additional communication hardware are solved. Nevertheless, the impact of a non-ideal communication link on the cooperative relative positioning system will be analyzed by modeling the packet drops and the V2V communication link performance will be assessed separately with real-world experiments in Line-of-Sight (LoS) and non-LoS situations. The following sections will explain in detail the sensors installed inside the test vehicles.

7.1.1. GNSS receiver

Each vehicle is equipped with a Ublox LEA-4T Global Positioning System (GPS) receiver. This mid-range receiver for L1 GPS signals was already introduced in Chapter 6 for the controlled experiments with the GNSS simulator. The GPS receiver is configured to output GNSS raw measurements, i.e. pseudorange, Doppler and carrier phase measurements at a rate of 4 Hz. Along with the measurements towards each satellite, the Carrier-to-Noise Ratio (CN0) ratio is recorded. The receiver itself automatically computes a navigation solution. Hence, receiver position and velocity, as well as clock bias and clock drift are also available at 4 Hz. The navigation motion model for the receiver internal Extended Kalman Filter (EKF) is configured as "automotive". However, as the particular internal functionality of the receiver is unknown, the navigation solution values are logged but only used for validation purposes. Further on, the receiver is configured not to use the European Geostationary Navigation Overlay Service (EGNOS) satellites for ranging, nor for correcting the position solution.

On the roof of each vehicle a magnetic-mount patch antenna from Ublox is placed. This antenna requires a ground plane in order to properly receive the GPS signals. It is an active antenna with a low noise 27 dB amplifier directly connected to the Ublox GPS receiver. The antenna is placed in the center point above the rear axle of each car. The exact location towards the vehicle frame reference point in the front of the vehicle has been precisely measured.

Instead of logging the satellite ephemeris inside each vehicle and consequently consuming processing and storage resources, the broadcasted ephemeris were post-mission downloaded from the International GNSS Service (IGS) network website[1]. This ephemeris data is equal to the one broadcasted by the satellites and should not be confused with other IGS products like post processed ephemerides that are made available after a few days or weeks and have very accurate satellite orbits. The format in which the ephemeris data is downloaded from the IGS network is Receiver Independent Exchange Format (RINEX).

7.1.2. Inertial Measurement Unit

To obtain inertial measurements an Xsens MTx Inertial Measurement Unit (IMU) is installed in each vehicle. The IMU outputs the measurements from the 3-axis accelerometer and 3-axis gyroscope at a rate of 100 Hz. The IMU is attached rigidly to the chassis of the car at a central point above the rear axis. This is the pivot point of the vehicles around which it performs the turns. When mounting the device inside the vehicle, care was taken to align the sensor frame to the vehicle frame. Any misalignment between both axis would yield a non identity matrix $\mathbf{M}_{\omega}$ and $\mathbf{M}_{\mathrm{a}}$ in Equation 5.51 and Equation 5.52 respectively, and, therefore, non-constant biases in the acceleration and turn rate measurements.

7.1.3. Speedometer

Since the year 2001, it is mandatory for vehicles in Europe to be equipped with an On-board Diagnostics (OBD) connector to read various vehicle sub-systems, mainly to monitor the emissions requirements [231]. The OBD standard specifies the connector and the pinout, the electrical interface and the messaging format. OBD can be communicated over five different signaling protocols, including ISO 9114-2, also known as K-line, and ISO 15765-2, commonly known as CAN. While the G400 test vehicle used the former, the Clio 3 communicates over the later. According to SAE J1979, one of the mandatory values that have to be made available through OBD is the vehicle's speed, which is output at both vehicles at a rate of 5 Hz. Unfortunately, the speed measurement given through the OBD interface is subjected to quantization errors due to the effect of rounding to the next whole $\frac{\mathrm{km}}{\mathrm{h}}$, in addition to a speed dependent bias.

For this reason, both sensors were calibrated prior to the tests by comparing the OBD speed output to the speed given by the GPS receivers. A GNSS receiver is able to compute the velocity by measuring the Doppler shift towards at least four satellites as explained is Chapter 5. For the test, the vehicles drove on a highway and on a rural environment. Speed steps of 5 $\frac{\mathrm{m}}{\mathrm{s}}$ from 10 $\frac{\mathrm{km}}{\mathrm{h}}$ to 120 $\frac{\mathrm{km}}{\mathrm{h}}$ were performed. Figure 7.2a and 7.2b show the speed error plotted against the GPS

[1] http://www.igs.org/products

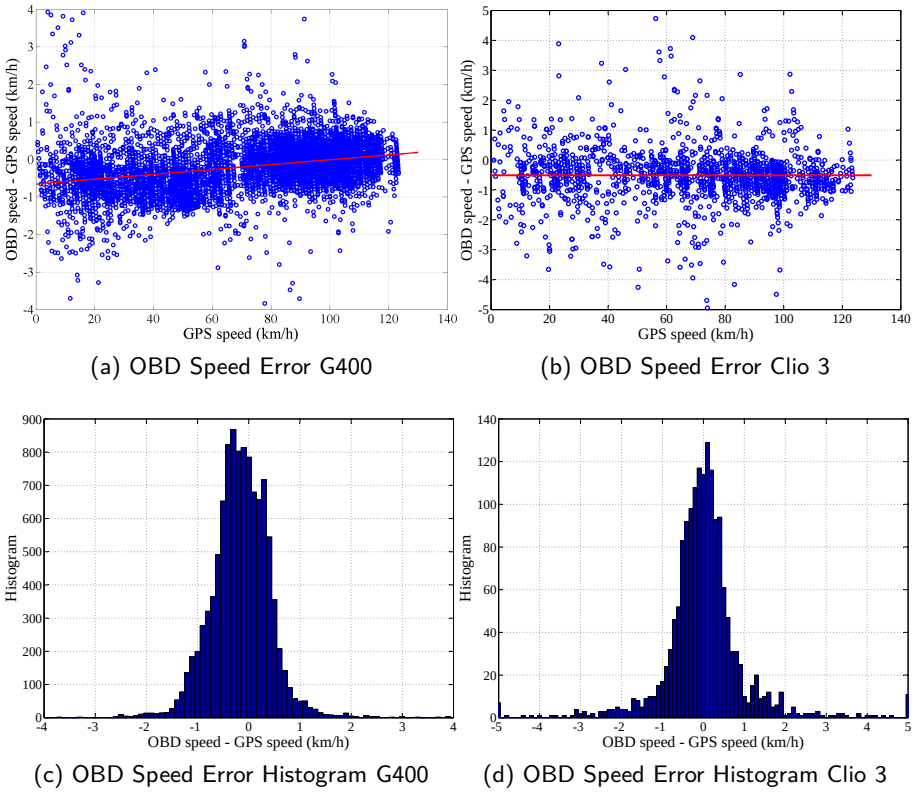

(a) OBD Speed Error G400

(b) OBD Speed Error Clio 3

(c) OBD Speed Error Histogram G400

(d) OBD Speed Error Histogram Clio 3

Figure 7.2.: Speed measurements from OBD compared to GNSS derived speed for both test vehicles. A speed dependent bias can be observed for the G400 test vehicle, while the Clio 3 has a constant bias over the regarded speed range. The lower figures show the bias compensated speed error histogram.

speed for both test vehicles. The red lines are the linear model used to model each of the sensors. In Figure 7.2a, a speed dependent bias of the speed sensor inside the G400 test vehicle can be appreciated. The Clio 3 test vehicle, on the other hand, has an OBD speed error curve that is independent of the true speed of the vehicle (see Figure 7.2b). The residual after applying the linear model is shown in Figure 7.2c and 7.2d respectively. For simplicity, this error is modeled as white Gaussian noise with standard deviation of 0.16 $\frac{m}{s}$ and 0.24 $\frac{m}{s}$ for the G400 and the Clio 3 respectively. In this way, the Kalman filter requirements of zero mean and Gaussianess for this sensor are fulfilled.

7.2. Reference System

As a reference system for the relative position between the two vehicles a Sick LD-MRS automotive laser scanner was chosen[2]. The LD-MRS is a four layer laser scanner which uses a rotating mirror

[2]SICK Vertriebs-GmbH, http://www.sick.com/

(a) Laser Scanner (b) Sensor Placement

Figure 7.3.: The left figure shows the SICK LD-MRS laser scanner mounted on the Mercedes G400 test vehicle. The laser scanner is used as a reference system for the relative position and the relative speed between the ego and the target vehicle. The right figure shows the placement of the different sensors in the vehicle and their measurement frames.

and several pulsed laser beams to calculate the distance towards reflecting objects based on Time of Arrival (ToA) principle. At the default 12.5 Hz frequency, an angular resolution of 0.5° is achieved on each layer. The scanning aperture ranges from 50° to 60°. The laser scanner detects objects in its range of view and tracks their position and their speed, which are given relative to the ego vehicle's reference frame. Hence, the longitudinal and lateral component of the baseline and baseline velocity can be obtained with this reference system every 80 ms. As can be appreciated in Figure 7.3a, the laser scanner is located on top of the front bumper of the G400 test vehicle at a height of 64 cm above the road. A small lateral displacement to the origin of the ego vehicle reference frame has been corrected in the evaluation phase. Figure 7.3b shows the placement of the laser scanner, the IMU and the GNSS antenna with respect to the ego vehicle reference frame.

The laser scanner is one possible reference system for relative positioning [176]. Many research groups favor the use of an Inertial Navigation System (INS)/GNSS approach to obtain a reference position of each vehicle [122, 232, 233]. In many cases, dual-frequency receivers with Real Time Kinematics (RTK) technology are used to this aim. The GNSS carrier phase based positioning solution can reach subcentimeter accuracies in open sky conditions. However, these systems are extremely sensitive and are easily disturbed by satellite signal obstructions, falling back to a pseudorange-only solution. The INS is able to track the position for some time but the errors grow quickly to the order of meters if no fix on the carrier phase is achieved. The laser scanner, on the contrary, is not dependent on good GNSS signal reception and, thus, presents an orthogonal measuring device to the system under test. There are, however, some limitations that should be mentioned. The laser scanner is only able to give a ground truth if the target vehicle drives in front of the ego vehicle in the range of view of the sensor. The target vehicle is detected with a separation of up to 100 m and while located inside the 110° opening angle.

(a) Highway (b) Rural (c) Urban

Figure 7.4.: Three different driving scenarios where cooperative relative positioning has been tested. Not only the quality of the GNSS signals is different in each scenario, but also the vehicle dynamics are different on a highway, on a rural road or while driving in an urban area.

When using a reference system the most important parameter is its accuracy. The accuracy of the system has been analyzed in a series of experiments prior to its usage as a reference system for cooperative relative positioning [176]. For these experiments the baseline towards a static receiver was accurately measured with different devices, including a tape measure, an RTK system and a Leica tachymeter. The experiments revealed a longitudinal accuracy of 10 cm up to a distance of 60 m and up to 40 cm at 100 m range. The lateral accuracy degrades due to the limited angular resolution, with an error of around 1 m at a distance above 100 m.

A further important characteristic is the availability of the reference system. Besides the limited scanning range of the device, environmental effects have an important impact on the performance of the device. Specially rain, snow and fog might degrade the measurement accuracy, making the device not suited to be used in this circumstances. Also the direct sun light during sunrise and sun set hours has a negative impact leading to an increase in the measurement noise.

7.3. Test Scenarios

Three different driving scenarios were chosen to assess the performance of the cooperative relative positioning algorithms. Each of the scenarios has different characteristics regarding GNSS availability and dynamic constraints. Figure 7.4 shows exemplary pictures of the scenarios where the tests were performed.

Highway The test vehicles drove on the A96 highway between Munich and Landsberg am Lech. The highway is mostly two lane per direction with hard shoulder and divided by a grass median strip. The mean total width of the highway is around 30 m. Overhead bridges, foot bridges or gantries are overhead obstacles that are encountered on this highway. Several tunnels longer than 100 m exist as well. On the sides of the highway either flat fields, forests, earth berms or noise

protection walls can be found.

In general, the GNSS coverage is good with line-of-sight view to a high number of satellites. Tracking 7 or more satellites is usual in this environment. However, some of the roadside structures might temporarily block the visibility of satellites below 30° of elevation. Bridges cause sudden short fades in the pseudorange signals, while in tunnels signal tracking is not possible. Large pseudorange errors occur at the entry, when the signal level is low, and at the exit, when the signal has to be re-acquired.

As expected on highways, curve radii are very large, leading to small yaw angular rates. Although no speed limit exists on most parts of the highway, the test vehicles drove at speeds between 80 $\frac{\text{km}}{\text{h}}$ and 120 $\frac{\text{km}}{\text{h}}$. The magnitude of the accelerations on highways is below 1 $\frac{\text{m}}{\text{s}^2}$. The test vehicles drove at varying distance from each other, but always below the maximum range of the laser scanner in order not to loose the reference measurements. The minimum distance was given by the sense for safety and comfort of the ego vehicle driver and could be as low as 20 m. The maximum driving distance was 100 m. The lateral component of the baseline vector between the vehicles is usually low.

Rural The test vehicles drove on various secondary roads in the region south-west of Munich. The rural scenario is characterized by two lane secondary road, with no median and no hard shoulder. The roads pass over fields, through forests and alleys, partially under tree canopy, and through small towns.

The GNSS coverage in the rural scenario is in general worse than in the previously described highway scenario. Trees next to the road shadow and scatter the signal from the satellites, while forests with high trees will even completely block the visibility to the satellites. When driving through towns, two-story buildings will as well shadow the signal and produce multipath effects.

Although the general maximum speed on German secondary roads is 100 $\frac{\text{km}}{\text{h}}$, the test vehicles were usually driving at a speed around 80 $\frac{\text{km}}{\text{h}}$. When passing through towns, the speed limit drops to 50 $\frac{\text{km}}{\text{h}}$, or even 30 $\frac{\text{km}}{\text{h}}$ in pedestrian protection zones. Occasional standstills are encountered in this scenario due to traffic lights or pedestrian crossings. In general, the distance between the vehicles is smaller than on the highway, between 5 m and 50 m. Speed changes and relative speed between the vehicles is generally grater than in the highway scenario.

Urban Finally, the test vehicles drove in the city of Munich, which represents a typical urban environment. Both, large avenues with two driving lanes per direction, as well as narrow streets were regarded, with four to six story high buildings on both sides.

In an urban environment, the direct view to satellites located perpendicular to the road is difficult, with the LoS being highly attenuated. Often, only a refracted path is receiver with the consequent

large bias in the estimate of the satellite-to-vehicle range. Satellites at low elevation are, in general, hard to track as they are easily masked-out by the environment.

The test vehicles drove in this environment at a maximum speed of 50 $\frac{\text{km}}{\text{h}}$. Intersections, traffic lights and surrounding traffic cause the test vehicles to often come to a stand still. Due to regular accelerations and decelerations of the vehicles, the relative speed is large compared to the previous two scenarios. The baseline length varies between 5 m and 30 m.

7.4. Measurement Runs

This section presents the results from the different measurement runs in the three scenarios. Special situations, as for instance a tunnel or an urban canyon will be regarded in detail. The cooperative relative positioning system presented in this thesis aims at estimating the relative position of a target vehicle in an ego vehicle reference frame. In some cases also the relative velocity vector will be regarded. Both, relative position and relative velocity are given by the baseline vector and baseline velocity vector as explained in Chapter 4. To display the error in the baseline estimate, the longitudinal (x-axis) and the lateral (y-axis) components are split up and the error of each, with respect to the laser scanner reference is displayed. To get insight into the statistical distribution of the longitudinal and lateral errors for the whole test run in one driving scenario, a Cumulative Distribution Function (CDF) plot is chosen. The reliability of the cooperative relative positioning filter is evaluated using a 2D histogram which counts the events when the estimation error was above the stated 3σ bound. The size of the 3σ bound is displayed in a different CDF plot to conclude on the availability of a solution.

7.4.1. GNSS-only Relative Positioning

In first place, a dedicated analysis is done using only GNSS measurements from two receivers and without using a Bayesian filter to estimate the baseline. The objective is to compare the benefit of using pseudorange differentiation over absolute positioning in real-world environments and assessing the quality of the GNSS pseudorange double difference measurements.

Static Baseline The first test uses a baseline of constant length on the roof of one test vehicle. The advantage of this configuration is that possible errors of the laser scanner reference system can be discarded. Two Ublox LEA 4T receivers are carried on-board of the Mercedes G400 test vehicle. The antennas are mounted on the roof of the car separated by a distance of 2.13 m. The direction of the baseline coincides with the direction of movement of the vehicle. The true baseline is computed by rotating the true baseline length into the east-north planar coordinate frame by using the estimated headings of both receivers. This approach yields minor errors while

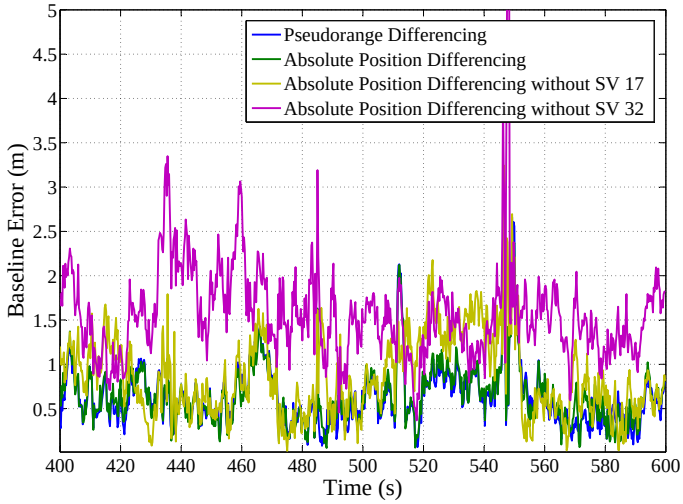

Figure 7.5.: Comparison between *pseudorange differencing* and *absolute position differencing* for a 2.13 m baseline on the top of one test vehicle driving in a highway environment. When one of the receivers is using a different constellation of satellites to calculate its absolute position, it is possible that the relative position suffers from an error above one meter.

driving in a curve, since the heading angles of the receiver in the front and the receiver in back are not exactly the same. This error is minimized by taking the arithmetic mean of both estimates.

A weighted Least Squares (LS) has been used for calculating the absolute position of each antenna, where the weighting matrix has been set according to the CN0 value stated by the receiver for each satellite. Satellites below an elevation angle of 10° have been discarded. The atmospheric delays have been modeled, using the Klobuchar model for the ionospheric delay and a modified Hopfiled model for the tropospheric delay respectively. The *pseudorange differencing* solution has also been calculated using a weighted LS and creating double differences from all pseudoranges above 15° elevation.

Figure 7.5 shows the planar components of the baseline errors for *pseudorange differencing* (blue) and *absolute position differencing* using the same set of satellites in ego and target vehicle (green). Both yield approximately the same errors with a standard deviation of 76 cm for the 200 second section (800 samples). The curves in yellow and magenta represent the solution with *absolute position differencing* where one satellite was taken out artificially from the satellite set of the target receiver. Satellite 17 has an elevation of around 40°, whereas satellite 32 has a lower elevation of around 30°. It can be appreciated that when taking out one of the satellites out of the LS absolute position computation an error in the relative position occurs. For satellite 17, this error is hardly appreciable. However, for satellite 32 a biased estimation of the relative position occurs. Usually, two receivers track the same set of satellites and, consequently, common errors cancel out in *absolute position differencing*. However, if one of the receivers tracks one or several different

satellites an error in the order of 1 m can be expected in real environments.

An analysis on the number of tracked satellites by each of the receivers and the duration of the intervals in which the receivers tracked different satellites is shown in Figure 7.6. The data for this statistic is taken from the measurement runs described in the next section, comprising a 30 minute drive on a highway, another 30 minute drive in a rural environment and a 40 minute drive in an urban area. The left plots show for each of the environments the percentage of time in which the ego and the target receivers were tracking a certain number of satellites (blue and green) and the percentage of time in which they tracked the same set of satellites (red) and when they tracked one or more different satellites (turquoise). The right plots show for each of the scenarios the histogram over the duration of intervals in which a different set of satellites was tracked in each receiver. For the highway environment, 15 % of the time the receivers were tracking one or more different satellites (see Figure 7.6a). In three cases, the duration of this events was above 20 s (see Figure 7.6b). This time is enough for a filter using the absolute positions as updates for the estimation of the relative position to get biased. In the rural area, situations in which the receivers tracked different satellites longer than 30 s occurred (see Figure 7.6d). Due to the blockage of the view to the satellites due to buildings and other obstacles, the probability of tracking one different satellite in urban environments increases to 27 % and that of tracking two different satellites is 5 % (see Figure 7.6e). The duration of these events can be as long as one minute (see Figure 7.6f). This analysis shows that it is indeed important to exchange pseudoranges between vehicles and use only the common satellites to estimate the baseline.

Next, the estimation error using a static baseline setup is presented. The test vehicle drove 20 minutes on the A96 highway from Wessling to Landsberg am Lech. The rural section was performed driving 12 minutes from Wessling to Germering over Unterbrunn and Pentenried. The urban section was a 30 minute journey from the neighborhood of Pasing into the city center and back again. Figure 7.7 shows the CDF curves for the three environments in one common plot.

For the highway scenario good CN0 values yielded a good estimation of the baseline. In 80 % of the time the horizontal baseline error was below 95 cm. Bridges and tunnels produced larger pseudorange errors due to the drop in signal power. Overhead bridges produce errors of about 3 m, while entering a tunnel errors as high as 10 m occur. It is a typical feature of low-cost receivers to track satellite signals, even when very low power levels are available in order to offer high availability. In this case, the receivers still output pseudorange measurements although the signal level has dropped more than 15 dB. The availability of the baseline estimate was lowered due to the two tunnels encountered on the route. These were traversed in 25 s and 30 s respectively.

On both, the rural and the urban environment, the baseline error was disregarded when the vehicles were at a standstill. At standstill, multipath propagation errors have a stronger impact as they are not averaged out inside the receiver's Delay-lock Loop (DLL). In the rural environment, 80 % of the time the error is below 1.6 m. The largest errors are produced while driving under dense

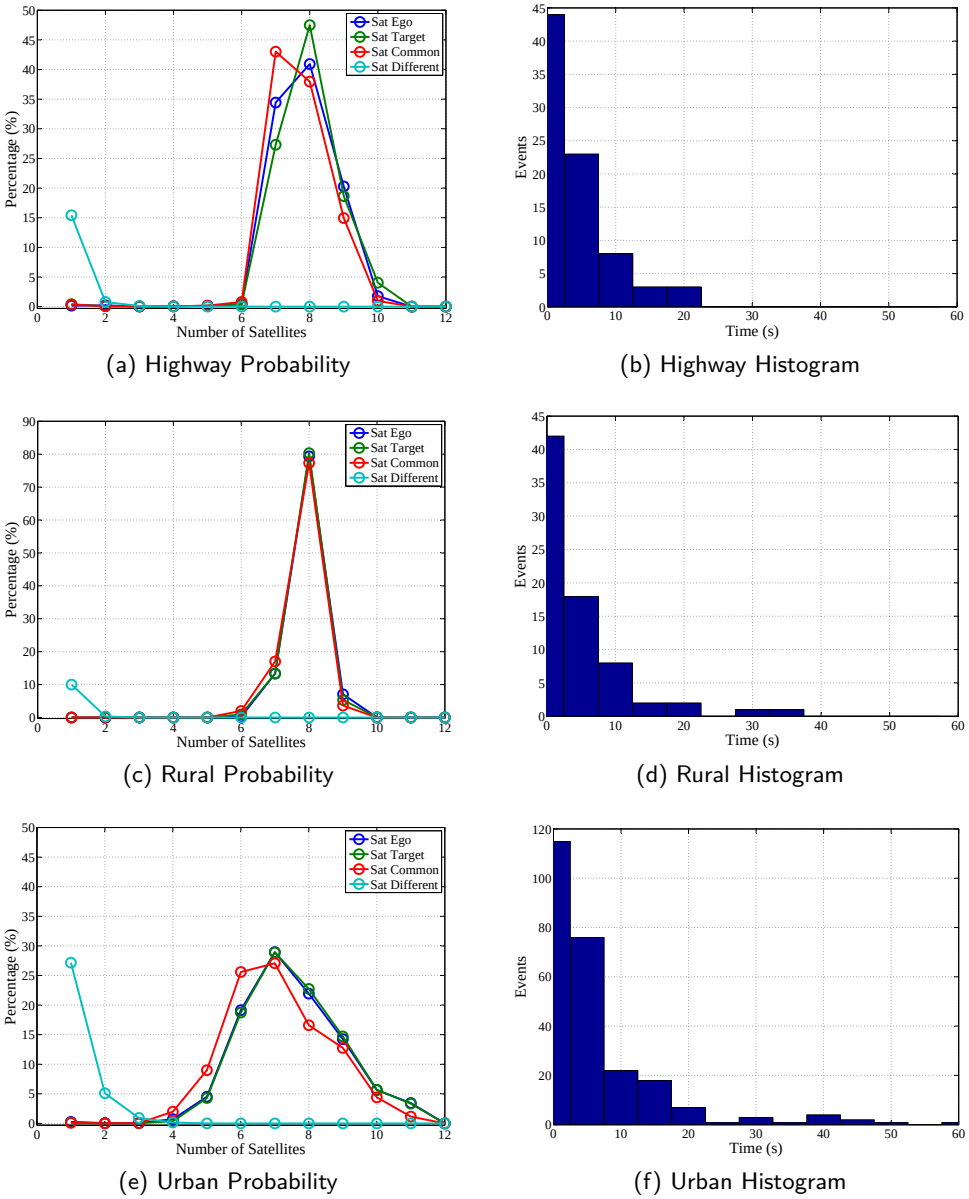

(a) Highway Probability (b) Highway Histogram

(c) Rural Probability (d) Rural Histogram

(e) Urban Probability (f) Urban Histogram

Figure 7.6.: The figures show the probability of tracking a certain number of satellites in each receiver (left) and a histogram over the duration of the intervals in which ego and target receiver tracked different satellites (right) for the three different driving environments.

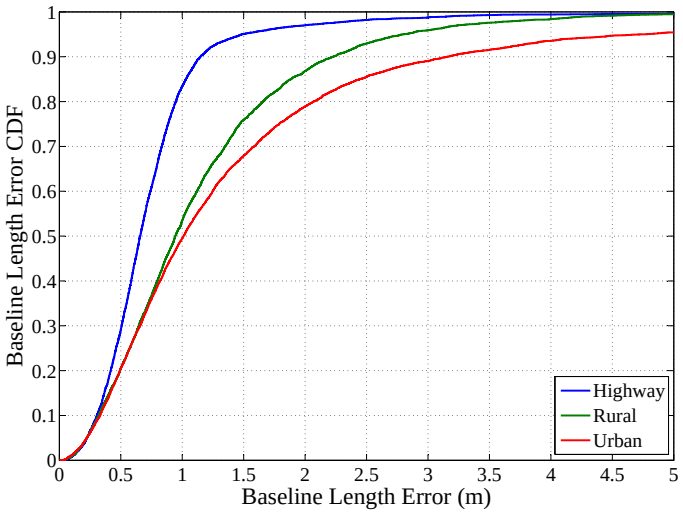

Figure 7.7.: The figure shows the cumulative distribution function for the horizontal baseline error for three different driving scenarios. The experiment was performed using a static baseline on the roof of a vehicle, whereas the baseline is estimated using a weighted least-squares using all pseudorange double differences above 15°.

canopy and through small towns, reaching values of up to 5 m. In the urban area, 80 % of the time the error is below 2 m, but could reach up to 20 m in seldom situations.

These tests aim to show the expected quality in the estimation of the relative position by using only GNSS measurements. In these tests, only the baseline length was regarded and not the orientation of the baseline, which represents a further challenge. When moving towards the multisensor fusion approach several improvements are expected. The use of a Bayesian filter with its time-relationship will help improve short GNSS signal power drops as the ones caused when entering and sorting tunnels and when driving under bridges. This will minimize the effect of sudden multipath induced errors that have a short-term impact on the baseline.

The usage of on-board sensors will help during longer GNSS outages as for instance inside tunnels or in urban canyons when the GNSS outlier rejector minimizes the number of used satellites. On-board sensors will also help while driving on rural roads when partial GNSS degradation occurs while driving through forests or towns.

Zero-Baseline Now, a zero-baseline setup is used to visualize the pseudorange double difference measurements while driving in different scenarios. Pseudorange double differences serve as updates for the baseline estimate in the cooperative relative positioning filter. As explained in Chapter 5, an outlier rejector has been proposed, to discard double differences with large errors that are not likely to fit the a-priori baseline estimate. These experiments give insight of when these errors appear and how large they are.

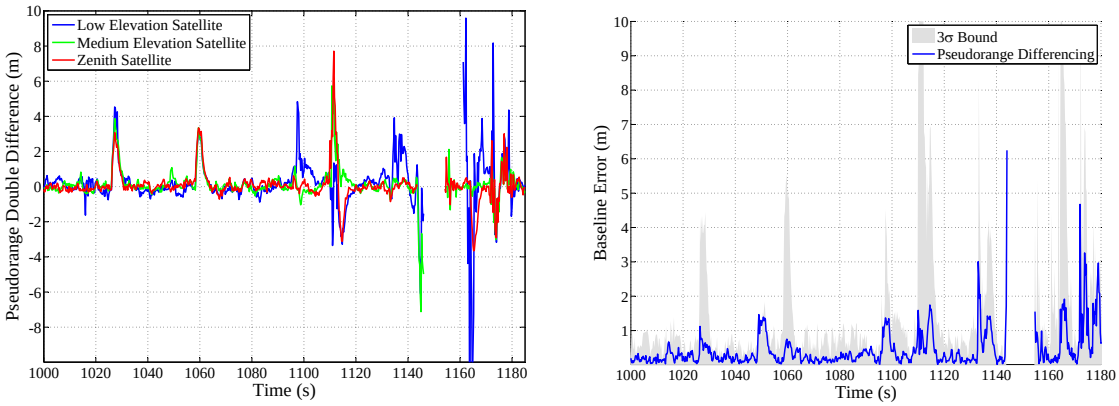

(a) Double Differences (b) Baseline Estimation

Figure 7.8.: The left figure shows the double difference measurements towards three satellites while driving on a highway. The right figure shows the resulting horizontal baseline error estimate when using an epoch-wise weighted least-squares using all double differences above 10°.

A zero-baseline experiment makes it simple to compare the baseline length. The baseline length and therefore also the pseudorange differences would ideally be equal to zero. A zero-baseline configuration has been setup inside the Mercedes G400 test vehicle by connecting two receivers to one antenna mounted on the roof of the vehicle, while driving in different scenarios. Figures 7.8 to 7.10 show on the left side the measured double differences towards three different satellites and on the right side the baseline estimation error and its uncertainty using a weighted LS algorithm.

Figure 7.8a shows that the errors on the double differences are normally below one meter. Two larger highway gantries cause a momentary loss in signal strength producing sudden meter-level error on all double differences (second 1030 and 1060). When crossing below bridges even larger errors can be expected (second 1100). A tunnel is responsible for a complete drop in the GNSS signal power (second 1450). Noise protection walls at the entrance and exit block the view to the low-elevated satellite and errors above 10 m are the result. The receivers output values for the pseudoranges also while entering the tunnel. Consequently, pseudoranges at the entrance of tunnels should be carefully filtered out. During reacquisition after exiting the tunnel, the double differences show large errors. Thus, it is recommendable to wait for at least five seconds until the signals are used for updating the baseline estimate. Figure 7.8b shows the horizontal error when computing the baseline with a weighted LS using all satellites above 10°. It can be seen how the baseline error is below 1 m. Normally, the error stays inside the 3σ bound, indicating that the usage of the CN0 to weight the double difference measurements is, in general, a suited approach. However, some of the over-head obstacles cause the error to exceed the bound, indicating the presence of multipath propagation.

Figure 7.9a shows three double differences while driving in a rural environment. Around second

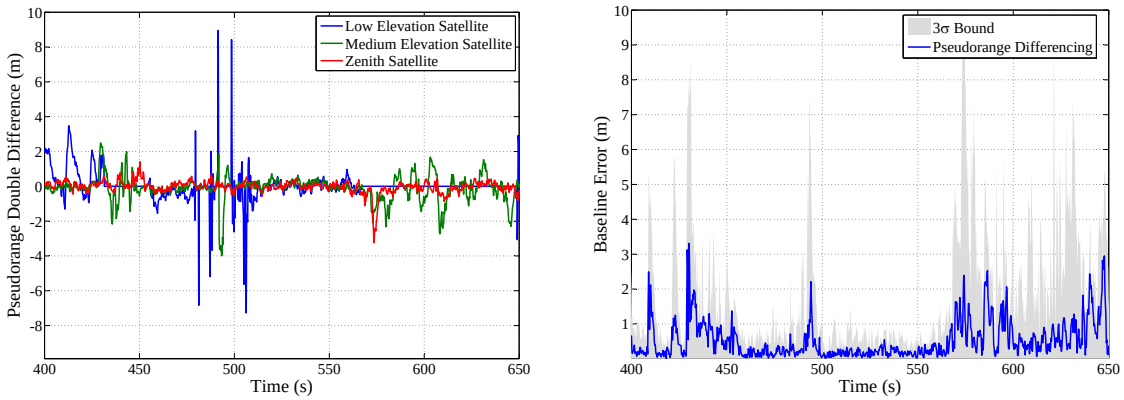

(a) Double Differences (b) Baseline Estimation

Figure 7.9.: The left figure shows three exemplary pseudorange double differences while driving in a rural environment. The right figure shows the horizontal baseline estimation error when processing all double differences above 10° elevation every epoch with a weighted least-squares.

500 the vehicle drives through a small village, causing meter-level errors in the low and medium elevated satellites. Thereafter, the vehicle drives on an open-sky road and the error on all double differences shrinks to below 1 m due to the good signal strength. When driving through a forest from second 570 on, the dense canopy causes the loss of the low elevation satellite and meter-level errors even on high elevated satellites. The baseline estimation error using an epoch-wise weighted LS is displayed in Figure 7.9b. Forests next to the road and villages cause meter-level errors in the baseline estimate due to the drop in signal power. In almost all the run, the baseline error is correctly caught by the baseline uncertainty.

Last but not least, the results for a drive in an urban environment is depicted in Figure 7.10. Please note the larger scaling on the vertical axis of Figure 7.10a in comparison to the previous scenarios. Two characteristic sections around second 1540 and second 1610, correspond to instants when the vehicle was driving through a narrow city street with four to five storey high buildings on each side and a line of trees on one of the sides. Not only the low elevated satellite suffers from large errors above 15 m due to satellite LoS blockage, but also the high-elevated satellite shows deviations up to 4 m. A look on the baseline estimation errors in Figure 7.10b shows that a worse performance can be expected in urban area when compared to the rural and highway environments. Here, the relative positioning errors easily exceed 3 m. Nevertheless, the instants where the 3σ bound is actually exceeded are only a few during the whole run. This is promising, since multipath propagation is an important source of positioning errors in urban environments and whose impact is, in general, not easy to quantify. The figures suggest that a correlation between the CN0 and the occurrence of multipath errors exists and that correlation can be exploited to weight correctly the pseudorange double differences.

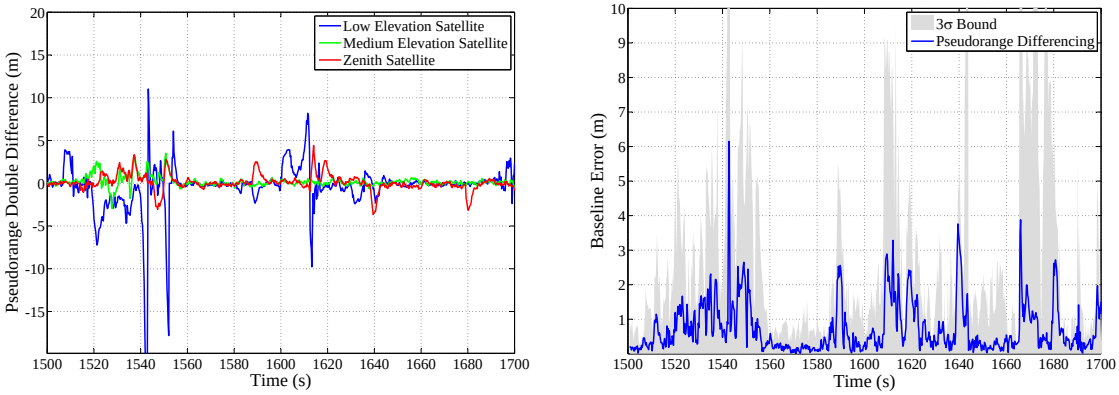

(a) Double Differences (b) Baseline Estimation

Figure 7.10.: The left figure shows the three exemplary double differences while driving in a urban environment. The right figure shows the horizontal baseline estimation error when processing all double differences above 10° elevation every epoch with a weighted least-squares.

7.4.2. Multisensor Fusion Relative Positioning

The previous section has shown the performance of relative positioning using only GNSS pseudoranges in a static-baseline and a zero-baseline configuration. Only the length of the baseline vector was considered, disregarding the orientation of the vector in space. On the highway, the best results are achieved, as a higher number of unobstructed satellites are available. Strong multipath propagation is rather seldom. Nevertheless, full continuity is not achieved due to tunnels that completely block the reception of GNSS signals. The rural, and specially the urban scenario, revealed several meters of errors in the baseline coordinates. The aim of the multisensor fusion approach presented in this thesis is to keep the sub-meter baseline estimation accuracy that is achieved in open-sky environments and bridging the error-prone situations.

For instance, on the highway, the aim is to eliminate the errors when driving below highway gantries and bridges and offer continuity in relative positioning when driving inside a tunnel. In rural environments, the multisensor fusion approach should be capable to bridge small forest sections next to the road or when driving through villages. Longer drives through forests will still remain a challenge on rural roads. In urban environment, high buildings will block the LoS towards GNSS satellites. Additionally, the elevation mask will be increased in order to discard error-prone satellites. Consequently, in urban environments the on-board sensors are expected to help stabilizing the baseline estimate when fewer satellite signals are available.

In the previous analysis, a baseline in east-north coordinates was considered. A relative position in terms of longitudinal and lateral position of the target vehicle in the ego vehicle coordinate frame requires the heading of the ego vehicle. In the subsequent analysis the baseline is given

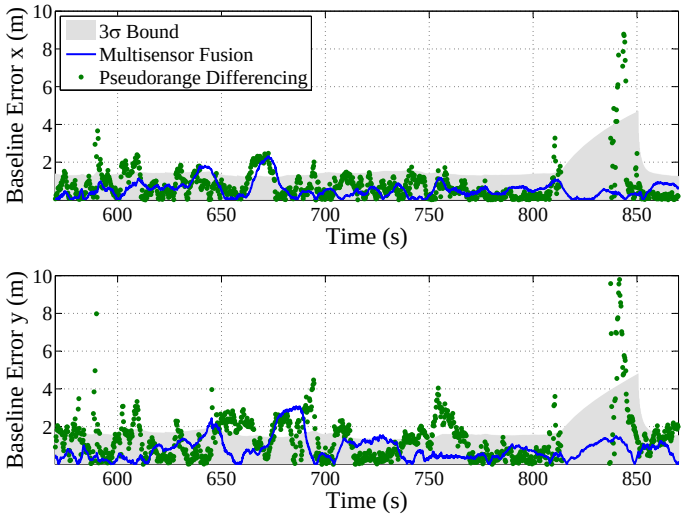

Figure 7.11.: The figures show the error in the estimation of the baseline vector between ego and target vehicle while driving on a highway. Around second 810, the vehicles enter a tunnel and the GNSS measurements are unavailable. Here, the baseline estimate relies solely on the on-board sensors.

in x-y-coordinates of the ego vehicle frame. This is how radar or laser scanners provide its relative positioning measurements and how Advanced Driver Assistance System (ADAS) require the information for collision warning and lane change assistants or for automatic cruise control.

Highway Scenario For the highway test, the vehicles were driving for approximately 30 minutes behind each other at varying distance and different relative speed. Figure 7.11 shows the baseline estimation error in longitudinal and lateral direction for a 300 second period. This section of the highway includes a 300 m tunnel around second 830. In blue the error of the multisensor fusion for relative position is displayed along with its 3σ deviation in gray. In general, the estimation error stays inside the uncertainty bound. This is important in order to trust the relative position estimate. The uncertainty is usually greater in lateral, than in longitudinal direction. This is due to the uncertainty in the yaw angle of the ego vehicle and its rate of change. The green dots represent the snapshot-wise baseline solution using *pseudorange differencing* rotated into the vehicle frame using the ego vehicle yaw. It can be seen, how the sensor fusion approach correctly smooths the strong peaks caused by multipath in the pseudorange double differences. It also correctly bridges the time without GNSS view inside the tunnel from second 810 to 840.

Figure 7.12 shows the error in the estimation of the relative velocity between the target and the ego vehicle. A small error in longitudinal direction of about 0.25 $\frac{\text{m}}{\text{s}}$ remains. When GNSS is unavailable, as for instance during the tunnel around second 830, the longitudinal error enlarges, since speed information falls back to the Controller Area Network (CAN) bus speedometer. The lateral error is about three times as large and, due to its lower observability, the uncertainty is

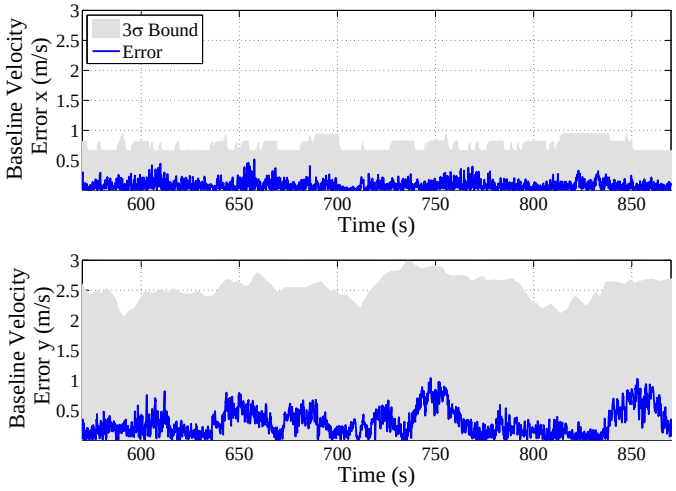

Figure 7.12.: The figures show the error in the estimation of the baseline velocity in the longitudinal component (upper plot) and in the lateral component (bottom plot) while driving on a highway.

above 2 $\frac{m}{s}$.

The CDF for the baseline and the baseline speed accuracy in longitudinal and lateral coordinate for the whole 30 minute trip on the highway is shown in Figure 7.13. It can be seen how 68 % of the time the baseline error is below 1 m and 90 % below 1.5 m. Since good GNSS reception is available, a good heading estimate exists and, consequently, the lateral component is estimated equally well as the longitudinal. The longitudinal baseline velocity error is below 0.15 $\frac{m}{s}$ in 68 % of the time. This good value is also associated to the accurate GNSS speed that is available. The lateral relative velocity has a half the accuracy, due to the driving configuration of the vehicles one behind the other and the consequent observability of the lateral speed.

To compare the benefit of the multisensor approach against the epoch-wise *pseudorange differencing* approach, Figure 7.14 shows the error of both compared to the laser scanner by means of its overall statistical performance in a CDF plot. In 68 % of the time, the horizontal baseline error is reduced from 2 m to 0.9 m by using a sensor fusion with on-board sensors, while at 90 % of the time the error shrinks from 3 m to 1.5 m. Since also the estimation is available while driving inside tunnels, the availability can be increased from 97 % to 100 %.

Figure 7.15a and Figure 7.15b show the reliability assessment of the cooperative approach for relative positioning by counting events in which the error exceeded the 3σ uncertainty. Up to 18 events were counted in longitudinal direction. Most of the events are below 1 m and for a duration of less than 10 seconds. In lateral direction, the number of events is similar but with an amplitude of up to 8 m, but also for short duration of time (less than 5 s). Finally, Figure 7.16 shows the availability CDF. In 90 % of the time the 3σ uncertainty in lateral and longitudinal direction is below 1.6 m and 2.4 m respectively.

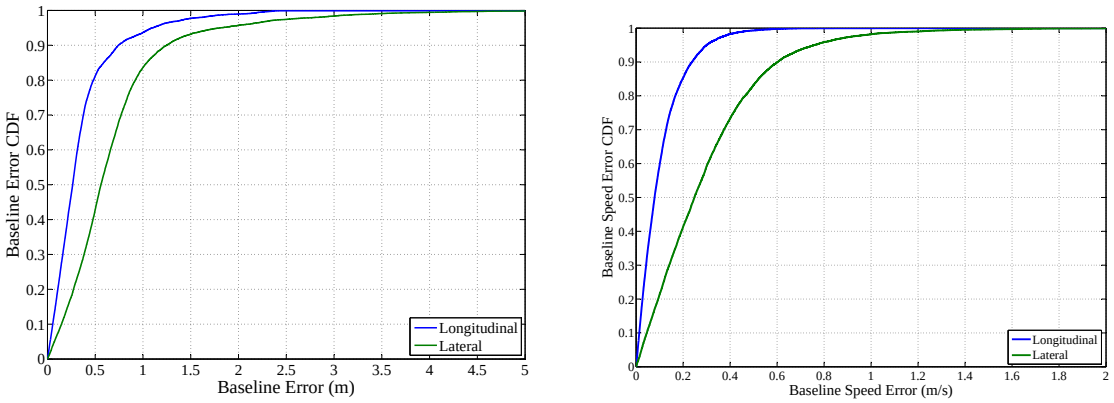

(a) Baseline (b) Baseline Speed

Figure 7.13.: The figures show the CDF curves of the estimation errors in the relative position and relative speed in the highway scenario. The baseline coordinates yields an approximate error of below 1 m (1σ) and similar in both coordinates. Since the target vehicle is driving in the same direction in-front of the ego vehicle, the relative speed is better observed in the longitudinal direction. The errors are small, below 0.1 $\frac{\text{m}}{\text{s}}$ (1σ) due to the high availability of GNSS measurements in the highway scenario.

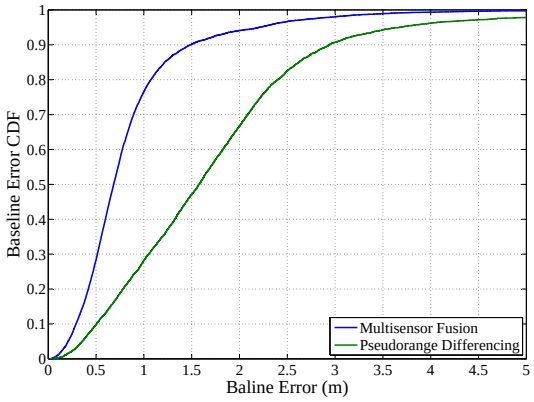

Figure 7.14.: The figure compares the horizontal baseline estimation error CDF curves for the cooperative multisensor fusion approach (blue) compared to the epoch-by-epoch computation of the baseline with pseudorange differencing and a weighted LS (green).

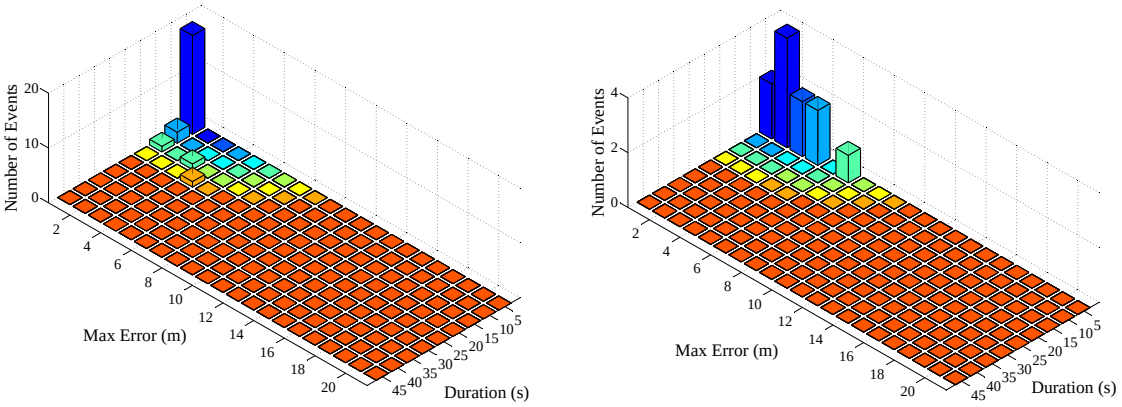

(a) Longitudinal (b) Lateral

Figure 7.15.: The figures display a histogram with the number of times the estimation error exceeded the 3σ bound in dependance of the duration of the exceed and its magnitude in both, the longitudinal and lateral coordinate.

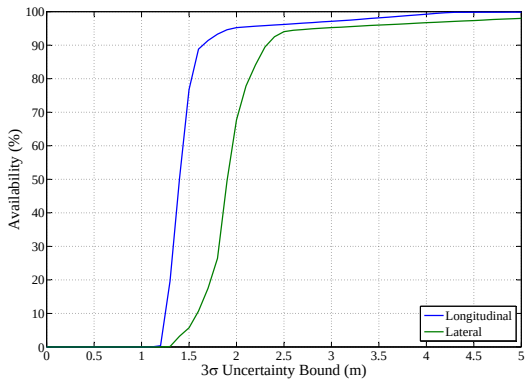

Figure 7.16.: The figure shows the availability of the cooperative multisensor approach for relative positioning in a highway environment.

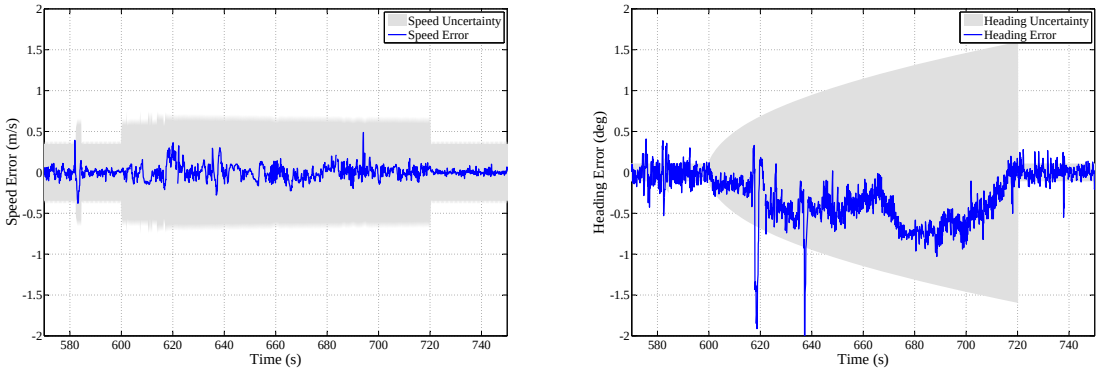

(a) Speed (b) Heading

Figure 7.17.: The figures show the estimation error in vehicle speed and heading during during a 120 second GNSS outage. The speed estimation falls back to the CAN bus speedometer information, while the heading is estimated by integrating the gyroscopes inside the kinematic filter inside the vehicle.

The performance during a GNSS outage of the Fully Bayesian lower kinematic filter presented in Chapter 5 is depicted in Figure 7.17. Here, a 2 minute tunnel between second 600 and 720 was emulated by artificially deactivating the GNSS measurements. Figure 7.17a shows the error in the estimation of the longitudinal speed of the ego vehicle during such an outage. The increase in uncertainty is due to the fact that the CAN bus speedometer has a higher error than the GNSS derived velocity. The error stays bounded and is correctly estimated by the filter. The heading estimation error is shown in Figure 7.17b. The error is not bounded, but grows over time due to the integration of the gyroscope signal. Thanks to the correct estimation of the gyroscope biases a maximum error of 1° is reached in this time interval. This is less than 1 m lateral error for a target vehicle located 50 m in front. The peaks at second 620 and 640 are not due to errors in the heading estimate, but due to multipath errors that corrupt the GNSS heading, against which the estimate is compared to.

In addition, the influence of a realistic communication channel has been evaluated. Obstructions and signal blockage, fading due to multipath multipath propagation or packet collisions lead to an increase in the update delay (see Chapter 5). When this happens, the ego vehicle has to predict the relative position of the target vehicle using the last The aim is to analyze how the relative position of the target vehicle can be estimated when short communication outages occur in a specific scenario. In the first test, Cooperative Awareness Message (CAM) outages of five seconds (50 dropped messages) have been emulated every 30 seconds.

In Figure 7.18, it can be seen how large errors of several meters in the longitudinal component occur every time a communication outage occurs. This is due to the errors accumulated by predicting the longitudinal speed of the target vehicle. Using a CA model helps partly to overcome

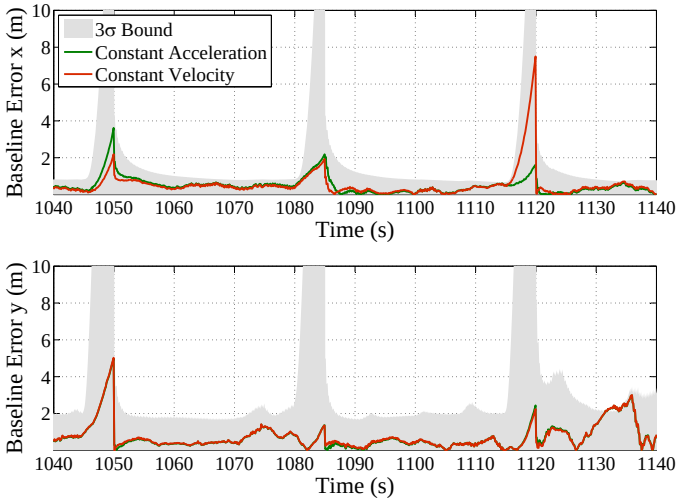

Figure 7.18.: The figure shows the estimation of the baseline in longitudinal and lateral coordinates during a communication outages. Once using a CV (red) and once using a CA prediction model (green)

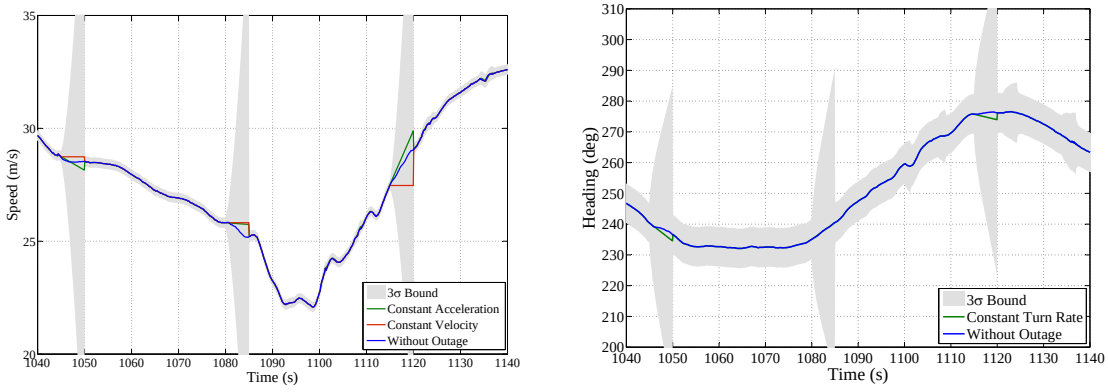

(a) Speed (b) Heading

Figure 7.19.: The left figure shows the estimation of the target vehicle's speed and the right figure the heading during three successive five second communication outages. For the speed estimation, the prediction performance of a CA model (green) is compared to the CV model (red). For the heading estimation, a constant tun rate model is used.

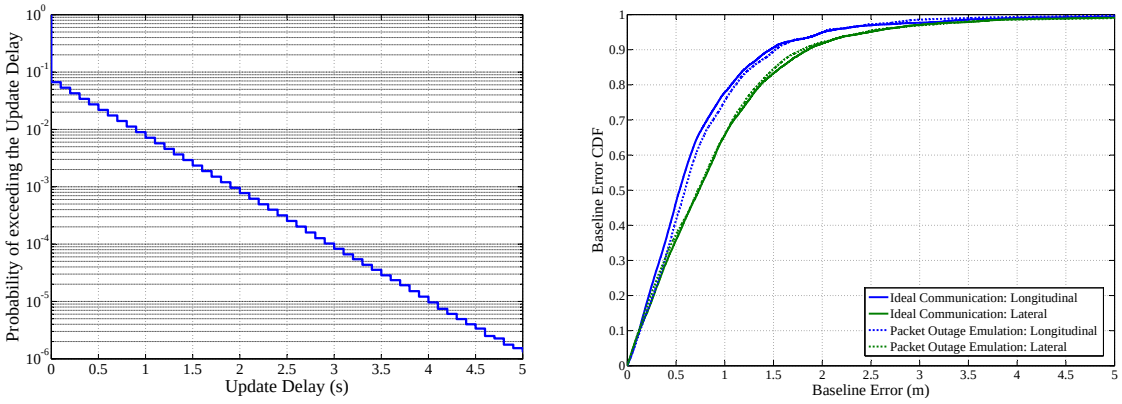

(a) Update Delay (b) Baseline Error

Figure 7.20.: The left figure shows the Update Delay CDF curve for the emulated packet drops applied on the highway scenario. The vehicles transmit with 10 Hz update rate. Hence, an update delay of 2 s corresponds to the loss of 20 consecutive V2V packets. The right curve is the baseline estimation error CDF curve for the whole 30 minute run once with an ideal communication channel and once emulating the drops of packets.

short outages, since the instantaneous acceleration of a vehicle cannot be extrapolated for longer periods of time. This is shown in Figure 7.19a for the same successive communications outages. The lateral component in Figure 7.18 has less errors due to the correct prediction of the heading of the target vehicle. A constant turn rate model, either Constant Turn Rate and Velocity (CTRV) or Constant Turn Rate and Acceleration (CTRA), use the heading rate to predict the heading angle in the next steps. Smaller heading estimation errors can be found in the first and third outage in Figure 7.19b. Nevertheless, the relative positioning filter is able to correctly estimate the uncertainty during the outages and no reliability event has been accounted for.

Since the accurate statistical modeling of the communication channel is not object of research within this thesis a simple and widely used model for correlated packet drops has been used [234]. The Gilbert-Elliot model uses a two-state Markov Model to switch from a receiving state to a not-receiving state [235]. The probability to switch to the not-receiving state was set to 0.2, while the probability to switch back to the receiving state was set to 0.35. This simulation yields an update delay probability displayed in Figure 7.20a. Due to the simple model, the shape of the update delay curve does not correctly reassemble the update delay curve considered in Chapter 5 for a congested highway (see Figure 5.22). By comparing both plots, it can be noticed that a worse case is considered here. Regarding the baseline estimation error in Figure 7.20b, it can be seen how these outages have no practical influence on the overall statistical performance of the relative positioning filter. Thus, the sensor errors and modeling errors still have a stronger impact on the relative position than the possible loss of V2V communication packets.

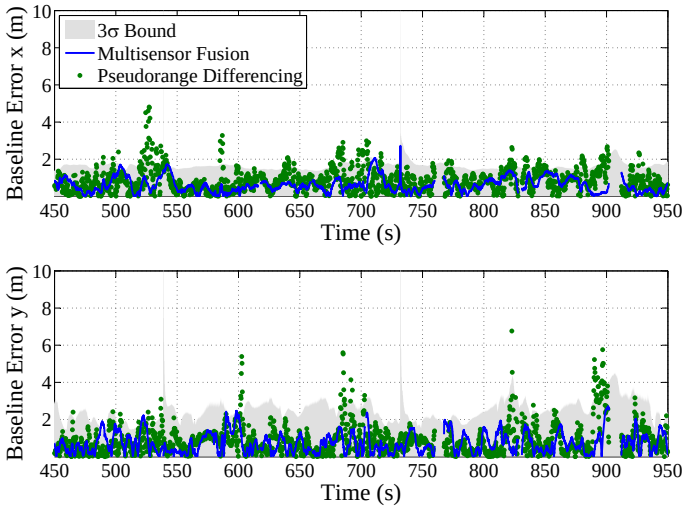

Figure 7.21.: The figures show the error in the estimation of the baseline vector between ego and target vehicle while driving in a rural environment.

Rural Scenario Figure 7.21 shows a 500 second section of the baseline estimation error while both vehicles drive in a rural environment. In blue, the multisensor fusion solution can be compared to the snapshot based *pseudorange differencing* solution in green. Again, the gray area depicts the 3σ uncertainty in the multisensor fusion estimate. As expected, the quality of the GNSS signals is in general worse than on a highway. Satellite shadowing and LoS blockage occur due to trees while driving through forests and buildings while circulating in towns. This leads to fades in received signal power and consequently to errors in the GNSS pseudoranges. Buildings in towns might induce multipath propagation and lead to additional errors in the GNSS pseudoranges. Although, low-elevated satellites are easily masked in a rural environment, normally eight common satellites were available and only in some sections, seven or six common satellites could be used. Around second 540 a section through a small town causes errors in the GNSS pseudoranges. The *pseudorange differencing* solution has errors up to 5 m, while the multisensor fusion is able to stay inside the 3σ bound. The errors in the pseudorange solution around seconds 600, 700 and 900 are due to over-head tree canopy and forests next to the road. Also here errors up to 6 m in the relative position are the result. Since these are only momentary events lasting around 30 s, the multisensor fusion is able to eliminate their impact and stabilize the baseline estimate. Longer drives through deep forests however incur in strong errors.

The overall statistical performance of a 30 minute run in a rural environment is shown in Figure 7.22. Compared to the overall performance in the Highway environment a degradation can be seen in both, the baseline and the baseline velocity. While the longitudinal baseline component stays at around 0.6 m (1σ), the lateral baseline component increases the error from below 1 m in the highway environment (see Figure 7.13a) to around 1.7 m in the rural scenario. 90 % of the time the lateral component of the relative position is below 3 m. The increased error is,

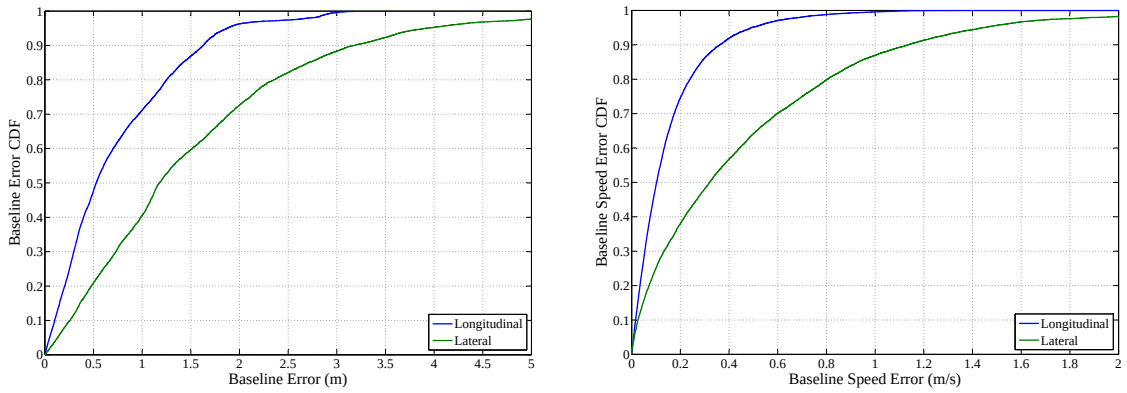

(a) Baseline (b) Baseline Speed

Figure 7.22.: The figures show the CDF curves for longitudinal and lateral error in the estimation of the baseline (left) and baseline velocity (right) while driving in a rural environment.

in general, due to GNSS errors that occur more often in the rural scenarios and that impact the overall error statistic. In the rural scenario often changes of driving direction occur and the lateral displacement is, generally, correctly followed by the relative movement model. In the same way, regarding the baseline velocity in Figure 7.22b, the lateral baseline velocity increases from 0.3 $\frac{\text{m}}{\text{s}}$ in the highway environment to 0.4 $\frac{\text{m}}{\text{s}}$ in the rural case. Both curves, the longitudinal and lateral components flatten out towards higher error values, yielding twice the error in the 90 % bound when comparing highway and rural scenarios.

An increased error can also be appreciated when comparing the multisensor fusion approach to the *pseudorange differencing* snapshot approach in Figure 7.23. In the rural environment, the difference between both is much more pronounced as compared to the highway environment (see Figure 7.14). Although the GNSS pseudorange double differences are strongly degraded in a rural environment (horizontal error of 2.6 m in rural compared to 2.10 m in highway 1σ), the on-board sensors correctly support the estimation of the relative position with only a partial detriment (horizontal error of 1.8 m in rural compared to 1.25 m on highway 1σ).

Figure 7.24 shows the reliability and availability analysis for the rural scenario. A few events of short duration (below 10 s) and small magnitude (below 4 m) happen during the test. Generally, these errors are caused by GNSS signal degradation. However, certain longitudinal errors are caused by strong accelerations and decelerations that are likely to happen in a rural environment, and that were not completely caught by the movement model. Some lateral reliability events occurred in bends, caused by a wrong tracking of the lateral vehicle position, which is a hint that the CTRA movement model is in certain conditions not accurate enough for tracking a real vehicle. Figure 7.25 shows the availability of the cooperative relative positioning system during the 30 minute drive. The longitudinal uncertainty is tightly bounded to 2 m for 90 % of the time. This is a 3σ-uncertainty matching one length of the vehicle. Considering that the width of a standard

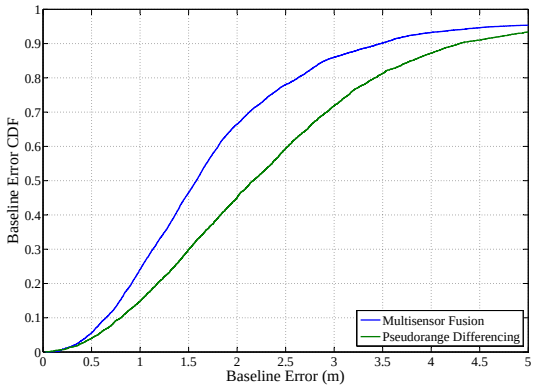

Figure 7.23.: The figure compares the horizontal baseline estimation error CDF curves for the multisensor fusion approach compared to the epoch-by-epoch computation of the baseline with pseudorange double differences and a weighted Least Squares in a rural environment.

rural road in Germany is 2.75 m, the lateral uncertainty spans over two lanes in 84 % of the cases. Thus, in the rural environment it is, in general, not possible to distinguish on which lane a target vehicle is driving solely by using a GNSS-based cooperative approach for relative positioning.

Last but not least, Figure 7.26 shows the estimation of the speed and heading of the ego vehicle with the fully Bayesian kinematic filter for a 250 second section on a rural road. While driving through a forest with overhead tree canopy up to second 2960 speed errors in the GNSS measurements of up to 2 $\frac{\text{m}}{\text{s}}$ can be seen. The filter correctly detects these outliers and falls back to using the CAN bus derived speed. Also the heading estimate has to cope with errors of up to 5° to 10°. The correct use of GNSS quality detectors makes it possible to correctly bridge the gap and use the gyroscope information to predict the heading of the vehicle. The kinematic filter is able to correctly bridge these gaps of GNSS coverage in rural environments and offer an acceptable heading and speed estimates. From 2960 an obstacle free section makes it possible to use again the GNSS information. The errors in the ego vehicle heading are the cause of the increased lateral error in the relative position shown in Figure 7.21 and Figure 7.22a.

Urban Scenario The urban environment represents the most challenging of the chosen scenarios regarding relative vehicle positioning, due to signal blockage and the impact of strong multipath on GNSS pseudorange and Doppler measurements in each of the receivers. The GNSS pseudorange measurements might have errors of several tens of meters, causing a corresponding error on the baseline estimate. For the urban analysis, the test vehicles drove behind each other for 40 minutes around the city of Munich. Figure 7.27 shows a 1000 second snapshot of this drive. In order to correctly display the baseline estimation errors, both vertical axes have been increased to 20 m compared to the previous driving scenarios. It can be noticed how the epoch-wise estimation of the baseline using a weighted LS yields errors above 20 m. Only the section between second

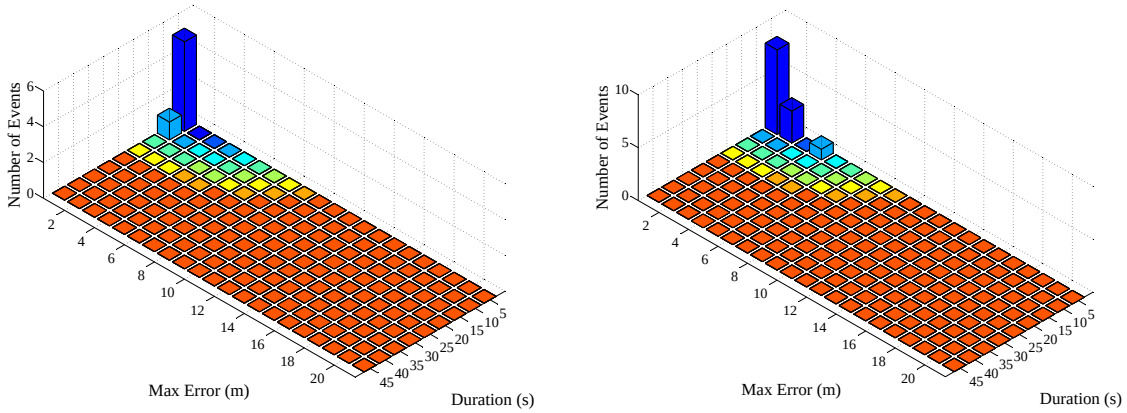

(a) Reliability Longitudinal (b) Reliability Lateral

Figure 7.24.: The figures display a histogram with the number of times the estimation error exceeded the 3σ bound in dependance of the duration of the exceed and its magnitude in both, the longitudinal and lateral coordinate.

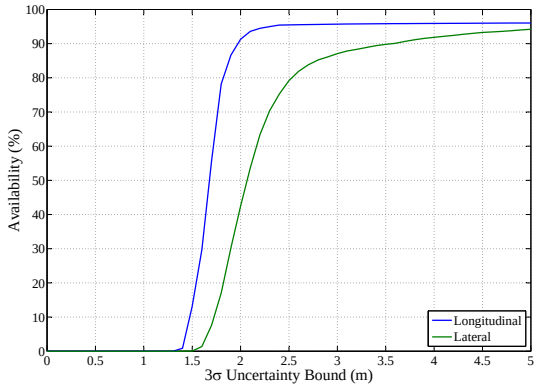

Figure 7.25.: The figure shows the availability of the cooperative multisensor approach for relative positioning in a rural environment.

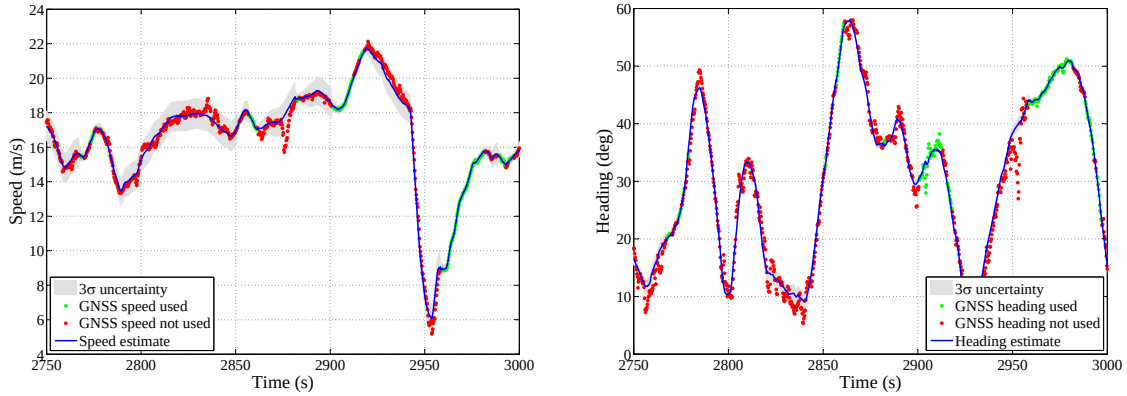

(a) Speed (b) Heading

Figure 7.26.: The figure shows the estimation of the speed and the heading in a rural environment using the fully Bayesian kinematic filter. Unlike the highway scenario, the challenge in a rural environment are not complete GNSS blockages, but overall degraded GNSS reception while driving through forests or towns. Nevertheless, the speed sensor and gyroscope information are able to correctly bridge these gaps.

3220 and 3400 has smaller errors when the vehicles were driving in a large four-lane avenue (Leopoldstraße). The fusion with on-board sensors is crucial to minimize the errors in both coordinates. In longitudinal direction the error is usually below 5 m, but large outliers above 10 m exceeding the 3σ-bound occur in lateral direction.

In comparison to the highway and rural scenarios, the elevation mask has been increased to 30°. The purpose is not to track satellites, whose LoS is likely to be blocked by surrounding buildings and which are probably received over secondary paths. In order to have sufficient double difference measurements, the CN0 threshold had to be lowered to as low as 25dBHz. The consequence is that the used pseudoranges will, in general, have a lower quality. Usually, three to four pseudorange double differences were available to update the baseline estimate.

The overall performance for the 40 minute drive is shown in Figure 7.28. For deriving these CDF curves only the instants when the vehicles were moving were considered. Figure 7.28a shows the CDF curve for the baseline coordinate errors. The horizontal axes have been increased to 10 m, compared to the 5 m from the previous CDF curves in the highway and rural case. As early mentioned, the longitudinal baseline component is relatively bounded to below 4 m in 90 % of the cases. The lateral component has larger errors yielding 10 m 90 %. Regarding the baseline velocity, a decrease in performance can be observed when compared to the rural case. The longitudinal velocity component is below 0.8 $\frac{\text{m}}{\text{s}}$ in 90 % of the time. As will be explained later, this is mainly because GNSS derived speed is not often used due to the large errors it has in the urban environment. The lateral component has a similar performance due to the geometrical disposition of the vehicles and the less observation of the lateral speed through the on board

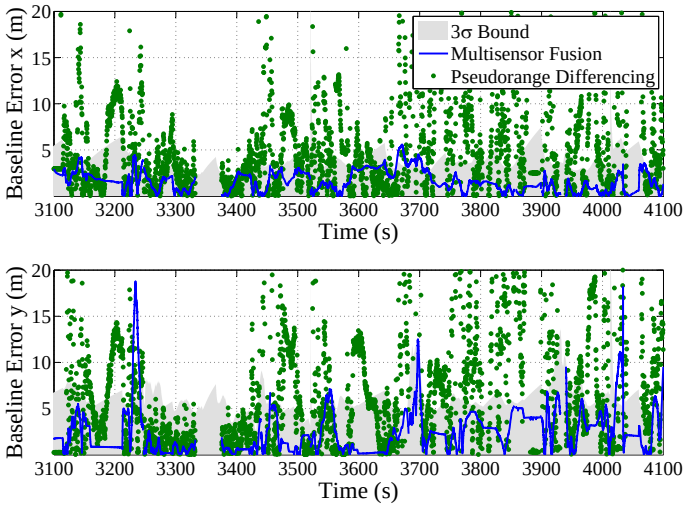

Figure 7.27.: The figure shows the longitudinal and lateral baseline estimation errors for a 1000 second section while driving in an urban environment in blue. In green the epoch-wise baseline estimation is presented.

sensors.

Figure 7.29 shows the reliability analysis in the urban environment. Again, with the help of a two-dimensional histogram the count of the times the estimation error exceeds the 3σ bound in dependance of the duration and the magnitude is shown. In Figure 7.29a, a rather good reliability is found in the longitudinal direction. Only few events occur with meter-level errors and with durations up to 20 s. The event with 17 m error and 40 s duration is related to the initialization of the system, when the heading of the vehicle is unknown, and can therefore be disregarded. A look on the lateral component in Figure 7.29b reveals often, long and large reliability failures. Some events are beyond 40 s and far beyond 10 m. Last but not least, the Figure 7.30 shows the reduced system availability. The reduced number of GNSS signals, the increase in the pseudorange model noise and the prediction of the heading angles for long periods of time cause an increase in the relative position uncertainty. A 3σ uncertainty lower than the size of one vehicle is never obtained. An estimated uncertainty lower than 6 m is achieved 75 % of the time in longitudinal and 52 % in lateral coordinate.

Fortunately, the often stops in the urban environment help estimating the drift of the gyroscope sensors more precisely. This makes it possible to have a better estimate of the heading rate and to use the heading during long periods of GNSS degradation. Figure 7.31a shows the estimation of the heading for a 400 second section driving in Schwabing, a dense built neighborhood in Munich. GNSS-derived heading measurement are strongly corrupted in such an environment and errors above 20° are not seldom (e.g. second 2900). This is mainly due to the influence of reflections and multipath on the sensitive Doppler measurements. The heading estimation inside the lower kinematic filter is able to cope with long heading measurement unavailability. However, the

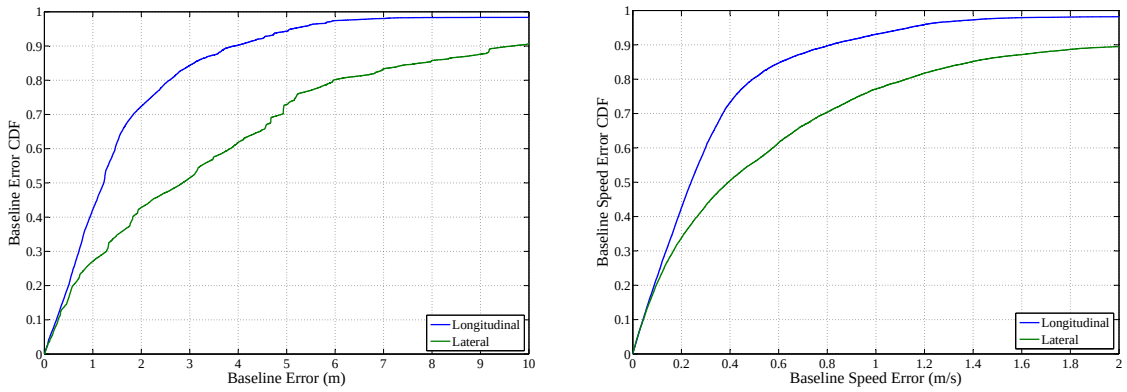

(a) Baseline (b) Baseline Speed

Figure 7.28.: The figures show the CDF curves for longitudinal and lateral error in the estimation of the baseline (left) and baseline velocity (right) while driving for 40 minutes in an urban environment.

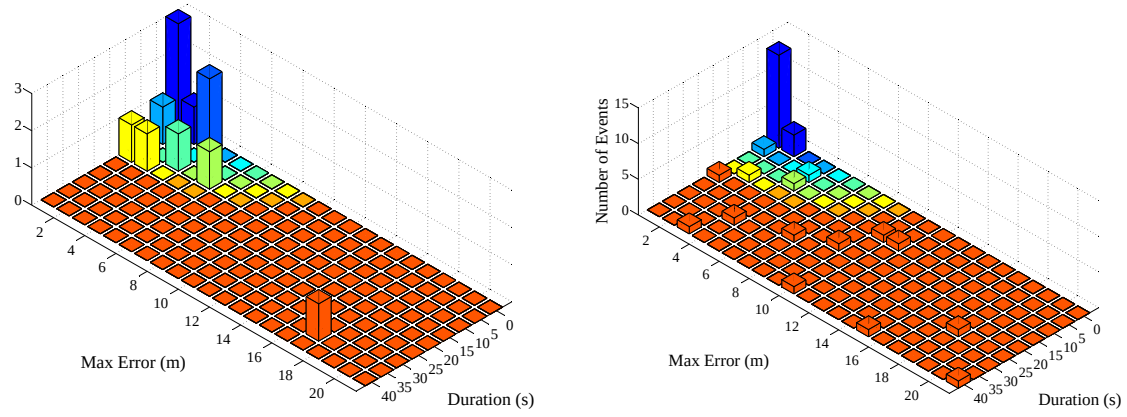

(a) Longitudinal (b) Lateral

Figure 7.29.: The figures display the histogram with the number of times the estimation error exceeded the 3σ bound in dependance of the duration of the exceed and its magnitude in both, the longitudinal and lateral coordinate.

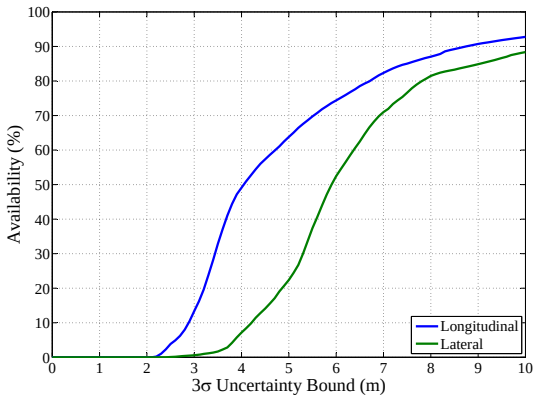

Figure 7.30.: The figure shows the availability of the cooperative multisensor approach for relative positioning in a urban environment.

discriminator of corrupted GNSS heading measurements often fails to reject faulty measurements and strong state updates are performed. These are the main responsible for the large lateral errors in the baseline estimate. The speed estimation by the lower kinematic filter is shown in Figure 7.31b. It can be observed how the filter mostly discards GNSS derived speed measurements and tracks the CAN bus speed instead (e.g. second 2950 to 3000). GNSS derived speed has up to 1 $\frac{m}{s}$ error (e.g. in second 2670).

7.5. V2V Communication

The previous measurements were performed without explicit communication between the vehicles. The sensor data was stored on-board of each vehicle and the cooperative multisensor fusion algorithms were evaluated off-line. One of the advantages of a cooperative approach based on V2V communication is the extension of the awareness range beyond the capabilities of on-board ranging sensors, as for instance radar sensors or laser scanners. In this section, the performance of V2V communication in both LoS and non-LoS situations is inspected [236].

Each test vehicle was equipped with a Cohda Wireless MK5 V2V communication unit. A 5 dBi magnetic-mount antenna was fixed on the roof. The communication unit at the target vehicle was configured to transmit 400 Byte long test messages at 3 Mbps on channel 180 (5.9 GHz) at a rate of 100 Hz. The transmit power was set to 24 dBm. The test messages contained an identifier, an increasing message counter and the position and velocity of the test vehicle. At the ego vehicle, the messages were stored along with the received power and the vehicle's position and velocity.

The first test aimed at evaluating the communication range capabilities of the test setup under ideal conditions. The test was performed in an air-field where a LoS situation could be evaluated. The vehicles started at each end of the runway and drove towards each other to the opposite

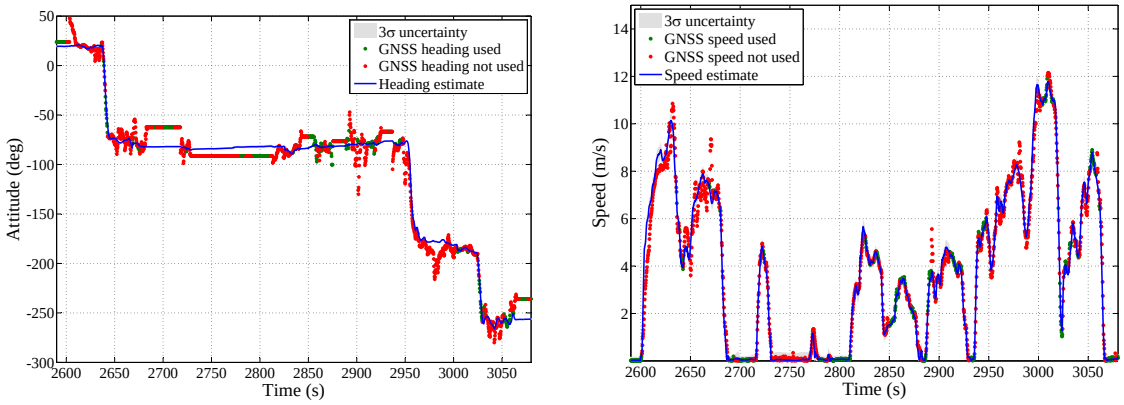

(a) Heading (b) Speed

Figure 7.31.: The figure shows the estimation of the heading and the speed in an urban environment using the fully Bayesian kinematic filter. In green and red the GNSS related heading and speed measurements are displayed. The green ones correspond to measurements that have been used to update the kinematic state, while red measurements have been discarded.

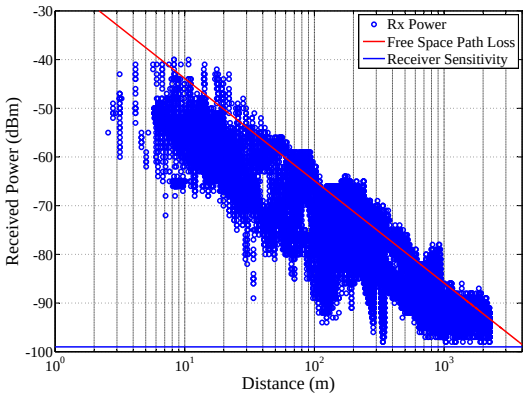

Figure 7.32.: The figure shows the received signal power for each message over distance between the vehicles (blue dots). The red line represents the theoretical received signal power assuming a free space path loss model. The receiver sensitivity is $-98\,\mathrm{dBm}$ (blue line).

end. The test was performed 3 times. Figure 7.32 shows the received power in dependance of the distance of the two test vehicles on a double-logarithmic scale. The maximum communication range obtained with this setup was 2 km. The red curve represents the received signal power over distance using a free-space path loss model according to:

$$P_{\text{rx}} = P_{\text{tx}} - L_{\text{tx}} + G_{\text{tx}} - L_{\text{FSPL}} + G_{\text{rx}} - L_{\text{rx}}, \tag{7.1}$$

where P_{rx} is the received power, P_{tx} is the transmit power of 24dBm, L_{tx} and L_{rx} are the losses due to cables and connectors at the transmitter and receiver respectively and G_{tx} and G_{rx} are the gain of the antenna at the transmitter and receiver. The free-space path loss L_{FSPL} is equal to:

$$L_{\text{FSPL}} = 20 \cdot \log(d) + 20 \cdot \log(f) + 20 \cdot \log(\frac{4\pi}{c}), \tag{7.2}$$

where d is the distance between transmitter and receiver, f is the center frequency and c is the speed of light. When the received signal power falls under the receiver sensitivity threshold of -98 dBm, the correct reception of the messages is not possible and a lost message is the consequence.

It can be observed that the theoretical model for the received power correctly matches the experimental values in the LoS situation. Here, a great increase of the awareness range can be achieved when compared to on-board ranging sensors, which have sensing ranges of up to 200 m. To assess the performance in real-world scenarios and specially in non-LoS situations, where on-board ranging sensors are unavailable, a second experiment with the same test setup was performed driving on a highway and in a rural area.

Nineteen non-LoS situations were inspected, including obstructions due to different types of vehicles on the highway and due to obstacles and terrain in the rural area. In Annex C, the tables comparing the actual received power against the theoretical LoS received power for each situation can be found. On the highway, large obstacles such as trucks caused drops in received signal power between 5 dB and 11 dB when driving at distances up to 106 m. At larger distance, the occlusion effect of other vehicles was found to be less likely. The vehicles were driving between 20 m and 290 m and no drop of messages was recorded. In general, higher signal attenuation was measured in the rural environment. Crests and bends with vegetation lowered the received signal power up to 29 dB. Under these circumstances and considering Figure 7.32, a reliable communication above 200 m is challenging.

The received power over time for two sections on the highway and the rural environment are shown in Figure 7.33. Each dot in blue represents one received message from the target at the ego vehicle with its associated received signal power. The green dots represent the theoretical received power using the aforementioned model for LoS situations. The red line at -98 dBm is the receiver sensitivity. Below this value messages cannot be correctly decoded and are dropped. In

Figure 7.33a, the sections when the LoS is obstructed on the highway can be identified, since here the received signal power is below the theoretical received power. From second 560 to 580, two vans were driving between the ego and target vehicle. A short LoS gap occurred around second 585, after which a big truck blocked again the direct sight. In both obstructed situations, enough power was received and all messages were decoded. At second 600 and 610 the vehicles passed below bridges, which represented a good reflection surface for the signal to propagate from the target to the ego vehicle on a secondary path and producing the distinctive peaks in received signal power. From second 510 to 540, the vehicles entered a tunnel. A strong increase in the received signal power is the result, since the tunnel has a wave guiding effect, reflecting the signal at the walls and ceiling and bringing the power towards the receiver.

From second 1210 to 1235 in Figure 7.33b, the impact of the antenna pattern on the received power can be observed. The vehicles were driving from a flat road to a steep road climbing up a hill. Since the antenna gain is different for different elevations, the received power also varies, which is not captured by the theoretical received power curve that assumed an omnidirectional antenna. Around second 1240, the target vehicle disappears behind a curve, where terrain and a forest block the LoS. The result is more than 16 dB drop in received power. A second obstruction due to a thick forest in a curve in second 1250, led to a more severe drop in signal strength, which caused the drop of up to 4 % of messages. At this moment, the vehicles were driving at a distance of 180 m.

The experiments demonstrate that a cooperative approach based on V2V communication is able to offer a relative position estimate of another vehicle up to more than 1 km distance if a LoS exists between the vehicles, thus exceeding the capabilities of traditional automotive ranging sensors. In non-LoS situations, where ranging sensors fail to offer relative position information, V2V communication still allows to exchange sensor data between the vehicles in order to estimate their relative position. This was shown for distances up to 290 m on highways and and 250 m in rural environments.

7.6. Discussion

In this chapter, the cooperative relative positioning system presented in this thesis has been evaluated under real-world conditions. A test setup with two vehicles equipped with a GPS receiver, an IMU and access to the CAN bus speedometer has been used for the evaluation in three different environments, namely on a highway, in a rural environment and in an urban scenario. The requirements regarding accuracy, reliability and availability that were presented in Chapter 2, have been evaluated using the metrics defined in Chapter 4. In the cooperative approach for relative positioning presented in this thesis, GNSS is the source of positioning information, while the on-board sensors are used to stabilize the estimation when GNSS signals are impaired.

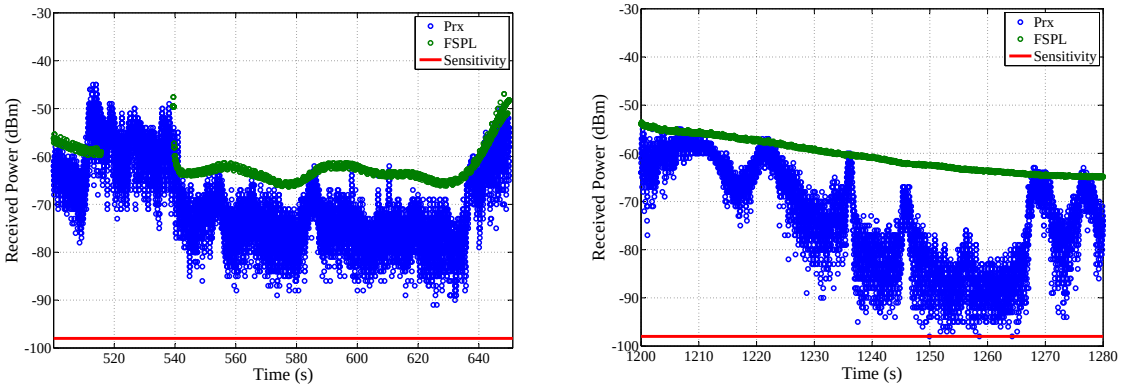

(a) Highway (b) Rural

Figure 7.33.: The figure shows the received power (blue) and the theoretical LoS received power (green) for a section driving on a highway (left) and a section on a curvy rural road (right). The red line represents the sensitivity threshold.

The GNSS-only tests revealed that in real-world conditions, systematic errors in the baseline estimate of up to two meters can be avoided by using a *pseudorange differencing* approach for relative positioning of vehicles instead of the differentiation of the absolute positions of each vehicle. These errors are related to common errors in the GNSS pseudoranges caused by the atmosphere or the GNSS satellites that bias the absolute position estimation in each receiver. When the receiver in each vehicle tracks a different set of satellites, this bias propagates to the baseline estimate. When using an epoch-wise pseudorange differentiation technique, the horizontal baseline error in a highway environment is found to be below 80 cm (1σ). Here, bridges and tunnels are the main source of GNSS errors. The error increases to 1.2 m (1σ) in rural environments. Specially, dense tree canopy when driving through forests produce large errors for low-elevated satellites. In a mixed urban environment, the baseline estimation accuracy only using GNSS degrades to 1.5 m (1σ). This is a consequence of less availability of satellite signals due to shadowing by buildings and degraded satellite signal reception due to decreased signal strength, LoS blockage and multipath reception.

However, vehicle safety-critical assistance systems require to have the relative position information of another vehicle in an ego vehicle reference frame. The proposed multisensor fusion approach for cooperative relative positioning estimates the baseline and baseline velocity in the ego vehicle frame. In a highway environment, thanks to the good view to GNSS satellites down to an elevation angle of 20° to 30° and rare occurrence of over-head obstacles, a relative position accuracy below 1 m (1σ) is achieved. Bridges cause small errors on the GNSS pseudoranges that are easily detected by the multisensor fusion filter and correctly filtered out. On highways, tunnels create GNSS outages of up to a minute. While outages of up to 10 s are correctly bridged using on-board sensors, longer outages are found to introduce large errors in the estimation of the baseline, especially due to

the heading error in the ego vehicle. Due to the disposition of the vehicles, the relative speed is estimated with higher accuracy in longitudinal than in lateral direction (less than 0.1 $\frac{\text{m}}{\text{s}}$ baseline velocity error against 0.35 $\frac{\text{m}}{\text{s}}$). A high reliability is achieved in a highway environment, with the baseline estimation error generally falling inside the 3σ bound. High availability is reached as well, with the 3σ uncertainty being 90 $\%$ of the time below 2.4 m. When communication outages between the vehicles occur, the baseline is predicted solely on past kinematic data from the target vehicle. Five-second outages lead to meter level errors in the longitudinal and lateral baseline components. A constant turn rate and acceleration model helps limiting this error in situations when changes in speed or heading occur. Consecutive message drops related to the wireless medium access that can be expected in dense traffic scenarios have no impact on the overall statistic relative position statistic.

In a rural environment, short gaps of 20 to 30 seconds of GNSS degraded measurements are easily bridged with the available on-board sensors. GNSS heading and speed measurements get easily corrupted when driving next to or though dense forests. By correctly detecting these periods, the kinematic state estimation can rely on the on-board sensors. The overall relative positioning errors are 0.75 m (1σ) and 1.6 m (1σ) in longitudinal and lateral direction respectively. Regarding the system's reliability, a few events during the run were recorded in which the baseline error exceeded the 3σ uncertainty bound. These were associated to stronger lateral and longitudinal dynamics. This points towards a mismatch in the used movement models for the vehicles. A 90 $\%$ availability is achieved for uncertainties below 2 m in longitudinal and 3.5 m in lateral direction.

The urban environment reveals itself especially challenging due to the influence of GNSS satellite blockage and strong multipath effects. On the one hand, a reduced set of GNSS measurements are available when compared to the highway or rural scenarios due to the shadowing of buildings and the increased elevation mask. On the other hand, multipath and low signal strength has a strong impact on GNSS heading and speed measurements. Heading, cannot be used reliably and updates with corrupted heading measurements lead to errors in the vehicle heading estimation of up to 15°. This leads to a wrong location of the target vehicle in the ego vehicle frame and to long periods of lateral and longitudinal positioning errors of several meters. The overall longitudinal baseline error is 1.5 m (1σ), while the lateral error is above 4 m (1σ). The large estimation errors added to the large reliability events make the use of the proposed approach for cooperative positioning not appropriate in urban environments. If access to the steering wheel angle would be available, this information could support the IMU during long heading outages.

This chapter concludes with a discussion on the possibilities that a cooperative approach for relative positioning offers to overcome the limitations of modern ranging sensors, enhance their performance or represent a possible replacement in the future. A state-of-the-art, commercially available radar sensor found in today's vehicles is the Bosch LRR3 sensor. It states to have a distance accuracy of $\pm$0.1 m and a relative speed accuracy of $\pm$0.12 $\frac{\text{m}}{\text{s}}$. The ranging performance

clearly outperforms the relative position accuracy of the cooperative approach based on GNSS pseudorange differentiation. This radar sensor is specially designed for Automatic Cruise Control (ACC) applications, where the relative position in the longitudinal direction, i.e. the distance to an in-front driving vehicle, is of great importance. The angular accuracy of the radar sensor is around 0.5°, which leads to a lateral error of 0.5 m at 50 m and 1 m at 100 m. Hence, at larger distances the cooperative approach is able to offer a higher lateral accuracy than this radar sensor. Another commercial radar sensor, which operates in the 24 GHz band, is the UMRR-0A family from Smartmicro. Applications for these radars range from ACC and Forward Collision Warning (FCW) to blind spot detection. Its range accuracy goes from $\pm$0.25 m at 10 m to $\pm$2.5 m at 100 m distance. Thus, at medium ranges the presented cooperative approach is able to compete in accuracy with this sensor.

The LLR3 radar sensor is able to detect targets up to a range of 200 m, while the cooperative approach is able to extend this range up to 1 km. The radar sensor suffers from LoS blockage caused by other vehicles or the surrounding environment. On highways other vehicles driving in the same direction will block the radar sensor. In rural environments, bends with trees and forests, earth hills or crests can easily block the sight towards another car not driving immediately in-front. In urban environments mainly other driving or parked vehicles or buildings will block the LoS. Here, V2V offers a substantial opportunity in increasing the awareness range for future intelligent vehicles, since sensor information exchange is still possible in non-LoS situations up to several hundreds of meters. Additionally, the possibilities of discriminating between different targets is easily accomplished in a cooperative approach, whereas a radar sensor has difficulties to discriminate between targets driving close to each other and at a similar relative speed. Along with the benefits that a cooperative approach for relative positioning offers, challenges and new threads appear. A cooperative approach based on wireless communication, and specially on the current V2V communication standard, has to cope with possible security challenges. Jamming or spoofing are examples of deliberate attacks in order to prevent other parties to receive messages or to believe in false information. Without taking appropriate action, this attacks could theoretically lead to not detect other vehicles or, on the contrary, to perceive vehicles that are not present at all.

Thus, the cooperative approach is not able to compete with a modern ACC radar sensor on behalf of the accuracy in the relative position. However, it offers important advantages, regarding its robustness, its ability to correctly estimate the current uncertainty, its reliability and availability. Consequently, it is foreseen that the best performance can be achieved by unifying both independent sources of information in an overall cooperative relative positioning fusion system that increases the awareness for future safety critical applications.

Chapter 8.

Summary, Conclusions and Future Work

8.1. Summary and Main Contributions

In this thesis, the topic of relative positioning between road vehicles using a cooperative approach based on vehicle-to-vehicle communication, exchanged Global Navigation Satellite Systems (GNSS) measurements and on-board sensors has been addressed. The motivation of this work was to identify up to which extent such a cooperative approach could compete with on-board ranging sensors such as radar, laser scanners or camera-based systems and solve their shortcomings. Future safety-critical applications, as for instance automatic cruise control, collision avoidance systems or lane-change assistants, require that the relative position of other road participants is given in an ego vehicle reference frame, in the same way an on-board ranging sensor delivers the position of detected target vehicles. This is the first work to analyze the performance of GNSS-based cooperative localization to obtain a relative position of other vehicles in the ego vehicle frame.

A sensor fusion approach based on the use of differenced GNSS pseudoranges, on-board speed sensor and inertial measurement unit has been proposed following a Bayesian approach. The dynamic Bayesian network, which describes the causal dependency between the states and the evidences, has been presented. The advantage of following a Bayesian approach is that the impact of the uncertainty of each information source on the relative position is directly taken into account. The uncertainty in the final estimation of the relative position of the target vehicle will decisively depend on the quality of the GNSS pseudoranges, the given satellite constellation, the noise of the inertial and speed sensors, the number of lost communication messages and the relative disposition between the vehicles.

A key aspect in this thesis, is the usage of GNSS pseudorange double differences to cancel out common errors between two GNSS receivers. With such an approach atmospheric errors, satellite ephemeris errors and satellite clock errors are successfully eliminated without requiring additional infrastructure or an additional communication link for broadcasting differential GNSS correction data. The technique of pseudorange differencing was compared to the common approach of differencing absolute positions for relative positioning. The performance of both methods depends

on the magnitude of the common errors on the pseudoranges of both receivers and on the magnitude of the pseudorange noise. The number of satellites used in each receiver, as well as the constellation geometry, have a direct impact on which of the two approaches yields a smaller baseline error. A novel method based on GNSS Doppler extrapolation to synchronize pseudoranges from two different receivers has been proposed and has been validated to be used for cooperative relative positioning.

The proposed sensor fusion approach for cooperative relative positioning has been validated in a simulation environment that was developed in the frame of this thesis. Here, the impact on the relative position estimation of different Vehicle-to-Vehicle (V2V) update rates, number of available GNSS satellites, colored noise on the GNSS pseudorange measurements or different kinematic filters could be analyzed prior to the real-world experiments. Controlled hardware-in-the-loop simulations were specifically performed on the GNSS receivers in order to analyze their performance prior to the outdoor tests. The method to compute pseudorange double differences has been validated in a error-free environment. The remaining noise error from the receivers has been analyzed in terms of mean, variance, time correlation and amplitude distribution. The correct cancellation of common errors in both receivers has been successfully shown by simulating an atmospheric delay on different satellites. The code double differences resulting from this experiment are free of any possible bias. In a second set of experiments, the double difference signals are evaluated under the effect of multipath propagation. Different multipath models show that multipath is not canceled by double differencing. High dynamics in speed and acceleration, on the other hand, were found not to impact the estimation of the baseline. Extreme accelerations caused loss of signal lock inside the GNSS receiver.

Great emphasis has been put in the scope of this work on validating the proposed sensor fusion approach in real-world environments. For this purpose a nearly two hour drive has been performed with two vehicles driving in highway, rural and urban environments. The challenges of each scenario have been highlighted and the overall performance in accuracy, reliability and availability has been compared to each other by means of a statistical analysis. The test runs revealed that the pseudorange differencing approach is able to eliminate a possible bias of up to two meters that occurs when vehicles use different sets of satellites to compute their absolute position. The cooperative relative positioning sensor fusion has a good performance in a highway environment. Sub-meter positioning errors of the target vehicle were achieved. A good reliability is found, with seldom violations of the stated 3σ bound. It was shown that communication outages of a few seconds can be bridged with meter-level errors, but a correct accounting of the uncertainty. A non-ideal communication channel was simulated and it was found that when transmitting at 10 Hz the loss of packages due to medium access contention had a negligible impact on the overall estimation of the relative position. The rural area presents more challenges than the highway environment due to longer degraded GNSS signal reception when driving through forests or small towns and higher vehicle dynamics due to accelerations, decelerations and changes of direction. A better

accuracy and availability are achieved in the longitudinal (0.7 m) than in the lateral component (1.5 m). Last but no least, the urban scenario was found to be extremely challenging, mainly due to the difficult estimation of the ego vehicle heading, which led to meter-level errors in the longitudinal relative position coordinate and to often reliability failures.

8.2. Conclusions

It has been proven that exchanged pseudorange measurements can be successfully used for estimating the relative position between two vehicles while canceling out common errors. In the case of unobstructed view to the satellites, the approach yields a bias-less estimate of the relative position between the vehicle with less than one meter of error. Especially, when the vehicles track at least six common satellites, differencing pseudoranges has a advantageous effect. The two-step differentiation amplifies slightly the noise of the double difference when compared to each single pseudorange. Multipath propagation has a detrimental effect, yielding more than ten meters of errors in urban environments.

The GNSS based cooperative approach, yields a relative position estimate in an Earth fixed coordinate system. The heading of the ego vehicle is used to rotate this estimate into the ego vehicle frame. Consequently, the continuous and accurate estimation of the ego vehicle heading is of high importance to vehicular cooperative relative positioning. This has been found to be especially difficult in urban environments due to corrupted GNSS Doppler measurements, due to Line-of-Sight (LoS)blockage and multipath propagation.

In highway environments, the cooperative approach yielded a sub-meter accurate baseline estimate, bridging the errors created by overhead gantries and through short tunnels. Minute-long outages as through longer tunnels yielded meter-level errors that do not meet the requirements of modern Intelligent Transportation Systems (ITS) applications. The relative velocity between the vehicles, a parameter that is of great importance to many ITS applications, is correctly estimated with an error of 0.2 $\frac{\mathrm{m}}{\mathrm{s}}$ (1σ).

The sensor fusion approach based on on-board dynamic sensors helps increasing the continuity and the availability of the relative position estimate under bridges, small tunnels, through villages and forests and short urban canyons. Longer GNSS-outages remain a problem since the approach relies on the dynamic sensors in dead-reckoning mode. Here, the on-board Inertial Measurement Unit (IMU) and speed sensors are capable of maintaining a relative position estimate with errors below 3 m for up to 20 s. The presented multisensor fusion approach based on a Bayesian filter is able to correctly estimate the uncertainty in the relative position estimate depending on the available satellite signals, the satellite constellation, the loss of V2V communication messages or the errors in the on-board sensors.

It was found that a message update rate of 10 Hz is sufficient to follow regular changes in acceleration and turn rate of the vehicles. Extreme vehicle dynamics require a higher update rate of V2V communication messages. The total amount of data that needs to be transmitted for the proposed cooperative positioning approach is manageable. Without further compression, the broadcast of synchronized pseudorange measurements amounts to less than 100 Byte, compared to the 500 Byte required for today's Cooperative Awareness Messages (CAMs).

The evaluation of the V2V communication, revealed that communication between the vehicles above one kilometer is possible if a LoS exists. In non-LoS situations where on-board ranging sensors fail to offer relative position information, the vehicles are still able to exchange information up to several hundreds of meters. This was tested in both highway and rural environments.

Next, the proposed research questions are answered:

1. Which are the advantages and which is the gain in exchanging GNSS raw pseudoranges for relative positioning? One way to realize a cooperative approach is to exchange the absolute positions computed and, possibly, corrected with other sensor information, with other vehicles. The absolute positions, however, are biased estimates of the actual position of the vehicle due to the impact of atmospheric and satellite related errors. One way to overcome this problem is to exchange synchronized pseudorange measurements between vehicles and only use the pseudoranges common to both vehicles to create so-called double differences and update the relative position estimate. The error that can be avoided by doing this is under normal conditions around 1 or 2 meters. The price to pay is a slight increase in noise. However, it is more convenient to have an increase in noise that averages out in a Bayesian filter, than having a bias that offsets the relative position estimate.

2. Which increase in robustness is achieved by fusing GNSS raw pseudoranges with sensors available in today's vehicles? The subtraction of exchanged GNSS pseudoranges offers an information about the relative position of both vehicles in an Earth-fixed reference frame. In order to bring this relative position information into the ego vehicle frame and make it meaningful for an Advanced Driver Assistance System (ADAS), information about the heading of the vehicle is necessary. A Bayesian approach offers the possibility to correctly account for the uncertainty of the relative position in the vehicle frame under changing conditions. The fusion with available on-board sensors offers an increased robustness against GNSS outages in tunnels and while driving under bridges or in urban canyons where major errors in both speed and heading occur. By correctly relying on the IMU and the speedometer, short outages of several seconds can be bridged. A lower horizontal error in the relative position and an increased availability are the benefits of using a Bayesian sensor fusion approach.

3. Which performance in the estimation of the relative position can be expected in every automotive environment regarding accuracy, reliability and availability? The cooperative relative positioning approach based on Bayesian sensor fusion yields a good performance in highway and rural environments. In a highway environment, sub-meter relative position accuracy is achieved. GNSS outages due to tunnels can be bridged for up to around 10 seconds along with an ever-increasing uncertainty. In a rural environment, the worse quality in GNSS signals yields an overall accuracy batter than 2 meters. In urban environments, multipath and shadowing of GNSS signals cause large errors in the heading estimate, which lead to large errors in the relative position, especially in its lateral component. Due to the difficulty in accounting for these errors, the cooperative approach behaves extremely unreliable in this type of environment.

4. Is it possible to achieve, with a cooperative approach, a comparable performance to modern on-board ranging sensors? Regarding accuracy, a cooperative approach for relative positioning can only compete with on-board ranging sensors at higher distance. At distances below 100 meters, 70 GHz-radar sensors have a higher accuracy, which a cooperative approach based on GNSS pseudoranges cannot beat. However, also at low distances the cooperative approach is capable of working when the LoS is obstructed, either due to other vehicles or due to the surrounding topography. In this cases, the cooperative approach can help support a ranging sensor with an increased field-of-view, an inherent identification of targets along with a correct estimation of the uncertainty in the relative position.

8.3. Future Work

This thesis has limited its scope to analyze the relative position between two vehicles. Part of the future work includes analyzing the benefit in relative position within *clusters of vehicles*. Already three vehicles, which are all in range of each other, build up an over-determined system for relative positioning. This leads to an enhancement in the precision of the relative position determination as an increased number of measurements become available. The cooperative relative positioning approach in this thesis is based on the exchange of GNSS pseudoranges. *GNSS carrier phase measurements* offer a more precise distance estimate to the satellites in view. Their drawback, however, is the unknown number of L1 wavelengths each measurement has associated and that needs to be resolved. The estimation of this so-called integer ambiguity is a complicated an tedious problem, but once it is solved a relative position with a sub-centimeter accuracy becomes possible. The technique known as Real Time Kinematics (RTK) for absolute positioning, could be extended with sensor fusion for cooperative relative positioning of vehicles. One of the assumptions performed in the scope of this thesis is that the vehicles drive on the same plane surface. Changes in the height coordinate were absorbed by increasing the system and measurement noise in the

Bayesian filters. Thus, the extension towards *full 3D positioning* is suggested as future work. This could, on the one hand increase the accuracy in the estimation, and, on the other hand, be used for discrimination between traffic on different levels (e.g. on bridges). In the scope of this work, the cooperative approach was compared quantitatively and qualitatively to on-board ranging sensors. However, it is envisioned that none of these two systems is determined to replace the other, but rather will both be used in parallel to overcome each other's limitations. A cooperative approach offers an extended perception range and the identification capabilities of objects in the vicinity, whereas it can benefit from the increase accuracy of on-board ranging sensors. Therefore, future research should investigate the possibilities to *fuse on-board ranging sensors with cooperative approaches* in order to offer extended capabilities for safety-critical transport applications.

Appendix A.

Relative Positioning Error for Absolute Position Differencing and Pseudorange Differencing

The satellite constellation corresponding to the 4th of June 2013 has been simulated. Figure A.1 shows on a skyview plot the location of the twelve satellites above the horizon as seen from Wessling, south-west of Munich (Germany) at 18:30. A mask of 10° was used in the experiments, yielding a constellation of eight useful satellites. The ego and the target receiver tracked between four and eight satellites. All possible combinations were simulated and the relative positioning error for *absolute position differencing* and *pseudorange differencing* was computed. The following tables show the maximum, minimum and mean error for both approaches in the case of only noise (Table A.1 and Table A.2) and only common errors (Table A.3 and Table A.4). The noise level was set at a value of 1 m (1σ) and the common errors were equal to the ionospehric delay modeled by the Klobuchar parameters on that day.

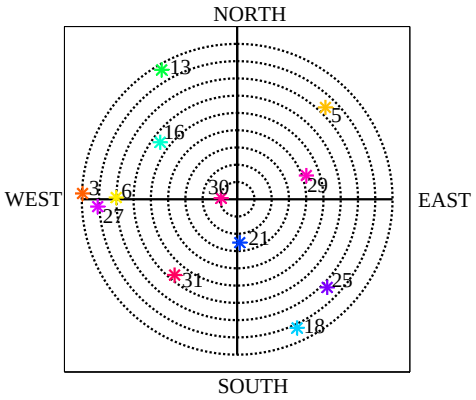

Figure A.1.: Skyview plot with the location of the twelve satellites as viewed from Wessling, south-west of Munich (Germany), on the 4th of June 2013 at 18:30.

Table A.1.: Only Noise - PRD

Satellites	8	7	6	5
5	max. 15.31 m mean 4.38 m min. 2.76 m	max. 420.10 m mean 15.39 m min. 2.76 m	max. 420.10 m mean 19.06 m min. 2.76 m	max. 420.10 m mean 20.89 m min. 2.76 m
6	max. 4.42 m mean 3.28 m min. 2.64 m	max. 15.31 m mean 4.11 m min. 2.64 m	max. 420.10 m mean 13.78 m min. 2.64 m	
7	max. 3.19 m mean 2.81 m min. 2.56 m	max. 4.42 m mean 3.22 m min. 2.56 m		
8	max. 2.49 m mean 2.49 m min. 2.49 m			

Table A.2.: Only Noise - APD

Satellites	8	7	6	5
5	max. 10.88 m mean 3.51 m min. 2.57 m	max. 10.97 m mean 3.63 m min. 2.62 m	max. 11.15 m mean 3.84 m min. 2.67 m	max. 15.21 m mean 4.41 m min. 2.75 m
6	max. 3.40 m mean 2.81 m min. 2.49 m	max. 3.68 m mean 2.96 m min. 2.54 m	max. 4.19 m mean 3.20 m min. 2.59 m	
7	max. 2.77 m mean 2.54 m min. 2.43 m	max. 3.10 m mean 2.70 m min. 2.47 m		
8	max. 2.38 m mean 2.38 m min. 2.38 m			

Table A.3.: Only Common Errors - PRD

Satellites	8	7	6	5
5	max. 0.01 m mean 0 m min. 0 m	max. 0.01 m mean 0 m min. 0 m	max. 0.01 m mean 0 m min. 0 m	max. 0 m mean 0 m min. 0 m
6	max. 0.01 m mean 0 m min. 0 m	max. 0 m mean 0 m min. 0 m	max. 0 m mean 0 m min. 0 m	
7	max. 0 m mean 0 m min. 0 m	max. 0 m mean 0 m min. 0 m		
8	max. 0 m mean 0 m min. 0 m			

Table A.4.: Only Common Errors - APD

Satellites	8	7	6	5
5	max. 9.51 m mean 2.43 m min. 0.54 m	max. 11.29 m mean 2.60 m min. 0.09 m	max. 12.16 m mean 2.89 m min. 0.06 m	max. 13.18 m mean 3.50 m min. 0 m
6	max. 4.47 m mean 1.51 m min. 0.19 m	max. 5.70 m mean 1.73 m min. 0.04 m	max. 6.64 m mean 2.13 m min. 0 m	
7	max. 1.93 m mean 0.77 m min. 0 m	max. 3.09 m mean 1.15 m min. 0 m		
8	max. 0 m mean 0 m min. 0 m			

Appendix B.

Cooperative Relative Positioning Simulator

B.1. Kinematic Filter Evaluation

The kinematic filters described in Section 6.1.3 were tested using the Cooperative Relative Positioning Simulator. Table B.1 lists the simulation parameters for the True Value Simulator. The true value simulator runs at 1 kHz. The position, velocity, acceleration, jerk and turn rates for two vehicles driving behind each other were simulated.

Table B.2 lists the simulation parameters for the Measurement Simulator. The satellite positions and velocities were simulated using the GPS broadcasted ephemeris of the 26^{th} of July 2012 (brdc2080.12n). The time at which the simulation run starts is at 14:15 GPS time. The Klobuchar model parameters used to simulated the ionospheric error stem from the same navigation file.

Table B.1.: True Value Simulator

Simulator Parameter	**Unit**	**Value**
Initialization Duration [ego, target]	s	[20, 17]
Initial Position Ego	°, °, m	[48.08454, 11.27777, 581]
Initial Distance	m	5
Starting Jerk	$\frac{m}{s^3}$	0.5
Stopping Jerk	$\frac{m}{s^3}$	0.5
Starting Duration [ego, target]	s	[12, 12]
Stopping Duration [ego, target]	s	[12, 12]
Mass of Vehicle [ego, target]	kg	[2600, 2600]
Suspension Factor x-axis [ego, target]	$\frac{°}{m\,s^2}$	[3, 3]
Suspension Factor y-axis [ego, target]	$\frac{°}{m\,s^2}$	[-2, -2]
Centrifugal jerk [ego, target]	$\frac{m}{s^3}$	[0.5, 0.5]
Number of Bends		3
Bend Radius	m	[120, -80, 100]
Bend Angles	°	[40, 17, 80]

Table B.2.: Sensor Simulator

Simulator Parameter	**Unit**	**Value**
OS Clock Jitter	s	0
Speed Sensor Sample Rate	Hz	5
Noise Speed Sensor	$\frac{m}{s}$	0
IMU Sample Rate	Hz	100
IMU Misalignment	°	[0, 0, 0]
Accelerometer Noise	$m/s^2/\sqrt{Hz}$	0.003
Accelerometer Bias	$\frac{m}{s^2}$	[0, 0, 0]
Accelerometer Bias Stability	$\frac{°}{h}$	20
Gyroscope Noise	$°/s/\sqrt{Hz}$	0.005
Gyroscope Bias	$\frac{°}{s}$	[0.2, 0.1, -0.2]
Gyroscope Bias Stability	$\frac{°}{h}$	20
Noise on GNSS Pseudorange	m	1
Noise on GNSS Doppler	Hz	0.1
Noise on GNSS Carrier Phase	m	0.001
GPS Sample Rate	Hz	4
GPS Antenna Displacement	m	[0, 0, 0]
GPS Clock Bias	ns	640 000
GPS Clock Drift	$\frac{ns}{s}$	-2200
Temperature	°C	20
Pressure	mbar	1015.25
Water Vapor Pressure	mbar	25

Appendix C.

V2V Communication Evaluation

The following tables compare the received power with the theoretical LoS received power for nine and ten non-LoS events while driving on a highway and on a rural road respectively. The first column describes the non-LoS situation and the second column shows the distance between the ego and target vehicle. The third column contains the theoretical received power with a Free Space Path Loss model, while the fourth column contains the actual received power measured by the receiver at the ego vehicle. Finally, the fifth column shows the drop in power for the corresponding event.

Table C.1.: Highway

Run	Distance	Path Loss	Rx Power	Difference
Two vans	106 m	-65dBm	-70dBm	-5dB
Heavy truck	73 m	-64dBm	-75dBm	-11dB
Small truck	90 m	-63dBm	-69dBm	-6dB
Heavy truck	85 m	-62dBm	-71dBm	-9dB
Car	21 m	-55dBm	-61dBm	-6dB
Truck (curtain)	82 m	-63dBm	-70dBm	-7dB
Van	50 m	-59dBm	-64dBm	-5dB
Car with trailer	100 m	-64dBm	-69dBm	-5dB
Truck	90 m	-65dBm	-72dBm	-7dB

Table C.2.: Rural

Run	Distance	Path Loss	Rx Power	Difference
Hill crest	240 m	-69dBm	-79dBm	-10dB
Fence + trees	150 m	-65dBm	-74dBm	-9dB
Bend + trees	171 m	-66dBm	-82dBm	-16dB
Fence + trees	80 m	-58dBm	-70dBm	-12dB
Bend high terrain	120 m	-65dBm	-77dBm	-8dB
Bend thick forest	180 m	-67dBm	-83dBm	-16dB
House 2 Story	105 m	-61dBm	-73dBm	-12dB
Bend thick bushes	124 m	-63dBm	-92dBm	-29dB
Bend single tree	115 m	-63dBm	-69dBm	-6dB
Hill Crest	115 m	-62dBm	-70dBm	-8dB

List of Figures

List of Tables

Mathematical Notation

General Notation Rules

Throughout this thesis, the following notation will be used:

- All vectors are interpreted as column vectors.
- Vectors are denoted by bold small letters and matrices by bold capital letters.
- $(\cdot)^{\mathsf{T}}$, and $(\cdot)^{-1}$ stand for matrix (or vector) transpose and inverse, respectively.
- $E\{x\}$ stands for the expectation or sample mean of x.
- $p(x)$ stands for the probability distribution of random variable x.
- $\hat{x}$ is an estimation of the unknown parameter x.
- $\tilde{x}$ is a prior estimation of the unknown parameter x.
- $\dot{x}$ is the time derivative of x.
- $\|\mathbf{x}\|$ is the norm of vector $\mathbf{x}$.
- $|\mathbf{X}|$ is the determinant of matrix $\mathbf{X}$.
- $[\mathbf{X}]_{i,j}$ denotes the component in row i and column j of matrix $\mathbf{X}$.
- $[\mathbf{x}\times]$ is the skew symmetric matrix form of vector $\mathbf{x}$.
- $\mathbf{x} \sim \mathcal{N}(\boldsymbol{\mu}, \mathbf{P})$ denotes a Gaussian distributed random variable $\mathbf{x}$ with mean $\boldsymbol{\mu}$ and variance-covariance matrix $\mathbf{P}$.
- $exp\{\cdot\}$ is the natural exponential function.
- $\mathbf{I}_n$ is an identity matrix of order n.
- $\mathbf{0}_{m\times n}$ is a $m \times n$ matrix filled with zeros.
- k as a superindex is reserved for timestep.
- e and t as subindeces stand for ego and target GNSS receiver or vehicle.
- l, m and n as superindeces stand for three GNSS satellites.

- i, e, n and v as superindeces stand for inertial, Earth, local navigation and vehicle frame, respectively.
- $x^{\mathsf{a}}_{\mathsf{b,c}}$ is the inertial measurement x in the c frame with respect to the b frame expressed in a frame coordinates.

List of Symbols

$\mathbf{b}$	Baseline vector
$\dot{\mathbf{b}}$	Baseline velocity
$\mathbf{p}_{\mathsf{e}}$	Position of receiver e
$\mathbf{d}^k_{\mathsf{e}}$	Kinematic state of the ego vehicle at time step k
$\mathbf{d}^k_{\mathsf{t}}$	Kinematic state of the target vehicle at time step k
$\mathbf{e}^k$	Error state containing all memory components of the measurements at time step k such as biases
$\boldsymbol{\nabla\Delta\rho}^k$	Double difference pseudorange measurements at time step k
v^k_{CAN}	Speed measurement from the CAN bus at time step k
$\mathbf{i}^k$	Measurements from an IMU at time step k
$\mathbf{v}^k_{\mathsf{GNSS}}$	Velocity from a GNSS receiver at time step k
κ	Normalization constant in Bayes Formula
r^l_{e}	True range between receiver e and satellite l
Δr^l_{et}	Single difference true range from receiver e and t to satellite l
$\nabla\Delta r^{lm}_{\mathsf{et}}$	Double difference true range from receiver e and t to satellite l and m
ρ^l_{e}	Pseudorange from receiver e to satellite l
$\Delta\rho^l_{\mathsf{et}}$	Pseudorange single difference from receiver e and t to satellite l
$\nabla\Delta\rho^{lm}_{\mathsf{et}}$	Pseudorange double difference from receiver e and t to satellite l and m
$\boldsymbol{\nabla\Delta\rho}_{\mathsf{et}}$	Pseudorange double difference vector from receiver e and t
$\mathbf{R}_\rho$	Is the pseudorange measurement variance-covariance matrix
ρ_{cmc}	Code Minus Carrier (CMC) measurement
$\dot{\Phi}^l_{\mathsf{e}}$	Doppler measurement from receiver e to satellite l
Φ^l_{e}	Carrier phase measurement from receiver e to satellite l
N^l_{e}	Carrier phase ambiguity at receiver e to satellite l
s_{I}	In-phase component of a down-conversion mixer
$s_{\mathsf{R,P}}$	Prompt code replica in Delay-lock Loop (DLL)
$s_{\mathsf{R,E}}$	Early code replica in DLL
$s_{\mathsf{R,L}}$	Late code replica in DLL
$s_{\mathsf{I,P}}$	In-Phase signal correlated with Prompt code replica
$s_{\mathsf{I,E}}$	In-Phase signal correlated with Early code replica

$s_{\mathsf{I,L}}$	In-Phase signal correlated with Late code replica
$s_{\mathsf{Q,P}}$	Quadrature signal correlated with Prompt code replica
$s_{\mathsf{Q,E}}$	Quadrature signal correlated with Early code replica
$s_{\mathsf{Q,L}}$	Quadrature signal correlated with Late code replica
$\mathbf{u}^l$	Unitary vector to satellite l
$\mathbf{u}^{lm}$	Differenced unitary vector to satellites l and m
$\mathbf{G}_{\mathsf{u}}$	Matrix of unitary vectors to satellites
$\mathbf{G}_{\mathsf{uu}}$	Matrix of differenced unitary vectors to satellites
$\mathbf{I}$	Fischer information matrix
ϵ_ρ	Pseudorange error in meters
$\epsilon_{\dot{\Phi}}$	Doppler error in Hertz
ϵ_Φ	Carrier phase error in cycles
ϵ_{e}	Pseudorange error at receiver e towards satellite l in meters
ϵ_{sat}	Pseudorange error at receiver e due to satellite clock bias
ϵ_{user}	Pseudorange error at receiver e due to user clock
ϵ_{eph}	Pseudorange error at receiver e due to satellite ephemeris
ϵ_{ion}	Pseudorange error at receiver e due to ionospheric delay
ϵ_{trop}	Pseudorange error at receiver e due to tropospheric delay
ϵ_{mp}	Pseudorange error at receiver e due to multipath propagation
ϵ_{n}	Pseudorange error at receiver e due to non-modeled errors
$\Delta\epsilon^l_{\mathsf{et}}$	Pseudorange error in a single difference of receivers e and t towards satellite l
$\nabla\Delta\epsilon^{lm}_{\mathsf{et}}$	Pseudorange error in a double difference of receivers e and t towards satellite l and m
δt_{e}	Receiver clock offset at receiver e
t_0	Measurement instant in ego GNSS receiver
Δt	Difference in measurement instants in GNSS receiver e and t
τ	Sampling rate of inertial sensor
B_ρ	DLL loop bandwidth in Hertz
T_{c}	Chip width of C/A code in metres
T	Averaging time of the DLL in the GNSS receiver
d	Distance between early and late correlators in relation to chip width
n	Gaussian noise
ψ	Yaw or heading angle
θ	Pitch angle
ϕ	Roll angle
$\boldsymbol{\alpha}$	Attitude
$\boldsymbol{\omega}$	Turn rate
$\mathbf{b}_\omega$	Turn rate bias
$\mathbf{M}_\omega$	Turn rate misalignment
B_{s}	Bias stability of a gyroscope

$\dot{\psi}$	Z-Axis turn rate (yaw rate)
$\dot{\theta}$	Y-axis turn rate (pitch rate)
$\dot{\phi}$	X-Axis turn rate (roll rate)
$b_{\dot{\psi}}$	Z-axis turn rate bias
$\mathbf{C}_{\mathsf{e}}^{\mathsf{i}}$	Transformation matrix from earth coordinate frame to inertial coordinate frame
$\mathbf{C}_{\mathsf{n}}^{\mathsf{e}}$	Transformation matrix from local navigation frame to earth coordinate frame
$\mathbf{C}_{\mathsf{v}}^{\mathsf{n}}$	Transformation matrix from vehicle frame to local navigation frame
$\mathbf{C}_{\mathsf{s}}^{\mathsf{v}}$	Transformation matrix from sensor frame to vehicle frame
$\mathbf{p}$	Position
$\boldsymbol{\alpha}$	Attitude Angles
$\mathbf{v}$	Velocity
$\mathbf{v}_{\mathsf{GNSS}}$	Velocity from the GNSS receiver
$\mathbf{a}$	Acceleration
$\mathbf{f}$	Specific Force
$\mathbf{j}$	Jerk
v	Longitudinal speed
v_{CAN}	Longitudinal speed from the CAN bus
a	Longitudinal acceleration
$\mathbf{b}_{\mathsf{a}}$	Acceleration bias
$\mathbf{M}_{\mathsf{a}}$	Acceleration misalignment
A	Speed sensor scale factor
b_{v}	Speed sensor bias
S_{x}	Vehicle suspension factor in x direction
S_{y}	Vehicle suspension factor in y direction
$\boldsymbol{\Omega}$	Skew symmetric matrix representation of turn rate vector $\boldsymbol{\omega}$
$\boldsymbol{\sigma}$	Micro-rotation vector. This vector can be approximated with $\omega \cdot \tau$
σ	Norm of the micro-rotation vector $\boldsymbol{\sigma}$
$\hat{\mathbf{x}}^k$	Posterior state vector in a Bayesian filter
$\tilde{\mathbf{x}}^k$	Prior state vector in a Bayesian filter
$\mathbf{P}^k$	Posterior variance-covariance matrix of the state in a Bayesian filter
$\tilde{\mathbf{P}}^k$	Prior variance-covariance matrix of the state in a Bayesian filter
$\mathbf{Q}$	Process noise variance-covariance matrix in a Bayesian filter
$\mathbf{R}$	Measurement noise variance-covariance matrix in a Bayesian filter
$\mathbf{J}$	Jacobian matrix
σ_ρ	Pseudorange noise standard deviation
γ	DLL bandwidth parameter
ζ	Pseudorange double difference autocorrelation coefficient
P_{tx}	Transmitted signal power
P_{rx}	Received signal power

G_{tx}	Antenna gain at the transmitter
G_{rx}	Antenna gain at the receiver
L_{tx}	Losses due to cables and connectors at the transmitter
L_{rx}	Losses due to cables and connectors at the receiver
L_{FSPL}	Free space path loss
d	Distance
f	Frequency
c	Speed of light
λ	GPS L1 wavelength
g	Gravity magnitude
$\mathbf{g}$	Gravity vector
sc	Semi-circle

List of Acronyms

ETSI	European Telecommunications Standards Institute	51
V2V	Vehicle-to-Vehicle	200
ITS	Intelligent Transportation Systems	201
CAM	Cooperative Awareness Message	202
LDM	Local Dynamic Map	50
RSU	Road Side Unit	21
GLOSA	Green Light Optimal Speed Advisory	3
UWB	Ultra-Wideband	12
ToA	Time of Arrival	167
AoA	Angle of Arrival	16
ToF	Time of flight	16
FoV	Field of View	12
CMOS	Complementary metal–oxide–semiconductor	18
TDOA	Time Difference of Arrival	21
RTD	Round-Trip Delay	12
RSS	Received Signal Strength	14
EIRP	Equivalent Isotropic Radiated Power	121
ACC	Automatic Cruise Control	198
FCW	Forward Collision Warning	198
LCA	Lane Change Assistant	10
ADAS	Advanced Driver Assistance System	202
CAN	Controller Area Network	178
OBD	On-board Diagnostics	165
ABS	Anti-lock Braking System	145
ESP	Electronic Stability Program	97
LIDAR	Light Detection and Ranging	16
IMU	Inertial Measurement Unit	201
MEMS	Microelectromechanical Systems	110
FOG	Fiber Optic Gyroscope	111
RLG	Ring Laser Gyroscope	111
INS	Inertial Navigation System	167

DCM	Direction Cosine Matrix	127
CA	Constant Acceleration	101
CV	Constant Velocity	100
CTRV	Constant Turn Rate and Velocity	184
CTRA	Constant Turn Rate and Acceleration	184
ECEF	Earth-Centered-Earth-Fixed	74
ENU	East-North-Up	112
ECI	Earth-Centered-Inertial	33
ETSI	European Telecommunications Standards Institute	51
KS	Kolmogorov-Smirnov	95
GNSS	Global Navigation Satellite Systems	199
GPS	Global Positioning System	164
DLL	Delay-lock Loop	219
PLL	Phase-lock Loop	29
FLL	Frequency-lock Loop	30
C/A	Coarse Acquisition	71
S/A	Selective Availability	22
CMC	Code Minus Carrier	214
CN0	Carrier-to-Noise Ratio	164
LoS	Line-of-Sight	201
NLOS	Non-line-of-Sight	21
EGNOS	European Geostationary Navigation Overlay Service	164
TEC	Total Electron Content	69
TECU	Total Electron Content Unit	69
SISRE	Signal In Space Range Error	67
RMS	Root Mean Square	10
RINEX	Receiver Independent Exchange Format	165
IGS	International GNSS Service	165
RTK	Real Time Kinematics	203
BPSK	Binary Phase Shift Keying	29
OCS	Operation Control Segment	66
DBN	Dynamic Bayesian Network	43
HMM	Hidden Markov Model	43
LS	Least Squares	171
WLS	Weighted Least Squares	75
EKF	Extended Kalman Filter	164
UKF	Unscented Kalman Filter	100
UT	Unscented Transform	49

PDF Probability Density Function . . . 95
CDF Cumulative Distribution Function . . . 170
MSE mean squared error . . . 81
CRLB Cramér-Rao Lower Bound . . . 217
FIM Fisher Information Matrix . . . 76
FFT Fast Fourier Transform . . . 92
RF radio frequency . . . 148
ITU International Telecommunication Union . . . 119
OSI Open Systems Interconnection . . . 120

Glossary

Absolute Position Differencing	A technique to estimate the baseline vector between two GNSS receivers by a) estimating the absolute geographic position of each receiver and b) subtracting both positions to find the baseline vector.
Baseline Vector	The baseline vector is the 3D vector in space pointing from the foremost center point of the ego vehicle to the foremost center point at the target vehicle (see Figure 4.3). This vector can be expressed in a local navigation frame like east-north-up frame or a body frame like the vehicle's coordinate frame.
Common Satellite	Usually, when computing $N-1$ independent double differences from a set of N single difference pseudoranges, the single difference to one satellite is chosen to subtract all other single differences. This satellite is the one nearest to the zenith, since it is less obstructed and suffers less from multipath propagation.
Double Difference	In GNSS, double differences are post processed measurements where the pseudoranges from two receivers towards two satellite are subtracted from each other. Common errors to each pair of pseudoranges are canceled out by this procedure.
Ego vehicle	In the scope of this thesis, the ego vehicle is the one that is interested to know the position of another vehicle, i.e. the target vehicle, in relation to him. In analogy to a radar system, the ego vehicle would be the vehicle where the radar sensor is mounted on.
Euler angles	Euler angles are used to describe the orientation or attitude of an object's body frame in a local navigation frame. They describe the three rotations that have to be performed around each of the body frame's coordinate axis to transform the body frame into the local navigation frame.

Global Navigation Satellite System	A Global Navigation Satellite System consists of a constellation of satellites and a network of ground monitoring stations that enable that a user equipped with an appropriate receiver positions himself by means of trilateration.
Inertial Measurement Unit	An inertial measurement unit is a self-contained sensor unit consisting of a triad of mutually orthogonal accelerometers and a triad of mutually orthogonal turn rate sensors or gyroscopes.
Intelligent Transportation Systems	The term Intelligent Transportation Systems (ITS) embraces all strategies where new technologies are brought into the world of transportation. With ITS, it is envisioned that transportation is made safer, more efficient, environmentally friendly and comfortable in the future.
Kalman Filter	A Kalman filter is an optimal implementation of a sequential Bayesian filter for linear and Gaussian systems.
Least Squares	Is a method to approximate the solution of an overdetermined system by minimizing the square of the residual error.
No-rotation Assumption	The assumption of a vehicle not rotating while being at a standstill is used in a Bayesian filter as an additional information and implemented into the filter's update step. This assumption is useful as it makes the gyroscope biases become observable for their estimation.
Pseudorange Differencing	In the context of this thesis, a technique by which to estimate the baseline vector between to receivers by subtracting the pseudoranges common to both receivers, creating double differences and solving a linear system of equations.
Pseudorange	In the context of GNSS, a pseudorange is an estimate of the user-to-satellite range that is biased by the unknown receiver clock offset and is corrupted by certain errors, as for instance satellite position error, ionospheric and tropospheric delay errors, noise and multipath propagation.
Target vehicle	In the context of this thesis, a target vehicle is a vehicle that broadcasts situational information in order to enable the ego vehicle to estimate its relative position.
Zero Baseline	In a zero baseline experiment, two GNSS receivers are connected to the same GNSS antenna and, consequently, receive the exact same signal at their input. In a zero baseline experiment, the baseline vector is equal to zero.

Bibliography

[1] European Commission, *EU Transport in Figures - Statistical PocketBook 2012*, 2012.

[2] European Commission, *EU Transport in Figures - Statistical PocketBook 2013*, 2013.

[3] European Commission, *Road Safety Evolution in EU*, 2015.

[4] Directorate-General for Mobility and Transport - European Commission, *Roadmap to a single European Transport Area - Towards a competitive and Resource-efficient Transport System*, 2011.

[5] Commission of the European Communities, *On the Intelligent Car Initiative "Raising Awareness of ICT for Smarter, Safer and Cleaner Vehicles"* , February 2006.

[6] N. A. Stanton and P. Marsden, "From fly-by-wire to drive-by-wire: Safety implications of Automation in Vehicles," *Safety Science*, vol. 24, no. 1, pp. 35 – 49, 1996.

[7] C. Grover, I. Knight, F. Okoro, I. Simmons, G. Couper, and B. Smith, "Automated Emergency Brake Systems: Technical requirements, cost and benefits," tech. rep., TRL Inc., 2008.

[8] Federal Communications Commission, *FCC 98-119*, June 1998.

[9] European Commission, *Commission Decision of 5 August 2008 on the harmonised use of radio spectrum in the 5875 - 5905 MHz frequency band for safety-related applications of Intelligent Transport Systems (ITS)*, official journal of the european union ed., August 2008.

[10] "IEEE Standard for Information technology-Telecommunications and information exchange between systems-Local and metropolitan area networks-Specific requirements - Part 11: Wireless LAN Medium Access Control (MAC) and Physical Layer (PHY) Specifications," December 2007.

[11] "ETSI ES 202 663 - Intelligent Transport Systems (ITS); European profile standard for the physical and medium access control layer of Intelligent Transport Systems operating in the 5 GHz frequency band," November 2009.

[12] "Status of ITS Communication Standards - Document HTG3-1," tech. rep., EU-US ITS

Task Force - Standards Harmonization Working Group - Harmonization Task Group 3, November 2012. ec2012.

[13] "ETSI TS 102 637-2 Intelligent Transport Systems (ITS); Vehicular Communications; Basic Set of Applications; Part 2 : Specification of Cooperative Awareness Basic Service," tech. rep., European Telecommunications Standards Institute (ETSI), 2010.

[14] C. des Dorides, "GNSS Market Report," tech. rep., European Global Navigation Satellite Systems Agency (GSA), 2013.

[15] B. Hoffmann-Wellenhof and M. Wieser, *Navigation - Principles of Positioning and Guidance*. Springer Wien New York, 2003.

[16] L. R. W. Mohinder S. Grewal and A. P. Andrews, *Global Positioning Systems, Inertial Navigation, and Integration*. Wiley-Intersience, 2nd ed., 2007.

[17] I. Skog and P. Handel, "In-Car Positioning and Navigation Technologies - A Survey," *Intelligent Transportation Systems, IEEE Transactions on*, vol. 10, pp. 4–21, March 2009.

[18] J. Huang and H.-S. Tan, "A low-order dgps-based vehicle positioning system under urban environment," *Mechatronics, IEEE/ASME Transactions on*, vol. 11, pp. 567–575, Oct 2006.

[19] T. Li, M. G. Petovello, G. Lachapelle, and C. Basnayake, "Ultra-tightly Coupled GPS/Vehicle Sensor Integration for Land Vehicle Navigation," *Navigation - Journal of the Institute of Navigation*, vol. 57, no. 4, pp. 263–274, 2010.

[20] J.-i. M. Yoshiko, K. Noriyoshi, and S. Eiji, "Positioning Technique Based on Vehicle Trajectory Using GPS Raw Data and Low-cost IMU," *International Journal of Automotive Engineering*, vol. 3, pp. 75–80, 2012.

[21] D. Randeniya, S. Sarkar, and M. Gunaratne, "Vision-IMU Integration Using a Slow-Frame-Rate Monocular Vision System in an Actual Roadway Setting," *IEEE Transactions on Intelligent Transportation Systems*, vol. 11, pp. 256–266, June 2010.

[22] N. Mattern, R. Schubert, and G. Wanielik, "High-accurate vehicle localization using digital maps and coherency images," in *IEEE Intelligent Vehicles Symposium (IV)*, pp. 462–469, June 2010.

[23] J. Levinson and S. Thrun, "Robust Vehicle Localization in Urban Environments using Probabilistic Maps," in *IEEE International Conference on Robotics and Automation (ICRA)*, pp. 4372–4378, May 2010.

[24] S. Sand, A. Dammann, and C. Mensing, *Positioning in Wireless Communications Systems*. Wiley, 2014.

[25] H. Winner, S. Hakuli, and G. Wolf, *Handbuch Fahrerassistenzsysteme: Grundlagen, Komponenten und Systeme für aktive Sicherheit und Komfort*. Vieweg+Teubner Verlag, 2012.

[26] S. Oncu, J. Ploeg, N. van de Wouw, and H. Nijmeijer, "Cooperative Adaptive Cruise Control: Network-Aware Analysis of String Stability," *IEEE Transactions on Intelligent Transportation Systems*, vol. 15, pp. 1527–1537, Aug 2014.

[27] S. E. Shladover and S.-K. Tan, "Analysis of Vehicle Positioning Accuracy Requirements for Communication-based Cooperative Collision Warning," *Journal of Intelligent Transportation Systems*, vol. 10, no. 3, pp. 131–140, 2006.

[28] P. Misra and P. Enge, *Global Positioning System: Signals, Measurements, and Performance*. Ganga-Jamuna Press, Lincoln MA, 2nd ed., 2006.

[29] H. Wallentowitz and K. Reif, *Handbuch Kraftfahrzeugelektronik: Grundlagen - Komponenten - Systeme - Anwendungen*. ATZ/MTZ-Fachbuch, Vieweg+Teubner Verlag, 2010.

[30] V. Milanes and S. E. Shladover, "Modeling Cooperative and Autonomous Adaptive Cruise Control Dynamic Responses using Experimental Data," *Transportation Research Part C: Emerging Technologies*, pp. 285–300, 2014.

[31] J. Törnros, L. Nilsson, J. Ostlund, and A. Kircher, "Effects of ACC on Driver Behaviour, Workload and Acceptance in relation to Minimum Time Headway," in *9th World Congress on Intelligent Transport Systems*, 2002.

[32] G. Stein, O. Mano, and A. Shashua, "Vision-based acc with a single camera: bounds on range and range rate accuracy," in *IEEE Intelligent Vehicles Symposium (IV)*, pp. 120–125, June 2003.

[33] "RAA - Richtlinien für die Anlage von Autobahnen."

[34] "RAL - Richtlinien für die Anlage von Landstraßen."

[35] J. Ploeg, D. Shukla, N. van de Wouw, and H. Nijmeijer, "Controller synthesis for string stability of vehicle platoons," *Intelligent Transportation Systems, IEEE Transactions on*, vol. 15, pp. 854–865, April 2014.

[36] J. Nurmi, E. S. Lohan, S. Sand, and H. Hurskainen, *GALILEO Positioning Technology*. Springer Netherlands, 2015.

[37] P. B. Ober, *Integrity Prediction & Monitoring of Navigation Systems*. Intergicom Publishers, 2003.

[38] E. Kaplan, *Understanding GPS - Principles and applications*. Artech House, 2nd edition ed., December 2005.

[39] "Road Vehicles Functional Safety: ISO DIS 26262."

[40] B. Spanfelner, D. Richter, S. Ebel, U. W. W. Branz, and C. Patz, "Challenges in applying the iso 26262 for driver assistance systems," in *5. Tagung Fahrerassistenz*, 2012.

[41] R. K. Schmidt, B. Kloiber, F. Schüttler, and T. Strang, "Degradation of communication range in vanets caused by interference 2.0 - real-world experiment," in *Proceedings of the Third International Conference on Communication Technologies for Vehicles*, (Berlin, Heidelberg), pp. 176–188, Springer-Verlag, 2011.

[42] M. Obst, L. Hobert, and P. Reisdorf, "Multi-sensor data fusion for checking plausibility of v2v communications by vision-based multiple-object tracking," in *Vehicular Networking Conference (VNC), 2014 IEEE*, pp. 143–150, Dec 2014.

[43] A. Preuschat, "German spectrum auction to set benchmark in europe," *The Wall Street Journal*, 2010.

[44] M. Schneider, "Automotive radar - status and trends," in *German Microwave Conference (GeMiC)*, (Ulm, Germany), Robert Bosch GmbH, April 2005.

[45] M. Goppelt, H. L. Blöcher, and W. Menzel, "Analytical investigation of mutual interference between automotive FMCW radar sensors," in *German Microwave Conference (GeMIC)*, pp. 1–4, March 2011.

[46] M. Goppelt, H. L. Blöcher, and W. Menzel, "Automotive Radar - Investigation of Mutual Interference Mechanisms," *Advances in Radio Science*, vol. 8, pp. 55–60, 2010.

[47] S. Salous, *Radio Propagation Measurement and Channel Modelling*. John Wiley & Sons, 2013.

[48] N. Alam, A. Balaie, and A. Dempster, "Dynamic Path Loss Exponent and Distance Estimation in a Vehicular Network Using Doppler Effect and Received Signal Strength," in *IEEE 72nd Vehicular Technology Conference Fall (VTC 2010-Fall)*, pp. 1–5, Sept 2010.

[49] R. Parker and S. Valaee, "Cooperative vehicle position estimation," in *IEEE International Conference on Communications (ICC)*, pp. 5837–5842, June 2007.

[50] K. Whitehouse, C. Karlof, and D. Culler, "A Practical Evaluation of Radio Signal Strength for Ranging-based Localization," *SIGMOBILE Mobile Computing and Communications Review*, vol. 11, pp. 41–52, January 2007.

[51] V. Kukshya, H. Krishnan, and C. Kellum, "Design of a system solution for relative positioning of vehicles using vehicle-to-vehicle radio communications during GPS outages," in *IEEE 62nd Vehicular Technology Conference (VTC Fall)*, vol. 2, pp. 1313–1317, Sept 2005.

[52] H. L. Bloecher, A. Sailer, G. Rollmann, and J. Dickmann, "79 ghz uwb automotive short

range radar-spectrum allocation and technology trends," *Advances in Radio Science*, vol. 7, no. 4, pp. 61–65, 2009.

[53] "Commission implementing decision of 29 july 2011 amending decision 2005/50/ec on the harmonisation of the 24 ghz range radio spectrum band for the time-limited use by automotive short-range radar equipment in the community."

[54] V. Issakov, *Microwave Circuits for 24 GHz Automotive Radar in Silicon-based Technologies*. Springer, 2010.

[55] R. H. Rasshofer and K. Gresser, "Automotive Radar and Lidar Systems for Next Generation Driver Assistance Functions," *Advances in Radio Science*, vol. 3, pp. 205–209, 2005.

[56] M. Schoor and B. Yang, "High-resolution angle estimation for an automotive fmcw radar sensor," in *Proceedings of the International Radar Symposium (IRS)*, 2007.

[57] M. Röckl, J. Gacnik, J. Schomerus, T. Strang, and M. Kranz, "Sensing the environment for future driver assistance combining autonomous and cooperative appliances," in *4th International Workshop on Vehicle-to-Vehicle Communications (V2VCOM)*, pp. 45–56, 2008.

[58] K. Fürstenberg and V. Willhoeft, "New Sensor for 360 Vehicle Surveillance," *IEEE Intelligent Vehicles Symposium (IV)*, pp. 3–6, 2001.

[59] D. Gohring, M. Wang, M. Schnurmacher, and T. Ganjineh, "Radar/Lidar Sensor Fusion for Car-following on Highways," in *5th International Conference on Automation, Robotics and Applications (ICARA)*, pp. 407–412, Dec 2011.

[60] R. H. Rasshofer, M. Spies, and H. Spies, "Influences of Weather Phenomena on Automotive Laser Radar Systems," *Advances in Radio Science*, vol. 9, pp. 49–60, 2011.

[61] M. Montemerlo, J. Becker, S. Bhat, H. Dahlkamp, D. Dolgov, S. Ettinger, D. Haehnel, T. Hilden, G. Hoffmann, B. Huhnke, D. Johnston, S. Klumpp, D. Langer, A. Levandowski, J. Levinson, J. Marcil, D. Orenstein, J. Paefgen, I. Penny, A. Petrovskaya, M. Pflueger, G. Stanek, D. Stavens, A. Vogt, and S. Thrun, "Junior: The Stanford Entry in the Urban Challenge," *Springer Tracts in Advanced Robotics*, vol. 56, no. October 2005, pp. 91–123, 2009.

[62] M. Harris, "Google's Self-Driving Car Pals Revealed," January 2015.

[63] A. Soloviev, "Tight coupling of GPS, Laser Scanner, and Inertial Measurements for Navigation in Urban Environments," in *IEEE/ION Position, Location and Navigation Symposium (PLANS)*, pp. 511–525, May 2008.

[64] P. Lindner and G. Wanielik, "3D LIDAR Processing for Vehicle Safety and Environment

Recognition," in *IEEE Workshop on Computational Intelligence in Vehicles and Vehicular Systems*, pp. 66–71, March 2009.

[65] M. Hansard, S. Lee, O. Choi, and R. Horaud, *Time-of-Flight Cameras - Principles, Methods and Applications*. SpringerBriefs in Computer Science, 2013.

[66] S. Acharya, C. Tracey, and A. Rafii, "System Design of Time-of-Flight Range Camera for Car Park Assist and Backup Application," in *IEEE Computer Society Conference on Computer Vision and Pattern Recognition Workshops*, pp. 1–6, June 2008.

[67] R. Lange and P. Seitz, "Solid-state Time-of-flight Range Camera," *IEEE Journal of Quantum Electronics*, vol. 37, pp. 390–397, March 2001.

[68] S. Foix, G. Alenya, and C. Torras, "Lock-in Time-of-Flight (ToF) Cameras: A Survey," *IEEE Sensors Journal*, vol. 11, pp. 1917–1926, September 2011.

[69] O. Elkhalili, O. Schrey, W. Ulfig, W. Brockherde, B. Hosticka, P. Mengel, and L. Listl, "A 64x8 Pixel 3-D CMOS Time Of Flight Image Sensor for Car Safety Applications," in *Proceedings of the 32nd European Solid-State Circuits Conference (ESSCIRC)*, pp. 568–571, Sept 2006.

[70] S. Hussmann, T. Ringbeck, and B. Hagebeuker, "A performance review of 3D TOF vision systems in comparison to stereo vision systems," *Stereo Vision*, no. November, pp. 103–120, 2008.

[71] S. Hsu, S. Acharya, A. Rafii, and R. New, "Performance of a Time-of-Flight Range Camera for Intelligent Vehicle Safety Applications," in *Advanced Microsystems for Automotive Applications 2006* (J. Valldorf and W. Gessner, eds.), VDI-Buch, pp. 205–219, Springer Berlin Heidelberg, 2006.

[72] P. Dollar, C. Wojek, B. Schiele, and P. Perona, "Pedestrian Detection: An Evaluation of the State of the Art," *Pattern Analysis and Machine Intelligence, IEEE Transactions on*, vol. 34, pp. 743–761, April 2012.

[73] M. Haberjahn and R. Reulke, "Object Discrimination and Tracking in the Surroundings of a Vehicle by a Combined Laser Scanner Stereo System," in *Proceedings of the 2010 International Conference on Computer Vision - Volume Part II*, ACCV'10, (Berlin, Heidelberg), pp. 225–234, Springer-Verlag, 2011.

[74] M. Haberjahn, *Multilevel Datenfusion Konkurrierender Sensoren in der Fahrzeugumfelderfassung*. PhD thesis, Humboldt-Universität zu Berlin, 2013.

[75] M. Perrollaz, R. Labayrade, C. Royere, N. Hautiere, and D. Aubert, "Long Range Obstacle Detection Using Laser Scanner and Stereovision," in *IEEE Intelligent Vehicles Symposium (IV)*, pp. 182–187, 2006.

[76] G. Stein, Y. Gdalyahu, and A. Shashua, "Stereo-Assist: Top-down Stereo for Driver Assistance Systems," in *IEEE Intelligent Vehicles Symposium (IV)*, pp. 723–730, June 2010.

[77] R. Labayrade, C. Royere, D. Gruyer, and D. Aubert, "Cooperative Fusion for Multi-Obstacles Detection With Use of Stereovision and Laser Scanner," *Autonomous Robots*, vol. 19, pp. 117–140, September 2005.

[78] S. Nedevschi, R. Danescu, D. Frentiu, T. Marita, F. Oniga, C. Pocol, T. Graf, and R. Schmidt, "High Accuracy Stereovision Approach for Obstacle Detection on Non-planar Roads," in *IEEE Intelligent Engineering Systems (INES)*, pp. 211–216, 2004.

[79] J. L. Giesbrecht, H. K. Goi, T. D. Barfoot, and B. A. Francis, "A vision-based Robotic Follower Vehicle," in *SPIE Defense, Security, and Sensing*, vol. 7332, pp. 73321O–73321O–12, 2009.

[80] A. Broggi and P. Cerri, "A radar driven Fusion with Vision for Vehicle Detection," *PReVENT Fusion Forum e-Journal*, vol. 1, pp. 17–18, September 2006.

[81] L. Bombini, P. Cerri, P. Medici, and G. Alessandretti, "Radar-Vision Fusion for Vehicle Detection," in *Proceedings of the International Workshop on Intelligent Transportation*, pp. 65–70, March 2006.

[82] P. Lindner, U. Scheunert, and E. Richter, "Multi Level Fusion for Environment Recognition," *ProFusion2 e-Journal*, vol. 2, pp. 24–30, 2008.

[83] L. Walchshäusl, R. Lindl, K. Vogel, and T. Tatschke, "Detection of road users in fused sensor data streams for collision mitigation," in *Advanced Microsystems for Automotive Applications*, pp. 53–65, Springer, 2006.

[84] M. G. Petovello, K. O'Keefe, B. Chanv, S. Spiller, C. Pedrosa, P. Xie, and C. Basnayake, "Demonstration of inter-vehicle uwb ranging to augment dgps for improved relative positioning," *Journal of Global Positioning Systems*, vol. 11, no. 1, 2012.

[85] G. MacGougan, K. O'Keefe, and R. Klukas, "Ultra-wideband ranging precision and accuracy," *Measurement Science and Technology*, vol. 20, no. 9, 2009.

[86] Y. Gao, X. Meng, C. M. Hancock, S. Stephenson, and Q. Zhang, "UWB/GNSS-based Cooperative Positioning Method for V2X Applications," in *27th International Technical Meeting of The Satellite Division of the Institute of Navigation*, pp. 3212–3221, September 2014.

[87] Y. Morgan, "Accurate positioning using Short-Range Communications," in *International Conference on Ultra Modern Telecommunications Workshops (ICUMT)*, pp. 1–7, October 2009.

[88] A. Peker, T. Acarman, C. Yaman, and E. Yuksel, "Vehicle localization enhancement with VANETs," in *IEEE Intelligent Vehicles Symposium (IV)*, pp. 661–666, June 2014.

[89] E. Staudinger and A. Dammann, "Round-trip Delay Ranging with OFDM signals - Performance Evaluation with Outdoor Experiments," in *Positioning, Navigation and Communication (WPNC), 2014 11th Workshop on*, pp. 1–6, March 2014.

[90] N. Alam, A. T. Balaei, and A. G. Dempster, "Range and range-rate measurements using DSRC: facts and challenges," in *IGNSS Symposium*, 2009.

[91] "Interface Specification IS-GPS-200."

[92] "Global Navigation Satellite System GLONASS - Interface Control Document - Navigation Radiosignals in bands L1, L2," 2008.

[93] B. Parkinson and J. Spilker, *Global Positioning System: Theory and Applications*. American Institute of Aeronautics & Astronautics Inc., 1996.

[94] "Specification for the Wide Area AugmeAugment System," 2001.

[95] J. Ventura-Traveset and D. Flament, eds., *EGNOS - TheEuropean Geostationary Navigation Overlay System - A Cornerstone of Galileo*. ESA Publications, 2006.

[96] M. Felux, D. Dautermann, and H. Becker, "GBAS Approach Guidance Performance - A comparison to ILS," in *Proceedings of the 2013 International Technical Meeting of The Institute of Navigation*, 2013.

[97] P. Groves, *Principles of GNSS, Inertial, and Multisensor Integrated Navigation Systems*. GNSS/GPS, Artech House, 2nd ed., 2013.

[98] D. H. Titterton and J. L. Weston, *Strapdown Inertial Navigation Technology*. Peter Peregrinus Ltd. /IEE, 2004.

[99] E. H. Shin and N. El-Sheimy, *Accuracy Improvement of Low Cost INS/GPS for Land Applications*. PhD thesis, University of Calgary, Department of Geomatics Engineering, 2001.

[100] O. Le Marchand, P. Bonnifait, J. Ibañez-Guzmán, D. Bétaille, F. Peyret, *et al.*, "Characterization of GPS Multipath for Passenger Vehicles Across Urban Environments," *ATTI dell'Istituto Italiano di Navigazione*, no. 189, pp. 77–88, 2009.

[101] M. Obst, S. Bauer, and G. Wanielik, "Urban multipath detection and mitigation with dynamic 3D maps for reliable land vehicle localization," in *IEEE/ION Position Location and Navigation Symposium (PLANS)*, pp. 685–691, April 2012.

[102] Z. Li and H. Leung, "GPS/INS Integration Based Navigation with Multipath Mitigation for Intelligent Vehicles," in *4th IEEE International Conference on Mechatronics (ICM)*, pp. 1–5, 2007.

[103] A. Giremus, J.-Y. Tourneret, and V. Calmettes, "A Particle Filtering Approach for Joint Detection/Estimation of Multipath Effects on GPS Measurements," *IEEE Transactions on Signal Processing*, vol. 55, pp. 1275–1285, April 2007.

[104] M. Lentmaier, B. Krach, and P. Robertson, "Bayesian time delay estimation of GNSS signals in dynamic multipath environments," *International Journal of Navigation and Observation*, vol. 2008, 2008.

[105] D. A. Grejner-Brzezinska, Y. Yi, and C. K. Toth, "Bridging GPS gaps in urban canyons: The benefits of ZUPTs," *Navigation - Journal of the Institute of Navigation*, vol. 48, no. 4, pp. 217–225, 2001.

[106] N. El-Sheimy, E. H. Shin, and X. Niu, "Kalman Filter Face-off: Extended vs. Unscented Kalman Filters for Integrated GPS and MEMS Inertial," *Inside GNSS*, vol. 1, no. 2, pp. 48–54, 2006.

[107] V. Honkavirta, T. Perala, S. Ali-Loytty, and R. Piche, "A comparative survey of WLAN location fingerprinting methods," in *6th Workshop on Positioning, Navigation and Communication (WPNC)*, pp. 243–251, March 2009.

[108] G. Hejc, J. Seitz, and T. Vaupel, "Bayesian sensor fusion of Wi-Fi signal strengths and GNSS code and carrier phases for positioning in urban environments," in *IEEE/ION Position, Location and Navigation Symposium (PLANS)*, pp. 1026–1032, May 2014.

[109] H. Lu, S. Zhang, Y. Dong, and X. Lin, "A Wi-Fi/GPS integrated system for urban vehicle positioning," in *13th International IEEE Conference on Intelligent Transportation Systems (ITSC)*, pp. 1663–1668, September 2010.

[110] J. Laneurit, C. Blanc, R. Chapuis, and L. Trassoudaine, "Multisensorial Data Fusion for Global Vehicle and Obstacles Absolute Positioning," in *Proceedings of the IEEE Intelligent Vehicles Symposium (IV)*, pp. 138–143, June 2003.

[111] T.-D. Vu, *Vehicle Perception: Localization, Mapping with Detection, Classification and Tracking of Moving Objects*. PhD thesis, Institut National Polytechnique de Grenoble - INPG, September 2009.

[112] R. Toledo-Moreo, D. Betaille, F. Peyret, and J. Laneurit, "Fusing GNSS, Dead-Reckoning, and Enhanced Maps for Road Vehicle Lane-Level Navigation," *IEEE Journal of Selected Topics in Signal Processing*, vol. 3, pp. 798–809, October 2009.

[113] R. J., S. T., and T. G.F., "Cooperative GNSS-Based Method for Vehicle Positioning," *Gyroscopy and Navigation*, vol. 3, no. 4, pp. 245–254, 2012.

[114] N. Alam, A. Tabatabaei Balaei, and A. G. Dempster, "A DSRC Doppler-Based Cooperative

Positioning Enhancement for Vehicular Networks With GPS Availability," *IEEE Transactions on Vehicular Technology*, vol. 60, pp. 4462–4470, November 2011.

[115] T. S. Dao, K. Y. K. Leung, C. M. Clark, and J. P. Huissoon, "Markov-based Lane Positioning using Intervehicle Communication," *IEEE Transactions on Intelligent Transportation Systems*, vol. 8, pp. 641–650, December 2007.

[116] F. Berefelt, B. Boberg, J. Nygårds, and P. Strömbäck, "Collaborative GPS/INS Navigation in Urban Environment," in *Proceedings of the 2004 National Technical Meeting of The Institute of Navigation (ION-NTM)*, 2004.

[117] R. Garello, L. Lo Presti, G. Corazza, and J. Samson, "Peer-to-Peer Cooperative Positioning Part I: GNSS Aided Acquisition," *Inside GNSS*, no. March/, pp. 55–63, 2012.

[118] M. Röckl, T. Strang, and M. Kranz, "V2V Communications in Automotive Multi-Sensor Multi-Target Tracking," in *IEEE 68th Vehicular Technology Conference (VTC Fall)*, pp. 1–5, September 2008.

[119] C. C. Kellum, "Basic Feasibility of GPS Positioning without Carrier-Phase Measurements as a Relative Position Sensor between Two Vehicles," in *Proceedings of the 2005 National Technical Meeting of The Institute of Navigation*, pp. 903–910, 2005.

[120] E. Richter, M. Obst, R. Schubert, and G. Wanielik, "Cooperative relative localization using vehicle-to-vehicle communications," in *12th International Conference on Information Fusion (FUSION)*, pp. 126–131, July 2009.

[121] N. Alam, A. Balaei, and A. Dempster, "Positioning Enhancement with Double Differencing and DSRC," in *Proceedings of the 23rd International Technical Meeting of The Satellite Division of the Institute of Navigation (ION GNSS 2010)*, (Portland, OR), pp. 1210–1218, September 2010.

[122] N. Alam, A. Tabatabaei Balaei, and A. G. Dempster, "Relative Positioning Enhancement in VANETs: A Tight Integration Approach," *IEEE Transactions on Intelligent Transportation Systems*, vol. PP, no. 99, pp. 1 –9, 2012.

[123] D. Yang, F. Zhao, K. Liu, H. B. Lim, E. Frazzoli, and D. Rus, "A GPS Pseudorange Based Cooperative Vehicular Distance Measurement Technique," in *IEEE 75th Vehicular Technology Conference (VTC Spring)*, pp. 1–5, IEEE, 2012.

[124] S. Zeng, "Performance Evaluation of Automotive Radars Using Carrier-Phase Differential GPS," *IEEE Transactions on Instrumentation and Measurement*, vol. 59, pp. 2732–2741, October 2010.

[125] N. Luo, *Precise Relative Positioning of Multiple Moving Platforms Using GPS Carrier Phase*

Observables. PhD thesis, University of Calgary, Department of Geomatics Engineering, 2001.

[126] N. Luo and G. Lachapelle, "Relative positioning of multiple moving platforms using GPS," *IEEE Transactions on Aerospace and Electronic Systems*, vol. 39, no. 3, pp. 936–948, 2003.

[127] C. Basnayake, C. Kellum, J. Sinko, and J. Strus, "GPS-Based Relative Positioning Test Platform for Automotive Active Safety Systems," in *Proceedings of the 19th International Technical Meeting of the Satellite Division of The Institute of Navigation (ION GNSS 2006)*, 2006.

[128] S. S. Hwang and J. Speyer, "Particle Filters With Adaptive Resampling Technique Applied to Relative Positioning Using GPS Carrier-Phase Measurements," *IEEE Transactions on Control Systems Technology*, vol. 19, pp. 1384–1396, Nov 2011.

[129] W. Travis and D. Bevly, "Trajectory duplication using relative position information for automated ground vehicle convoys," in *IEEE/ION Position Location and Navigation Symposium (PLANS)*, pp. 1022–1032, May 2008.

[130] W. E. Travis III, *Path duplication using GPS carrier based relative position for automated ground vehicle convoys*. PhD thesis, Auburn University, 2010.

[131] K. Ansari, C. Wang, L. Wang, and Y. Feng, "Vehicle-to-vehicle Real-time Relative Positioning using 5.9 GHz DSRC Media," in *IEEE 78th Vehicular Technology Conference (VTC-Fall)*, pp. 1–7, September 2013.

[132] K. Ansari, Y. Feng, and M. Tang, "A Runtime Integrity Monitoring Framework for Real-Time Relative Positioning Systems Based on GPS and DSRC," *IEEE Transactions on Intelligent Transportation Systems*, vol. PP, no. 99, pp. 1–13, 2014.

[133] F. de Ponte Müller, D. Navarro Tapia, and M. Kranz, "Precise relative positioning of vehicles with on-the-fly carrier phase resolution and tracking," *International Journal of Distributed Sensor Networks*, 2015.

[134] T. Logsdom, *The Navstar Global Positioning System*. Van Nostrand Reinhold, 1992.

[135] "BeiDou Navigation Satellite System - Signal In Space - Interface Control Document - Open Service Signal B1I," 2012.

[136] K. Borre, D. Akos, N. Bertelsen, P. Rinder, and S. Jensen, *A Software-Defined GPS and Galileo Receiver: Single-Frequency Approach*. Birkhäuser, 2007.

[137] J. Rosen and L. Q. Gothard, *Encyclopedia of Physical Science*. Facts on File, 2009.

[138] N. Bowditch, *The American Practical Navigator*. National Imagery and Mapping Agency, U.S. Government, 2002.

[139] J. Wendel, *Integrierte Navigationssysteme - Sensordatenfusion, GPS und Inertiale Navigation*. Oldenbourg Verlag, 2011.

[140] A. v. d. Bos, *Parameter Estimation for Scientists and Engineers*. John Wiley & Sons, 2007.

[141] R. C. Rao, "Information and the accuracy attainable in the estimation of statistical parameters," *Bull. Calcutta Math. Soc.*, vol. 37, pp. 81–91, 1945.

[142] J. Joyce, "Bayes' Theorem," in *The Stanford Encyclopedia of Philosophy* (E. N. Zalta, ed.), Stanford University, 2008.

[143] S. Thrun, W. Burgard, and D. Fox, *Probabilistic Robotics (Intelligent Robotics and Autonomous Agents)*. The MIT Press, 2005.

[144] A. Papoulis, *Probability, Random Variables and Stochastic Processes*. New York: McGraw-Hill, 2 ed., 1984.

[145] M. S. Arulampalam, S. Maskell, and N. Gordon, "A tutorial on particle filters for online nonlinear/non-Gaussian Bayesian tracking," *IEEE Transactions on Signal Processing*, vol. 50, pp. 174–188, 2002.

[146] R. E. Kalman, "A New Approach to Linear Filtering and Prediction Problems," *Journal of Basic Engineering*, 1960.

[147] Y. Bar-Shalom, *Tracking and Data Association*. San Diego, CA, USA: Academic Press Professional, Inc., 1987.

[148] S. J. Julier and J. K. Uhlmann, "A New Extension of the Kalman Filter to Nonlinear Systems," in *Proceedings of Signal Processing, Sensor Fusion, and Target Recognition VI (SPIE 3068)*, pp. 182–193, 1997.

[149] B. Krach, *Sensor Fusion by Bayesian Filtering for Seamless Pedestrian Navigation*. PhD thesis, Universität Erlangen, 2010.

[150] M. R. Endsley, "Toward a Theory of Situation Awareness in Dynamic Systems," *Human Factors: The Journal of the Human Factors and Ergonomics Society*, vol. 37, pp. 32–64, 1995.

[151] M. Röckl, *Cooperative Situation Awareness in Transportation.* PhD thesis, University of Innsbruck, 2010.

[152] Z. Papp, C. Brown, and C. Bartels, "World modeling for cooperative intelligent vehicles," in *IEEE Intelligent Vehicles Symposium (IV)*, pp. 1050–1055, June 2008.

[153] H. Menouar, F. Filali, and A. Abu-Dayya, "Efficient and unique identifier for V2X events aggregation in the Local Dynamic Map," in *11th International Conference on ITS Telecommunications (ITST)*, pp. 369–374, August 2011.

[154] "ETSI EN 302 895 V1.0.0 (2014-01) Intelligent Transport Systems (ITS); Vehicular Communications; Basic Set of Applications; Local Dynamic Map (LDM)," tech. rep., European Telecommunications Standards Institute (ETSI), 2014.

[155] R. Schmidt, R. Lasowski, T. Leinmu?ller, C. Linnhoff-Popien, and G. Schafer, "An approach for selective beacon forwarding to improve cooperative awareness," in *IEEE Vehicular Networking Conference (VNC)*, pp. 182–188, December 2010.

[156] J. Mittag, F. Thomas, J. Härri, and H. Hartenstein, "A Comparison of Single- and Multi-hop Beaconing in VANETs," in *Proceedings of the 6th ACM International Workshop on Vehicular Internetworking (VANET)*, pp. 69–78, 2009.

[157] "Recommended Practice J670 Vehicle Dynamics Terminology," July 1976.

[158] S. J. Russell and P. Norvig, *Artificial Intelligence: A Modern Approach*. Pearson Education, 2 ed., 2003.

[159] V. Katukoori, "Standardizing availability definition," Master's thesis, University of New Orleans, 1995.

[160] D. Warren, *Broadcast vs. Precise GPS Ephemerides: A Historical Perspective*. BiblioBazaar, 2012.

[161] A. Roulston, N. talbot, and K. Zhang, "An Evaluation of Various GPS Satellite Ephemerides," in *Proceedings of the 13th International Technical Meeting of the Satellite Division of The Institute of Navigation (ION GPS 2000)*, pp. 45–54, 2000.

[162] W. Marquis and M. Shaw, "GPS III Bringing New Capabilities to the Global Community," *Inside GNSS*, 2011.

[163] B. W. Parkinson and P. K. Enge, "Differential GPS," *Global Positioning System: Theory and Applications*, vol. 2, pp. 3–50, 1996.

[164] F. Vannicola, R. Beard, J. White, K. Senior, T. Kubik, D. Wilson, and J. Buisson, "GPS Block IIF Rubidium Frequency Standard Life Test," tech. rep., DTIC Document, 2009.

[165] J. Saastamoinen, "Atmospheric Correction for the Troposphere and Stratosphere in Radio Ranging Satellites," *The use of artificial satellites for geodesy*, pp. 247–251, 1972.

[166] C. C. Goad and L. Goodman, "A modified Hopfield Tropospheric Refraction Correction Model," in *Proceeding of the Fall Annual Meeting of the American Geophysical Union*, (San Francisco, California), The American Institute of Aeronautics and Astronautics, Inc., 12 1974.

[167] T. A. Skidmore and F. van Graas, "An Investigation of Tropospheric Errors on Differential

GNSS Accuracy and Integrity," in *Proceedings of the 17th International Technical Meeting of the Satellite Division of The Institute of Navigation (ION GNSS)*, pp. 2752–2760, 2004.

[168] D. Lawrence, R. B. Langley, D. Kim, F. Chan, and B. Pervan, "Decorrelation of Troposphere across Short Baseline," in *IEEE/ION Position, Location and Navigation Symposium (PLANS)*, pp. 97–102, 2006.

[169] J. Klobuchar, "Ionospheric Time-Delay Algorithm for Single-Frequency GPS Users," *IEEE Transactions on Aerospace and Electronic Systems*, vol. AES-23, no. 3, pp. 325–331, 1987.

[170] W. Feess and S. Stephens, "Evaluation of the GPS Ionospehric Model," *IEEE Transactions on Aerospace and Electronic Systems*, vol. AES-23, no. 3, pp. 332–338, 1987.

[171] S. Khanafseh, S. Pullen, and J. Warburton, "Carrier Phase Ionospheric Gradient Ground Monitor for GBAS with Experimental Validation," *Navigation - Journal of the Institute of Navigation*, vol. 59, no. 1, pp. 51–60, 2012.

[172] D. Zhang and Z. Xiao, "Study of Ionospheric Response to the 4B flare on 28 October 2003 using International GPS Service Network Data," *Journal of Geophysical Research: Space Physics*, vol. 110, no. A3, pp. 1978–2012, 2005.

[173] R. A. Nelson, "Relativistic time transfer in the solar system," in *IEEE International Frequency Control Symposium*, pp. 1278–1283, May 2007.

[174] G. Strang and K. Borre, *Linear Algebra, Geodesy, and GPS*. Wellesley-Cambridge Press, 1997.

[175] F. de Ponte Müller, A. Steingass, and T. Strang, "Zero-Baseline Measurements for Relative Positioning in Vehicular Environments," in *Proceedings of the 6th European Workshop on GNSS Signals and Signal Processing*, 2013.

[176] F. de Ponte Müller, L. M. Navajas, and T. Strang, "Characterization of a Laser Scanner Sensor for the use as a Reference System in Vehicular Relative Positioning," in *Communication Technologies for Vehicles*, pp. 146–158, Springer Berlin Heidelberg, 2013.

[177] A. Lehner, A. Steingass, and F. Schubert, "A Novel Channel Model for Land Mobile Satellite Navigation," *ATTI Journal dell'Istituto Italiano di Navigazione* , pp. 108–119, 2009.

[178] J. Zhang, K. Zhang, R. Grenfell, and R. Deakin, "GPS Satellite Velocity and Acceleration Determination using theBroadcast Ephemeris," *Journal Of Navigation*, vol. 59, pp. 293–305, 2006.

[179] W. Stockwell, "Angle Random Walk," tech. rep., Crossbow Technology, Inc., 2003.

[180] O. Woodman, "An Introduction to Inertial Navigation," tech. rep., University of Cambridge - Computer laboratory, 2007.

[181] D. W. Allan, N. Ashby, and C. Hodge, "The Science of Timekeeping," tech. rep., Hawlett-Packard, 1997.

[182] "IEEE Standard Specification Format Guide and Test Procedure for Single-Axis Interferometric Fiber Optic Gyros," *IEEE Std 952-1997*, 1998.

[183] R. van der Merwe, E. A. Wan, and S. I. Julier, "Sigma-Point Kalman Filters for Nonlinear Estimation and Sensor-Fusion: Applications to Integrated Navigation," in *Proceedings of the AIAA Guidance, Navigation & Control Conference*, pp. 16–19, 2004.

[184] L. Serrano, D. Kim, R. B. Langley, K. Itani, and M. Ueno, "A GPS Velocity Sensor: How Accurate can it be? A First Look," in *Proceedings of the National Technical Meeting of The Institute of Navigation*, pp. 875–885, January 2004.

[185] P. Zhang, J. Gu, E. Milios, and P. Huynh, "Navigation with IMU/GPS/digital Compass with Unscented Kalman Filter," in *IEEE International Conference Mechatronics and Automation*, vol. 3, pp. 1497–1502, 2005.

[186] S. Sukkarieh, *Low Cost, High Integrity, Aided Inertial Navigation Systems for Autonomous Land Vehicles*. PhD thesis, ACFR - University of Sydney, March 2000.

[187] S. Rezaei and R. Sengupta, "Kalman Filter Based Integration of DGPS and Vehicle Sensors for Localization," in *IEEE International Conference Mechatronics and Automation*, vol. 1, pp. 455–460, July 2005.

[188] B. Mourllion, D. Gruyer, and A. Lambert, "Variance Behavior and Signification in Probabilistic Framework Applied to Vehicle Localization," in *IEEE Intelligent Vehicles Symposium (IV)*, pp. 294–299, 2006.

[189] R. Pepy, A. Lambert, and H. Mounier, "Path Planning using a Dynamic Vehicle Model," in *Information and Communication Technologies (ICTTA)*, vol. 1, pp. 781–786, 2006.

[190] B. H. Dwiggins, *Automotive Steering Systems*. Delmar Publishers, 1968.

[191] M. Mählisch, W. Ritter, and K. Dietmayer, "ACC Vehicle Tracking with Joint Multisensor Multitarget Filtering of State and Existence," *PReVENT Fusion Forum e-Journal*, vol. 1, pp. 37–43, 2006.

[192] K. Jo, K. Chu, and M. Sunwoo, "Interacting Multiple Model Filter-Based Sensor Fusion of GPS With In-Vehicle Sensors for Real-Time Vehicle Positioning," *IEEE Transactions on Intelligent Transportation Systems*, vol. 13, pp. 329–343, March 2012.

[193] S. Blackman and R. Popoli, *Design and Analysis of Modern Tracking Systems*. Artech House, 1999.

[194] D. Aloi and O. Korniyenko, "Comparative Performance Analysis of a Kalman Filter and

a Modified Double Exponential Filter for GPS-Only Position Estimation of Automotive Platforms in an Urban-Canyon Environment," *IEEE Transactions on Vehicular Technology*, vol. 56, pp. 2880–2892, September 2007.

[195] N. M. Drawil and O. Basir, "Intervehicle-Communication-Assisted Localization," *IEEE Transactions on Intelligent Transportation Systems*, vol. 11, no. 3, pp. 678–691, 2010.

[196] E. D. Martí, D. Martín, J. García, A. de la Escalera, J. M. Molina, and J. M. Armingol, "Context-aided sensor fusion for enhanced urban navigation," *Sensors*, vol. 12, no. 12, pp. 16802–16837, 2012.

[197] R. Schubert, E. Richter, and G. Wanielik, "Comparison and evaluation of advanced motion models for vehicle tracking," in *11th International Conference on Information Fusion*, pp. 1–6, June 2008.

[198] T. C. Ng, J. Guzman, and M. Adams, "Autonomous vehicle-following systems : a virtual trailer link model," in *IEEE/RSJ International Conference on Intelligent Robots and Systems (IROS)*, pp. 3057–3062, August 2005.

[199] M. Tsogas, A. Polychronopoulos, and A. Amditis, "Unscented Kalman filter design for curvilinear motion models suitable for automotive safety applications," in *8th International Conference on Information Fusion*, vol. 2, pp. 1295–1302, July 2005.

[200] G. Dissanayake, S. Sukkarieh, E. Nebot, and H. Durrant-Whyte, "The Aiding of a low-cost Strapdown Inertial Measurement Unit using Vehicle Model Constraints for Land Vehicle Applications," *IEEE Transactions on Robotics and Automation*, vol. 17, pp. 731–747, Oct 2001.

[201] A. Brakemeier, "White Paper on Network Design Limits and VANET Performance (V0.6)," tech. rep., Car 2 Car Communication Consortium (C2C-CC), 2009.

[202] B. Kloiber, "Bigger is Better - Combining Contention Window Adaptation with Geo-based Backoff Generation in DSRC Networks," in *Proceedings of the International Conference on Connected Vehicles and Expo*, 2014.

[203] U. Keskin, "Evaluating Message Transmission Times in Controller Area Network (CAN) without Buffer Preemption Revisited," in *IEEE 78th Vehicular Technology Conference (VTC Fall)*, pp. 1–5, Sept 2013.

[204] D. M. Hawkins, *Identification of Outliers*. Chapman and Hall, 1980.

[205] M. Obst, C. Adam, G. Wanielik, and R. Schubert, "Probabilistic Multipath Mitigation for GNSS-based Vehicle Localization in Urban Areas," in *Proceedings of the 24th International Technical Meeting of The Satellite Division of the Institute of Navigation (ION GNSS)*, 2012.

[206] P. C. Mahalanobis, "On the Generalized Distance in Statistics," in *Proceedings National Institute of Science*, vol. 2, pp. 49–55, April 1936.

[207] B. Kloiber, T. Strang, M. Rockl, and F. de Ponte-Muller, "Performance of CAM based safety applications using ITS-G5A MAC in high dense scenarios," in *IEEE Intelligent Vehicles Symposium (IV)*, pp. 654–660, June 2011.

[208] J. Breu, A. Brakemeier, and M. Menth, "Analysis of Cooperative Awareness Message rates in VANETs," in *13th International Conference on ITS Telecommunications (ITST)*, pp. 8–13, November 2013.

[209] J. Awange, *Environmental Monitoring Using GNSS*. Springer-Verlag Berlin Heidelberg, 2012.

[210] "ETSI TS 102 636-4-1 Intelligent Transport Systems (ITS); Vehicular communications; GeoNetworking; Part 4: Geographical addressing and forwarding for point-to-point and point-to-multipoint communications; Sub-part 1: Media-Independent Functionality."

[211] International Telecommunication Union, "Reference Model of Open Systems Interconnection for CCITT Applications." ITU-T Recommendation X.200, 1988.

[212] H. Hartenstein and K. Laberteaux, "A Tutorial Survey on Vehicular Ad Hoc Networks," *IEEE Communications Magazine*, vol. 46, pp. 164–171, June 2008.

[213] J.-C. Lin, C.-S. Lin, C.-N. Liang, and B.-C. Chen, "Wireless Communication Performance based on IEEE 802.11p R2V Field Trials," *IEEE Communications Magazine*, vol. 50, pp. 184–191, May 2012.

[214] V. Shivaldova and C. Mecklenbrauker, "A Two-State Packet Error Model for Vehicle-to-Infrastructure Communications," in *IEEE 78th Vehicular Technology Conference (VTC Fall)*, pp. 1–5, September 2013.

[215] F. Bai and H. Krishnan, "Reliability Analysis of DSRC Wireless Communication for Vehicle Safety Applications," in *IEEE Intelligent Transportation Systems Conference (ITSC)*, pp. 355–362, September 2006.

[216] B. Kloiber, C. Rico-Garcia, J. Härri, and T. Strang, "Update Delay: A new Information-Centric Metric for a Combined Communication and Application Level Reliability Evaluation of CAM based Safety Applications," in *ITS World Congress*, 2012.

[217] R. N. Jazar, *Vehicle Dynamics: Theory and Application*. Springer, 2008.

[218] E. D. Dickmanns, *Dynamic Vision for Perception and Control of Motion*. Springer, 2007.

[219] K. A. Atkinson, *An Introduction to Numerical Analysis*. New York: John Wiley, 2nd ed., 1989.

[220] W. Gurtner and L. Estery, "RINEX - The Receiver Independent Exchange Format - Version 3.00," 2007.

[221] B. Hofmann-Wellenhof, H. Lichtenegger, and J. Collins, *Global Positioning System: Theory and Practice*. Springer-Verlag Wien GmbH, 1998.

[222] B. van Arem, C. van Driel, and R. Visser, "The Impact of Cooperative Adaptive Cruise Control on Traffic-Flow Characteristics," *IEEE Transactions on Intelligent Transportation Systems*, vol. 7, pp. 429–436, December 2006.

[223] P. Li, L. Alvarez, and R. Horowitz, "AHS Safe Control Laws for Platoon Leaders," *IEEE Transactions on Control Systems Technology*, vol. 5, pp. 614–628, November 1997.

[224] P. Greibe, "Braking Distance, Friction and Behaviour - Findings, Analyses and Recommendations based on Braking Trials," tech. rep., Trafitec, 2007.

[225] T. Warne, ed., *A Policy on Geometric Design of Highways and Streets*. American Association of State Highway and Transportation Officials, 2001.

[226] D. Simon, *Optimal State Estimation*. John Wiley & Sons, 2006.

[227] H. Kuhlmann, "Kalman-filtering with Coloured Measurement Noise for Deformation Analysis," in *Proceedings of the 11th FIG International Symposium on Deformation Measurements*, pp. 25–28, John Wiley and sons, 2003.

[228] F. Gustafsson, S. Ahlqvist, U. Forssell, and N. Persson, "Sensor Fusion for Accurate Computation of Yaw Rate and Absolute Velocity," in *Society of Automotive Engineers World Congress*, 2001.

[229] M. Braasch, "Isolation of GPS Multipath and Receiver Tracking Errors," *Navigation - Journal of the Institute of Navigation*, vol. 41, no. 4, pp. 511–521, 1994.

[230] North Atlantic Treaty Organization, *NATO Standard Agreement STANAG 4294 Issue 1*, 1993.

[231] A. Santini, *OBD-II: Functions, Monitors and Diagnostic Techniques*. Cengage Learning, 2010.

[232] M. Obst, E. Richter, and G. Wanielik, "Accurate Relative Localization for Land Vehicles with SBAS Corrected GPS/INS Integration and V2V Communication," in *Proceedings of the 24th International Technical Meeting of The Satellite Division of the Institute of Navigation (ION GNSS 2011)*, pp. 363–371, 2011.

[233] M. Petovello, K. O'Keefe, and B. Chan, "Demonstration of inter-vehicle UWB ranging to augment DGPS for improved relative positioning," in *Proceedings of the 23rd International*

Technical Meeting of The Satellite Division of the Institute of Navigation (ION GNSS), 2010.

[234] T. Abbas, F. Tufvesson, and J. Karedal, "Measurement based Shadow Fading Model for Vehicle-to-Vehicle Network Simulations," *International Journal of Antennas and Propagation*, vol. abs/1203.3370, 2015.

[235] E. N. Gilbert, "Capacity of a burst-noise channel," *Bell System Technical Journal*, vol. 39, pp. 1253–1265, September 1960.

[236] F. de Ponte Müller, E. Munoz Diaz, and I. Rashdan, "Cooperative Positioning and Radar Sensor Fusion for Relative Localization of Vehicles," in *Proceedings of the IEEE Intelligent Vehicles Symposium*, 2013.